Schémas numériques mimétiques et conservatifs pour la simulation d'écoulements multiphasiques compressibles

Thibaud Vazquez Gonzalez

NNT : 2016SACLC051

Thèse de doctorat de l'Université Paris-Saclay préparée à CentraleSupélec

Ecole doctorale n°574
Mathématiques Hadamard
Spécialité de doctorat : Mathématiques appliquées

par

M. Thibaud Vazquez-Gonzalez

Schémas numériques mimétiques et conservatifs pour la simulation d'écoulements multiphasiques compressibles

Thèse présentée et soutenue à Châtenay-Malabry, le 17 Juin 2016.

Composition du Jury :

M.	Olivier Simonin	Professeur INP Toulouse	(Président du jury)
M.	Aziz Hamdouni	Enseignant Chercheur Université de La Rochelle	(Rapporteur)
M.	Raphaël Loubère	Chargé de recherche Université de Toulouse	(Rapporteur)
M.	Michaël NDJINGA	Ingénieur de recherche CEA/DEN	(Examinateur)
M.	Theofanis Theofanous	Professeur Université de Californie	(Examinateur)
M.	David Youngs	Ingénieur de recherche AWE	(Examinateur)
M.	Antoine Llor	Ingénieur de recherche CEA/DAM	(Codirecteur de thèse)
M.	Marc Massot	Professeur Centrale Supélec	(Codirecteur de thèse)
M.	Christophe Fochesato	Ingénieur de recherche CEA/DEN	(Invité)
M.	Peppino Terpolilli	Ingénieur TOTAL	(Invité)

université PARIS-SACLAY | École doctorale de mathématiques Hadamard (EDMH)

Titre : Schémas numériques mimétiques et conservatifs pour la simulation d'écoulements multiphasiques compressibles

Mots clefs : schéma compatible, conservation énergie, choc, multiphasique, écoulement compressible, Arbitrary Lagrangian–Eulerian

Résumé : Dans certaines simulations numériques exigeantes de mécanique des fluides, il est nécessaire de simuler des écoulements multiphasiques impliquant de nombreuses contraintes simultanées: nombre de fluides important, évolutions compressibles à la fois isentropes et fortement choquées, équations d'états variables et contrastées, déformations importantes et transport sur des longues distances. Afin de remplir ces objectifs de manière robuste, il est nécessaire que la cohérence thermodynamique du schéma numérique soit vérifiée.
Dans le premier chapitre, un schéma de type Lagrange plus projection est proposé pour la simulation d'écoulements diphasiques avec un modèle squelette à six équations et sans termes de dissipation. L'importance de la propriété de préservation des écoulements isentropiques est mise en évidence à l'aide d'une comparaison avec des résultats issus de la littérature pour le test de Ransom. Ce chapitre souligne aussi certaines limitations de l'approche Lagrange plus projection pour simuler des modèles multiphasiques.
Afin de pallier ces limitations, une nouvelle procédure de dérivation est proposée afin de construire un schéma mimétique pour la simulation d'écoulements instationnaires compressibles dans un formalisme ALE direct (Arbitrary Lagrangian–Eulerian). La possibilité de choisir a priori les degrés de liberté permet de s'inscrire dans une continuité avec les schémas historiques décalés, tout en imposant les conservations au niveau discret. L'équation de quantité de mouvement discrète est obtenue par application d'un principe variationnel, assurant par construction la cohérence thermodynamique des efforts de pression. Cette approche est appliquée au cas d'écoulements monofluides comme preuve de concept au Chapitre 3, puis elle est étendue au cas d'écoulements à N-phases compressibles au Chapitre 4. Des tests mono et multiphasiques montrent un comportement satisfaisant en terme de conservativité, versatilité aux mouvements de grilles et robustesse.

Title : Conservative and mimetic numerical schemes for compressible multiphase flows simulation

Keywords : compatible scheme, energy conservation, shock, multi-fluid, compressible flow, Arbitrary Lagrangian–Eulerian

Abstract : In some highly demanding fluid dynamics simulations, it appears necessary to simulate multiphase flows involving numerous constraints at the same time: large numbers of fluids, both isentropic and strongly shocked compressible evolution, highly variable and contrasted equations of state, large deformations, and transport over large distances. Fulfilling such a challenge in a robust and tractable way demands that thermodynamic consistency of the numerical scheme be carefully ensured.
In the first chapter, a Lagrange plus remap scheme is proposed for the simulation of two-phase flows with a dissipation-free six-equation backbone model. The importance of the property of isentropic flow preservation is highlighted with a comparison with Ransom test results from the literature. This chapter also also point out certain limitations of the Lagrange plus remap approach for multiphase simulations.
In order to overcome these limitations, a novel derivation procedure is proposed to construct a mimetic scheme for the simulation of unsteady and compressible flows in a direct ALE (Arbitrary Lagrangian-Eulerian) formalism. The possibility to choose a priori the degrees of freedom allows to obtain a continuity with historical staggered scheme, while imposing conservativity at discrete level. The discrete momentum evolution equation is obtained by application of a variational principle, thus natively ensuring the thermodynamic consistency of pressure efforts. This approach is applied to single-fluid flows as a proof of concept in Chapter 3, then it is extended to N-phase compressible flows in Chapter 4. Single- and multi-phase tests show satisfactory behavior in terms on conservation, versatility to grid motions, and robustness.

Université Paris-Saclay
Espace Technologique / Immeuble Discovery
Route de l'Orme aux Merisiers RD 128 / 91190 Saint-Aubin, France

He who says he can and he who says he can't are both usually right.

Confucius

Only those who will risk going too far can possibly find out how far one can go.

T.S. Eliot

Remerciements

Contrairement à la croyance populaire, le déroulement d'une thèse de doctorat n'est en rien un travail solitaire durant lequel le doctorant se retrouve, tel un ermite, à devoir avancer péniblement le long d'un chemin tortueux et fatiguant. Même si la thèse implique une remise en question permanente et comporte son lot de difficultés, d'incertitudes, d'épreuves, d'échecs et de rebondissements, j'ai toujours pu compter sur un soutien permanent de ma hiérarchie, de mon équipe d'encadrement et de ma famille.

Commencer une thèse de doctorat au Commisariat à l'Énergie Atomique n'est pas une chose aisée. Entre les contraintes liées aux applications industrielles et la nécessité d'obtenir des résultats pertinents sur le plan académique, l'étudiant peut facilement se retrouver perdu et avoir l'impression, à la manière d'Ulysse, d'osciller constamment entre Charybde et Scylla. Néanmoins, j'ai toujours pu compter sur le soutien et la compréhension de Stéphane Bernard et Jean-Philippe Perlat qui m'ont accueilli comme doctorant dans leur service et laboratoire respectif.

La qualité et l'originalité d'un travail de thèse est étroitement liée à l'alchimie entre l'étudiant et son directeur de thèse. Dans mon cas, le soutien et la disponibilité dont a fait preuve Antoine Llor ont joué pour beaucoup dans l'accomplissement de ce travail de doctorat. En me permettant d'être à la fois autonome et encadré, il a su créer des conditions de travail très favorables à ma maitrise progressive du sujet et aux contributions que j'ai pu apporter.

Je tiens également à remercier l'École Centrale Paris en la personne de Marc Massot. Son cours sur les écoulements à particules dispersées dans un fluide porteur m'a permis de situer mon sujet par rapport aux différentes approches utilisées dans la communauté scientifique aujourd'hui.

Je remercie aussi chaleureusement mon encadrant CEA, Christophe Fochesato, pour ses

conseils avisés, que ce soit pour la dérivation du schéma, la préparation des exposés en conférence ou la rédaction des articles et du présent manuscrit de thèse. Ses relectures méticuleuses et son insistance à mettre en valeur les nouveautés de mes travaux m'ont grandement aidé à préciser mon propos.

Je remercie l'ensemble des membres du jury d'avoir accepté d'étudier, de comprendre et d'évaluer mon travail de thèse. Je remercie les rapporteurs Raphaël Loubère et Aziz Hamdouni pour la qualité et la clarté de leur rapport.

Je remercie les membres de LSI, mon laboratoire d'accueil au CEA, pour leurs conseils et leurs remarques sur mon travail. Une mention spéciale pour Claire Boulier qui m'a aidé à effectuer toutes les démarches administratives avec une bonne humeur à toute épreuve.

Un grand merci aux doctorants, post-doctorants et stagiaires du couloir O du bâtiment B. Merci à Alan, Guillaume, Raphael, Nicolas, Lucile, Clément, Florian, Thibaut et tous ceux qui ont activement participé aux discussions des repas de midi.

Un immense merci à ma famille (française et espagnole) et à mes amis pour leur soutien indéfectible durant ces trois années de thèse. Merci à l'ensemble de la famille Annen, pour leur soutien et leurs encouragements (et aussi pour les vacances et les week-end au soleil loin de la grisaille parisienne). Merci à ma maman et à ma petite soeur pour le courage, la compréhension et l'ouverture d'esprit dont elles ont fait preuve durant mes longues études.

Enfin, je souhaiterais remercier ma compagne, Fanny qui a subi cette thèse au quotidien. Elle a su me motiver dans les moments de doute et de découragement, partageant mes difficultés, mes peines et mes épreuves en me forçant à donner le meilleur de moi-même à chaque instant.

Table des matières

Table des figures

Chapitre 1

Introduction générale

1.1 Motivations

Ce travail s'inscrit dans le cadre d'études prospectives pour la simulation numérique d'écoulements à particules dispersées dans un fluide porteur — encore appelés sprays — notamment pour les applications rencontrées au CEA/DAM de Bruyères-le-Châtel. La modélisation de sprays est d'une importance industrielle majeure dans de nombreux domaines scientifiques. Les applications s'étendent des moteurs diesels dans l'automobile [1], aux moteurs de la fusée Ariane dans l'aéronautique [23], à l'étude des flammes [36], en passant par l'impact des sprays pharmaceutiques et des dépôts nicotineux dans les poumons en biologie [35]. Généralement, cette modélisation repose sur une description cinétique sous la forme d'une fonction de probabilité des particules. Cette fonction de probabilité dépend alors du temps, de la position, de la taille, de la vitesse et de la température des particules. L'évolution de la phase dispersée est décrite par une équation de transport de type Boltzmann — pour les particules — alors que le fluide porteur est régi par les équations de l'hydrodynamique [53, 44, 3, 43, 37]. L'équation de Boltzmann est le plus souvent discrétisée par une approche stochastique de type Monte–Carlo [4, 5, 50]. Il s'agit d'une description particulaire de l'équation de Boltzmann qui permet de suivre l'évolution du spray. Cependant, même si cette méthode permet de décrire de nombreux phénomènes de manière satisfaisante, elle est rapidement contrainte par sa faible robustesse dans le régime dit des sprays

denses [44] — la fraction volumique de la phase dispersée peut alors être localement supérieure à 10% — et par son coût de calcul qui peut être élevé. En effet, cette méthode particulaire nécessite un nombre important de particules numériques afin d'obtenir une statistique suffisante et être physiquement pertinente. En outre, la parallélisation de ce type de méthode n'est pas facilement optimale à cause du déséquilibrage de charge qu'il faut gérer dans le cadre d'une décomposition en sous-domaines de la phase porteuse.

Pour s'affranchir de ces contraintes, une idée consiste à considérer, en lieu et place de l'approche particulaire classique, une approche alternative dite multigroupe, ou multifluide. Cette approche utilise une discrétisation par groupes de l'équation de Boltzmann qui réduit la phase dispersée à un ensemble de milieux continus — les « fluides » de l'approche multigroupes. Chacun de ces fluides correspond soit à une moyenne statistique effectuée sur un intervalle de taille ou de masse de gouttes fixées — modèle de sections [46], — soit à un moment de la fonction de distribution — modèle aux moments [34]. Dans cette approche alternative, chacun des groupes du système est décrit de manière macroscopique et l'ensemble est régi par un système d'équations de type équations d'Euler, pondérées par la fraction de présence de chaque fluide. La modélisation des différents termes d'échanges entre groupes — collision, coalescence, trainée, conduction thermique, ou encore fragmentation de gouttelettes — se fait alors via le choix de la forme de la fonction de distribution dans chaque groupe [45, 2, 12, 30, 25]. Le système d'équations d'évolution à résoudre se réduit alors à un système d'équations multifluides. Ce système peut compter un nombre élevé de fluides afin de représenter avec suffisamment de précision la polydispersion et les aspects polycinétiques comme les croisements de particules dans les écoulements dispersés [36, 30, 25].

Les applications rencontrées au CEA/DAM sont compliquées à simuler numériquement car elles font intervenir plusieurs contraintes simultanées : i) un nombre de fluides élevé (plusieurs douzaines pour des simulations gaz–particules avec des modèles multigroupes afin de prendre en compte à la fois la gamme de rayons de particules mise en jeu et le croisement de particules) ; ii) des régions de compressions et d'expansions fortes et régulières — et donc isentropiques ; — iii) des chocs forts qui génèrent de l'entropie ; iv) des équations d'état raides en régime quasi-incompressible (les phases liquides sont aussi traitées comme étant compressibles en raison des

déformations mises en jeu dans les différentes compressions–dilatations) ; et v) le transport de fluides à des fortes vitesses et sur des distances importantes ;

A cela s'ajoute le fait que dans le cadre multiphasique général — les descriptions multifluides sont un sous-ensemble des modèles multiphasiques, — les phases peuvent se mélanger sous l'effet d'instabilités hydrodynamiques [29] : par exemple, l'instabilité de Kelvin–Helmholtz lorsque les vitesses tangentielles des phases à l'interface sont différentes, l'instabilité de Rayleigh–Taylor qui intervient lorsqu'une accélération (par exemple la gravité) agit dans un mélange de phases de densités différentes, ou encore l'instabilité de Richtmyer–Meshkov où une onde de choc traverse un mélange de phases d'impédances acoustiques différentes (ρc^2 avec ρ et c la densité et la vitesse du son dans le fluide).

1.2 Cohérence thermodynamique et modèle multiphasique squelette

Afin de simuler des écoulements comportant ce type de caractéristiques, il est nécessaire d'utiliser une méthode numérique robuste garantissant une capture des forces de pression (et donc de l'entropie) qui soit thermodynamiquement cohérente. La cohérence thermodynamique signifie que le système vérifie les trois propriétés suivantes [28] : i) conservation de l'énergie totale du système (premier principe de la thermodynamique) ; ii) augmentation de l'entropie dans un système fermé (second principe de la thermodynamique) ; et iii) préservation de l'entropie pour des écoulements réguliers (isentropiques). Cette cohérence thermodynamique se traduit par le respect de ces trois propriétés au niveau discret. L'énergie totale doit être conservée exactement (à l'erreur d'arrondi informatique près) afin de vérifier les relations de Rankine–Hugoniot. Si cela n'est pas vérifié, il est connu que le schéma numérique peut ne pas converger vers la bonne solution [7]. Les deux propriétés d'augmentation de l'entropie pour un système fermé et préservation des écoulements isentropiques doivent être vérifiées au moins de façon approchée. Dans le contexte multiphasique, une entropie est définie pour chaque phase et les propriétés de conservation de quantité de mouvement et d'énergie totale doivent être vérifiées de manière globale pour toutes les phases d'un volume de contrôle. La propriété de conservation de la masse doit être vérifiée

au niveau discret pour chacune des phases du système. En général, des efforts sont fournis pour construire des schémas numériques assurant la croissance de l'entropie, mais la préservation des écoulements isentropiques est rarement prise en compte.

Il existe de nombreux modèles multiphasiques disponibles dans la littérature. Ces modèles sont basés sur les caractéristiques des phases, les relations de dispersion, les régimes de l'écoulement, les processus de dissipation, ou encore sur les conditions aux limites. Tous ces modèles partagent la même structure qui se compose d'équations de bilan de masse, quantité de mouvement et énergie, pondérées par leur fraction volumique. Une fois dépouillés de tous les termes d'échange et effets dissipatifs, tous ces modèles se réduisent à un squelette commun dans lequel les équations des différentes phases sont couplées entre elles par les forces de pression et la conservation du volume (via les fractions volumiques). En particulier, dans de nombreuses applications dont celles qui nous intéressent, l'équilibre mécanique peut être considéré comme instantané. Les pressions des différentes phases sont alors identiques dans tout volume de contrôle. En revanche, les équilibres cinématique et thermique ne sont pas aussi rapides et chaque phase peut ainsi être décrite par sa propre vitesse et son propre champ de température. Le modèle squelette considéré dans la suite de ce travail est donc composé des équations de bilan de masse, quantité de mouvement et énergie pour des phases compressibles, sans termes dissipatifs, ni termes d'échanges autres que le couplage par les forces d'une pression commune et les fractions volumiques, avec une vitesse par phase. L'annulation des différents termes d'échanges permet dans un premier temps d'étudier le comportement de la partie convective du modèle (généralement c'est cette partie qui regroupe le plus de problème). Cela permet d'obtenir un point de départ cohérent avant d'ajouter les termes d'échanges propres aux écoulements physiques étudiés. L'obtention du modèle squelette par la méthode dite des moyennes d'ensemble conditionnées est présentée dans l'Annexe.1 dans le cas multifluide.

Ce modèle squelette correspond à la partie convective des modèles multiphasiques complets. Il apparaît comme un point d'entrée pertinent pour l'étude de solutions numériques destinées à simuler des écoulements N-phases compressibles. Il partage notamment avec les modèles complets les difficultés suivantes : i) le modèle n'est pas écrit sous forme conservative à cause des termes

de gradient de pression ; ii) les équations d'états peuvent devenir raides lorsque les propriétés des fluides sont très contrastées ; et iii) la cohérence thermodynamique des forces de pression peut ne pas être assurée par les techniques d'intégration numérique usuelles. En effet, les erreurs commises sur le calcul de l'entropie peuvent venir des variations sur le volume des mailles de la grille, de l'advection des fluides par rapport à cette grille et enfin de l'influence du couplage de fractions volumiques entre des fluides dérivants. De plus, il est connu que le modèle squelette présente un défaut d'hyperbolicité — à petites échelles, la solution est instable par rapport à des petites perturbations. Une discussion est proposée au Chapitre 2 afin de justifier l'utilisation du modèle squelette elliptique à partir du moment où la cohérence thermodynamique est assurée et le schéma numérique utilisé est robuste.

1.3 Formulations ALE

Du point de vue numérique, deux systèmes de coordonnées sont traditionnellement utilisés dans les codes de calcul pour la simulation de problèmes hydrodynamiques : l'approche lagrangienne [38] utilise un maillage qui suit le mouvement du fluide, tandis que l'approche eulérienne [19] utilise un maillage fixe. Les méthodes lagrangiennes ont été développées initialement par les industries de défense [52]. Elles fournissent des résultats non diffusifs avec une capture de l'entropie précise, mais elles peuvent produire des déformations de grilles critiques pour des écoulements fortement cisaillés ou à forte vorticité. De plus, dans le cadre multiphasique où les différentes phases ont leur propre champ de vitesse, il n'est pas possible de suivre l'évolution lagrangienne des phases avec une grille commune à cause des différents couplages entre phases (termes d'échanges, conditions aux limites). Les méthodes eulériennes en revanche, développées initialement pour des applications en aérodynamique [55] produisent des résultats robustes. Ces méthodes sont néanmoins généralement affectées par une diffusion numérique excessive, spécialement pour des intégrations aux temps longs. De plus, ces méthodes ne vérifient pas systématiquement les propriétés de préservation des écoulements isentropiques au niveau discret.

Afin de conserver les avantages des approches lagrangienne et eulérienne sans souffrir de leurs déficiences respectives, Trulio et Trigger [48] introduisent une nouvelle approche dans laquelle

les mouvements des fluides sont calculés par rapport à un maillage mobile. Les déplacements de ce maillage peuvent être ajustés par l'utilisateur ou contraints par les caractéristiques de l'écoulement afin de respecter certaines propriétés de régularité et de robustesse. Cette nouvelle classe de méthodes, désignée « Arbitrary Lagrangian–Eulerian » (ALE) par Hirt et al. [22], peut être décomposée en deux catégories principales [13] : ALE indirecte et ALE directe.

Les méthodes ALE indirectes [39, 8, 9, 54, 11, 10] utilisent un découpage en une étape d'évolution lagrangienne, durant laquelle les nœuds du maillage sont déplacés et les variables du fluide sont calculées à partir des équations d'évolution, et une étape de remaillage, durant laquelle les variables issues de l'étape lagrangienne sont projetées sur un maillage régularisé après un nombre arbitraire de cycles de calcul. Ces méthodes ALE indirectes peuvent : i) étendre les solveurs lagrangiens en permettant de poursuivre le calcul en cas de fortes déformations de mailles ; et ii) étendre les solveurs eulériens en réduisant la diffusion numérique en cas d'écoulements fortement cisaillés ou à forte vorticité en remaillant à chaque cyle. En revanche, les méthodes ALE directes [26, 27, 49] n'utilisent pas de remaillage car les différents flux de masse, quantité de mouvement et énergie pour chaque maille de la grille sont directement pris en compte dans les équations d'évolution du fluide.

Historiquement, les applications au CEA qui nécessitent une prise en compte précise de la cohérence thermodynamique s'appuient sur des approches de type ALE indirectes. Les codes de calcul, à l'origine lagrangiens, ont été étendus à l'ALE indirect par l'ajout d'une étape de régularisation de la grille lagrangienne puis d'un remaillage sur cette grille régularisée. Ce type de méthodes assure généralement la cohérence thermodynamique du travail de la pression grâce à la séparation naturelle entre la phase d'évolution lagrangienne et la phase de remaillage géométrique (il suffit pour cela que le remaillage soit monotone). Pour les écoulements multiphasiques, une extension de ces méthodes a été proposée par Cournède dans le cadre de la simulation d'écoulements diphasiques compressibles sans termes d'échanges [10]. Dans la continuité de ce travail, la première approche numérique suivie lors de la thèse a consisté à étendre le schéma proposé par Cournède en ajoutant les équations d'énergie. La mise en place d'un schéma bi-Lagrange plus projection pour les écoulements diphasiques, en complément avec une discussion sur l'utilisation du modèle

squelette et l'importance de la préservation des écoulements isentropiques est présenté dans le Chapitre 2.

1.4 Schéma bi-Lagrange plus projection pour la simulation d'écoulements bifluides

Un schéma numérique de type Lagrange plus projection est proposé dans le Chapitre 2 pour la simulation d'écoulements diphasiques avec un modèle squelette à six équations (2 vitesses, 2 énergies et une seule pression) sans termes dissipatifs, ni termes d'échanges. Bien que ce modèle présente un défaut d'hyperbolicité, son utilisation est justifiée à l'aide d'une comparaison de résultats de simulation sur le cas test du robinet de Ransom. L'importance de la propriété de préservation des écoulements isentropiques est mise en évidence, de même que la capacité du schéma numérique proposé à répondre aux attentes fixées.

Le modèle squelette est introduit dans le cadre de la simulation d'écoulements diphasiques compressibles sans termes d'échanges. Les équations d'évolution du modèle — pour la masse, quantité de mouvement et énergie interne — sont écrites de manière à séparer et à rendre apparents les différents processus associés au travail de la pression. Ce modèle est ensuite discrétisé à l'aide d'un schéma ALE indirect bi-Lagrange plus projection afin de simuler des écoulements bifluides en une dimension. Ce schéma numérique, à l'origine proposé dans la thèse de Cournède [10], est étendu dans le cadre de ce travail au cas d'un modèle bifluides à six équations avec une étape de relaxation instantanée des pressions. Une évolution de ce schéma est proposée afin de garantir la conservation de la quantité de mouvement grâce à une phase de remaillage conservative sur grilles décalées — les vitesses sont discrétisées aux nœuds et les variables thermodynamiques (densités, pression et énergies internes) sont discrétisées au centre des mailles. Ce type de schéma numérique, largement utilisé au CEA/DAM, comporte trois étapes distinctes : i) une étape d'évolution lagrangienne durant laquelle les deux fluides évoluent avec leur vitesse propre sur deux maillages lagrangiens distincts ; ii) une étape de projection conservative comprenant le remaillage des deux grilles lagrangiennes sur une grille finale commune pour les deux fluides ; et iii) une étape de relaxation instantanée des pressions des deux fluides au sein des cellules du maillage

commun aux deux fluides. Dans ce travail, ce maillage commun est le maillage initial eulérien fixe. Les résultats obtenus avec ce schéma sont comparés avec les résultats issus de la littérature pour le cas test du robinet de Ransom [42], permettant ainsi de mettre en évidence l'importance de la cohérence thermodynamique du travail de la pression, spécialement lorsque le modèle squelette inclut des équations d'évolution pour l'énergie.

L'extension de ce schéma bi-Lagrange plus projection en deux ou trois dimensions reste problématique compte tenu du coût de calcul de l'étape de remaillage : le suivi lagrangien des N fluides implique N grilles lagrangiennes et donc N étapes de remaillage. Cette étude a contribué aux réflexions concernant : i) l'utilisation du modèle squelette est pertinente afin de s'assurer une bonne prise en compte de la partie convective (couplée par la pression unique des fluides) des schémas multiphasiques ; ii) la cohérence thermodynamique est indispensable afin d'obtenir des résultats robustes ainsi qu'une préservation des écoulements isentropiques ; et iii) l'utilisation d'une méthode ALE directe semble nécessaire afin de limiter le coût de calcul pour des écoulements N-fluides en deux ou trois dimensions.

1.5 Approche mimétique

Afin de construire un schéma numérique ALE direct respectant notre cahier des charges, une nouvelle procédure de dérivation de schémas numériques est proposée afin d'assurer par construction la vérification des propriétés principales vérifiées par les modèles continus. C'est l'approche de dérivation mimétique ou « physics-compatible » qui connaît un succès grandissant ces dernières années grâce à la qualité des résultats obtenus [24].

La cohérence thermodynamique du travail de la pression peut être obtenue en utilisant une approche dite mimétique. Ce type d'approche consiste à transposer des contraintes physiques importantes en équations discrètes [41, 47]. Contrairement à la procédure habituelle consistant à appliquer l'approche mimétique directement aux équations aux dérivées partielles en utilisant les différences finies, éléments finis, ou volumes finis, dans ce travail l'approche mimétique est appliquée à l'aide d'un principe variationnel sur une intégrale d'action. Cela permet de déduire directement les équations discrètes d'évolution du système. Un principe variationnel est une

affirmation selon laquelle une quantité définie pour tous les processus possibles atteint sa valeur minimum — ou maximum ou stationnaire — pour le processus réel. Le principe variationnel est devenu un ingrédient fondamental de la physique qui permet de trouver les équations d'évolution pour de nombreux systèmes depuis l'oscillateur harmonique jusqu'aux théories de jauge en mécanique quantique [20].

Pour des systèmes numériques, les intégrateurs variationnels sont basés sur un principe de moindre action discrète. Cela permet de transposer au niveau discret les propriétés particulières d'un modèle continu : lois de conservation, solutions autosimilaires, ou encore groupe de symétrie. Ce type d'intégrateur permet d'obtenir une procédure systématique pour la dérivation de méthodes numériques variationnelles. Cependant, les intégrateurs variationnels vérifient uniquement deux des trois propriétés suivantes [51, 17] : symplecticité (préservation du volume dans l'espace des phases du système dynamique), conservation de la quantité de mouvement et conservation de l'énergie totale. Ainsi, les intégrateurs variationnels sont divisés en trois catégories principales : conservatifs en quantité de mouvement et en énergie totale, conservatifs en quantité de mouvement et symplectiques, ou conservatifs en énergie totale et symplectiques. Pour des applications faisant intervenir des écoulements avec des chocs, la catégorie des intégrateurs variationnels garantissant la conservation de la quantité de mouvement et de l'énergie totale est la plus utilisée car elle assure le respect des conditions de Rankine–Hugoniot permettant ainsi la convergence du schéma numérique vers les bons plateaux et vitesses des chocs.

En hydrodynamique continue, l'application d'un principe variationnel pour décrire le mouvement d'un fluide compressible n'est pas un problème récent. Dans le cas monophasique, Eckart [15], Herivel [21] et Lin [31] ont montré qu'il est possible de dériver un système d'équations d'Euler–Lagrange dans le référentiel eulérien ou lagrangien directement à partir du principe variationnel. Cependant, dans le cas eulérien, il est indispensable de rajouter des contraintes supplémentaires — sous la forme de multiplicateur de Lagrange — afin d'obtenir un système d'équations sans limitation aux écoulements irrotationnels.

L'application du principe de moindre action à un système multiphasique correspond à une généralisation de l'approche variationnelle monophasique. Ce type d'approche fut tout d'abord

utilisé afin de dériver des équations du mouvement pour l'Hélium superfluide dans un référentiel eulérien — en une dimension et pour un système bifluides [18]. L'adaptation au référentiel lagrangien fut réalisée par Drumheller et Bedford [14] dans le cas de mélange sans vide (les fluides occupent la totalité du volume du système).

Pour la simulation numérique de problèmes CFD compressibles (Computational Fluid Dynamics), l'utilisation de l'approche variationnelle reste très limitée. En effet, une discrétisation du groupe des difféomorphismes ne préservant pas le volume reste à expliciter. En cause, le fait que les advections de masse et de quantité de mouvement ne peuvent *a priori* pas être simultanément holonomes et monotones. Pour simplifier, une contrainte sera considérée comme non-holonome si ses variables dépendent à la fois de la position et de la vitesse — en général, les systèmes non-holonomes ne sont pas symplectiques [6].

À notre connaissance, seules deux dérivations de schéma numérique variationnel ont été publiées dans le cas monofluide. Dans la première dérivation, Fahrenthold et Koo [16] développent une description variationnelle pour un fluide compressible dans le cas eulérien. Cette description est ensuite étendue au formalisme ALE par Koo et Fahrenthold [27]. Leur méthode est semi-discrète : i) le principe variationnel est d'abord appliqué sur une action discrète en espace mais continue en temps, et ii) l'intégration en temps est réalisée séparément avec un algorithme de type Runge–Kutta. Cependant, cette approche génère des gradients d'entropie dont l'interprétation physique reste discutable. La seconde dérivation d'un schéma variationnel monofluide est réalisée dans le cas d'un fluide incompressible par Pavlov et al. [40]. Dans cette approche, les transports de masse et de volume sont capturés par des contraintes strictement holonomes. Le fluide évolue ainsi suivant une structure symplectique bien que non-monotone. À notre connaissance, il n'existe aucune dérivation variationnelle de schéma numérique pour la description d'écoulements multiphasiques.

1.6 Procédure générique de dérivation de schémas mimétiques

Afin de dériver un nouveau schéma numérique ALE qui soit thermodynamiquement cohérent et moins coûteux en temps de calcul, une nouvelle procédure de dérivation de schéma numérique est introduite afin de garantir les compatibilités suivantes : i) énergétique : la conservation de l'énergie

totale doit être assurée au niveau discret afin de capturer les plateaux et vitesses des chocs, et ce même si le système d'équations d'évolution est résolu en énergie interne ; ii) entropique : le respect de la seconde loi de la thermodynamique doit être assuré au niveau discret au moins au second ordre — l'entropie ne peut pas diminuer dans un système fermé et doit rester constante pour des écoulements isentropiques ; — et iii) géométrique : les variations de volumes liées aux compressions ou dilatations doivent être prises en compte de manière cohérente vis-à-vis de l'advection par rapport à la grille. Ce dernier point est particulièrement important dans le contexte ALE. Cette nouvelle procédure de dérivation est désignée par l'acronyme GEEC (Geometry, Energy, and Entropy Compatible).

Afin de garantir le respect de ces compatibilités au niveau discret, la procédure de dérivation GEEC se décompose en trois étapes principales [33] : i) afin de générer des forces de pression thermodynamiquement cohérentes, l'équation d'évolution de la quantité de mouvement est dérivée en utilisant un principe variationnel ; ii) afin de garantir une conservation exacte de l'énergie totale (à l'erreur d'arrondi informatique près), l'équation d'évolution de l'énergie interne est dérivée à partir de l'équation d'évolution de l'énergie cinétique ; et iii) afin de pouvoir capturer les chocs et stabiliser le schéma, un terme de viscosité artificielle est ajouté aux équations d'évolution sous la forme d'une contribution semblable à la pression.

Comme preuve de concept, cette nouvelle procédure de dérivation GEEC est d'abord appliquée dans le Chapitre 3 à un schéma mimétique ALE direct pour la simulation d'écoulements monofluides compressibles. Le corps de ce chapitre est constitué d'un article prêt à être soumis pour publication : A novel GEEC (Geometry, Energy, and Entropy Compatible) procedure applied to a staggered direct-ALE scheme for hydrodynamics. Ce schéma, désigné par l'acronyme GEECS (Geometry, Energy, and Entropy Compatible Scheme) possède les propriétés suivantes : i) formalisme ALE direct avec prise en compte des flux d'advection de masse, quantité de mouvement et énergie interne directement dans les équations d'évolution — pas de séparation entre phase d'évolution lagrangienne et phase de remaillage ; — ii) continuité avec les solveurs lagrangiens utilisés au CEA/DAM dans lesquels les champs de vitesses sont décalés à la fois en espace et en temps ; iii) discrétisation des énergies cinétique et interne au second ordre dans la limite lagran-

gienne — lorsque le maillage se déplace exactement à la vitesse du fluide — ; iv) discrétisation au premier ordre pour l'équation de transport de la masse en utilisant un schéma d'advection upwind ; v) formulation downwind non-standard du terme de gradient de pression, duale de la formulation upwind de l'opérateur d'advection. Cette formulation non-standard est directement liée à l'utilisation d'un principe variationnel pour la dérivation de l'équation de quantité de mouvement.

Les équations d'évolution de GEECS pour la masse, quantité de mouvement et énergie interne sont dérivées dans le cas général, sans aucune contrainte sur le nombre de dimensions ou la structure des mailles. Un code écrit en C++ a été développé à partir d'une maquette existante (nommée SHY) afin de pouvoir tester le schéma numérique en deux dimensions pour des maillages structurés de quadrangles. Plusieurs cas tests usuels issus de la littérature (vortex isentropique, tube à choc de Sod, explosion de Sedov, double tube à choc de Woodward et Colella et point triple) sont réalisés en utilisant différents mouvements de grille violents, par exemple des cisaillements supersoniques, afin de vérifier le comportement du schéma. Ces résultats confirment que GEECS respecte les propriétés suivantes : i) conservation exacte de la masse, quantité de mouvement et énergie interne, visible sur la capture des plateaux et vitesses des chocs ; ii) convergence au second ordre en limite lagrangienne et premier ordre en limite eulérienne pour la partie advective du schéma ; iii) préservation des écoulements isentropiques assurée au second ordre quelque soit le mouvement de la grille ; et iv) compatibilité géométrique entre le champ de vitesse et les variations de volumes de la grille en présence de fortes advections de fluide.

1.7 Schéma multiphasique ALE direct mimétique

Un schéma numérique de type ALE direct est proposé dans le Chapitre 4 pour la simulation d'écoulements multiphasiques avec le modèle squelette déjà introduit dans le Chapitre 2. Le corps de ce chapitre est constitué d'un article prêt à être soumis pour publication intitulé : A multiphase flow mimetic numerical scheme with thermodynamic and geometric compatibility on an arbitrary moving grid. Afin d'obtenir une discrétisation compatible du modèle squelette dans le formalisme ALE direct, la procédure générique de dérivation de schéma numérique

mimétique GEEC introduite au Chapitre 3 est appliquée à un schéma ALE direct multiphasique compressible. Ce schéma, nommé multiGEECS (Geometry, Energy, and Entropy Compatible multiphase Scheme), constitue l'extension naturelle du schéma GEECS au cas N-fluides. Cette extension diffère de la dérivation monofluide sur deux points : i) les variations liées aux fractions volumiques des phases doivent être prises en compte de manière cohérente afin de garantir la compatibilité géométrique du schéma numérique ; et ii) les propriétés de conservation de la quantité de mouvement et énergie totale doivent être vérifiées pour le système global — pour l'ensemble des fluides. Des corrections analogues à celles présentées au Chapitre 3 sont réalisées afin d'obtenir un système d'équations d'évolution conservatives garantissant une compatibilité géométrique, énergétique et entropique au niveau discret. L'équation d'évolution de l'énergie interne de chaque fluide est discrétisée à partir de l'équation d'énergie interne du modèle squelette continu présentée au Chapitre 2 afin de garantir la cohérence thermodynamique du travail de la pression. Les équations d'évolution multiphasiques discrètes pour la masse, quantité de mouvement et énergie interne de chaque fluide sont écrites pour un nombre arbitraire de fluides, sans aucune contrainte de dimension ou de structure de mailles.

Le code C++ utilisé pour GEECS a été étendu afin de pouvoir simuler des écoulements compressibles avec un nombre de fluides arbitraires en deux dimensions pour des maillages structurés de quadrangles. Des tests sont réalisés afin de vérifier le comportement du schéma pour un nombre de fluides allant de deux à neuf et des mouvements de maillage violents. Tout d'abord, des tests multi-matériaux sont réalisés (tube à choc de Sod, tube à choc eau–air et point triple) en moyennant les vitesses absolues de chaque fluide à chaque itération — le modèle multiphasique est alors réduit à un modèle mono-vitesse avec ajout d'une contrainte de relaxation instantanée des vitesses. Ces tests multi-matériaux permettent d'étudier le comportement du schéma en présence de fortes discontinuités de fractions volumiques — ces discontinuités correspondent alors à des interfaces artificielles entre les fluides. Ensuite des problèmes multiphasiques sont réalisés afin de vérifier la cohérence thermodynamique du schéma lorsque les fluides dérivent les uns par rapport aux autres. Le cas test du robinet de Ransom, déjà introduit au Chapitre 2, permet ainsi la mise en évidence de la propriété de préservation des écoulements isentropiques en formalisme ALE. Enfin,

plusieurs cas tests de croisement de groupes de fluides denses dans un gaz sont présentés dans la Section 4.5 du Chapitre 4. Comme aucun terme d'échange (trainée, collision, ou évaporation) n'est présent dans le modèle multifluides discrétisé, ces cas tests restent préliminaires car les fluides n'interagissent que par l'intermédiaire des forces de pression. Cependant, ils représentent un point de départ pour la simulation d'écoulements gaz–particules réalistes tels qu'ils sont rencontrés au CEA/DAM. L'exemple de sprays constitués de gouttelettes d'étain évoluant dans l'air est particulièrement important car les gouttelettes d'étain sont très denses par rapport au fluide environnant.

Les travaux contenus dans ce manuscrit ont été présentés aux conférences suivantes :

En 2013

- 14$^{\text{th}}$ International Workshop on Trends in Numerical and Physical Modeling for Industrial Multiphase Flows, Cargèse (France).

En 2014

- 2$^{\text{nd}}$ International Conference on Numerical Methods in Multiphase Flows, Darmstadt (Allemagne),
- Séminaire interne du groupe TOTAL, Journées MATHIAS, Paris (France),
- 15$^{\text{th}}$ International Workshop on Trends in Numerical and Physical Modeling for Industrial Multiphase Flows, Cargèse (France).

En 2015

- SIAM Conference on Computational Science and Engineering, Salt Lake City (États-Unis),
- Numerical Methods for Multi-Material Fluid Flow (MULTIMAT), Würzburg (Allemagne),
- Séminaire interne du groupe TOTAL, Journées MATHIAS, Paris (France),
- 15$^{\text{th}}$ International Workshop on Trends in Numerical and Physical Modeling for Industrial Multiphase Flows, Cargèse (France).

En 2016

- 9$^{\text{th}}$ International Conference on Multiphase Flow, Florence (Italie).

Les travaux contenus dans ce manuscrit sont issus des publications suivantes :

- Étude d'un schéma numérique bi-Lagrange plus projection pour les écoulements bi-fluides, T.Vazquez-Gonzalez, A. Llor, M. Peybernes, C. Fochesato, Rapport Interne CEA/DAM/DIF, (2014).
- Ransom test results from various two-fluid schemes : is enforcing hyperbolicity a thermodynamically consistent option ?, T. Vazquez-Gonzalez, A. Llor, C. Fochesato, Int. J. Multiphase Flow, 81 (2016), 104-112.
- A novel GEEC (Geometry, Energy, and Entropy Compatible) procedure applied to a staggered direct-ALE scheme for hydrodynamics, T. Vazquez-Gonzalez, A. Llor, C. Fochesato, in preparation.
- A multiphase flow mimetic numerical scheme with thermodynamic and geometric compatibility on an arbitrary moving grid, T. Vazquez-Gonzalez, A. Llor, C. Fochesato, in preparation.

.1 Dérivation continue du modèle squelette multifluide

La méthode dite des moyennes d'ensemble conditionnées est utilisée afin d'obtenir les équations d'évolution du modèle squelette pour la masse, quantité de mouvement et énergie interne dans le cas multifluide [32].

Dans le cas monofluide, les équations d'évolution pour la masse, quantité de mouvement et énergie interne sont

$$\partial_t \rho + (\rho v_j)_{,j} = 0 \ , \tag{1a}$$

$$\partial_t (\rho v_i) + (\rho v_i v_j)_{,j} = -p_{,i} \ , \tag{1b}$$

$$\partial_t (\rho e) + (\rho e v_j)_{,j} = -p v_{i,i} + S \ , \tag{1c}$$

avec ρ, $\boldsymbol{v}$, e, p et S respectivement la densité, vitesse, énergie interne, pression et terme source d'énergie interne du fluide. Afin de simplifier les notations, les notations d'Einstein sont utilisées dans la suite : $\boldsymbol{\nabla} \cdot \boldsymbol{a} = a_{i,i}$ et $\boldsymbol{\nabla} b = b_{,i}$.

La méthode des moyennes d'ensemble conditionnées consiste à multiplier chacune des équations d'évolution de (1) par la fraction massique c^φ du fluide φ, puis à appliquer un opérateur de moyenne d'ensemble sur les équations obtenues. Par définition, les fractions massiques d'un ensemble de M fluides vérifient la relation suivante

$$\sum_{\varphi=1}^{M} c^\varphi = 1 \ . \tag{2}$$

Pour l'équation d'évolution de la masse (1a), la méthode des moyennes d'ensemble conditionnées conduit à

$$\overline{c^\varphi (\partial_t \rho)} + \overline{c^\varphi (\rho v_j)_{,j}} = 0 \ , \tag{3}$$

où $\overline{A}$ correspond à l'opérateur de moyenne d'ensemble de la variable A.

Comme l'opérateur de moyenne d'ensemble commute avec les opérateurs différentiels, (3) peut encore s'écrire

$$\partial_t (\overline{c^\varphi \rho}) + (\overline{c^\varphi \rho v_j})_{,j} = (\overline{\phi_j^\varphi})_{,j} \ , \tag{4}$$

avec $(\phi_j^\varphi)_{,j} = \rho(\partial_t c^\varphi + v_j (c^\varphi)_{,j})$. Dans ce travail, les échanges de masses entre les fluides sont négligés, il vient alors $(\phi_j^\varphi)_{,j} = 0$.

L'équation d'évolution de la masse (4) peut s'écrire

$$\partial_t(\alpha^\varphi \rho^\varphi) + (\alpha^\varphi \rho^\varphi v_j^\varphi)_{,j} = 0 \ , \tag{5}$$

avec α^φ, ρ^φ et $\boldsymbol{v}^\varphi$ respectivement la fraction volumique, densité moyenne et vitesse moyenne "de Favre" du fluide φ. Ces quantités sont définies par

$$\rho^\varphi = \frac{\overline{c^\varphi \rho}}{\overline{c^\varphi}} \ , \qquad v_j^\varphi = \frac{\overline{c^\varphi \rho v_j}}{\overline{c^\varphi \rho}} \ , \qquad \alpha^\varphi = \overline{c^\varphi} \ , \tag{6a}$$

avec la relation $\sum_{\varphi=1}^{M} \alpha^\varphi = 1$.

Un développement similaire pour l'équation d'évolution de la quantité de mouvement (1b) conduit à

$$\partial_t(\alpha^\varphi \rho^\varphi v_i^\varphi) + (\alpha^\varphi \rho^\varphi v_i^\varphi v_j^\varphi)_{,j} = -\alpha^\varphi (P)_{,i} - (\overline{c^\varphi \rho (v_i - v_i^\varphi)(v_j - v_j^\varphi)})_{,j} \ . \tag{7}$$

Le dernier terme de (7) correspond à un terme de fluctuation de quantité de mouvement. Afin d'obtenir (7), l'équilibre mécanique du système est considéré comme instantané. Par conséquent, les différences entre les pressions moyennes des différents fluides sont négligées : $\overline{c^\varphi p} = \overline{c^\varphi}\,\overline{p} = \alpha^\varphi P$.

Pour l'équation d'évolution de l'énergie interne (1c), la méthode des moyennes d'ensemble conditionnées donne

$$\partial_t(\alpha^\varphi \rho^\varphi e^\varphi) + (\alpha^\varphi \rho^\varphi e^\varphi v_j^\varphi)_{,j} = \alpha^\varphi S^\varphi - \overline{c^\varphi v_{i,i}} P - (\overline{c^\varphi \rho (e - e^\varphi)(v_j - v_j^\varphi)})_{,j} \ . \tag{8}$$

En utilisant l'équation d'évolution de la masse (5), le terme $\overline{c^\varphi v_{i,i}} P$ devient

$$\overline{c^\varphi v_{i,i}} P = P \, \mathrm{D}_t^\varphi \, \alpha^\varphi \ , \tag{9}$$

avec l'expression de la dérivée eulérienne $\mathrm{D}_t^\varphi \bullet = \partial_t \bullet + (\bullet \boldsymbol{v}_i^\varphi)_{,i}$.

Finalement, le système d'équations d'évolution pour la masse, quantité de mouvement et énergie interne dans le cas multi-fluide et en négligeant les termes de fluctuations peut s'écrire

$$\partial_t(\alpha^\varphi \rho^\varphi) + (\alpha^\varphi \rho^\varphi v_j^\varphi)_{,j} = 0 \ , \tag{10a}$$

$$\partial_t(\alpha^\varphi \rho^\varphi v_i^\varphi) + (\alpha^\varphi \rho^\varphi v_i^\varphi v_j^\varphi)_{,j} = -\alpha^\varphi (P)_{,i} \ , \tag{10b}$$

$$\partial_t(\alpha^\varphi \rho^\varphi e^\varphi) + (\alpha^\varphi \rho^\varphi e^\varphi v_j^\varphi)_{,j} = -P \, \mathrm{D}_t^\varphi \, \alpha^\varphi \ . \tag{10c}$$

Les Sections 2.3.3 (pour les écoulements bifluides) et 4.3.1.6 (pour les écoulements multifluides) présentent une fermeture explicite de l'équation d'évolution de l'énergie interne multifluide (10c) afin de séparer et de rendre apparents les différents processus associés au travail de la pression.

Bibliographie

[1] A.A. Amsden, P.J. O'Rourke, T.D. Butler, Kiva II, a computer program for chemical reactive flows with spray, Technical report Los Alamos National Laboratory, (1989).

[2] M. Boucker, Modélisation numérique multidimensionnelle d'écoulements diphasiques liquide–gaz en régime transitoire et permanent : méthodes et applications. PhD thesis, CMLA Ecole Normale Supérieure de Cachan, (1998).

[3] R. Caflish, G.C. Papanicolaou, Dynamic theory of suspensions with Brownian effects, SIAM J. Appl. Math. 43 (1983), 885-906.

[4] C. Cercignani, The Boltzmann equation and its applications, Applied Mathematical Sciences, Springer–Verlag New York, 67 (1988).

[5] S. Chapman, T.G. Cowling, The mathematical theory of no uniform gases, Cambridge Mathematical Library, (1990).

[6] N.M. Chhay, Intégrateurs géométriques : Application à la Mécanique des Fluides, PhD thesis, Université de la Rochelle,(2008).

[7] F. Coquel, P.G. LeFloch, Convergence of finite difference schemes for conservation laws in several space dimensions : a general theory, SIAM J. Numer. Anal., 30 (1993), 675-700.

[8] P. Colella, P.R. Woodward, The piecewise parabolic method (PPM) for gas–dynamic simulations, J. Comput. Phys., 54 (1984), 174-201.

[9] P. Colella, P.R. Woodward, The numerical simulation of two-dimensional fluid flow with strong shocks, J. Comput. Phys., 54 (1984), 115-173.

[10] P.-H. Cournède, Un schéma bi-Lagrange plus projection pour la simulation bifluide des instabilités de mélanges, PhD thesis, Ecole Centrale Paris, (2001).

[11] B. Desjardins, J. Francescatto, J.-M. Ghidaglia, A multidimensional multiphase flow finite volume solver using a Lagrangian step and a projection technique, Int. J. Finite Volumes, (2007).

[12] G. Dufour, Modélisation multi-fluide eulérienne pour les écoulements diphasiques à inclusions dispersées, PhD thesis, Université Paul Sabatier Toulouse III, (2005).

[13] J. Donea, A. Huerta, J.-Ph. Ponthot, A. Rodriguez–Ferran, Arbitrary Lagrangian–Eulerian methods, Encyclopedia of Computational Mechanics, (2004).

[14] D. S. Drumheller, A. Bedford, Arch. Rational Mech. Anal., 73 (1980), 257-.

[15] C. Eckart, Phys. Rev., 54 (1938), 920-.

[16] E.P. Fahrenthold, J.C. Koo, Discrete Hamilton's equations for viscous compressible fluid dynamics, Comput. Methods Appl. Mech.Engrg, 178 (1999), 1-22.

[17] Z. Ge, J.E. Marsden, Lie–Poisson integrators and Lie–Poisson Hamilton–Jacobi theory, Phys. Lett. A., 133 (1988), 134-139.

[18] J. A. Geurst, Phys. Rev. B, 22 (1980), 3207-.

[19] S.K. Godunov, Finite difference method for numerical computation of discontinuous solutions of the equations of fluid dynamics, Matematicheskii Sbornik, 47 (1959), 272-306.

[20] H. Goldstein, C. Poole, J. Safko, Classical mechanics, Addison–Wesley, (2002).

[21] J.W. Herivel, The derivation of the equations of motion of an ideal flow by Hamilton principle, Proc. Camb. Phil. Soc., 51 (1955).

[22] C.W. Hirt, A.A. Amsden, J.L. Cook, An Arbitrary Lagrangian–Euleriancomputing method for all flow speeds, J. Comput. Phys., 135 (1974), 203-216.

[23] J. Hylkema, Modélisation cinétique et simulation numérique d'un brouillard dense de gouttelettes. Applications aux propulseurs à poudre. PhD thesis, Ecole Nationale Supérieure de l'Aéronautique et de l'espace Toulouse, (1999).

[24] J. Comput. Phys., 257 Part B (2014).

[25] D. Kah, Prise en compte des aspects polydispersés pour la modélisation d'un jet de carburant dans les moteurs à combustion interne, PhD thesis, EM2C Ecole Centrale Paris, (2010).

[26] D. Kah, O. Emre, Q.H. Tran, S. de Chaisemartin, S. Jay, F. Laurent, M. Massot, High order moment method for polydisperse evaporating sprays with mesh movement : Application to internal combustion engines. Int. J. Multiphase Flow, 71 (2015), 38-65.

[27] J.C. Koo, E.P. Fahrenthold, Discrete Hamilton's equations for arbitrary Lagrangian–Eulerian dynamics of viscous compressible flow, Comput. Methods Appl. Mech. Engrg., 189 (2000), 875-900.

[28] L.D. Landau, E.M. Lifshitz, Fluid Mechanics (Volume 6 of A Course of Theoritical Physics), Pergamon Press, (1959).

[29] B.E. Launder, D.B. Spalding, Mathematical models of turbulence, Academic Press, (1972).

[30] F. Laurent, Modélisation mathématique et numérique de la combustion de brouillards de gouttes polydispersés, PhD thesis, Université Claude Bernard Lyon, (2002).

[31] C.C. Lin, Liquid Helium, Proceedings ot the international school of physics, 1963.

[32] A. Llor, Statistical hydrodynamic models for developed mixing instabilities flows : analytical 0D evaluation criteria, and comparison of single-and-two phase flow approaches, Lect. Notes Phys., 681 (2005).

[33] A. Llor, A. Claisse, C. Fochesato, Energy preservation and entropy in Lagrangian space- and time-staggered hydrodynamic schemes, J. Comput. Phys., 309 (2016), 324-349.

[34] D.L. Marchisio, R.D. Vigil, R.O. Fox, Quadrature method of moments for aggregation–breakage processes, Journal of Colloidal and Interfacial Science, 258 (2003), 322-334.

[35] B. Mauroy, Hydrodynamique dans les poumons, relations entre flux et géometries, PhD thesis, CMLA Ecole Normale Supérieure de Cachan, (2004).

[36] M. Massot, P. Villedieu, Modélisation multi-fluide eulérienne pour la simulation de brouillards denses polydispersés, C. R. Acad. Sci. Paris Sér. I Math., 332 (2001), 869-874.

[37] J. Mathiaud, Etude de systèmes de type gaz–particules, PhD thesis, CMLA Ecole Normale Supérieure de Cachan, (2006).

[38] J. von Neumann, R.D. Richtmyer, A method for the numerical calculation of hydrodynamic shocks, J. Appl. Phys., 21 (1950), 232-237.

[39] W.F. Noh, P. Woodward, SLIC (Simple Line Interface Calculation), Lectures notes in Physics, Springer Berlin, 59 (1976).

[40] D. Pavlov, P. Mullen, Y. Tong, E. Kanso, J.E. Marsden, M. Desbrun, Structure-preserving discretization of incompressible fluids, Physica D, 240 (2011), 443-458.

[41] J.B. Perot, C.J. Zusi, Differential forms for scientists and engineers, J. Comput. Phys., 257 (2014), 1373-1393.

[42] V.H. Ransom, Numerical benchmark testNo 2.1 : faucet flow. Multiphase Sci. Technol., 1 (1987), 465.

[43] M.W. Reeks, On a kinetic equation for the transport of particles in turbulent flows, Phys. Fluid A, 3 (1991).

[44] P.J. O'Rourke, Collective drop effects on vaporizing liquid sprays, PhD thesis, Princeton University, (1981).

[45] L. Sainsaulieu, Contribution à la modélisation mathématique et numérique des écoulements diphasiques constitués d'un nuage de particules dans un écoulement de gaz, Habilitation à diriger des recherches, Université Paris VI, (1995).

[46] Y. Tambour, A Lagrangian sectional approach for simulating droplet size distribution of vaporizing fuel in a turbulent jet, Combustion and flame, 60 (1985), 15-28.

[47] E. Tonti, Why starting from differential equations for computational physics ?, J. Comput. Phys., 257 (2014), 1260-1290.

[48] J.G. Trulio, K.R. Trigger, Numerical solution of the one-dimensional Lagrangian hydrodynamic equations, UC–LRL Report, (1966).

[49] A. Velghe, N. Gillet, J. Bohbot, A high efficiency parallel unstructured solver dedicated to internal combustion engine simulations, Comput. Fluids, 45 (2011), 116-121.

[50] C. Villani, A review of mathematical topics in collisional kinetic theory, Elsevier Science, (2002).

[51] J.M. Wendlandt, J.E. Marsden, Mechanical integrators derived from a discrete variational principle, Physica D, 106 (1997), 223-246.

[52] M.L. Wilkins, Calculation of elastic plastic flow methods, Comput. Phys., 3 (1964).

[53] F.A. Williams, Combustion theory, Benjamin Cummings, (1985).

[54] D.L. Youngs, Time–dependent multi-material flow with large fluid distortion, Num. Meth. Fluid Dynamics, (1982), 273-285.

[55] O.C. Zienkiewicz, The finite element method in engineering science, Mac Graw Hill, (1977).

Chapitre 2

Modèles bifluides, écoulements isentropiques et construction d'un schéma Lagrange plus projection : application au test du robinet de Ransom.

Le corps de ce chapitre est constitué d'un article accepté pour publication :
Ransom test results from various two-fluid schemes : is enforcing hyperbolicity a thermodynamically consistent option ?, T. Vazquez-Gonzalez, A. Llor, C. Fochesato, Int. J. Multiphase Flow, 81 (2016), 104-112.

2.1 Abstract

The basic elliptic ill-posedness of physical models and numerical schemes for two-fluid flows is a recurring issue that has motivated the introduction of numerous possible correction strategies. In practical applications physical terms are generally present and regularize the models (viscosity,

drag, surface tension, etc.). Yet, many numerical schemes were developed with the stringent and self-imposed constraint that the convective part of the models to be solved had to be hyperbolic, regardless of the type and magnitude of the particular physical regularizing terms. This leads to consider the simplest possible two-fluid "backbone" models corrected with the simplest "universal" terms to ensure hyperbolicity.

Among the proposed corrections is the introduction of an interfacial pressure, either closed by algebraic relations or by supplementary evolution equations. Concurrently with the shift to hyperbolic behavior, these techniques also affect other features of systems : Kelvin–Helmholtz type instabilities are notably quenched at all scales, a highly undesirable effect in many practical situations. Less commonly recognized are also distortions in the transfers between kinetic, reversible, and irreversible energies, sometimes up to thermodynamic inconsistency.

The present work aims at comparing on the standard Ransom-faucet test the results from various available hyperbolic and elliptic schemes and models against an explicit double Lagrange-plus-remap discretization of the basic elliptic, one-pressure, compressible, six-equations system (i.e. with energy equations). Four features are examined on this test : the entropy preservation, the stretched stream profile, the volume fraction discontinuity, and the unstable character of the analytical solution for the simplest backbone model.

The paper highlights the fact that the convective part of two-fluid models might not be necessarily hyperbolic provided that it is physically consistent and numerically robust. Observation of published results for Ransom's test shows that by enforcing hyperbolicity regardless of thermodynamical consistency, numerical models remove instabilities at the volume fraction discontinuity, but at the expense of distorted profiles of the stretched stream due to excessive numerical diffusion and to spurious forces in the momentum equation. The present approach provides a form of neutral starting point before including dissipative terms : robust but not excessively diffusive, with accurate capture of the stretched stream and volume fraction discontinuity for any practical mesh refinement. Moreover, and consistently with the chosen elliptic model, this numerical scheme eventually generates the elliptic instabilities for late times or fine meshes (but remains robust under the appropriate time step restrictions). It can be supplemented by any

kind of small-scale regularization term in order to introduce a cut-off under which physical or numerical stability may be necessary.

2.2 Introduction

2.2.1 The balancing act between physical consistency, well-posedness, and non-damping of small-scales

Over the last half century, the modeling and computation of two-fluid flows has found a wide and ever expanding range of industrial and academic applications. Despite this long lasting and successful development however, many models still raise some irritating issues related to their possible mathematical ill-posedness, fueling numerous and recurring controversies among physicists, modelers, numericists, and practitioners.

Two-fluid models come in a wealth of types and flavors—depending on fluid characteristics, dispersion geometry, flow regime, dissipation processes, source terms, boundary conditions...—but they all share a common "backbone" of evolution equations for the conserved quantities (mass, momentum, energy). This backbone model features six equations in its basic version which can be reduced to fewer under supplementary constraints (isentropic flows, incompressible fluids). All these are amenable to mathematical stability analysis which show ill-posed (elliptic) characters : small perturbations to a solution are unstable with unbounded growth rates at small scales. Therefore, no numerical scheme can converge towards a unique solution of the backbone equations for vanishing cell size, and recovering well-posedness requires amending the models with supplementary terms or supplementary equations.

This indisputable fact has triggered the development of numerous strategies to "fix" the ill-posedness. The present work does not intend to (critically) review the existing state of this art, and even less to provide (yet) another cure to the ailments of two-fluid models and schemes. Numerous publications are available on this topic, and the reader will be just referred here to the recent review by [25] which is mostly thorough and conveniently short enough.

In broad terms, previous works have tried to reconcile into a single model three important

constraints : physical consistency at large scales, mathematical well-posedness, and non-damping of small-scales (e.g. the dissipative–dispersive behavior at small scales to keep the "universality" of the backbone). However, in view of the mixed results accumulated over about four decades, it appears that these constraints are probably incompatible and only two out of the three can be retained : in this balancing act different investigators may choose between three broad options depending on their different objectives.

First is emphasis on well-posedness and non-dissipation–dispersion, a widely adopted approach in academic works ; however, physical distortions or inconsistencies can appear [29, 30, 39, § III], sometimes quite extreme when for instance, as commented by [25, § 3.2] and in contrast with experimental evidence, *two* different sound velocities are sustained by the mixed medium.

Second is emphasis on consistency and well-posedness, often implicitly adopted in practical applications ; as was shown in an early study by [33], the combination of diffusion, drag, surface tension, or similar terms stabilizes the system into a hyperbolic or mixed hyperbolic–parabolic behavior.

Third is emphasis on consistency and non-dissipation–dispersion, a somewhat controversial view as explained by [28] which however, has been justified on mathematical grounds by the corrections due to non-linearities and to transition to (hyperbolic) single-fluid behavior (see [42] or [21, § 4 & fig. 4] and comments by [12, § 2.1]). The present work follows this approach where both hyperbolic or elliptic models are a possible option as long as physical consistency is preserved.

2.2.2 Present approach : physical consistency and non-damping of small-scales

The last option above, by preserving the elliptic behavior of two-fluid models, is notably the only one which captures the linear Kelvin–Helmholtz instability of separated flows and the ensuing non-linear "slug-flow" regimes in pipes [14, and references therein]. In such cases a cut-off length scale is present [41, § 4], [42, § 4]—for instance the pipe diameter—below which all perturbations are damped. The instability of the system is thus retained but with an upper bound for the amplification rate. This is akin to the more general behavior of the Euler equation which produces

instabilities at all scales and requires a regularizing term such as viscosity to avoid singularities. These equations which are not hyperbolic can nevertheless be extremely useful in engineering applications, for instance in the sense of an asymptotic expansion. Quoting [19], the occurence of complex characteristics in the equations is a manifestation of genuine features that actually occur in nature. Consequently suitably interpreted non hyperbolic equations can be a useful neutral starting point before including complementary dissipative terms.

Numerical schemes must thus preserve as much as possible the characteristics of the system with its dissipation phenomena and avoid forcing non-ellipticity, even if the numerical cut-off due to the finite cell size inevitably distorts the small scales. If needed (for verification purposes for instance), an artificial term can also be added to mimic at mesh scales the possibly neglected small-scale phenomena [33, 15].

Another important property of the third option is its ability to preserve the physical consistency of energy transfers in the system, particularly regarding internal energy (and thus entropy production). This can be critical in the presence of shocks, as incidentally there is no unique solution to the Riemann problem in two-fluid flows : the details of small scale dissipation processes affect the final outcome. In this spirit, the energy evolution equations are first reformulated in Section 2.3.3 to make explicit the different contributions of the pressure work.

Because numerical schemes based more or less explicitly on characteristic curves are difficult to adapt to elliptic systems, the model is here discretized by a first order in time, second order in space, Lagrange-plus-remap scheme with a relaxation step on the volume fractions for imposing pressure equilibrium between phases. A summary of the numerical procedure is provided in Section 2.4. To the scheme order, this approach should provide robustness with respect to positivity and entropic constraints, minimal diffusion, and reduced sensitivity to elliptic-unstable numerical artifacts.

The Ransom water-faucet problem [34] is an elementary but important benchmark for two-fluid schemes and the impact of non-hyperbolicity. It features the advection and amplification of a volume fraction discontinuity, with marginal compressibility effects. It can thus be run with various possible reductions of the two-fluid system to two, four, or six equations : fully

incompressible, polytropic compressible, or fully entropic. Section 2.5 presents results of the six-equation Ransom test with the double Lagrange-plus-remap scheme under various numerical conditions on the elliptic and hyperbolized versions of the system. Comparisons with four and six equation results from the literature are provided, showing the impact of hyperbolization and thermodynamical inconsistency in terms of diffusion and profile distortions.

2.3 Two-fluid model

2.3.1 The six-equation one-pressure dissipation-free two-fluid model

General two-fluid mass, momentum, and internal energy equations can be obtained by applying a statistical averaging operator on the corresponding elementary conservation laws conditioned by the presence of each fluid. This produces numerous fluctuation correlation terms which must be closed, generally by input of supplementary physical properties of the system. However, as exposed in Section 2.2, for physical or numerical benchmarking it is usual to cancel all unknown terms, at the risk of a significant impact on the waves' behavior : the resulting "simple" backbone model is then elliptic, displaying two imaginary characteristics [12]. However, the ensuing model also represents a neutral starting point on which adding appropriately closed correlation terms to generate models of industrial relevance.

This cancellation of all non closed terms *including all pressure fluctuations* yields the well-known evolution equations of the one-pressure six-equation two-fluid model

$$\mathrm{D}_t^{\pm}(\alpha^{\pm}\rho^{\pm}) = 0 \ , \tag{2.1a}$$

$$\mathrm{D}_t^{\pm}(\alpha^{\pm}\rho^{\pm}u_i^{\pm}) = -\alpha^{\pm}P_{,i} + \alpha^{\pm}\rho^{\pm}g_i \ , \tag{2.1b}$$

$$\mathrm{D}_t^{\pm}(\alpha^{\pm}\rho^{\pm}e^{\pm}) = -P\,\mathrm{D}_t^{\pm}\,\alpha^{\pm} + \alpha^{\pm}\rho^{\pm}\dot{W}^{\pm} \ , \tag{2.1c}$$

where fluids are labeled as "+" and "−;" $\alpha^{\pm}$, $\rho^{\pm}$, $\boldsymbol{u}^{\pm}$ and $e^{\pm}$ are respectively the averaged volume fractions, densities, velocities and internal energies of the two fluids; $P = p^{\pm}$ is the common pressure of the fluids; $\dot{W}^{\pm}$ are heat sources including exchange; and $\mathrm{D}_t^{\pm}$ are the "Eulerian"

derivative operators along velocities $\boldsymbol{u}^{\pm}$ defined as

$$\mathrm{D}_t^{\pm} \cdot = \partial_t \ \cdot \ + \ (\ \cdot \ u_i^{\pm} \ )_{,i} \ . \tag{2.2}$$

The system (2.1) is closed through the fluids' equations of state $P = P^{\pm} = \mathcal{P}^{\pm}(\rho^{\pm},e^{\pm})$. The energy equations are written here in terms of the *internal* energies instead of the *total* energies. Although these are perfectly equivalent—at least for the continuous model equations—the former will here appear more convenient for analysis despite the much more widespread usage of the latter.

As mentionned by [41], and [42], neglecting the correlation of pressure and velocity fluctuations when averaging the governing equations implies the occurence of local Kelvin–Helmholtz instabilities in the mean flow equations.

2.3.2 Artificial drag force

In a realistic two-fluid model some exchange terms are present, for example drag forces that regularize the model. However, when omitting these physical drag forces either for studying the convective part of the model or because they are negligible at the scale solved by the mesh, an artificial drag can still be added in the backbone model in order to force the regularization at mesh scale.

As introduced in many studies in order to warrant hyperbolic behavior [38, 7], an artificial drag force $\mp\boldsymbol{D}$ can be added to the right hand side of the momentum equations (2.1b) with

$$\boldsymbol{D} = \delta \frac{\alpha^+\alpha^-\rho^+\rho^-}{\alpha^+\rho^- + \alpha^-\rho^+} (\boldsymbol{u}^+ - \boldsymbol{u}^-)^2 \, \boldsymbol{\nabla}\alpha^+ \ . \tag{2.3}$$

The magnitude is controlled by δ, hyperbolicity being ensured for $\delta > 1$ in the limit of vanishing $\boldsymbol{u}^+ - \boldsymbol{u}^-$. However, this is obtained at the cost of a loss of energy conservation.

Compared to other (more physical) drag forces, the simple artificial drag $\mp\boldsymbol{D}$ has the advantage of regularizing instabilities at all scales in the same way : all the wavelengths can be simultaneously brought to the stability limit. Therefore, the Stuhmiller–Bestion drag force is widely used and it is

added here for the practical comparisons with published Ransom test results done in Section 2.6. Furthermore, the emphasis here is placed on thermodynamical consistency and the work of the drag force does not comply with the second principle of thermodynamics whenever $\boldsymbol{D} \cdot \delta\boldsymbol{u} > 0$ or $\boldsymbol{\nabla}\alpha \cdot \delta\boldsymbol{u} > 0$ (demixing). Following usual practice the work of the drag force is thus not taken into account in the per-fluid internal energy equations.

2.3.3 Explicit pressure work contributions : per-fluid volume changes and inter-fluid drift

In its usual form given by (2.1), the one-pressure six-equation two-fluid model involves time derivatives of the fluid volume fractions $-P\mathrm{D}_t\alpha^\pm$ in the internal energy equations (or equivalently $-P\partial_t\alpha^\pm$ in the total energy equations). This formulation results in an implicit coupling between energies, volume fractions, and pressure which not only requires complex numerical solvers but also obscures the possible stiff processes at work.

In order to eliminate time derivatives and thus avoid the implicit closure, the right hand sides of the energy equations can be reformulated through the use of thermodynamic relationships (simultaneously obtained by [17], and in a somewhat similar spirit by [24, eq. 47] and by [29, eq. 49]). The details of the derivation are presented in Appendix .1 and lead to the following form in place of (2.1c)

$$\mathrm{D}_t^\pm(\alpha^\pm\rho^\pm e^\pm) = -\beta^\pm P V_{i,i} \pm \mu P_{,i}(u_i^+ - u_i^-) \mp \mu(\Gamma^+\rho^+\dot{W}^+ - \Gamma^-\rho^-\dot{W}^-) + \alpha^\pm\rho^\pm\dot{W}^\pm \ , \tag{2.4}$$

where $\boldsymbol{V}$ is the volume averaged velocity ; $\beta^\pm$ are the relative compressibility coefficients of the fluids ; μ is the coupling coefficient under along-pressure-gradient drift ; and $\Gamma^\pm$ are the Grüneisen coefficients of the fluids. These first three quantities are given by

$$\boldsymbol{V} = \alpha^+\boldsymbol{u}^+ + \alpha^-\boldsymbol{u}^- \ , \tag{2.5a}$$

$$\beta^\pm = \frac{\alpha^\pm/\gamma^\pm}{\alpha^+/\gamma^+ + \alpha^-/\gamma^-} \ , \tag{2.5b}$$

$$\mu = \frac{\alpha^+\alpha^-/\gamma^+\gamma^-}{\alpha^+/\gamma^+ + \alpha^-/\gamma^-} \ , \tag{2.5c}$$

where $\gamma^{\pm}$ are the polytropic coefficients of the fluids. With the assumption of identical fluid pressures $P = P^{\pm}$ and from the definition of the fluids' speeds of sound $[c^{\pm}]^2 = (\gamma^{\pm} P)/\rho^{\pm}$, the more common alternative expression for (2.5b) is obtained by substituting $\gamma^{\pm}$ with $\rho^{\pm}[c^{\pm}]^2$.

Form (2.4) of the energy equations may appear somewhat convoluted but it separates and makes visible the various processes associated with the pressure work in a rigorous and thermodynamically consistent way : i) $-\beta^{\pm} P V_{i,i}$ is the internal energy production through overall volume change, ii) $\pm\mu P_{,i}(u_i^+ - u_i^-)$ is the internal energy exchange between fluids through relative drift in a pressure gradient (a form of internal inter-fluid "nozzle" effect), iii) $\mp\mu(\Gamma^+\rho^+\dot{W}^+ - \Gamma^-\rho^-\dot{W}^-)$ is the internal energy transfer due to differential heating between fluids. Incidentally, although the driving sources $\dot{W}^{\pm}$ *produce* entropy, this last process is *reversible* and does not produce entropy as it is mediated by pressure. The total energy equations can be decomposed in a similar way, resulting in the same terms complemented by kinetic energy production and exchange terms.

Numerically, the form (2.4) can be easily discretized in an explicit approach and enables a direct analysis of the potentially stiff processes that may constrain the time step. A well-known but seldom elaborated effect is the compression stiffening on one of the fluids, for instance "+," whenever $\beta^+ \gg \alpha^+$; this is equivalent to

$$1 \gg \alpha^+ + \alpha^- \frac{\gamma^+}{\gamma^-} \ , \tag{2.6}$$

which occurs for a small volume fraction of fluid "+" included in a much less compressible fluid "−," a situation which does appear in numerous applications : for instance the air–water mixture has $\gamma^+/\gamma^- \approx 10^{-4}$. The authors contend that far above concerns on ellipticity, numericists must make sure that schemes remain robust in the face of such potentially strenuous stiff terms.

2.4 Two-fluid double Lagrange-plus-remap scheme

2.4.1 Overview of the scheme

Lagrange-plus-remap schemes are used in single fluid applications involving large displacements and deformations. After a Lagrangian step which solves the equations on a grid moving at the

fluid velocity, a remap step which is associated to the advection terms gives all the quantities back on the original grid. This approach has some significant advantages when including physical models which are naturally written in Lagrangian formulation : the remap step is essentially a geometric procedure on advected quantities, which most notably ensures consistency between mass and entropy transport. Moreover it does not involve any explicit or implicit reconstruction of characteristic curves and can thus be used even on elliptic models as in the present case.

Our double Lagrange-plus-remap approach is a six equation extension of an already published four equation scheme [9] and is described here in 1D. Each time step is made of three sub-steps : a Lagrangian evolution of each fluid on a staggered mesh, a remap on a common mesh, and an instantaneous pressure relaxation closed by the equation of state. Compared to Cournede's scheme, the present one is only first-order in time but still second-order in space.

As for usual Lagrangian schemes, stability and shock capture are obtained by adding an artificial viscosity stress Q to the pressure in the momentum and internal energy conservation equations (2.1b) and (2.4). The formulation for this artificial viscosity for two-phase flows takes into account the contrast of fluids' compressibilities and was given in [27, § 8.3].

In all the following, the elementary cells and nodes are respectively labeled by i and $i+1/2$ with $i \in [1; I]$. Cell and dual cell volumes are respectively $\mathcal{V}_i$ and $\mathcal{V}_{i+1/2} = \frac{1}{2}(\mathcal{V}_{i+1} + \mathcal{V}_i)$. The labels 'lgr' and 'rmp' denote quantities at the end of the respectively Lagrangian and remap steps.

2.4.2 Lagrangian evolution

At each time step, nodes of each fluid are first evolved as

$$[x^{\pm}]^{\text{lgr}}_{i+1/2} = x^n_{i+1/2} + \Delta t [u^{\pm}]^n_{i+1/2} \ , \tag{2.7}$$

and thus

$$[\mathcal{V}^{\pm}]^{\text{lgr}}_i = [x^{\pm}]^{\text{lgr}}_{i+1/2} - [x^{\pm}]^{\text{lgr}}_{i-1/2} \ . \tag{2.8}$$

The conservative quantities at time t^{n+1} are given by a finite volume approach on the Lagrangian form of (2.4)

$$[\alpha^\pm\rho^\pm]_i^{\rm lgr}[\mathcal{V}^\pm]_i^{\rm lgr} = [\alpha^\pm\rho^\pm]_i^n\,\mathcal{V}_i^n\ , \tag{2.9a}$$

$$\begin{aligned}[\alpha^\pm\rho^\pm u^\pm]_{i+1/2}^{\rm lgr}[\mathcal{V}^\pm]_{i+1/2}^{\rm lgr} &= [\alpha^\pm\rho^\pm u^\pm]_{i+1/2}^n\mathcal{V}_{i+1/2}^n \\ &- \Delta t\Big([\alpha^\pm]_{i+1/2}^n\big([P{+}Q]_{i+1}^n - [P{+}Q]_i^n\big) \mp D_{i+1/2}^n\Big)\ ,\end{aligned} \tag{2.9b}$$

$$\begin{aligned}[\alpha^\pm\rho^\pm e^\pm]_i^{\rm lgr}[\mathcal{V}^\pm]_i^{\rm lgr} &= [\alpha^\pm\rho^\pm e^\pm]_i^n\mathcal{V}_i^n - \Delta t[\beta^\pm]_i^n[P+Q^\pm]_i^n[U_{i+1/2}^n - U_{i-1/2}^n] \\ &\pm \tfrac{1}{4}\Delta t\mu_i^n\big(P_{i+1}^n - P_{i-1}^n\big)\big([u^+]_{i+1/2}^n + [u^+]_{i-1/2}^n - [u^-]_{i+1/2}^n - [u^-]_{i-1/2}^n\big)\ .\end{aligned} \tag{2.9c}$$

where $D_{i+1/2}^n$ is a basic second-order consistent discretization of the artificial drag force (2.3). The irreversible source terms are not included from there on.

The nodal volume fractions are simply given by an arithmetic average $[\alpha^\pm]_{i+1/2}^n = \frac{1}{2}([\alpha^\pm]_i^n + [\alpha^\pm]_{i+1}^n)$. The time step value Δt is bounded by usual constraints : CFL, non crossing of nodes, and, as mentioned before in Section 2.3.3, stiffness of exchange terms in (2.4).

2.4.3 Remap

The two Lagrangian meshes are remapped onto the fixed Eulerian initial mesh common to both fluids, according to a MUSCL methodology [43]. Linear and conservative interpolations in cells $\big[[x^\pm]_{i-1/2}^{\rm lgr}; [x^\pm]_{i+1/2}^{\rm lgr}\big]$ and dual cells $\big[[x^\pm]_i^{\rm lgr}; [x^\pm]_{i+1}^{\rm lgr}\big]$ are respectively performed for mass, energy, and momentum—with $[x^\pm]_i^{\rm lgr} = \frac{1}{2}([x^\pm]_{i-1/2}^{\rm lgr} + [x^\pm]_{i+1/2}^{\rm lgr})$

$$[\alpha^\pm\rho^\pm A]_i(x) = [\alpha^\pm\rho^\pm A]_i^{\rm lgr} + \nabla(\alpha^\pm\rho^\pm A)_i\big(x - [x^\pm]_i^{\rm lgr}\big)\ , \tag{2.10a}$$

$$[\alpha^\pm\rho^\pm u^\pm]_{i+1/2}(x) = [\alpha^\pm\rho^\pm u^\pm]_{i+1/2}^{\rm lgr} + \nabla(\alpha^\pm\rho^\pm u^\pm)_{i+1/2}\big(x - [x^\pm]_{i+1/2}^{\rm lgr}\big)\ , \tag{2.10b}$$

where $A = 1$ and $e^{\pm}$ for respectively masses and internal energies, and slopes $\nabla(\cdot)$ are calculated using a van Leer limiter. Integrating profiles over overlaps between Lagrangian and initial cells readily yields the 2nd order remap.

This remapping on conservative variables ensures the positivity of masses and volume fractions in every cell. For momentum it differs somewhat from the usual remap with mass fluxes [9, eq. 4.29]

$$[\alpha^{\pm}\rho^{\pm}u^{\pm}]_{i+1/2}(x) = \tfrac{1}{2}\big([\alpha^{\pm}\rho^{\pm}]_i^{\text{lgr}} + [\alpha^{\pm}\rho^{\pm}]_{i+1}^{\text{lgr}}\big)[u^{\pm}]_{i+1/2}^{\text{lgr}} + \tfrac{1}{2}[u^{\pm}]_{i+1/2}^{\text{lgr}}\big(\nabla(\alpha^{\pm}\rho^{\pm})_i + \nabla(\alpha^{\pm}\rho^{\pm})_{i+1}\big)\big(x - [x^{\pm}]_{i+1/2}^{\text{lgr}}\big) \ , \quad (2.11)$$

which is non conservative but verifies the DeBar condition [10, p. 13] whereby a uniform velocity field is unaffected by density gradients [23].

Finally, as internal energies are remapped in place of total energies, energy conservation requires a dissipative correction to compensate kinetic energy losses produced by momentum remap. This usual procedure leads to a fully conservative numerical scheme which is necessary to properly capture shocks.

2.4.4 Instantaneous pressure relaxation

Pressure work is fully taken into account during the Lagrangian step (2.9c) which closely discretizes (2.4). However, a residual pressure imbalance between fluids is present due to truncation errors and to dissipation during remap. An instantaneous pressure relaxation in each cell is thus performed at each time step, whereby fluid volume fractions are adjusted with an iterative Newton–Raphson method until reaching the following identities

$$1 = \alpha_i^+ + \alpha_i^- \ , \quad (2.12a)$$

$$P_i^{n+1} = \mathcal{P}^{\pm}\begin{pmatrix} [\alpha^{\pm}\rho^{\pm}]_i^{\text{rmp}}/[\alpha^{\pm}]_i^{n+1} \ , \\ [\alpha^{\pm}\rho^{\pm}e^{\pm}]_i^{\text{rmp}}/[\alpha^{\pm}\rho^{\pm}]_i^{\text{rmp}} \end{pmatrix} , \quad (2.12b)$$

where functions $\mathcal{P}^{\pm}(\rho^{\pm},e^{\pm})$ are provided by the equations of state of the fluid. For example, in the case of perfect gases $\mathcal{P}^{\pm}$ is given by

$$\mathcal{P}^{\pm}(\rho^{\pm},e^{\pm}) = (\gamma^{\pm} - 1)\rho^{\pm}e^{\pm} \ . \tag{2.13}$$

The set of equations (2.12) may be poorly conditioned for extreme volume fractions values or for singular equations of state (see comments in Section 2.3.3). Conditioning can then be necessary but will not be elaborated here. The Newton–Raphson algorithm was used in the present tests with perfect and stiffened gases, despite the fact that explicit formulas exist in this case.

Note that if the initial implicit system (2.1) had been discretized, the pressure equilibrium condition would have lead to a coupled solver for i) evolution equations of internal energy, ii) equations of state, and iii) pressure equality constrained by the volume fraction evolution. The corresponding nonlinear system would then involve six non-linear unknowns, whereas in the present work the split pressure relaxation only leaves one non-linear unknown.

2.5 Ransom water faucet test

2.5.1 The Ransom faucet test case

The water faucet test, designed by [34], has become a basic benchmark for two-fluid numerical methods. It consists of a 12 m vertical pipe initially filled with an air–water mixture at a water volume fraction of 0.8. The boundary condition at the top of the tube is a fixed 10 m/s water inflow on the volume fraction of 0.8, with no air flux. the bottom of the pipe is at open ambient pressure. Under these conditions, the water jet accelerates and stretches under the action of gravity. In the limit of incompressible water, an analytical solution is known and allows the comparison of numerical solutions. In practical calculations, the equations of state of water and air are approximated by respectively stiffened and perfect gases.

This test case is simply captured by the backbone two-fluid models, of three to seven equations, depending on closure assumptions on pressure balance between fluids, compressibility of water, computation of energy, etc. Four important features of the flow can be examined for elliptic

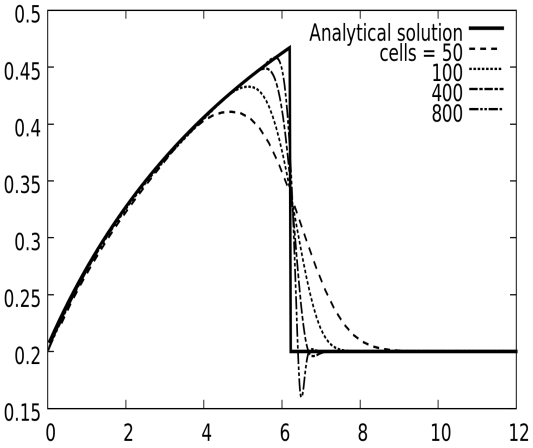

FIGURE 2.1 – Profiles of water volume fractions in Ransom tests of the (elliptic) 6 equation model with $\delta = 0$: double Lagrange-plus-remap scheme with 2nd order remapping, $t = 0.5$, $I = 50$ to 800 cells, CFL = 0.2.

models such as (2.1) : i) the *entropy preservation*, as this is an isentropic flow, which requires an overall consistent discretization of pressure work and transport in the energy and momentum equations ; ii) the *stretched stream profile*, to be matched with the smooth analytical solution ; iii) the *volume fraction discontinuity*, which must be captured without too much numerical diffusion ; and iv) in the case of elliptic models, the *unstable character*, which must be preserved while retaining the robustness of the calculation.

2.5.2 Present results

Grid convergence results are shown on Figure 2.1 for the double Lagrange-plus-remap scheme. For fine meshes, some undershoot appears upstream of the volume fraction discontinuity (a form of Kelvin–Helmholtz instability), which is recognized to be a consequence of the non-hyperbolic behavior of the backbone two-fluid model [12]. The amplification of this *physical* oscillation is always present, even if not visible at early times, and occurs sooner when the mesh is refined. As shown in Figure 2.2 a solution can be computed even at late times close to volume fraction saturation provided the time step is appropriately reduced. Other investigators working with schemes non dependent on characteristic curves have consistently obtained similar unstable

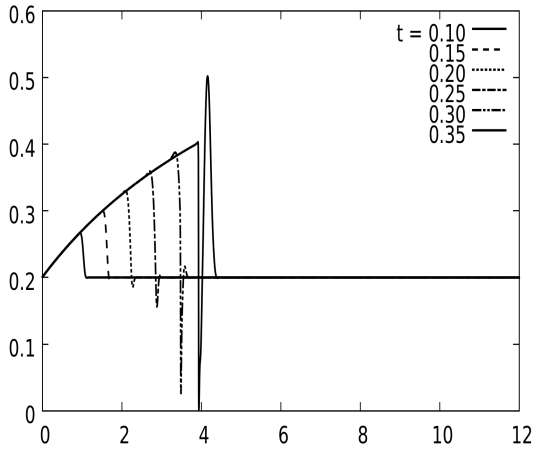

FIGURE 2.2 – Profiles of water volume fractions in Ransom tests of the (elliptic) 6 equation model with $\delta = 0$: double Lagrange-plus-remap scheme with 2nd order remapping, $t = 0.1$ to 0.35, $I = 3200$ cells. At final time the volume fraction at undershoot is close to zero.

solutions from their discretized models [18, 26, 15].

Adding the artificial drag force (2.3) damps this undershoot as shown in Figure 2.3 but also smears the discontinuity. Values above $\delta = 1$ are not necessary as hyperbolicity is ensured but should further be avoided so as to keep a good compromise between the numerical diffusion and the capture of the stretched stream profile.

Figure 2.4 presents the grid convergence study with a fixed artificial drag parameter of $\delta = 0.2$. At final time, this small value is still sufficient to completely remove the undershoot and to produce an excellent agreement with the exact solution, even if the backbone two-fluid model remains elliptic. However, as in the study of [12], for any given $\delta < 1$, the undershoot eventually appears for fine enough meshes or late enough times. The competition between numerical diffusion and undershoot depends on the duration of the simulation.

2.6 Cross assessment with published results

Sixteen of the retained results are produced in similar conditions (identical flow parameters, final time between $t = 0.4$ and 0.6, around 200 cells), and the corresponding volume fraction

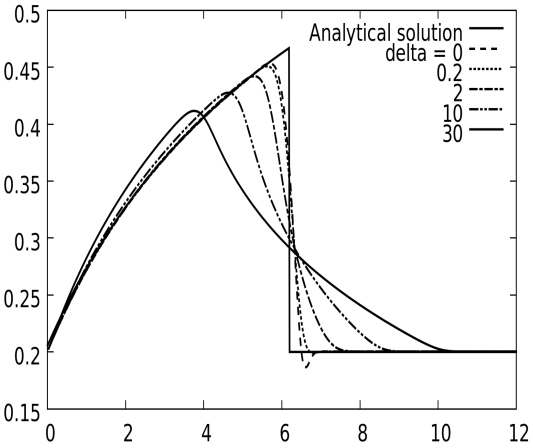

FIGURE 2.3 – Profiles of water volume fractions in Ransom tests of the 6 equation model with $\delta = 0$ to 30 : double Lagrange-plus-remap scheme with 2nd order remapping, $t = 0.5$, $I = 600$ cells, CFL $= 0.2$.

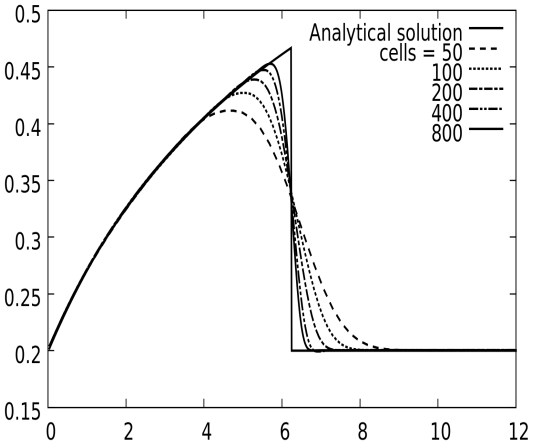

FIGURE 2.4 – Profiles of water volume fractions in Ransom tests of the (elliptic) 6 equation model with $\delta = 0.2$: double Lagrange-plus-remap scheme with 2nd order remapping, $t = 0.5$, $I = 50$ to 800 cells, CFL $= 0.2$.

profiles have been extracted and fit to identical plot scales ($[0 : 12] \times [0.15 : 0.5]$ as in Figures 2.1 to 2.4) for easy graphical comparison. Figures. 2.5 and 2.6 regroup results of respectively 4(+1) and 6(+1) equation models. Despite their relevance to the present discussion, the other four will not be considered in the following. In the 6+1 equation result of [36] the number of mesh cells is

not reported. In the 6+1 equation result of [1] the final time $t = 0.1$ is too small. In the 6 equation result of [12] the initial condition of the volume fraction in the pipe as well as the water inlet flow are non standard. In the 4 equation result of [3] the number of mesh cells is too small ($I = 60$).

Reference (and figures therein)	Model			Type of scheme	Figure
[9, fig. 5.3 & 5.2]	4		E	Double Lagrange-plus-remap	2.5a&b
[11, fig. 20]	4			Hybrid finite volumes	2.5c
[13, fig. 9]	4			Hybrid central upwind	2.5d
[3, fig. 5]	4			TVD Lax–Friedrichs	—
[6, fig. 6]	4			Non-homogeneous Riemann solver	2.5e
[2, fig. 12]	4+1	P+P		Approximative Riemann solver	2.5f
[30, fig. 4]	4+1			Musta	2.5g
[35, fig. 2]	4+1			Gforce and Gmusta	2.5h
[18, fig. 3]	6-1	I+P		Fvcf	2.5i
[12, fig. 5]	6			Eno–Weno	—
[31, fig. 3]	6			Ausm+	2.6b
[40, fig. 8]	6			First order upwind finite volumes	2.6c
[8, fig. 10]	6	P+P	E	Upwind finite volumes	2.6d
[32, fig. 4]	6		E	Ausm+	2.6e
[22, fig. 5]	6			Ausm	2.6f
[4, fig. 7]	6+1			Godunov	2.6g
[36, fig. 13]	6+1			Godunov	—
[1, fig. 14]	6+1			Finite volumes	—
[16, fig. 3]	6+1	P+P		VFRoe-ncv	2.6h
[20, fig. 5.9]	6+1		E	Central Upwind	2.6i

Table 2.1 – Basic characteristics of the (generally) hyperbolic two-fluid schemes compared here on Ransom's faucet test. The label "P+P" (resp. "I+P") refers to the models using two perfect gas equations of state (resp. one perfect gas and one incompressible gas). The label "E" stands for the models that can be made elliptic.

We have selected twenty published results of the Ransom test listed in Table 2.1 which represent current but different trends on two-fluid numerical approaches. As summarized in Table 2.1, they are characterized by the number of conservation equations (four or six, without or with energy equations), a possible evolution equation for pressure relaxation, different equations of state for water (incompressible, stiffened gas, perfect gas), a possible elliptic behavior. The schemes involved will not be analysed in depth and are just reported here by generic designations. The models are all hyperbolic except in four of these works.

At first glance results of 4(+1) equation models in Figure 2.5 appear similar and, except for an inevitable numerical diffusion of the volume fraction discontinuity, the profile is captured in an accurate and converging way without artifacts. [9] further tested the elliptical version of his model by setting $\delta = 0$ (see Figure 2.5a) then producing profiles of similar quality to the hyperbolic version (see Figure 2.5b) except for some undershoot upstream of the discontinuity at the highest resolutions ($I > 100$) : this behavior is similar to what was shown here in Section 2.5.2, and is consistent with the fact that the 4 equation model and scheme of [9] is the reduced version of the present 6 equation approach.

Now, closer inspection of Figure 2.5 reveals significant differences in the amount of numerical smearing of the discontinuity. Compared to the similar results of [9], [11], [18], and [6] (see Figures 2.5b, 2.5c, 2.5i, and 2.5e), results of [13], [2], [30], and [35] (see Figures 2.5d, 2.5f, 2.5g, and 2.5h) display higher numerical diffusion as they require typically one order of magnitude more mesh cells in order to achieve comparable peak values of the profiles. It may be conjectured that the "fifth" evolution equation could induce a significant part of the diffusion in the cases of [2], [30], and [35].

Results of 6(+1) equation models in Figure 2.6 appear to follow similar trends of diffusion : profiles in [4] and possibly [16] considering the high 20000 cells test (see Figure 2.6f and Figure 2.6g) are significantly more diffusive and involve a "seventh" evolution equation. Yet, result in [20] (see Figure 2.6h) involve the "seventh" equation though appear less diffusive with an elliptic system. Beyond diffusion however, artifacts that were not present for 4(+1) equation models can also be observed : a significant and lasting overshoot downstream of the discontinuity in

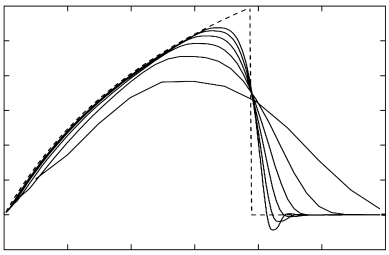

a) [9], elliptic :
$t = 0.6$, $I = 12$ to 200 cells
4 eq. Double Lagrange-plus-remap.

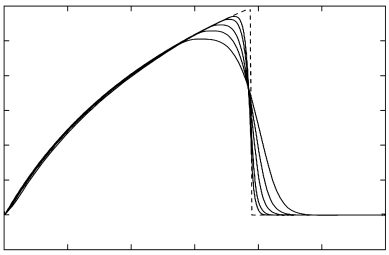

b) [9] :
$t = 0.6$, $I = 100$ to 2000 cells
4 eq. Double Lagrange-plus-remap.

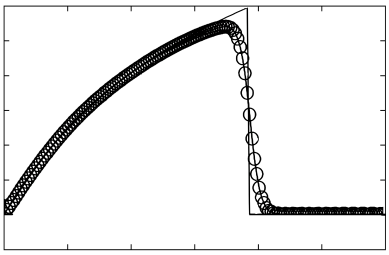

c) [11] :
$t = 0.6$, $I = 160$ cells
4 eq. Hybrid finite volumes.

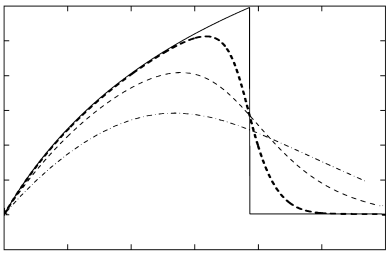

d) [13] :
$t = 0.6$, $I = 24$ to 1200 cells
4 eq. Hybrid central upwind.

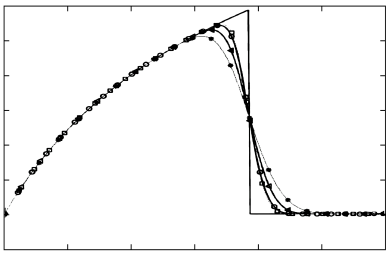

e) [6] :
$t = 0.6$, $I = 100$ to 500 cells
4 eq. Non-homogeneous Riemann solver.

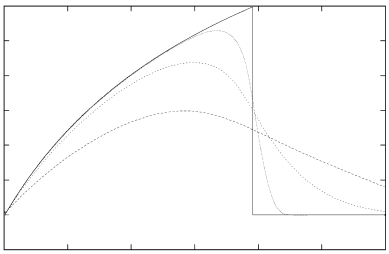

f) [2] :
$t = 0.6$, $I = 10$ to 10000 cells
5 eq. Approximative Riemann solver.

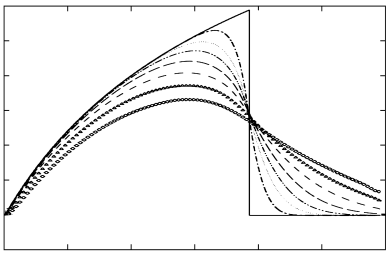

g) [30] :
$t = 0.6$, $I = 100$ to 10000 cells
5 eq. Musta.

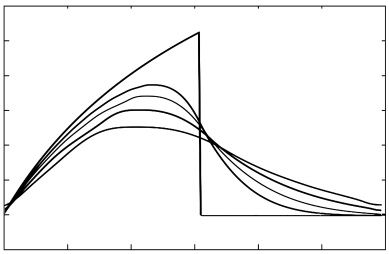

h) [35] :
$t = 0.5$, $I = 200$ to 1600 cells
5 eq. Gforce and Gmusta.

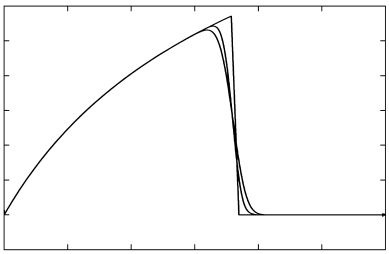

i) [18] :
$t \lesssim 0.6$, $I = 768$ to 1536 cells
6-1 eq. Fvcf.

Figure 2.5 – Profiles of water volume fractions in Ransom tests of 4 and 5 equation models with various schemes.

results by [8], [32], and [20] (see Figures 2.6c, 2.6d, and 2.6h), and a slight localized overshoot with an asymmetric discontinuity smearing in [31] and [22] (see Figures 2.6b and 2.6e). As also observed by [18], similar overshoots can be produced in our results for excessively large values of the artificial drag coefficient δ (see Figure 2.3). Substitution of perfect gas EOS for the more physically consistent stiffened gas or incompressible EOS also appears to impact the production of artifacts and possibly part of the smearing, as can be observed in results by [8] and [16] (see

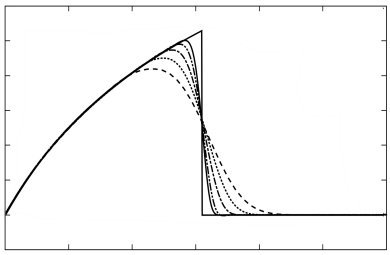

a) Present work, elliptic :
$t = 0.5$, $I = 50$ to 800 cells
6 eq. Double Lagrange-plus-remap.

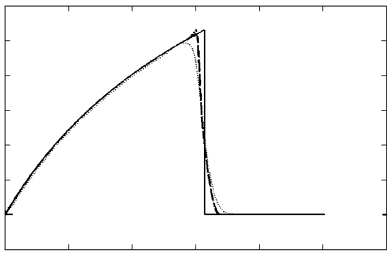

b) [31] :
$t = 0.5$, $I = 100$ to 1000 cells
6 eq. AUSM+.

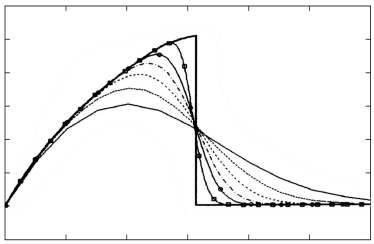

c) [40] :
$t = 0.5$, $I = 12$ to 768 cells
6 eq. First order upwind finite volumes.

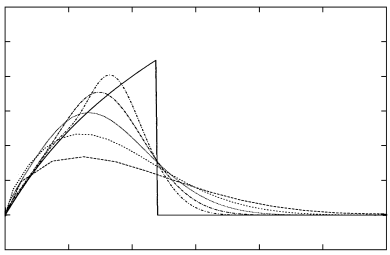

d) [8], elliptic :
$t = 0.4$, $I = 12$ to 200 cells
6 eq. Upwind finite volumes.

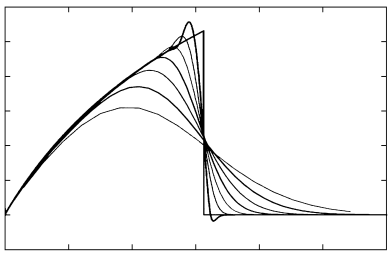

e) [32], elliptic :
$t = 0.5$, $I = 20$ to 1280 cells
6 eq. AUSM+.

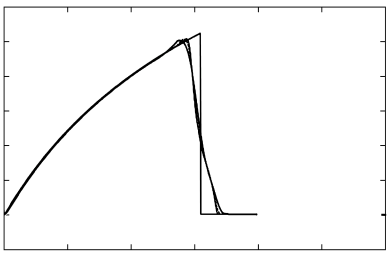

f) [22] :
$t = 0.5$, $I = 500$ to 2000 cells
6 eq. AUSM.

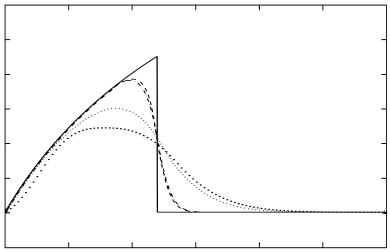

g) [4] :
$t = 0.4$, $I = 100$ to 1000 cells
7 eq. Godunov.

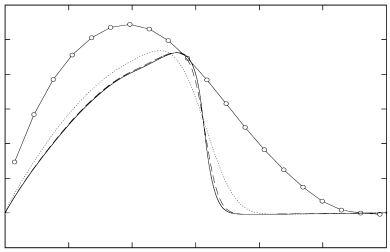

h) [16] :
$t = 0.5$, $I = 20$ to 20000 cells
7 eq. VFROE-NCV.

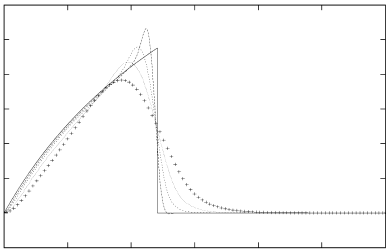

i) [20], elliptic :
$t = 0.4$, $I = 100$ to 800 cells
7 eq. Central Upwind.

FIGURE 2.6 – Profiles of water volume fractions in Ransom tests of 6 and 7 equation models with various schemes.

Figures 2.6c and 2.6g).

The present results—along with those of [31] and [40]—show that the approach developed here is a satisfactory "neutral starting point" which balances between physical and numerical artifacts such as under- and overshoots and numerical diffusion.

The emphasis is on the ability of the elliptic backbone model to give satisfactory results with practical meshes provided that thermodynamical consistency is ensured. When simulating real

flows, the usual supplementary physics-based terms (drag, diffusion or surface tension) are added in the backbone model and regularize the system without competing with pre-existing artificial regularizing terms.

In the present approach and even with $\delta = 0$ overshoots are reduced and appear at late times as compared to other elliptic results (see Figures 2.6c, 2.6d, and 2.6h). The present explicit six-equation extension of the scheme of [9] guarantees that pressure work is captured in a thermodynamically consistent way so that the isentropic character of the flow is preserved.

2.7 Conclusion

This work has investigated the acceptability of using an elliptic model for the convective part of two-fluid models instead of forcing the backbone model to be hyperbolic as it is often proposed in the litterature. The key point highlighted here is the mandatory constraint of a physically consistent model, in particular regarding thermodynamics—i.e. compliance with the entropy condition—when the model includes energy equations.

As a special case here, an improved double Lagrange-plus-remap numerical scheme has been presented which ensures an explicit capture of the pressure work and positivity. This approach is also suitable for both hyperbolic or elliptic two-fluid models with energy equations. Results on the Ransom water faucet problem show satisfactory accuracy with the analytical solution with or without the artificial drag force.

Compared to other published Ransom tests, the present approach provides a form of neutral starting point : robust but not excessively diffusive, with accurate capture of the stretched stream and volume fraction discontinuity for any practical mesh refinement. The numerical scheme does not require the prototypical two-fluid model to be hyperbolic and a small artificial drag force term can be added, only for delaying the development of the instability that arises just upstream of the discontinuity for fine meshes (due to the presence of Kelvin–Helmholtz instability in the model and captured by the scheme).

Regularization procedures must be kept to minimum or even discarded as they distort the physical behavior of Kelvin–Helmholtz waves, and perturb the conservation and transfers of

energy. The drawback of discretizing the elliptic model is that the numerical scheme must remain robust with respect to the stiff behavior which can appear at saturated volume fractions. The simple Lagrange-plus-remap approach ensures positivity and entropy consistency, and thus stays robust under the appropriate time step constraints due to its explicit character.

The prescription suggested by the present work is not that hyperbolic models should be pushed into oblivion, but merely that elliptic models deserve just as much attention. Both approaches may be relevant provided that thermodynamical consistency is ensured [5]. Neither should elliptic models be a priori discarded, nor could hyperbolized models be used without verifying their physical consistency—especially if energy transfers are of some importance in the studied application.

It remains to be investigated what specific properties of the Lagrange-plus-remap approach can be transposed to other more traditional schemes in order to preserve the appropriate accuracy and robustness with respect to elliptical features. Detailed analysis of the present scheme's behavior in other situations (for example bubbly or slug flows) are postponed to later publications.

.1 Derivation of explicit pressure work terms

In the basic thermodynamic relationships

$$\mathrm{d}\, e = p\frac{\mathrm{d}\,\rho}{\rho^2} + \delta\, W \ , \tag{14a}$$

$$\mathrm{d}\, p = \gamma p\frac{\mathrm{d}\,\rho}{\rho} + \Gamma\rho\,\delta\, W \ , \tag{14b}$$

where γ and Γ are respectively the polytropic and Grüneisen coefficients, the second relationship can be replaced by

$$\rho\,\mathrm{d}\, e = \frac{\mathrm{d}\, p}{\gamma} + \Big(1 - \frac{\Gamma}{\gamma}\Big)\rho\,\delta\, W \ , \tag{15}$$

obtained by simple elimination of $\mathrm{d}\,\rho$. Along Lagrangian trajectories of fluids "+" and "−," and using the mass conservation equation $\mathrm{D}_t^{\pm}(\alpha^{\pm}\rho^{\pm}) = 0$, (14a) and (15) yield after some elementary

rearrangements

$$\mathrm{D}_t^{\pm}(\alpha^{\pm}\rho^{\pm}e^{\pm}) = -p^{\pm}\,\mathrm{D}_t^{\pm}\,\alpha^{\pm} + \alpha^{\pm}\rho^{\pm}\dot{W}^{\pm}\ , \tag{16a}$$

$$\mathrm{D}_t^{\pm}(\alpha^{\pm}\rho^{\pm}e^{\pm}) = \frac{\alpha^{\pm}}{\gamma^{\pm}}\,\mathrm{d}_t^{\pm}\,p^{\pm} + \Big(1 - \frac{\Gamma^{\pm}}{\gamma^{\pm}}\Big)\alpha^{\pm}\rho^{\pm}\dot{W}^{\pm}\ , \tag{16b}$$

where $\mathrm{d}_t^{\pm}$ are the "Lagrangian" derivative operators along velocities $\boldsymbol{u}^{\pm}$ defined as

$$\mathrm{d}_t^{\pm}\cdot = \partial_t\ \cdot\ + (\ \cdot\ )_{,i}u_i^{\pm}\ . \tag{17}$$

Now, in order to obtain explicit expressions for $\mathrm{D}_t^{\pm}(\alpha^{\pm}\rho^{\pm}e^{\pm})$—i.e. devoid of time derivatives—it is possible to take advantage of the volume closure and the instantaneous pressure relaxation between phases, which are here written in differential form as $\partial_t\alpha^+ + \partial_t\alpha^- = 0$ and $\partial_t p^+ = \partial_t p^- = \partial_t P$. From $\sum_{\pm}(16\mathrm{b})^{\pm} = \sum_{\pm}(16\mathrm{a})^{\pm}$ one obtains

$$\Big(\frac{\alpha^+}{\gamma^+} + \frac{\alpha^-}{\gamma^-}\Big)\partial_t P + \Big(\frac{\alpha^+}{\gamma^+}u_i^+ + \frac{\alpha^-}{\gamma^-}u_i^-\Big)P_{,i} + \sum_{\pm}\Big(1 - \frac{\Gamma^{\pm}}{\gamma^{\pm}}\Big)\alpha^{\pm}\rho^{\pm}\dot{W}^{\pm}$$
$$= -P(\alpha^+u_i^+ + \alpha^-u_i^-)_{,i} + \sum_{\pm}\alpha^{\pm}\rho^{\pm}\dot{W}^{\pm}\ , \tag{18}$$

hence

$$\Big(\frac{\alpha^+}{\gamma^+} + \frac{\alpha^-}{\gamma^-}\Big)\,\mathrm{d}_t^{\pm}\,P = -P(\alpha^+u_i^+ + \alpha^-u_i^-)_{,i} \pm \frac{\alpha^{\mp}}{\gamma^{\mp}}(u_i^+ - u_i^-)P_{,i} + \sum_{\pm}\frac{\alpha^{\pm}}{\gamma^{\pm}}\Gamma^{\pm}\rho^{\pm}\dot{W}^{\pm}\ . \tag{19}$$

Substituting this expression of $\mathrm{d}_t^{\pm}\,P$ for $\mathrm{d}_t^{\pm}\,p^{\pm}$ in (16b) yields (2.4) with (2.5).

Bibliographie

[1] R. Abgrall, R. Saurel, Discrete equation for physical and numerical compressible multiphase mixtures. J. Comput. Phys. 186 (2003), 361.

[2] A. Ambroso, C. Chalons, F. Coquel, T. Galié, Relaxation and numerical approximation of a two-fluid two-pressure diphasic model. ESAIM-Math. Model. Num. 43 (2009), 1063.

[3] M.R. Ansari, V. Shokri, Numerical modeling of slug flow initiation in a horizontal channels using a two-fluid model. Int. J. Heat Fluid Fl. 32 (2011), 145.

[4] N. Andrianov, R. Saurel, G. Warnecke, A simple method for compressible multiphase mixtures and interfaces. Int. J. Numer. Meth. Fluids 41 (2003), 109.

[5] G.S. Arnold, D.A. Drew, R.T. Lahey Jr, An assessment of multiphase flow models using the second law of thermodynamics. Int. J. Multiphase Flow 16 (1990), 491.

[6] F. Benkhaldoun, L. Quivy, A non homogeneous Riemann Solver for shallow water and two phase flows. Flow Turbul. Combust. 76 (2006), 391.

[7] D. Bestion, The physical closure laws in the CATHARE code. Nucl. Eng. Des. 124 (1990), 229-245.

[8] F. Coquel, K. El Amine, E. Godlewski, B. Perthame, P. Rascle, A numerical method using upwind schemes for the resolution of two-phase flows. J. Comput. Phys. 136 (1997), 272.

[9] P.H. Cournède, Un schéma bi-lagrange plus projection pour la simulation bifluide des instabilités de mélanges. PhD. dissertation – École centrale Paris, (2001).

[10] R. DeBar, Fundamentals of the KRAKEN code. LLNL report UCID-17366, (1974).

[11] F. De Vuyst, Stable and accurate hybrid finite volume methods based on pure convexity arguments for hyperbolic systems of conservation law. J. Comput. Phys. 193 (2004), 426.

[12] T. Dinh, R. Nourgaliev, T. Theofanous, Understanding the ill-posed two-fluid model. Proceedings of the 10th International Topical Meeting on Nuclear Reactor Thermal Hydraulics (NURETH10), (2003) Seoul, Korea.

[13] S. Evje, T. Flåtten, Hybrid central-upwind schemes for numerical resolution of two-phase flows. ESAIM-Math. Model. Num. 39 (2005), 253.

[14] W.D. Fullmer, V.H. Ransom, M.A. Lopez de Bertodano, Linear and nonlinear analysis of an unstable, but well-posed, one-dimensional two-fluid model for two-phase flow based on the inviscid Kelvin–Helmholtz instability. Nucl. Eng. Des. 268 (2014), 173.

[15] W.D. Fullmer, S.Y. Lee, M.A. Lopez de Bertodano, An artificial viscosity for the ill-posed one-dimensional incompressible two-fluid model. Nucl. Tech. 185 (2014), 296.

[16] T. Gallouët, J.M. Hérard, N. Seguin, Numerical modeling of two-phase flows using the two-fluid two-pressure approach. Math. Mod. and Meth. in App. Sci. 14 (2004), 663.

[17] J.M. Ghidaglia, Personal communication, (2000).

[18] J.M. Ghidaglia, A. Kumbaro, G. Le Coq, On the numerical solution to two-fluid models via a cell centered finite volume method. Eur. J. Mech. B-Fluid 10 (2001), 841.

[19] F.H. Harlow, Heat Transfer VII 164 (1974).

[20] S. Karni, E. Kirr, A. Kurganov, G Petrova, Compressible two-phase flows by central and upwind schemes. ESAIM-Math. Model. Num. 38 (2004), 477.

[21] B.L. Keyfitz, R. Sanders, M. Sever, Lack of hyperbolicity in the two-fluid model for two-phase incompressible flow. Discrete Cont. Dyn.–B 3 (2003), 541.

[22] K. Kitamura, M.S. Liou, Comparative study of AUSM-family schemes in compressible multiphase flow simulations. Proceedings of the Seventh International Conference on Computational Fluid Dynamics (ICCFD7), Big Island, Hawaii, (2012).

[23] A. Kurganov, Well-balanced central-upwind scheme for compressible two-phase flows. Proceedings of the European Conference on Computational Fluid Dynamics (ECCOMAS CFD), Egmond aan Zee, The Netherlands, (2006).

[24] J.J. Kreeft, B. Koren, A new formulation of Kapila's five-equation model for compressible two-fluid flow, and its numerical treatment. J. Comput. Phys. 229 (2010), 6220.

[25] D. Lhuillier, C.H. Chang, T. Theofanous, On the quest for a hyperbolic effective-field model of disperse flows. J. Fluid. Mech. 731 (2013), 184.

[26] M.S. Liou, C.H. Chang, L. Nguyen, T. Theofanous, How to solve compressible mutlifluid equations : a simple, robust, and accurate method. AIAA J. 46 (2008), 9.

[27] A. Llor, Statistical hydrodynamic models for developed mixing instability flows : analytical '0D' evaluation criteria, and comparison of single-and-two-phase flow approaches. Lect. Notes Phys. 681 (2005).

[28] R.W. Lyczkowski, The history of multiphase computational fluid dynamics. Ind. Eng. Chem. Res. 49 (2010), 5029.

[29] S.T. Munkejord, S. Evje, T. Flåtten, A MUSTA scheme for a nonconservative two-fluid model. SIAM J. Sci. Comput. 31 (2009), 2587.

[30] S.T. Munkejord, A numerical study of two-fluid models with pressure and velocity relaxation. Adv. Appl. Math. Mech. 2 (2010), 131.

[31] Y. Niu, Y. Lin, C. Chang, A further work on multi-phase two-fluid approach for compressible multi-phase flows. Int. J. Num. Meth. Fluid. 58 (2008), 879.

[32] H. Paillère, C. Corre, J.R. García Cascales, On the extension of the AUSM+ scheme to compressible two-fluid models. Comput. Fluids 32 (2003), 891.

[33] J.D. Ramshaw, J.A. Trapp, Characteristics, stability, and short-wavelength phenomena in two-phase flow equation systems. Nucl. Sci. Eng. 66 (1978), 93.

[34] V.H. Ransom, Numerical benchmark test No 2.1 : faucet flow. Multiphase Sci. Technol. 1 (1987), 465.

[35] E. Romenski, D. Drikakis, E. Toro, Conservative models and numerical methods for compressible two-phase flow. J. Sci. Comput. 42 (2010), 68.

[36] R. Saurel, R. Abgrall, A multiphase Godunov method for compressible multifluid and multiphase flows. J. Comput. Phys. 150 (1999), 425.

[37] H.B. Stewart, B. Wendroff, Two phase flows : models and methods. J. Comput. Phys. 56 (1984), 363.

[38] J.H. Stuhmiller, The influence of interfacial pressure forces on the character of two-phase flow model equations. Int. J. Multiphase Flow 3 (1977), 551.

[39] T. Theofanous, C.H. Chang, On the computation of multiphase interactions in transonic and supersonic flows. Proceedings of AIAA, Conference Reno, 7 (2008).

[40] I. Toumi, An upwind numerical method for two-fluid two-phase flow models. Nucl. Sci. Eng. 123 (1996), 147.

[41] J.A. Trapp, The mean flow character of two-phase flow equations. Int. J. Multiphase Flow 12 (1986), 263.

[42] A. Thyagaraja, D.F. Fletcher, The nonhyperbolicity of multiphase flow equations : a non linear non problem ? Comput. Phys. Comm. 56 (1989), 115.

[43] B. van Leer, Towards the ultimate conservative difference scheme. V. A second order sequel to Godunov's method. J. Comput. Phys. 32 (1979), 101.

Chapitre 3

Procédure générique de dérivation de schémas ALE direct mimétiques : application aux écoulements monophasiques

Le corps de ce chapitre est constitué d'un article prêt à être soumis pour publication : A novel GEEC (Geometry, Energy, and Entropy Compatible) procedure applied to a staggered direct-ALE scheme for hydrodynamics, T. Vazquez-Gonzalez, A. Llor, C. Fochesato, in preparation.

3.1 Abstract

The simulation of transient compressible single-fluid flows, modeled by the Euler's classical equation, requires numerical schemes that comply with various stringent physical constraints such as thermodynamic consistency, robustness, and stability when shocks, large volume, and transport effects are present. In order to meet these requirements in extreme conditions such as those encountered in defense applications, the present work aims at developing a novel generic

GEEC (Geometry, Energy, and Entropy Compatible) procedure for the discrete derivation of physics-compatible numerical schemes ensuring the following features : i) *energetic compatibility*, even if solving with primitive variables, so that total energy is exactly conserved at discrete level for an accurate capture of shock levels and shock velocities ; ii) *entropic compatibility* which ensures the compliance with the second law of thermodynamics at least to second-order—entropy must increase in general and must be conserved for isentropic flows ; —and iii) *geometric compatibility* where volume variations (compressions and dilatations) must be consistently taken into account with advection relative to the grid.

This novel generic GEEC procedure is addressed in the present work over a three-step mimicking derivation : i) for a prescribed mass transport equation, a variational least action principle is used to generate the proper pressure forces in the discrete momentum evolution equation—thus ensuring a compatible exchange between kinetic and internal energies ; — ii) corrections are systematically performed on numerical residues in order to force conservation at discrete level up to round-off errors ; and iii) an artificial viscosity term is added as a pressure-like contribution in the evolution equations in order to capture shocks and to stabilize the scheme.

As a proof of concept, this procedure is applied in the present work for the simulation of compressible flows leading to a novel ALE (Arbitrary Lagrangian–Eulerian) scheme named GEECS (Geometry, Energy, and Entropy Compatible Scheme). The main features of the scheme are : i) a *direct* ALE formalism where mass, momentum, and energy transport fluxes are directly taken into account without separation in the discrete equations ; ii) continuity with Lagrangian solvers used at CEA/DAM where velocity fields are space-and-time staggered ; iii) second-order accuracy in the Lagrangian limit ; and as a consequence iv) a somewhat non-standard downwind formulation of the pressure gradient, dual of the upwind transport operator—as a consequence of the application of the variational least action principle.

Results on standard numerical test cases involving shocks and large deformations confirm the expected built-in properties of GEECS. In particular, the entropic compatibility leads to the preservation of entropy to second-order for isentropic flows, regardless of mesh motions and regardless of the first-order accuracy of the discrete mass transport equation. Indifference

and versatility with respect to strenuous grid motion strategies are demonstrated in various situations—including supersonic shearing for new variants of Sod's shock tube and Sedov's blast wave—highlighting the advantages of the compatibility between velocity fields and volume variations in the presence of strong fluids advection.

3.2 Introduction

3.2.1 Motivations

Two different coordinate systems are traditionally used in simulations of fluid or solid mechanics (see for example the reviews [25, 1, 2, 36]) : Eulerian approaches employ fixed meshes [19], whereas Lagrangian approaches use meshes that follow material motion [42]. These systems were originally developed mostly for aerodynamic (Eulerian) and defense (Lagrangian) problems, but the range of applications has broadened considerably since the sixties. In the continuous limit, both Eulerian and Lagrangian coordinate frames are equivalent to each other [62] and can produce the exact solutions of fluid flows. However, from the computational point-of-view, Eulerian and Lagrangian approaches are not equivalent as numerical residues depend strongly on coordinate and grid settings. Eulerian simulations are stable and robust but are usually plagued by excessive diffusion. In contrast, Lagrangian simulations provide non diffusive results but are often limited in time as they can produce critical grid deformations in the presence of strong shear or vorticity.

In order to retain advantages of Eulerian and Lagrangian methods without suffering their deficiencies, Trulio and Trigger [57] introduced the idea that fluid flow can be computed with respect to a moving grid. This grid may be adjusted to best follow the fluid while preserving at the same time some regularity and robustness. Such methods have been designated as "Arbitrary Lagrangian–Eulerian" (or ALE) [23]. The grid motion can be either arbitrarily specified by the user (as an input data of the problem), or adaptively constrained by the flow and computed on the fly (to track discontinuities, near-Lagrangian motions, boundary conditions, etc...), see for example [34] and [47].

So far, numerous ALE strategies have been designed in order to optimize accuracy, robustness,

or computational efficiency for simulating, among others, wave propagation [46], non-Newtonian flows [11], free surface flows [18], impact dynamics [6], magneto-hydrodynamics [49], multiphase flows [4, 48], combustion [60], low Mach number flows [12], incompressible fluids [44], and defense-related applications [36, and references therein]. In most of these works, strict thermodynamic consistency—compliance with the second law of thermodynamics which forbids entropy reduction in a closed system—appears to have been a relatively minor concern. However, it is a primary issue in the presence of both isentropic and strong shock evolutions of possibly complex materials, and it will be at the core of the present development which emphases the proper capture of pressure work even when the grid is not moving at the fluid velocity. Entropy errors may then come from numerical residues on both cell volume variations and relative-to-grid advection. In a multiphase flow context, which will be discussed in a forthcoming publication, this will become even more critical due to the added influence of volume fraction coupling between drifting fluids.

Two broad categories of ALE strategies exist [38, and references therein] : *indirect* and *direct*. Indirect ALE approaches perform a splitting between a Lagrangian phase—where conserved variables are solved using evolution equations—and a remapping procedure—where the Lagrangian evolved state is interpolated onto an updated mesh after an arbitrary number of time steps. In contrast, no remap step is used in direct ALE approaches as mass, momentum and energy fluxes at moving cell boundaries are directly taken into account without separation in the discrete evolution equations. Due to the natural splitting between the Lagrangian phase and the remap step, indirect ALE methods readily ensure the thermodynamic consistency of pressure work (at least to first-order) and can be extended to multiphase flows [9, and references therein]—Lagrangian and remap steps both comply with the thermodynamic entropy condition if remapping is monotonic. However, remapping procedures can become computationally expensive if used at every time cycle in two and three dimensions, especially if associated with rezoning techniques [30] or applied to multiphase flow systems. Direct ALE approaches appear more computationally efficient as they do not involve remapping nor rezoning steps [43], but they are challenged by the capture of the pressure work in a thermodynamically compatible way.

3.2.2 Existing approaches, variational approach

Ensuring consistency of pressure work can be achieved through so-called mimetic approaches. As reviewed recently in a full issue of Journal of Computational Physics [24], numerical mimetism consists in transposing as accurately as possible some critically important physical constraints into discrete equations. Usually, the mimetic procedure is directly applied to PDEs discretized with finite differences, elements or volumes. In the present work however, in the spirit of [56], the mimetic approach will be applied not directly to PDEs but to their underlying least action variational principle. The least action principle is a fundamental ingredient of mathematical physics [20, 26] which allows to derive equations of motion from a unified theoritical framework for a wide range of physical systems—from the simple harmonic oscillator to convoluted gauge quantum field theories.

For numerical systems, which for practical purposes behave as discrete systems, variational integrators are based on the discretization of the least action principle and provide a systematic way to derive geometric numerical methods. In the context of integrators for systems of discrete particles, the usage of variational principles was recognized in the 1980's as a generic and fruitful approach to produce symplectic numerical schemes : for instance the Verlet integrator [61] can be derived from a least action principle [21]. This powerful approach can be extended to numerous other continuous systems (see for example the reviews [39, 32, 5, 10]). These variational integrators have been used recently for electromagnetic studies [54], Lagrangian field theories [58], Burgers' equation [8], and incompressible fluid flows [45].

For the hydrodynamics of a continuous medium, application of Hamilton's variational methods has been an area of sustained interest over the past few decades (see for example the review paper [40]). Variational derivations can be traced back to Eckart [14] who obtained the equation of fluid motion in an Eulerian framework. However, Eckart's approach is restricted to the case where the intrinsic energy is a function of the fluid density only, and the corresponding fluid motion is thus irrotational. Later, Herivel [22] gave a nearly complete variational formulation of compressible ideal fluid flows by using the velocity, density, and entropy field variables expressed in space-and-time coordinates in both Eulerian and Lagrangian frameworks. But Herivel's Eulerian approach can

describe rotational fluid flows only when they display non-uniform entropy—otherwise, a key ingredient is lost as trajectories of individual material elements cannot be followed. Serrin [51] and Lin [33] showed that, in order to recover the Eulerian variational description without any irrotational restriction, it is necessary to add a new constraint to Herivel's approach by means of a Lagrange multiplier to force the existence of (conserved) Lagrangian coordinates for all fluid elements.

For compressible Computational Fluid Dynamics (CFD), the mimicking of these continuous variational approaches has been severely restricted by a major impediment : a discretization of the group of non volume-preserving diffeomorphisms is still to be found and appears particularly complex—as mass and entropy advections cannot be a priori simultaneously holonomic and monotonic. Unsurprisingly, only two derivations of variational schemes for fluid dynamics thus appear to have been published. For viscous compressible flow problems, Fahrenthold and Koo [15] developed a variational description in an Eulerian reference frame, but in a semi-discrete way : stationarity is sought on a functional which is discrete in space variables but continuous in time, and then time-integration is performed with a Runge–Kutta algorithm. In this description, non-holonomic constraints are added for mass and entropy evolutions. Eventually, the differentiation of the Hamiltonian defines the generalized conservative forces for the system—some of them of questionable physical interpretation such as generated by entropy gradients. This Eulerian approach [15] was then extended to an ALE framework by Koo and Fahrenthold [29]. In a more rigorous approach but restricted to incompressible fluids, Pavlov et al. [45] introduced the idea of approximating in a weak sense the infinite-dimensional Lie group of volume-preserving diffeomorphisms with an appropriate grid-dependent finite-dimensional Lie group. In this framework, mass and volume preserving transport are captured by strictly holonomic constraints which make the fluid evolve over a mimicked symplectic though non-monotonic structure.

3.2.3 Present approach

A combination of a fully discrete in space-and-time variational approach and a direct ALE formalism is proposed in the present work for the simulation of compressible fluid flows which

guarantees mass, momentum and total energy conservation at discrete level. This combination is not trivial and is restricted by several impediments. The discrete derivation of the direct ALE scheme is adressed here over a novel generic GEEC (Geometry, Energy, and Entropy Compatible) procedure performed step-by-step in Section 3.3 as follows : i) in Section 3.3.1, the continuous standard variational Euler–Lagrange equations are derived in the Eulerian framework. This continuous derivation provides a mimicking guideline for the discrete variational equation ; ii) in Section 3.3.2, the space-and-time discretization of fields, mass transport and action integral are presented (see Sections 3.3.2.1). This discretization ensures a continuity with purely Lagrangian approaches used at CEA/DAM [42, 64] : staggered velocity fields are naturally compatible with Lagrangian geometry displacements and an artificial viscosity term is added in evolution equations as a pressure-like contribution in order to stabilize the scheme and capture shocks. Then the discrete version of the Euler–Lagrange equations is obtained by applying the least action principle to the discrete action integral (see 3.3.2.2) ; iii) in Section 3.3.3, corrections on numerical residues and “flux-in-time" terms are introduced in order to bring back the conservation of momentum while preserving a velocity equation which is explicit in time ; iv) in Section 3.3.4, an internal energy equation is derived from the kinetic energy equation by enforcing the total energy conservation—following an “energy tally" principle stated in [7] and [35] whereby internal and kinetic energy equations must match so that only flux terms are left.

The GEEC procedure is applied in the present work with some discretization choices in order to prove the satisfactory behavior of a scheme derived along these guidelines. Its main limitation lies in the choice of a simple first-order upwind advection scheme, which does not prevent from validating the proof of concept—the isentropic property of a smooth flow can be verified to second-order even if advection terms are only first-order accurate. The extension to full seccond-order is not excluded in principle by the novel generic GEEC procedure but involves technicalities which are postponed for future developments. For now, besides validating the concept, the proposed scheme GEECS (Geometry, Energy, and Entropy Compatible Scheme) can be immediately applied to weakly rotational flows, as a direct ALE extension of purely Lagrangian schemes.

Readers who are not interested in the step-by-step derivation of the scheme can just refer to Section 3.4 where the full set of equations for GEECS is condensed.

Finally in Section 3.5, results of several variants of the isentropic vortex, Sod's shock tube, Sedov's blast wave, Woodward–Colella's double shock tube, and the triple point shock tube are presented in order to verify the behavior of the scheme in terms of convergence rates, thermodynamic consistency, energy conservation, jump conditions, constraints on time step, robustness, and stability. In particular, new variants of Sod's shock tube and Sedov's blast wave are proposed to highlight the built-in capabilities of GEECS especially in the presence of strenuous grid displacements and distortions.

3.3 Discrete derivation of the direct ALE scheme

The definition and notation of the variables used in the derivation are given in Appendix .1. In Section 3.3.1, the variational derivation is performed step-by-step in the continuous case in order to provide a guideline for the discrete derivation. In Section 3.3.2, the main steps of the discrete derivation are presented in the ALE framework—for clarity the step-by-step discrete derivation is postponed to Appendix .3.

3.3.1 Derivation of continuous Eulerian hydrodynamic equations

All fields will be described in the present work as functions of *Eulerian coordinates* $\boldsymbol{x}$ (in the laboratory frame). This does not match the discrete ALE description to follow which is referenced with respect to *grid coordinates*—a continuous version of the derivation in grid coordinates would have unnecessarily complicated the reasoning for the needs of the present work.

3.3.1.1 Fields, transports, and action integral

Consider the isentropic flow of an inviscid compressible fluid with polytropic properties. Following Herivel's [22] and Lin's [33] approaches, the continuous Lagrangian of hydrodynamics

can be written

$$\mathcal{L} = \tfrac{1}{2}\rho v_i v_i - \rho e(\rho) + \phi\left(\partial_t \rho + (\rho v_i)_{,i}\right) + \lambda\left(\partial_t(\rho\chi) + (\rho\chi v_i)_{,i}\right) \ , \tag{3.1}$$

where ρ, $\boldsymbol{v}$, and e are respectively the density, Eulerian velocity, and isentropic internal energy of the fluid. Einstein's notation of implicit summation on repeated indices is assumed—$\boldsymbol{\nabla}\cdot\boldsymbol{a} = a_{i,i}$ and $\boldsymbol{\nabla} b = b_{,i}$.

This Lagrangian $\mathcal{L}$ consists in the balance between kinetic energy $\frac{1}{2}\rho v_i v_i$ and internal energy $\rho e(\rho)$ with two constraints added through Lagrange multipliers : i) ϕ for mass conservation which relates velocity and density fields, and ii) λ for Lin's constraint associated with the conservation of a Lagrangian coordinate χ.

3.3.1.2 Euler–Lagrange equations

The variation of the action (i.e. space-and-time integral of the Lagrangian) as a function of field variations $\delta\phi$, $\delta\lambda$, δv_i, $\delta\rho$, and $\delta\chi$ can then be written

$$\delta\mathcal{A} = \iint \left(\frac{\partial\mathcal{L}}{\partial\phi}\delta\phi + \frac{\partial\mathcal{L}}{\partial\lambda}\delta\lambda + \frac{\partial\mathcal{L}}{\partial v_i}\delta v_i + \frac{\partial\mathcal{L}}{\partial\rho}\delta\rho + \frac{\partial\mathcal{L}}{\partial\chi}\delta\chi\right)\mathrm{d}^3\,\boldsymbol{x}\,\mathrm{d}\,t \ . \tag{3.2}$$

These allowed variations in ϕ, λ, v_i, ρ, and χ are independent, continuously differentiable and vanish for x and t at domain boundaries. Using the least action principle $\delta\mathcal{A} = 0$ over (3.2) provides the Euler–Lagrange equations

$$\partial_t\rho + (\rho v_i)_{,i} = 0 \ , \tag{3.3a}$$

$$\partial_t(\rho\chi) + (\rho\chi v_i)_{,i} = 0 \ , \tag{3.3b}$$

$$v_i = \phi_{,i} + \chi\lambda_{,i} \ , \tag{3.3c}$$

$$\partial_t\phi = \tfrac{1}{2}v_j v_j - (e + P/\rho) - v_j\phi_{,j} - \chi\partial_t\lambda - \chi v_j\lambda_{,j} \ , \tag{3.3d}$$

$$\partial_t\lambda + v_i\lambda_{,i} = 0 \ , \tag{3.3e}$$

where $P = \rho^2 \partial e/\partial \rho$ is the pressure of the system. Equations (3.3a) and (3.3b) represent the conservation of respectively mass and Lagrangian coordinate χ. Equation (3.3c) shows that the presence of Lin's constraint into (3.1) lifts the irrotational restriction (visible when $\chi = 0$). Equations (3.3d) and (3.3e) give the time evolution equations for the Lagrange multipliers ϕ and λ.

3.3.1.3 Velocity equation

The velocity evolution equation is obtained by substituting $(3.3d)_{,i}$ into $\partial_t(3.3c)$, thus yielding

$$\partial_t v_i = -P_{,i}/\rho + v_j v_{j,i} - v_{j,i}\phi_{,j} - v_j \phi_{,ji} + \lambda_{,i}\partial_t \chi + \chi \partial_t \lambda_{,i} \ , \tag{3.4}$$

where for a polytropic fluid $e = e(\rho)$ and thus $\rho\big(e + P/\rho\big)_{,i} = P_{,i}$. Inserting expressions of $\partial_t \lambda$ and $\partial_t \chi$ from (3.3e) and (3.3b) into (3.4) yields

$$\partial_t v_i = -P_{,i}/\rho - v_j \left(\phi_{,ji} + \chi \lambda_{,ij}\right) - \lambda_{,i} v_j \chi_{,j} \ . \tag{3.5}$$

Using algebraic identities $(\chi\lambda_{,i})_{,j} = \chi\lambda_{,ij} + \lambda_{,i}\chi_{,j}$, $\phi_{,ji} = \phi_{,ij}$ and (3.3c), the velocity evolution equation eventually becomes

$$\partial_t v_i = -P_{,i}/\rho - v_j v_{i,j} \ . \tag{3.6}$$

3.3.1.4 Conservative momentum equation

The momentum equation is obtained from the combination $\rho \times (3.6) + (3.3a) \times v_i$

$$\partial_t(\rho v_i) = -P_{,i} - \rho v_j v_{i,j} - v_i(\rho v_j)_{,j} \tag{3.7a}$$

$$= -P_{,i} - (\rho v_i v_j)_{,j} \ . \tag{3.7b}$$

A momentum transport term is inserted into (3.7a) consistently with mass transport thus yielding the conservative momentum evolution equation (3.7b).

The rearrangements from (3.5) to (3.6) and from (3.7a) to (3.7b) appear trivial in the

continuous Eulerian case but are a source of numerical residues in the discrete derivation to follow which demand specific treatments.

3.3.2 Discrete variational derivation of evolution equations

In Section 3.3.2.1, the discretization in both space-and-time of the mesh, fields, transports, and action integral is presented. In Section 3.3.2.2, the discrete version of the Euler–Lagrange equations is then obtained by applying the least action principle to the discrete action integral.

3.3.2.1 Discretization of fields, transports, and action integral

As in existing variational schemes for continuum mechanics [29, 45], the discretization of various fields will not proceed through the usual approaches of finite differences, elements, or volumes on the PDEs. In the present ALE framework instead, accuracy in both space-and-time is sought on the action integral to second-order for all terms except for the relative transport which will be first-order in space-and-time—this apparently peculiar choice is discussed below after (3.14).

The mesh is defined at time t^n by nodes p at positions $\boldsymbol{x}_p^n$ thus delimiting cells labeled by c, without any constraint on structure or spatial dimension. The cell volume V_c^n only depends on positions of nodes p belonging to $\mathcal{P}(c)$, the set of nodes neighboring cell c. However, all tests reported in Section 3.5 are restricted to structured meshes of quadrangles bounded by straight segments in one or two dimensions as represented in Figure 3.1b.

The finite volume representation in space-and-time is used for the definition of density ρ_c^n and internal energy e_c^n at each cell c. The mass contained in each cell is thus $\rho_c^n V_c^n$. The internal energy integral is discretized by midpoint rules over space-and-time cells $\Delta t^n \times V_c^n$ thus yielding

$$\iint \rho e(\rho)\ \mathrm{d}^3\boldsymbol{x}\,\mathrm{d}\,t \rightsquigarrow \sum_n \sum_c \Delta t^n V_c^n \rho_c^n e_c^n\ , \tag{3.8}$$

where $\Delta t^n = (t^{n+1} - t^{n-1})/2$. For simplicity, symbols $\rightsquigarrow$ are used only to make the link between continuous quantities in the guideline continuous derivation of Section 3.3.1 and discrete quantities in the discrete derivation.

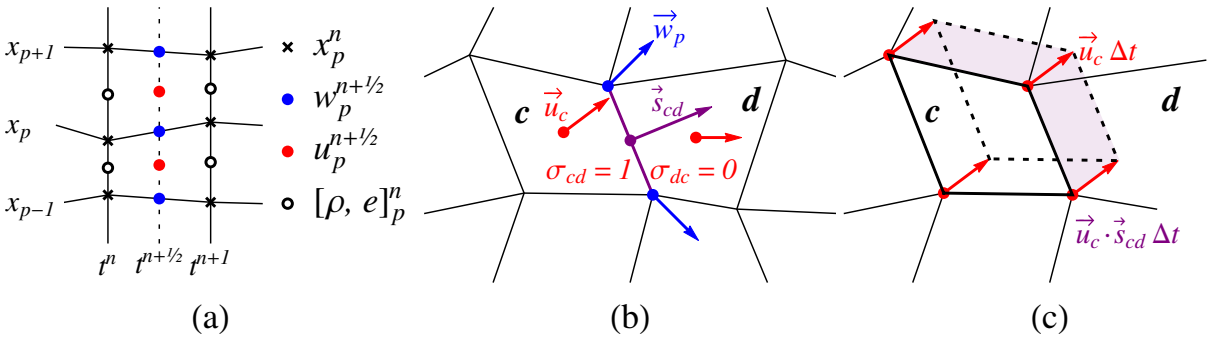

FIGURE 3.1 – (a) One-dimensional representation of space-and-time elements with the localisation of thermodynamic quantities and velocities ; (b) Space localisation of grid and relative-to-grid velocities, and of the corresponding off-centering factors ; (c) Schematic representation of the advection scheme as swept flux volumes.

From t^n and $\boldsymbol{x}^n$, the grid velocity $\boldsymbol{w}$ is discretized at nodes and at half-time steps as

$$\boldsymbol{w}_p^{n+1/2} = \left(\boldsymbol{x}_p^{n+1} - \boldsymbol{x}_p^n\right) / \Delta t^{n+1/2} \ , \tag{3.9}$$

where $\Delta t^{n+1/2} = t^{n+1} - t^n$. The *relative* (to the grid) and *absolute* (in the laboratory frame) fluid velocities $\boldsymbol{u}_c^{n+1/2}$ and $\boldsymbol{\mu}_c^{n+1/2}$ are defined at half time steps and at *cell centers* (Figure 3.1a). This deliberate choice may appear as counter-intuitive and inconsistent with our initial goal of ensuring continuity with usual space-and-time staggered Lagrangian schemes. In fact, the Lagrangian limit is defined by $\boldsymbol{u}_c^n = 0$ and grid velocity then matches that of space-staggered Lagrangian schemes. But moreover, this choice is simpler and eliminates various artifacts as discussed below. The relationship $\boldsymbol{\mu} = \boldsymbol{u} + \boldsymbol{w}$ is then discretized using an interpolation of the grid velocity at cell centers

$$\boldsymbol{\mu}_c^{n+1/2} = \boldsymbol{u}_c^{n+1/2} + \boldsymbol{w}_c^{n+1/2} \ , \qquad \text{with} \qquad \boldsymbol{w}_c^{n+1/2} = \frac{1}{|\mathcal{P}(c)|} \sum_{\mathcal{P}(c)} \boldsymbol{w}_p^{n+1/2} \ . \tag{3.10}$$

This choice of arithmetic averaging of $\boldsymbol{w}$ is not unique but represents the simplest interpolation strategy. Moreover, the second-order feature of (3.9) is ensured due to the fact that averaging of $\boldsymbol{w}$ is space-centered.

The kinetic energy integral is discretized over space-and-time cells $\Delta t^{n-1/2} \times V_c^n$ by midpoint

rules in space-and-time—except for $V\rho$ which is off-centered in time—

$$\iint \tfrac{1}{2}\rho(u_i+w_i)^2 \ \mathrm{d}^3\boldsymbol{x}\,\mathrm{d}\,t \ \rightsquigarrow \ \sum_n \sum_c \Delta t^{n-1/2} V_c^n \ \tfrac{1}{2}\,\rho_c^n \left(\boldsymbol{\mu}_c^{n-1/2}\right)^2 \ . \tag{3.11}$$

As will be seen in Section 3.3.2.2, the fact that absolute velocity $\boldsymbol{\mu}_c^{n-1/2}$ is $\Delta t^{n-1/2}/2$ behind density ρ_c^n allows to factorize ρ_c^n when obtaining the discrete expression of the continuous equation (3.3c). In the Lagrangian limit, where there are no mass fluxes between cells, mass is conserved in each cell $V_c^n\rho_c^n = V_c^{n-1/2}\rho_c^{n-1/2} = V_c^{n-1}\rho_c^{n-1}$ thus restoring an exact midpoint rule in time. The fact that internal and kinetic energy integrals (3.8) and (3.11) are not discretized over identical time intervals is not particularly constraining, especially as far as exact energy conservation and entropy consistency are concerned—as previously shown in the case of purely Lagrangian schemes [35], conservativity can be obtained by corrective "flux-in-time" terms.

It must be stressed that, as a function of each of the elementary velocities $\boldsymbol{u}_c^{n-1/2}$ or $\boldsymbol{w}_p^{n-1/2}$ the kinetic energy is respectively a *definite* or a *non-definite* positive quadratic form. This feature is a consequence of the node to cell interpolation of $\boldsymbol{w}$ (3.10) and in principle could make the scheme sustain non-physical modes of the grid motion, i.e. $\boldsymbol{w}_p \neq 0$ with $\boldsymbol{w}_c = 0$—akin to "hourglassing" and "chevron" like distortions in standard Lagrangian schemes [16]. In the present work however, these modes are not a concern as $\boldsymbol{w}$ is *arbitrarily defined by the user*, and as such can always be built free of non-physical modes. None of the tests performed in the course of this work, neither shown in Section 3.5 nor unreported, was ever plagued by such non-physical modes.

The mass transport equation is discretized by a first-order in space-and-time upwind explicit scheme as

$$\begin{aligned} V_c^{n+1}\rho_c^{n+1} - V_c^n\rho_c^n &= \Delta t^{n+1/2} \sum_{d\in\mathcal{D}(c)} \left(\sigma_{dc}^{n+1/2}\boldsymbol{s}_{dc}^{n+1/2}\cdot\boldsymbol{u}_d^{n+1/2}\rho_d^n - \sigma_{cd}^{n+1/2}\boldsymbol{s}_{cd}^{n+1/2}\cdot\boldsymbol{u}_c^{n+1/2}\rho_c^n\right) \\ &= \Delta t^{n+1/2} \sum_{d\in\mathcal{D}(c)} \left(\dot{V}_{dc}^{n+1/2}\rho_d^n - \dot{V}_{cd}^{n+1/2}\rho_c^n\right) \ , \end{aligned} \tag{3.12}$$

where $\dot{V}_{cd}^{n+1/2} = \sigma_{cd}^{n+1/2}\boldsymbol{s}_{cd}^{n+1/2}\cdot\boldsymbol{u}_c^{n+1/2}$ is the rate of volume transfer from cell c to cell d; $\boldsymbol{s}_{cd}^{n+1/2}$ is the outward pointing vector to the boundary between adjacent cells c and d at time $n+1/2$,

of magnitude given by the area of the c–d boundary element—given in practice by the simplest interpolation strategy $\boldsymbol{s}_{cd}^{n+1/2} = \frac{1}{2}(\boldsymbol{s}_{cd}^{n} + \boldsymbol{s}_{cd}^{n+1})$; and $\sigma_{cd}^{n+1/2}$ is the off-centering factor of transport from cell c to cell d defined as in Figure 3.1b

$$\sigma_{cd}^{n+1/2} = \tfrac{1}{2}\left(1 + \operatorname{sign}\left(\boldsymbol{s}_{cd}^{n+1/2} \cdot \boldsymbol{u}_{c}^{n+1/2}\right)\right) \ , \tag{3.13}$$

where $\sigma_{cd}^{n+1/2}$ is *unrelated* to $\sigma_{dc}^{n+1/2}$. Terms $\dot{V}_{dc}^{n+1/2}\rho_{d}^{n}$ and $\dot{V}_{cd}^{n+1/2}\rho_{c}^{n}$ correspond to rates of mass transport from respectively cells d to c and c to d, where d belongs to the set $\mathcal{D}(c)$ of cells adjacent to c. As represented in Figure 3.1c, this scheme can be viewed as a rudimentary swept-flux version of existing Lagrange-plus-remap approaches [9], whereby cell c is transported without distortion by a field of uniform velocity $\boldsymbol{u}_{c}^{n+1/2}$ and projection is restricted to adjacent cells (corner fluxes are thus neglected).

As later shown in Section 3.3.2.2, if the explicit mass transport equation (3.12) is used for the discrete variational derivation, the evolution equation of the absolute velocity becomes implicit. In order to obtain an explicit equation for the absolute velocity, the density must be $\Delta t^{n-1/2}/2$ ahead of the absolute velocity in (3.12) as already observed in the discrete definition of the kinetic energy (3.11). For this reason, the mass transport equation that is used for the following variational derivation of the scheme is the implicit version of (3.12)

$$V_{c}^{n+1}\rho_{c}^{n+1} - V_{c}^{n}\rho_{c}^{n} = \Delta t^{n+1/2} \sum_{d\in\mathcal{D}(c)} \left(\dot{V}_{dc}^{n+1/2}\rho_{d}^{n+1} - \dot{V}_{cd}^{n+1/2}\rho_{c}^{n+1}\right) \ . \tag{3.14}$$

Both schemes capture transport in very similar ways (order, upwinding, etc.) though the implicit scheme should rather be viewed as a "remap-plus-Lagrange" approach. It must be noticed that all developments presented in Section 3.3.3 can be carried out using the explicit mass transport (3.12) yielding however, an *implicit* absolute velocity equation similar to (3.24) with corrections for conservativity which become much more tedious—a solution for obtaining a fully explicit direct ALE scheme is presented in Section 3.3.5.

It must be noted here that mass transport equations (3.12) and (3.14) appear as an input data of the proposed generic GEEC procedure of derivation. A second-order extension of the present

work leads to important technicalities in order to take into account the more complex velocity dependance in the discrete derivation. This feature will be at the core of a future work. For now, the simple first-order upwind equations (3.12) and (3.14) are sufficient : i) as a proof of concept for obtaining a scheme ensuring the geometric, energetic, and entropic compatibility ; and ii) to be yet applicable to weakly rotational flows in which grids can be computed as close as possible to the Lagrangian limit, in which the scheme is second-order accurate in both space-and-time.

The cell-centered discretization of kinetic energy—and thus momentum—is made without nodal masses and therefore complies with the so-called DeBar condition [13, p. 13] whereby a uniform self-advecting velocity field must remain uniform regardless of density gradients. Positivity and DeBar condition will become fundamental features when extending the present scheme to multiphase flows.

As in the continuous derivation (3.1), mass transport is embedded in the variational approach through a Lagrange multiplier field ϕ. Lagrange multipliers are thus required for each of the relationships (3.12) or (3.14) and are arbitrarily labeled as $\phi_c^{n+1/2}$ in the following.

As already mentioned in Section 3.3.1, the discrete Lin constraint (invariance of Lagrangian coordinates) must be added in the action integral in order to lift the irrotational constraint on the flow. In the present work, the conservation of the Lagrangian coordinate χ is discretized consistently with the first-order in space-and-time upwind implicit mass transport as

$$V_c^{n+1}\rho_c^{n+1}\chi_c^{n+1} - V_c^n\rho_c^n\chi_c^n = \Delta t^{n+1/2}\sum_{d\in\mathcal{D}(c)}\left(\dot{V}_{dc}^{n+1/2}\rho_d^{n+1}\chi_d^{n+1} - \dot{V}_{cd}^{n+1/2}\rho_c^{n+1}\chi_c^{n+1}\right) , \qquad (3.15)$$

and embedded in the variational approach through a Lagrange multiplier field λ discretized as $\lambda_c^{n+1/2}$.

Eventually, the discrete action integral with its additional implicit constraints is

$$\mathcal{A} = \sum_n \sum_c \Bigg(\Delta t^{n-1/2} V_c^n \, \tfrac{1}{2} \, \rho_c^n (\boldsymbol{\mu}_c^{n-1/2})^2 - \Delta t^n V_c^n \rho_c^n e_c^n \\ + \phi_c^{n+1/2} \Bigg(V_c^{n+1} \rho_c^{n+1} - V_c^n \rho_c^n - \Delta t^{n+1/2} \sum_{d \in \mathcal{D}(c)} \left(\dot{V}_{dc}^{n+1/2} \rho_d^{n+1} - \dot{V}_{cd}^{n+1/2} \rho_c^{n+1} \right) \Bigg) \\ + \lambda_c^{n+1/2} \Bigg(V_c^{n+1} \rho_c^{n+1} \chi_c^{n+1} - V_c^n \rho_c^n \chi_c^n - \Delta t^{n+1/2} \sum_{d \in \mathcal{D}(c)} \left(\dot{V}_{dc}^{n+1/2} \rho_d^{n+1} \chi_d^{n+1} - \dot{V}_{cd}^{n+1/2} \rho_c^{n+1} \chi_c^{n+1} \right) \Bigg) \Bigg) \Bigg) . \tag{3.16}$$

3.3.2.2 Euler–Lagrange equations

So as to mimic the continuous derivation of field evolution equations, the least action principle is applied to the discrete action integral (3.16). Resulting variations of $\mathcal{A}$ under variations of Lagrange multipliers, fluid velocity, density and Lagrangian coordinate can be written

$$\delta \mathcal{A} = \sum_n \sum_c \Bigg(\frac{\partial \mathcal{A}}{\partial \phi_c^{n+1/2}} \delta \phi_c^{n+1/2} + \frac{\partial \mathcal{A}}{\partial \lambda_c^{n+1/2}} \delta \lambda_c^{n+1/2} \\ + \frac{\partial \mathcal{A}}{\partial \boldsymbol{u}_c^{n-1/2}} \cdot \delta \boldsymbol{u}_c^{n-1/2} + \frac{\partial \mathcal{A}}{\partial \rho_c^n} \delta \rho_c^n + \frac{\partial \mathcal{A}}{\partial \chi_c^n} \delta \chi_c^n \Bigg) = 0 \, . \tag{3.17}$$

Inserting (3.16) into (3.17) leads to the following discrete Euler–Lagrange equations

$$V_c^{n+1} \rho_c^{n+1} - V_c^n \rho_c^n + \Delta t^{n+1/2} \sum_{d \in \mathcal{D}(c)} \left(\dot{V}_{cd}^{n+1/2} \rho_c^{n+1} - \dot{V}_{dc}^{n+1/2} \rho_d^{n+1} \right) = 0 \, , \tag{3.18a}$$

$$V_c^{n+1} \rho_c^{n+1} \chi_c^{n+1} - V_c^n \rho_c^n \chi_c^n + \Delta t^{n+1/2} \sum_{d \in \mathcal{D}(c)} \left(\dot{V}_{cd}^{n+1/2} \rho_c^{n+1} \chi_c^{n+1} - \dot{V}_{dc}^{n+1/2} \rho_d^{n+1} \chi_d^{n+1} \right) = 0 \, , \tag{3.18b}$$

$$V_c^n \boldsymbol{\mu}_c^{n-1/2} = \sum_{d \in \mathcal{D}(c)} [\sigma \boldsymbol{s}]_{cd}^{n-1/2} \left(\phi_d^{n-1/2} - \phi_c^{n-1/2} \right) + \chi_c^n \sum_{d \in \mathcal{D}(c)} [\sigma \boldsymbol{s}]_{cd}^{n-1/2} \left(\lambda_d^{n-1/2} - \lambda_c^{n-1/2} \right) \, , \tag{3.18c}$$

$$V_c^n\left(\phi_c^{n+1/2}-\phi_c^{n-1/2}\right)=\tfrac{1}{2}\Delta t^{n-1/2}V_c^n\left(\boldsymbol{\mu}_c^{n-1/2}\right)^2-\Delta t^nV_c^n\left(e_c^n+P_c^n/\rho_c^n\right)$$
$$+V_c^n\chi_c^n\left(\lambda_c^{n-1/2}-\lambda_c^{n+1/2}\right)-\Delta t^{n-1/2}\sum_{d\in\mathcal{D}(c)}\dot{V}_{cd}^{n-1/2}\left(\phi_d^{n-1/2}-\phi_c^{n-1/2}\right)$$
$$-\Delta t^{n-1/2}\chi_c^n\sum_{d\in\mathcal{D}(c)}\dot{V}_{cd}^{n-1/2}\left(\lambda_d^{n-1/2}-\lambda_c^{n-1/2}\right)\ , \tag{3.18d}$$

$$V_c^n\left(\lambda_c^{n+1/2}-\lambda_c^{n-1/2}\right)+\Delta t^{n-1/2}\sum_{d\in\mathcal{D}(c)}\dot{V}_{cd}^{n-1/2}\left(\lambda_d^{n-1/2}-\lambda_c^{n-1/2}\right)=0\ . \tag{3.18e}$$

Velocity variations $\delta\boldsymbol{u}_c^{n-1/2}$ do not affect off-centering factors $\sigma_{cd}^{n-1/2}$ as these are almost everywhere independent of the relative velocity except for singularities at $\boldsymbol{u}=\boldsymbol{0}$. Despite the change of coordinates, it must be noted that mass transport (3.18a), Lagrangian coordinate conservation (3.18b), absolute velocity equation (3.18c), and evolution of Lagrange multipliers (3.18d) and (3.18e) mimick the continuous Euler–Lagrange equations (3.3) in Section 3.3.1.

In the discrete case, the Euler–Lagrange equations (3.18) display two noteworthy features : i) variations of the velocity in the divergence operator of (3.16) convert its upwind off-centering into downwind gradients of ϕ and λ in (3.18c), and ii) ρ_c has been removed from (3.18c) as density is $\Delta t^{n-1/2}/2$ ahead of absolute velocity in both (3.11) and (3.14),

The system of discrete equations (3.18) cannot be used in practice because the pressure gradient in (3.18d) involves external entropy forces and momentum is only approximately conserved.

3.3.3 Correction of the Euler–Lagrange equations into conservative and explicit equations

The derivation of the discrete momentum equation in the local grid frame is analogous to the continuous derivation in Section 3.3.1.

3.3.3.1 Non-conservative variational momentum equation

For the sake of clarity, all algebraic manipulations for the derivation of absolute velocity and momentum equations can be found in Appendix .3. The discrete mimetic momentum equation is

$$
\begin{aligned}
V_c^{n+1}\rho_c^{n+1}\boldsymbol{\mu}_c^{n+1/2} - V_c^n\rho_c^n\boldsymbol{\mu}_c^{n-1/2} = &-\Delta t^n\rho_c^n \sum_{d\in\mathcal{D}(c)} [\sigma \boldsymbol{s}]_{cd}^{n-1/2}\left(e_d^n - e_c^n + P_d^n/\rho_d^n - P_c^n/\rho_c^n\right)\\
&- \Delta t^{n+1/2}\boldsymbol{\mu}_c^{n+1/2}\sum_{d\in\mathcal{D}(c)}\left(\dot{V}_{cd}^{n+1/2}\rho_c^{n+1} - \dot{V}_{dc}^{n+1/2}\rho_d^{n+1}\right)\\
&- \tfrac{1}{2}\rho_c^n\Delta t^{n-1/2}\sum_{d\in\mathcal{D}(c)}[\sigma \boldsymbol{s}]_{cd}^{n-1/2}\left(\left(\boldsymbol{u}_d^{n-1/2}\right)^2 - \left(\boldsymbol{u}_c^{n-1/2}\right)^2 - \left(\boldsymbol{w}_d^{n-1/2}\right)^2 + \left(\boldsymbol{w}_c^{n-1/2}\right)^2\right)\\
&- \Delta t^{n-1/2}\rho_c^n\sum_{d\in\mathcal{D}(c)}[\sigma \boldsymbol{s}]_{cd}^{n-1/2}\left(\chi_c^n - \chi_d^n\right)\frac{\boldsymbol{u}_d^{n-1/2}}{V_d^n}\sum_{d'\in\mathcal{D}(d)}[\sigma \boldsymbol{s}]_{dd'}^{n-1/2}\left(\lambda_{d'}^{n-1/2} - \lambda_d^{n-1/2}\right)\\
&+ \Delta t^{n+1/2}\sum_{d\in\mathcal{D}(c)}[\sigma \boldsymbol{s}]_{dc}^{n+1/2}\left(\chi_c^{n+1} - \chi_d^{n+1}\right)\frac{\boldsymbol{u}_d^{n+1/2}\rho_d^{n+1}}{V_c^{n+1}}\sum_{d'\in\mathcal{D}(d)}[\sigma \boldsymbol{s}]_{dd'}^{n+1/2}\left(\lambda_{d'}^{n+1/2} - \lambda_d^{n+1/2}\right)\\
&+ \rho_c^n V_c^n\sum_{d\in\mathcal{D}(c)}\left(\frac{[\sigma \boldsymbol{s}]_{cd}^{n+1/2}}{V_c^{n+1}} - \frac{[\sigma \boldsymbol{s}]_{cd}^{n-1/2}}{V_c^n}\right)\left(\phi_d^{n+1/2} - \phi_c^{n+1/2} + \chi_c^n\left(\lambda_d^{n+1/2} - \lambda_c^{n+1/2}\right)\right) \quad . \qquad (3.19)
\end{aligned}
$$

The first three terms on the right hand side of (3.19) contain the pressure gradient and momentum transport fluxes. The last three terms of (3.19) are produced by the discrete derivation of absolute velocity and momentum evolution equations (Appendix .3) and are expected to cancel as (3.19) should be conservative and consistent with its continuous version (3.7b) in grid coordinates.

The variational momentum evolution equation (3.19) is not fully conservative due to both pressure gradient and momentum transport terms and requires further corrections in order to ensure the three following features : i) elimination of Lagrange multipliers ϕ and λ ; ii) exact conservation of momentum ; and iii) presence of pressure forces only (no entropy driven impulse). Moreover in the present work, we decide that the velocity equation must remain explicit (or at least linearly implicit). The global strategy of the derivation developed in this paper is thus to cancel numerical residues at the scheme order (i.e. second-order in Lagrangian limit and first-order in Eulerian limit) in order to comply with the constraints previously mentioned.

3.3.3.2 Elimination of entropy residues and conservative correction of pressure gradients

Unlike the continuous equation (3.5), the discrete pressure gradient indirectly appears in (3.19) and can be separated into

$$-\Delta t^n \rho_c^n \sum_{d\in\mathcal{D}(c)} [\sigma \boldsymbol{s}]_{cd}^{n-1/2} \left(e_d^n - e_c^n + P_d^n/\rho_d^n - P_c^n/\rho_c^n\right)$$
$$= -\Delta t^n \sum_{d\in\mathcal{D}(c)} [\sigma \boldsymbol{s}]_{cd}^{n-1/2} \left(P_d^n - P_c^n\right) + \mathcal{O}\Big[\Delta_x(e+P/\rho) - \Delta_x P/\rho\Big] \ , \quad (3.20)$$

where $\mathcal{O}\Big[\Delta_x(e+P/\rho) - \Delta_x P/\rho\Big]$ is a numerical residue of entropy $\mathcal{O}\Big[T\Delta_x S\Big]$. In order to capture shocks, an artificial viscosity term Q will be added as a pressure-like contribution to the pressure $P \longrightarrow P+Q$ where Q corresponds to a dissipation process [41]. The explicit formulation of Q is given later by (3.41). This artificial viscosity stress allows to neglect the entropic residue $\mathcal{O}\Big[\Delta_x(e+P/\rho) - \Delta_x P/\rho\Big]$ in (3.20) : i) in shocks, the entropic residue is not negligible but is substituted by an equally non-negligible artificial viscosity term ; and ii) elsewhere, both entropic residue and artificial viscosity are negligible because the flow is presumed isentropic. In the following $\tilde{P}$ will designate $P+Q$.

The remaining pressure gradient in the first term of the right hand side of (3.20) is not yet conservative due to the presence of the off-centering factors $\sigma_{cd}^{n-1/2}$. Therefore, conservativity for the pressure gradient must be recovered by separating centered and off-centered contributions of σ. The centered contribution is obviously conservative because $\sum_{d\in\mathcal{D}(c)} \boldsymbol{s}_{cd}^{n-1/2} = 0$, while the off-centered contributions from cells c to d and from cells d to c can be made conservative through averaging over their common edge. The residue of this averaging for cell c is thus exactly

compensated by cell d according to

$$\begin{aligned} c \to d \text{ in } (3.20)_c \quad & [\sigma \boldsymbol{s}]_{cd}^{n-1/2} \left(\tilde{P}_d^n - \tilde{P}_c^n \right) \\ &= \left(\tfrac{1}{2} + (\sigma_{cd}^{n-1/2} - \tfrac{1}{2}) \right) \boldsymbol{s}_{cd}^{n-1/2} \left(\tilde{P}_d^n - \tilde{P}_c^n \right) \\ &= \left(\tfrac{1}{2} + \tfrac{1}{2} \big((\sigma_{cd}^{n-1/2} - \tfrac{1}{2}) - (\sigma_{dc}^{n-1/2} - \tfrac{1}{2}) \big) \right) \boldsymbol{s}_{cd}^{n-1/2} \left(\tilde{P}_d^n - \tilde{P}_c^n \right) + \mathcal{O}\Big[\Delta_x(\sigma) s \Delta_x(\tilde{P}) \Big] \\ &= \tfrac{1}{2} \left(1 + \sigma_{cd}^{n-1/2} - \sigma_{dc}^{n-1/2} \right) \boldsymbol{s}_{cd}^{n-1/2} \left(\tilde{P}_d^n - \tilde{P}_c^n \right) + \mathcal{O}\Big[\Delta_x(\sigma) s \Delta_x(\tilde{P}) \Big] \ , \end{aligned} \tag{3.21a}$$

$$\begin{aligned} d \to c \text{ in } (3.20)_d \quad & [\sigma \boldsymbol{s}]_{dc}^{n-1/2} \left(\tilde{P}_c^n - \tilde{P}_d^n \right) \\ &= \tfrac{1}{2} \left(1 + \sigma_{dc}^{n-1/2} - \sigma_{cd}^{n-1/2} \right) \boldsymbol{s}_{dc}^{n-1/2} \left(\tilde{P}_c^n - \tilde{P}_d^n \right) + \mathcal{O}\Big[\Delta_x(\sigma) s \Delta_x(\tilde{P}) \Big] \ . \end{aligned} \tag{3.21b}$$

It can be observed that off-centered contributions in (3.21a) and (3.21b) are exact opposites up to numerical residues that cancel almost everywhere if $\boldsymbol{u} \neq \boldsymbol{0}$ for $\Delta x \to 0$. Furthermore, it should be noted that the approximation is actually exact at edges where transport has constant direction—where $\sigma_{cd} = 1$ and $\sigma_{dc} = 0$, or $\sigma_{cd} = 0$ and $\sigma_{dc} = 1$. Other important peculiarities of the pressure gradient are discussed in Section 3.3.6.

3.3.3.3 Conservative momentum evolution equation

As in the continuous derivation of (3.7b), the conservative transport term should mirror mass transport (3.18a) as obtained through a discrete integration by parts of $\left(\dot{V}_{cd}^{n+1/2} \rho_c^{n+1} - \dot{V}_{dc}^{n+1/2} \rho_d^{n+1} \right) \boldsymbol{\mu}_c^{n+1/2}$ in (3.19). Inserting the pressure gradient (3.21a), making the momentum transport term conservative, and neglecting all numerical residues at the scheme order, (3.19) becomes

$$\begin{aligned} V_c^{n+1} \rho_c^{n+1} \boldsymbol{\mu}_c^{n+1/2} - V_c^n \rho_c^n \boldsymbol{\mu}_c^{n-1/2} = & -\Delta t^n \sum_{d \in \mathcal{D}(c)} \tfrac{1}{2} \left(1 + \sigma_{cd}^{n-1/2} - \sigma_{dc}^{n-1/2} \right) \boldsymbol{s}_{cd}^{n-1/2} \left(\tilde{P}_d^n - \tilde{P}_c^n \right) \\ & - \Delta t^{n+1/2} \sum_{d \in \mathcal{D}(c)} \left(\dot{V}_{cd}^{n+1/2} \rho_c^{n+1} \boldsymbol{\mu}_c^{n+1/2} - \dot{V}_{dc}^{n+1/2} \rho_d^{n+1} \boldsymbol{\mu}_d^{n+1/2} \right) \ . \end{aligned} \tag{3.22}$$

This equation is fully conservative at discrete level and consistent with the continuous momentum equation (3.7b) in grid coordinates.

As already mentioned in Sections 3.2.2 and 3.2.3, discrete variational integrators can be of either energy–momentum, symplectic–momentum, or symplectic–energy types. In the present work emphasis is set on *exact conservation* of both momentum and total energy at discrete level—up to round-off errors. The discrete derivation of the evolution equation is thus variational but not fully symplectic. For this reason, all numerical residues present in the variational equation of $\boldsymbol{\mu}$, the corrected pressure gradient, and the discrete integration by parts are neglected in (3.22) in order to achieve these conservations. Consequently from now on, numerical residues representing differences between variational and conservative equations will be dropped. The discrete symplectic derivation, if not fully pursued, has given the needed compatibility of the main terms—notably between mass and momentum transports and pressure gradient—so that the thermodynamic consistency of the scheme is ensured.

3.3.3.4 Explicit velocity equation and compatible momentum equation

The momentum equation (3.22) cannot be easily solved due to the presence of the implicit factor ρ_c^{n+1} on its left hand side. A solution consists in solving the absolute velocity equation—which does not have factor ρ_c^{n+1}—in place of the momentum evolution equation. The absolute velocity evolution equation (55) needs to be adapted as it does not include corrections of the pressure gradient, momentum transport and residues of (3.22). Instead, the compatible absolute velocity equation is reconstructed from the combination (3.22) $-\ \boldsymbol{\mu}_c^{n+1/2} \times$ (3.18a) yielding

$$V_c^n \rho_c^n \left(\boldsymbol{\mu}_c^{n+1/2} - \boldsymbol{\mu}_c^{n-1/2}\right) = -\Delta t^n \sum_{d\in\mathcal{D}(c)} \tfrac{1}{2}\left(1 + \sigma_{cd}^{n-1/2} - \sigma_{dc}^{n-1/2}\right) \boldsymbol{s}_{cd}^{n-1/2} \left(\tilde{P}_d^n - \tilde{P}_c^n\right) + \Delta t^{n+1/2} \sum_{d\in\mathcal{D}(c)} \dot{V}_{dc}^{n+1/2} \rho_d^{n+1} \left(\boldsymbol{\mu}_d^{n+1/2} - \boldsymbol{\mu}_c^{n+1/2}\right) . \quad (3.23)$$

This equation is explicit except for the last contribution with the off-centered gradient of $\boldsymbol{\mu}$. In order to obtain a fully explicit version of (3.23), a straightforward solution consists in transforming the last term into a time flux, similarly to what was elaborated for conservative Lagrangian

space-and-time staggered schemes [35]. Equation (3.23) can thus be adapted into the fully explicit form

$$V_c^n \rho_c^n \left(\boldsymbol{\mu}_c^{n+1/2} - \boldsymbol{\mu}_c^{n-1/2}\right) = -\Delta t^n \sum_{d\in\mathcal{D}(c)} \tfrac{1}{2}\left(1 + \sigma_{cd}^{n-1/2} - \sigma_{dc}^{n-1/2}\right) \boldsymbol{s}_{cd}^{n-1/2} \left(\tilde{P}_d^n - \tilde{P}_c^n\right) + \Delta t^{n-1/2} \sum_{d\in\mathcal{D}(c)} \dot{V}_{dc}^{n-1/2} \rho_d^n \left(\boldsymbol{\mu}_d^{n-1/2} - \boldsymbol{\mu}_c^{n-1/2}\right) , \quad (3.24)$$

which corresponds to (3.24) = (3.23) + $\theta^{n+1} - \theta^n$
with $\theta^n = -\Delta t^{n-1/2} \sum_{d\in\mathcal{D}(c)} \dot{V}_{dc}^{n-1/2} \rho_d^n \left(\boldsymbol{\mu}_d^{n-1/2} - \boldsymbol{\mu}_c^{n-1/2}\right)$. It can be observed that $\theta^{n+1} - \theta^n \approx \mathcal{O}\Big[\Delta_t(\Delta t \boldsymbol{u} \rho \Delta_x(\boldsymbol{\mu}))\Big]$ which is a correction at the scheme order.

The absolute velocity equation (3.24) is now fully explicit and can be easily solved. The time flux term added in (3.24) must be transposed in the conservative momentum equation in order to keep a consistent link between momentum and absolute velocity equations. This leads to the compatible conservative momentum equation

$$\begin{aligned} V_c^{n+1}\rho_c^{n+1}\boldsymbol{\mu}_c^{n+1/2} - V_c^n \rho_c^n \boldsymbol{\mu}_c^{n-1/2} &= -\Delta t^n \sum_{d\in\mathcal{D}(c)} \tfrac{1}{2}\left(1 + \sigma_{cd}^{n-1/2} - \sigma_{dc}^{n-1/2}\right) \boldsymbol{s}_{cd}^{n-1/2} \left(\tilde{P}_d^n - \tilde{P}_c^n\right) \\ &\quad - \Delta t^{n+1/2} \sum_{d\in\mathcal{D}(c)} \left(\dot{V}_{cd}^{n+1/2} \rho_c^{n+1} \boldsymbol{\mu}_c^{n+1/2} - \dot{V}_{dc}^{n+1/2} \rho_d^{n+1} \boldsymbol{\mu}_d^{n+1/2}\right) \\ \underbrace{-\Delta t^{n+1/2} \sum_{d\in\mathcal{D}(c)} \dot{V}_{dc}^{n+1/2} \rho_d^{n+1} \left(\boldsymbol{\mu}_d^{n+1/2} - \boldsymbol{\mu}_c^{n+1/2}\right) + \Delta t^{n-1/2} \sum_{d\in\mathcal{D}(c)} \dot{V}_{dc}^{n-1/2} \rho_d^n \left(\boldsymbol{\mu}_d^{n-1/2} - \boldsymbol{\mu}_c^{n-1/2}\right)}_{\text{time flux derivative for the explicit velocity equation (3.24)}} &. \end{aligned} \quad (3.25)$$

As expected, both (3.24) and (3.25) are second-order accurate in the singular Lagrangian limit $\boldsymbol{u} = \boldsymbol{0}$ but only first-order in the Eulerian one.

3.3.4 Internal energy conservation

A discrete internal energy evolution equation is derived from the “energy tally" principle stated in [35, 7]. First a discrete kinetic energy equation is written from the discrete conservative momentum equation (3.25). Then an internal energy equation is obtained by matching the

expression of the kinetic energy equation in order to ensure the conservation of total energy.

3.3.4.1 Kinetic energy equation

The kinetic energy equation is obtained from (3.25) $\times \frac{1}{2}\left(\boldsymbol{\mu}_c^{n+1/2} + \boldsymbol{\mu}_c^{n-1/2}\right)$ − (3.18a) $\times \frac{1}{2}\left(\boldsymbol{\mu}_c^{n+1/2} \cdot \boldsymbol{\mu}_c^{n-1/2}\right)$ as

$$
\begin{aligned}
&\tfrac{1}{2}V_c^{n+1}\rho_c^{n+1}\left(\boldsymbol{\mu}_c^{n+1/2}\right)^2 - \tfrac{1}{2}V_c^{n}\rho_c^{n}\left(\boldsymbol{\mu}_c^{n-1/2}\right)^2 \\
&\quad = -\tfrac{1}{2}\Delta t^n \sum_{d\in\mathcal{D}(c)} \tfrac{1}{2}\left(1+\sigma_{cd}^{n-1/2}-\sigma_{dc}^{n-1/2}\right)\boldsymbol{s}_{cd}^{n-1/2}\cdot\left(\boldsymbol{\mu}_c^{n+1/2}+\boldsymbol{\mu}_c^{n-1/2}\right)\left(\tilde{P}_d^n-\tilde{P}_c^n\right) \\
&\qquad - \tfrac{1}{2}\Delta t^{n+1/2}\sum_{d\in\mathcal{D}(c)}\left(\dot{V}_{cd}^{n+1/2}\rho_c^{n+1}\left(\boldsymbol{\mu}_c^{n+1/2}\right)^2 - \dot{V}_{dc}^{n+1/2}\rho_d^{n+1}\left(\boldsymbol{\mu}_d^{n+1/2}\right)^2\right) \\
&\qquad - \tfrac{1}{2}\Delta t^{n+1/2}\sum_{d\in\mathcal{D}(c)}\dot{V}_{dc}^{n+1/2}\rho_d^{n+1}\left(\boldsymbol{\mu}_d^{n+1/2}-\boldsymbol{\mu}_c^{n+1/2}\right)\cdot\left(\boldsymbol{\mu}_d^{n+1/2}+\boldsymbol{\mu}_c^{n+1/2}\right) \\
&\qquad\quad + \tfrac{1}{2}\Delta t^{n-1/2}\sum_{d\in\mathcal{D}(c)}\dot{V}_{dc}^{n-1/2}\rho_d^{n}\left(\boldsymbol{\mu}_d^{n-1/2}-\boldsymbol{\mu}_c^{n-1/2}\right)\cdot\left(\boldsymbol{\mu}_c^{n+1/2}+\boldsymbol{\mu}_c^{n-1/2}\right) \quad . \qquad (3.26)
\end{aligned}
$$

This equation displays the following features : i) the first term on the right hand side is the work of pressure forces in the momentum equation (3.25) ; ii) the second term of the right hand side is a kinetic energy transport term obtained by discrete integration by parts similarly to the one performed in Section 3.3.3.3 for the momentum transport term ; iii) the resulting kinetic energy advection term is thus consistent with both momentum and mass transport divergence operators ; and iv) the last two terms on the right hand side of (3.26) are numerical residues produced by discrete integrations by parts.

In order to ensure total energy conservation, the internal energy equation must match the kinetic energy equation in such a way that only space-and-time fluxes are left. These flux terms correspond to physical fluxes (i.e. consistent with the pressure work and the internal energy transport) and numerical residues that ensure the conservation of the total energy at discrete level : these residues are thus consistent with zero (at the scheme order) when summing internal and kinetic energy equations. In contrast with neglected numerical residues coming from the variational derivation, these residues must be preserved in order to ensure total energy conservation

at discrete level. Numerous solutions are possible but in the present work we select a form which has to be as close as possible to the thermodynamic relationship $\mathrm{d}\, e = -P\, \mathrm{d}\, V$.

3.3.4.2 Pressure work decomposition

The discretization of the pressure work in the internal energy evolution equation is derived from the pressure gradient in (3.26) using constraints of causality, locality and thermodynamic consistency. These principles require that : i) all pressure terms from (3.26) appear with opposite signs in the internal energy equation (total energy conservation) ; ii) evolution of e_c^n into e_c^{n+1} must only include terms $\boldsymbol{\mu}^{n+1/2}$, $\tilde{P}_c^n$ and $\tilde{P}_c^{n+1}$ (thermodynamic consistency)—thus leading to an implicit evolution equation for e^{n+1} and $\tilde{P}^{n+1}$ through the equation of state ; and iii) whatever supplementary terms are left, they must not involve time indices beyond $n+1$ (causality). The first two constraints lead to

$$
\begin{aligned}
-P\,\mathrm{d}\,V \rightsquigarrow\ & -\tfrac{1}{4}\Delta t^{n+1/2}\tilde{P}_c^n \sum_{d\in\mathcal{D}(c)} \Big(\tfrac{1}{2}\left(1+\sigma_{cd}^{n-1/2}-\sigma_{dc}^{n-1/2}\right)\boldsymbol{s}_{cd}^{n-1/2}\cdot\boldsymbol{\mu}_c^{n+1/2} \\
& \qquad + \tfrac{1}{2}\left(1-\sigma_{cd}^{n-1/2}+\sigma_{dc}^{n-1/2}\right)\boldsymbol{s}_{cd}^{n-1/2}\cdot\boldsymbol{\mu}_d^{n+1/2}\Big) \\
& -\tfrac{1}{4}\Delta t^{n+1/2}\tilde{P}_c^{n+1} \sum_{d\in\mathcal{D}(c)} \Big(\tfrac{1}{2}\left(1+\sigma_{cd}^{n+1/2}-\sigma_{dc}^{n+1/2}\right)\boldsymbol{s}_{cd}^{n+1/2}\cdot\boldsymbol{\mu}_c^{n+1/2} \\
& \qquad + \tfrac{1}{2}\left(1-\sigma_{cd}^{n+1/2}+\sigma_{dc}^{n+1/2}\right)\boldsymbol{s}_{cd}^{n+1/2}\cdot\boldsymbol{\mu}_d^{n+1/2}\Big) \\
& -\tfrac{1}{4}\Delta t^{n-1/2}\tilde{P}_c^{n} \sum_{d\in\mathcal{D}(c)} \Big(\tfrac{1}{2}(1+\sigma_{cd}^{n-1/2}-\sigma_{dc}^{n-1/2})\boldsymbol{s}_{cd}^{n-1/2}\cdot\boldsymbol{\mu}_c^{n+1/2} \\
& \qquad + \tfrac{1}{2}(1-\sigma_{cd}^{n-1/2}+\sigma_{dc}^{n-1/2})\boldsymbol{s}_{cd}^{n-1/2}\cdot\boldsymbol{\mu}_d^{n+1/2}\Big) \\
& -\tfrac{1}{4}\Delta t^{n+3/2}\tilde{P}_c^{n+1} \sum_{d\in\mathcal{D}(c)} \Big(\tfrac{1}{2}(1+\sigma_{cd}^{n+1/2}-\sigma_{dc}^{n+1/2})\boldsymbol{s}_{cd}^{n+1/2}\cdot\boldsymbol{\mu}_c^{n+1/2} \\
& \qquad + \tfrac{1}{2}(1-\sigma_{cd}^{n+1/2}+\sigma_{dc}^{n+1/2})\boldsymbol{s}_{cd}^{n+1/2}\cdot\boldsymbol{\mu}_d^{n+1/2}\Big)
\end{aligned}
$$

$$= -\tfrac{1}{4}\Delta t^{n+1/2}\tilde{P}_c^n\langle\nabla\cdot\boldsymbol{\mu}\rangle_c^{n+1/4} - \tfrac{1}{4}\Delta t^{n+1/2}\tilde{P}_c^{n+1}\langle\nabla\cdot\boldsymbol{\mu}\rangle_c^{n+3/4}$$
$$- \tfrac{1}{4}\Delta t^{n-1/2}\tilde{P}_c^n\langle\nabla\cdot\boldsymbol{\mu}\rangle_c^{n+1/4} - \tfrac{1}{4}\Delta t^{n+3/2}\tilde{P}_c^{n+1}\langle\nabla\cdot\boldsymbol{\mu}\rangle_c^{n+3/4}\ , \quad (3.27)$$

with the following definitions for off-centered volume evolution rates

$$\langle\nabla\cdot\boldsymbol{\mu}\rangle_c^{n\pm1/4} = \sum_{d\in\mathcal{D}(c)}\left(\tfrac{1}{2}\left(1+\sigma_{cd}^{n-1/2}-\sigma_{dc}^{n-1/2}\right)\boldsymbol{s}_{cd}^{n-1/2}\cdot\boldsymbol{\mu}_c^{n\pm1/2}\right.$$
$$\left.+\tfrac{1}{2}\left(1-\sigma_{cd}^{n-1/2}+\sigma_{dc}^{n-1/2}\right)\boldsymbol{s}_{cd}^{n-1/2}\cdot\boldsymbol{\mu}_d^{n\pm1/2}\right)\ . \quad (3.28)$$

The last term of (3.27) requires the introduction of a time flux term in order to comply with the third constraint (causality) and eliminate $\Delta t^{n+3/2}$. The resulting time flux is inserted into the total energy equation and (3.27) is thus adapted as

$$-P\,\mathrm{d}\,V \rightsquigarrow -\tfrac{1}{2}\Delta t^{n+1/2}\left(\tilde{P}_c^n\langle\nabla\cdot\boldsymbol{\mu}\rangle_c^{n+1/4}+\tilde{P}_c^{n+1}\langle\nabla\cdot\boldsymbol{\mu}\rangle_c^{n+3/4}\right)$$
$$-\frac{\Delta t^{n+1/2}-\Delta t^{n-1/2}}{4}\tilde{P}_c^n\left(\langle\nabla\cdot\boldsymbol{\mu}\rangle_c^{n+1/4}-\langle\nabla\cdot\boldsymbol{\mu}\rangle_c^{n-1/4}\right)\ , \quad (3.29)$$

where (3.29) = (3.27) + $\theta^{n+1}-\theta^n$ with $\theta^n = -\tfrac{1}{4}\Delta t^{n+1/2}\tilde{P}_c^n\langle\nabla\cdot\boldsymbol{\mu}\rangle_c^{n-1/4}$. In the Lagrangian limit (i.e. all off-centering factors are equal to 1/2), the time decomposition of (3.29) ensures a capture of $P\,\mathrm{d}\,V$ to second-order—with control of the entropy at second-order [35]. The last term of (3.29) is a residue of order $\mathcal{O}\left[\Delta t^2\Delta_x\boldsymbol{\mu}\right]$ which appears for non constant time steps. A similar correction of same order is found for conservative space-and-time staggered Lagrangian schemes [35, eq. 12].

3.3.4.3 Internal energy evolution

The discrete internal energy transport term is added in the internal energy evolution equation—consistently with the swept-flux volume transfers in the mass transport (3.18a). The space-and-time centering of this transport term must be consistent with the expression of the discrete divergence operators for mass and momentum—the corresponding internal energy transport must match the entropy transport which is identical to mass transport. Inserting the pressure work (3.29), making

the internal energy transport appear and transposing numerical residues from (3.26) leads to the discrete internal energy evolution equation

$$
\begin{aligned}
V_c^{n+1}\rho_c^{n+1}e_c^{n+1} - V_c^n\rho_c^n e_c^n = &-\tfrac{1}{2}\Delta t^{n+1/2}\left(\tilde{P}_c^n\langle\nabla\cdot\boldsymbol{\mu}\rangle_c^{n+1/4} + \tilde{P}_c^{n+1}\langle\nabla\cdot\boldsymbol{\mu}\rangle_c^{n+3/4}\right)\\
&-\tfrac{1}{4}(\Delta t^{n+1/2}-\Delta t^{n-1/2})\tilde{P}_c^n\left(\langle\nabla\cdot\boldsymbol{\mu}\rangle_c^{n+1/4} - \langle\nabla\cdot\boldsymbol{\mu}\rangle_c^{n-1/4}\right)\\
&\underbrace{-\Delta t^{n+1/2}\sum_{d\in\mathcal{D}(c)}\left(\dot{V}_{cd}^{n+1/2}\rho_c^{n+1}e_c^{n+1} - \dot{V}_{dc}^{n+1/2}\rho_d^{n+1}e_d^{n+1}\right)}_{\text{internal energy transport}}\\
&\underbrace{-\tfrac{1}{2}\Delta t^{n+1/2}\sum_{d\in\mathcal{D}(c)}\dot{V}_{cd}^{n+1/2}\rho_c^{n+1}\left(\boldsymbol{\mu}_d^{n+1/2}-\boldsymbol{\mu}_c^{n+1/2}\right)\cdot\left(\boldsymbol{\mu}_d^{n+1/2}+\boldsymbol{\mu}_c^{n+1/2}\right)}_{\text{residue from discrete integration by parts of kinetic transport (3.26)}}\\
&\underbrace{+\tfrac{1}{2}\Delta t^{n-1/2}\sum_{d\in\mathcal{D}(c)}\dot{V}_{cd}^{n-1/2}\rho_c^{n}\left(\boldsymbol{\mu}_d^{n-1/2}-\boldsymbol{\mu}_c^{n-1/2}\right)\cdot\left(\boldsymbol{\mu}_d^{n+1/2}+\boldsymbol{\mu}_d^{n-1/2}\right)}_{\text{residue from time flux in (3.25)}} .
\end{aligned}
\tag{3.30}
$$

The last two terms on the right hand side of (3.30) are numerical residues that arise from the kinetic energy evolution (3.26) (up to permutations of cell indices c and d) in order to ensure the total energy conservation at discrete level.

3.3.4.4 Transport-implicit internal energy equation at half time steps

Because of the implicit character of the internal energy transport and of the $\tilde{P}_c^{n+1}$ terms, solving the internal energy evolution equation (3.30) requires solving an *implicit non-local and non-linear* set of equations (closed by the equation of state of the fluid). In order to solve only a linearly implicit evolution equation for the internal energy, a change of variable is performed in (3.30)

$$
e_c^{n+1} = e_c^{n+1/2} - \tfrac{1}{2}\frac{\Delta t^{n+1/2}}{V_c^{n+1}\rho_c^{n+1}}\tilde{P}_c^{n+1}\langle\nabla\cdot\boldsymbol{\mu}\rangle_c^{n+3/4} , \tag{3.31}
$$

which corresponds to a Strang splitting [55] of the pressure work in the internal energy evolution from e_c^n into e_c^{n+1}. Substituting e^{n+1} from (3.31) into (3.30) leads to the evolution equation for

internal energy at half time steps

$$
\begin{aligned}
V_c^{n+1}\rho_c^{n+1}e_c^{n+1/2} - V_c^n\rho_c^n e_c^n = &-\tfrac{1}{2}\Delta t^{n+1/2}\tilde{P}_c^n\langle\nabla\cdot\boldsymbol{\mu}\rangle_c^{n+1/4} \\
&- \tfrac{1}{4}(\Delta t^{n+1/2} - \Delta t^{n-1/2})\tilde{P}_c^n\left(\langle\nabla\cdot\boldsymbol{\mu}\rangle_c^{n+1/4} - \langle\nabla\cdot\boldsymbol{\mu}\rangle_c^{n-1/4}\right) \\
&- \Delta t^{n+1/2}\sum_{d\in\mathcal{D}(c)}\left(\dot{V}_{cd}^{n+1/2}\rho_c^{n+1}e_c^{n+1/2} - \dot{V}_{dc}^{n+1/2}\rho_d^{n+1}e_d^{n+1/2}\right) \\
&- \tfrac{1}{2}\Delta t^{n+1/2}\sum_{d\in\mathcal{D}(c)}\dot{V}_{cd}^{n+1/2}\rho_c^{n+1}\left(\boldsymbol{\mu}_d^{n+1/2} - \boldsymbol{\mu}_c^{n+1/2}\right)\cdot\left(\boldsymbol{\mu}_d^{n+1/2} + \boldsymbol{\mu}_c^{n+1/2}\right) \\
&+ \tfrac{1}{2}\Delta t^{n-1/2}\sum_{d\in\mathcal{D}(c)}\dot{V}_{cd}^{n-1/2}\rho_c^{n}\left(\boldsymbol{\mu}_d^{n-1/2} - \boldsymbol{\mu}_c^{n-1/2}\right)\cdot\left(\boldsymbol{\mu}_d^{n+1/2} + \boldsymbol{\mu}_d^{n-1/2}\right) \quad , \qquad (3.32)
\end{aligned}
$$

where (3.30) = (3.32) + $\mathcal{O}\big[\Delta t^2\Delta_x(u\tilde{P}\Delta_x\mu)\big]$. This last correction represents the non explicit residue which appears when substituting the transport of e^{n+1} by the transport of $e^{n+1/2}$. These fluxes being energy preserving, their difference will also be energy preserving. This high-order residue can thus be ignored without any impact on total energy conservation. Only a *local* non-linear relationship between e^{n+1} and $\tilde{P}^{n+1}$ is then left as in pure Lagrangian schemes.

The set of evolution equations for mass (3.18a), absolute velocity (3.24), internal energy at half time steps (3.32), and internal energy at integer time steps (3.31), together with an equation of state for the fluid forms the implicit direct ALE scheme named iGEECS (implicit Geometry, Energy, and Entropy Compatible Scheme).

3.3.5 GEECS : explicit version of iGEECS

In iGEECS, the implicit transport of ρ and e implies solving a linear system at each time step for both density and internal energy equations—incidentally the change of variables (3.31) leads to the same matrix inversion for both ρ and e. In one dimension, the linear system is band diagonal (of width three) and is solved efficiently using for instance an elementary LU decomposition algorithm whose complexity is $\mathcal{O}(I)$ where I is the total number of cells. However, in two dimensions the transport matrix is a $\sqrt{I}$ wide band matrix and the algorithmic complexity is thus $\mathcal{O}(I\sqrt{I})$ without any LU preconditioning.

Therefore, an explicit version of iGEECS is proposed for performance purposes. Three options

are possible for obtaining an explicit version of iGEECS : i) take explicit transports (3.12) in (3.16) and follow the same derivation as for iGEECS ; ii) take explicit transports in (3.18a), keep the Euler–Lagrange equations (3.18c) and (3.18d) unchanged, and follow the same discrete derivation as in Sections 3.3.3 and 3.3.4 ; or iii) take explicit transports directly in (3.18a), (3.25), and (3.32). As already explained in Section 3.3.2.1, the first option is discarded in the present work because it leads to an implicit absolute velocity equation. In the third option, compatibility between kinetic and internal energy equations is lost at discrete level, as the approximation of the explicit momentum transport taken in (3.25) is not consistently transposed into (3.32) by residual terms. In the present work, the second option is retained, taking explicit mass transport (3.18a) and following the same derivation as for iGEECS. This allows to preserve the consistency of corrective terms produced by discrete integration by parts in (3.25), and (3.32).

In the second option, the mass advection is first taken explicit

$$V_c^{n+1}\rho_c^{n+1} - V_c^n\rho_c^n = \Delta t^{n+1/2} \sum_{d\in\mathcal{D}(c)} \left(\dot{V}_{dc}^{n+1/2}\rho_d^n - \dot{V}_{cd}^{n+1/2}\rho_c^n\right) , \tag{3.33}$$

which differs from the implicit version (3.18a) only by a numerical residue at the scheme order (3.18a) = (3.33) + $\mathcal{O}\big[\Delta t\Delta_x(\boldsymbol{u}\Delta_t(\rho))\big]$. An absolute velocity equation—as well as the associated conservative momentum equation—is then derived from the Euler–Lagrange equations (3.33), (3.18c), and (3.18d) by closely following the procedure in Section 3.3.3 leading to

$$\begin{aligned} V_c^n\rho_c^n(\boldsymbol{\mu}_c^{n+1/2} - \boldsymbol{\mu}_c^{n-1/2}) = -\Delta t^n \sum_{d\in\mathcal{D}(c)} \tfrac{1}{2}\left(1 + \sigma_{cd}^{n-1/2} - \sigma_{dc}^{n-1/2}\right) \boldsymbol{s}_{cd}^{n-1/2} \left(\tilde{P}_d^n - \tilde{P}_c^n\right) \\ + \Delta t^{n-1/2} \sum_{d\in\mathcal{D}(c)} \dot{V}_{dc}^{n-1/2}\rho_d^{n-1} \left(\boldsymbol{\mu}_d^{n-1/2} - \boldsymbol{\mu}_c^{n-1/2}\right) , \end{aligned} \tag{3.34}$$

where (3.25) = (3.34) + $\mathcal{O}\big[\Delta t\boldsymbol{u}\Delta_t(\rho)\Delta_x(\boldsymbol{\mu})\big]$. Similarly an internal energy equation is exhibited

by following Section 3.3.4—matching kinetic energy and internal energy equations—yielding

$$
\begin{aligned}
V_c^{n+1}\rho_c^{n+1}e_c^{n+1} - V_c^n\rho_c^n e_c^n = &-\tfrac{1}{2}\Delta t^{n+1/2}\left(\tilde{P}_c^n\langle\nabla\cdot\boldsymbol{\mu}\rangle_c^{n+1/4} + \tilde{P}_c^{n+1}\langle\nabla\cdot\boldsymbol{\mu}\rangle_c^{n+3/4}\right)\\
&-\tfrac{1}{4}(\Delta t^{n+1/2}-\Delta t^{n-1/2})\tilde{P}_c^n\left(\langle\nabla\cdot\boldsymbol{\mu}\rangle_c^{n+1/4} - \langle\nabla\cdot\boldsymbol{\mu}\rangle_c^{n-1/4}\right)\\
&-\Delta t^{n+1/2}\sum_{d\in\mathcal{D}(c)}\left(\dot{V}_{cd}^{n+1/2}\rho_c^n e_c^n - \dot{V}_{dc}^{n+1/2}\rho_d^n e_d^n\right)\\
&-\tfrac{1}{2}\Delta t^{n+1/2}\sum_{d\in\mathcal{D}(c)}\dot{V}_{cd}^{n+1/2}\rho_c^n\left(\boldsymbol{\mu}_d^{n+1/2}-\boldsymbol{\mu}_c^{n+1/2}\right)\cdot\left(\boldsymbol{\mu}_d^{n+1/2}+\boldsymbol{\mu}_c^{n+1/2}\right)\\
&+\tfrac{1}{2}\Delta t^{n-1/2}\sum_{d\in\mathcal{D}(c)}\dot{V}_{cd}^{n-1/2}\rho_c^{n-1}\left(\boldsymbol{\mu}_d^{n-1/2}-\boldsymbol{\mu}_c^{n-1/2}\right)\cdot\left(\boldsymbol{\mu}_d^{n+1/2}+\boldsymbol{\mu}_d^{n-1/2}\right)\ ,
\end{aligned}
\tag{3.35}
$$

where the ρ-explicit internal energy transport term is added in (3.35) consistently with mass, momentum, and thus entropy transports. The resulting internal energy equation (3.35) is then fully explicit. Here however, an internal energy evolution equation at half time steps—with explicit transport—is obtained by performing an analogue of the change of variable (3.31) for iGEECS

$$
e_c^n = e_c^{n+1/2} + \tfrac{1}{2}\frac{\Delta t^{n+1/2}}{V_c^n\rho_c^n}\tilde{P}_c^n\langle\nabla\cdot\boldsymbol{\mu}\rangle_c^{n+1/4}\ . \tag{3.36}
$$

This change of variable (3.36) is not a necessary constraint as for iGEECS but it allows to ensure several additional properties : i) better control of the internal energy transport when simulating flows with large advections ; ii) similar internal energy decomposition as in iGEECS with (3.31) ; and iii) Strang splitting of the internal energy evolution from e^n into e^{n+1}. Substituting e_c^n from

(3.36) into (3.35) leads to

$$
\begin{aligned}
V_c^{n+1}\rho_c^{n+1}e_c^{n+1} - V_c^n\rho_c^n e_c^{n+1/2} = &-\tfrac{1}{2}\Delta t^{n+1/2}\tilde{P}_c^{n+1}\langle\nabla\cdot\boldsymbol{\mu}\rangle_c^{n+3/4} \\
&- \tfrac{1}{4}(\Delta t^{n+1/2} - \Delta t^{n-1/2})\tilde{P}_c^n\left(\langle\nabla\cdot\boldsymbol{\mu}\rangle_c^{n+1/4} - \langle\nabla\cdot\boldsymbol{\mu}\rangle_c^{n-1/4}\right) \\
&- \Delta t^{n+1/2}\sum_{d\in\mathcal{D}(c)}\left(\dot{V}_{cd}^{n+1/2}\rho_c^n e_c^{n+1/2} - \dot{V}_{dc}^{n+1/2}\rho_d^n e_d^{n+1/2}\right) \\
&- \tfrac{1}{2}\Delta t^{n+1/2}\sum_{d\in\mathcal{D}(c)}\dot{V}_{cd}^{n+1/2}\rho_c^n\left(\boldsymbol{\mu}_d^{n+1/2} - \boldsymbol{\mu}_c^{n+1/2}\right)\cdot\left(\boldsymbol{\mu}_d^{n+1/2} + \boldsymbol{\mu}_c^{n+1/2}\right) \\
&+ \tfrac{1}{2}\Delta t^{n-1/2}\sum_{d\in\mathcal{D}(c)}\dot{V}_{cd}^{n-1/2}\rho_c^{n-1}\left(\boldsymbol{\mu}_d^{n-1/2} - \boldsymbol{\mu}_c^{n-1/2}\right).\left(\boldsymbol{\mu}_d^{n+1/2} + \boldsymbol{\mu}_d^{n-1/2}\right) \quad , \qquad (3.37)
\end{aligned}
$$

where (3.35) = (3.37) + $\mathcal{O}\big[\Delta t^2\Delta_x(u\tilde{P}\Delta_x(\mu))\big]$.

The set of evolution equations for mass (3.33), momentum (3.34), internal energy at half time steps (3.36), and internal energy at integer time steps (3.37) forms GEECS, the explicit version of iGEECS. As expected, transports of mass (3.33), momentum (3.34), and internal energy (3.37) are now fully explicit.

3.3.6 Special structure of pressure gradient and pressure work

For usual Finite Volume-like schemes, divergence and gradient operators are integrated using Green–Ostrogradski's formula and numerical fluxes are defined at cell boundaries using an upwinding along particular waves (such as material waves as in the present work). In these schemes, the pressure gradient is generally upwinded similarly to the velocity divergence. If not, it is centered as in standard Finite Difference schemes. In contrast (and even if it not explicitly mentionned), indirect ALE Lagrange plus remap schemes naturally lead to some downwinding along material waves.

It must be stressed that in the present work, as already obtained [29, eq. 26], the use of a discrete least action principle together with an off-centered transport operator leads to a particular off-centered structure of the pressure gradient in the discrete momentum evolution equation (3.25) of iGEECS. Indeed, the advection of both mass and momentum is computed with the same

upwind discretization but the pressure gradient possesses a *downwind* structure

$$\begin{aligned} &\text{advection in (3.18a)} && \propto \sigma_{dc}\,\rho_d\ , \\ &\text{pressure gradient in (3.19)} && \propto \sigma_{cd}\,P_d\ . \end{aligned} \tag{3.38}$$

The symmetrization procedure in (3.25) also preserves this somewhat non-standard downwinding structure of the pressure gradient (when the fluid is advected with a uniform velocity)

$$\begin{aligned} &\text{mimetic pressure gradient in (3.19)} && \propto \sigma_{cd}\,P_d\ , \\ &\text{conservative pressure gradient in (3.25)} && \propto \tfrac{1}{2}(1+\sigma_{cd}-\sigma_{dc})\,P_d\ . \end{aligned} \tag{3.39}$$

Work of pressure forces in (3.32) is obtained from the pressure gradient in (3.25) through the kinetic energy equation (3.26) and the conservation of total energy. Pressure work thus involves volume evolution rates (3.28) which are off-centered with an again upwind structure. In contrast to purely Lagrangian schemes derived by variational approaches, these volume evolution rates—and thus the internal energy equation—are not linked to grid corner vectors but to off-center-weighted cell-boundary vectors.

It must be noted that the fully explicit version GEECS also involves the particular off-centered structure presented in this section : *upwind* for both mass and momentum transports, *downwind* for the pressure gradient, and *opposite upwind* for the pressure work.

3.4 Summary of iGEECS and GEECS algorithms

For clarity, summaries of the linearly implicit (iGEECS) and explicit (GEECS) algorithms are presented in this section, together with definitions of time step and artificial viscosity.

In the absence of a detailed stability analysis (to be given in a forthcoming publication) the time step of the simulation $\Delta t^{n+1/2}$ is bounded by a simple CFL condition (sound velocity and fluid advection) according to

$$\Delta t^{n+1/2} = \mathrm{CFL} \times \min_c \left(\frac{\Delta_c^n}{C_c^n + |\boldsymbol{\mu}_c^{n-1/2}|} \right)\ , \tag{3.40}$$

where C_c^n is the speed of sound of the fluid and Δ_c^n a characteristic length scale of cell c. In the present work Δ_c^n is taken as the length of the smallest of the diagonals and medians of cell c. Due to the explicit treatment of pressure forces, the time step constraint cannot be relaxed, even for iGEECS. Situations in which iGEECS is more stable than GEECS can be expected but, for all tests performed in the course of this work, differences between the schemes appear marginal.

The artificial viscosity stress Q is inserted in the equations in order to capture shocks [42, 31]. Many shock sensors based on the velocity field can be designed, usually as functionals of velocity and thermodynamic variables of cells. For simplicity, the form of Q chosen here for perfect gases is

$$Q_c^n = -a_1 \rho_c^n C_c^n \langle \nabla \cdot \boldsymbol{\mu} \rangle_c^{n+1/4} + \tfrac{1}{2} a_2 (\gamma + 1) \rho_c^n \min\left(\langle \nabla \cdot \boldsymbol{\mu} \rangle_c^{n+1/4}, 0 \right)^2 , \tag{3.41}$$

where γ is the isentropic coefficient of the fluid and $\langle \nabla \cdot \boldsymbol{\mu} \rangle_c^{n+1/4}$ the off-centered volume evolution rates given by (3.28). The use of the same off-centered structure in (3.41) and (3.32) ensures that the work of Q_c^n remains always positive for the term $(Q_c^n \langle \nabla \cdot \boldsymbol{\mu} \rangle_c^{n+1/4}) \cdot \langle \nabla \cdot \boldsymbol{\mu} \rangle_c^{n+1/4} > 0$. As already shown in [35], a predictor–corrector step on the momentum evolution equation could be added in order to further ensure the positivity of the work of Q_c^n for the term $(Q_c^n \langle \nabla \cdot \boldsymbol{\mu} \rangle_c^{n+3/4}) \cdot \langle \nabla \cdot \boldsymbol{\mu} \rangle_c^{n+3/4}$. All computations reported in Section 3.5 are performed with the optimal values $a_1 = a_2 = 0.5$ for the artificial viscosity coefficients, according to the definition in [42, 31].

Starting from the main quantities at step n, the time cycle to $n+1$ consists in successive applications of the following equations (on the right the updated variables are indicated)

At beginning of cycle	$\Delta t^{n-1/2}\boldsymbol{\mu}_c^{n-1/2}$	$\boldsymbol{w}_p^{n-1/2}\boldsymbol{x}_p^n$	$\boldsymbol{u}_c^{n-1/2}\sigma_{cd}^{n-1/2}$	$\rho_c^n Q_c^n$	$e_c^n P_c^n$
(3.40)	$\Delta t^{n+1/2}$				
(3.24) iGEECS,(3.34) GEECS	$\boldsymbol{\mu}_c^{n+1/2}$				
see for example .2		$\boldsymbol{w}_p^{n+1/2}$			
(3.9)		$\boldsymbol{x}_p^{n+1}$			
(3.10)			$\boldsymbol{u}_c^{n+1/2}$		
(3.13)			$\sigma_{cd}^{n+1/2}$		
(3.18a) iGEECS,(3.33) GEECS				ρ_c^{n+1}	
(3.41)				Q_c^{n+1}	
(3.32) iGEECS,(3.36) GEECS					$e_c^{n+1/2}$
(3.31) iGEECS,(3.37) GEECS					e_c^{n+1}
Equation of state					P_c^{n+1}

For the implicit scheme iGEECS, the resolution of equations (3.24), (3.18a), (3.32), and (3.31) is here performed using an elementary LU decomposition algorithm.

3.5 Numerical tests

The novel generic mimicking GEEC procedure developed in the present work has lead to the derivation of two schemes iGEECS (implicit) and GEECS (explicit). In this section, the behavior of GEECS is analyzed by performing several standard benchmark tests from the literature involving shocks or large fluid deformations—the isentropic vortex, Sod's shock tube, Sedov's blast wave, Woodward–Colella's double shock tube, and the triple point shock tube. All tests except the triple point shock tube have analytical solutions which allow the objective evaluation of the scheme performances and the verification of built-in properties such as exact conservation or entropy preservation.

As fluid and grid velocities have different space centerings, an exact Lagrangian grid motion is excluded in principle as already mentionned in Section 3.3.2.1. As a consequence a near-Lagrangian grid velocity is simply defined by minimizing mass fluxes around each node of the mesh (see Appendix .2). Although it is not explicitly reported in the present work, all test cases have been run at both large and small CFL numbers (≈ 0.9 and 10^{-3} respectively). As changing the CFL number only modifies the amount of numerical diffusion, all results displayed in the following sections are obtained using a close to maximal *no-crash* CFL number. To preserve the legibility of the figures, only one in ten or twenty grid lines are sometimes shown, which is still sufficient to render the topology of the grid.

Results of the test cases confirm several built-in properties for GEECS : i) exact conservation of mass, momentum, and total energy at discrete level (up to round-off errors) ; ii) second-order accuracy in the Lagrangian limit for advection ; iii) second-order accuracy for the thermodynamic consistency of pressure work (hence entropy) regardless of mesh motions ; iv) indifference and versatility to grid motions—including supersonic shearing, near-Lagrangian displacements, or linearly interpolated from fixed Eulerian edges to Lagrangian contact discontinuities ; —and iv) compatibility between velocity fields and volume variations in the presence of strong fluid

advections relative to the grid.

The five numerical test cases involve the following features :

– the isentropic vortex [3, 52] is mostly used to estimate convergence rates since the exact solution is smooth. All details of the construction of this test can be found in [3, and references therein]. In the following, is recalled only the necessary information to set up this test problem. The initial domain is $[0;10] \times [-5;5]$ and the vortex center is located at $(x_0,y_0) = (5,0)$. Initial conditions for density, pressure, and temperature are characterized by

$$\rho = T^{1/\gamma-1}, \qquad P = \rho T = \rho^{\gamma}, \qquad T = 1 - \frac{(\gamma-1)\beta^2}{8\gamma\pi^2}\exp(1-r^2), \tag{3.42}$$

where $\beta = 5$ and $r = \sqrt{(x-x_0)^2 + (y-y_0)^2}$ are respectively the vortex strength and vortex radius. Initial velocities in both x and y directions are

$$\mu_x = \frac{\beta}{2\pi}\exp(\frac{1-r^2}{2})(y_0 - y), \qquad \mu_y = \frac{\beta}{2\pi}\exp(\frac{1-r^2}{2})(x - x_0). \tag{3.43}$$

– Sod's shock tube [53] : this classical test is a Riemann problem which produces three waves—an expansion fan, a contact discontinuity, and a shock of medium strength. Initially an interface is located at $x = 0.5$ and the states on the left and the right sides of the interface are constant. The left state is a high pressure and high density fluid characterized by $(\rho_l,P_l,\mu_l) = (1,1,0)$, the right state is a low pressure and low density fluid defined by $(\rho_r,P_r,\mu_r) = (0.125,0.1,0)$. The isentropic coefficient for both states is $\gamma = 7/5$;

– Sedov's blast wave [50] : this test represents an explosion in a cold perfect gas at zero-pressure. Initial conditions are characterized by $(\rho,P,\mu) = (1,10^{-16},0)$ with the isentropic coefficient $\gamma = 5/3$. A point source of internal energy is initialized at the origin in the cell located at $x = y = 0$. The magnitude of this point source of internal energy is given by

$$e = E_{\text{blast}}/V_{\text{blast}} \ , \tag{3.44}$$

with V_{blast} the volume of the cell located at $x = y = 0$ and E_{blast} a constant per-unit

volume depending on both the isentropic coefficient and the geometry [27]. This prescribes the pressure at the origin—through the equation of state of the fluid— and creates an "infinitely strong" divergent shock that propagates in the numerical domain. Downstream of the shock, the isentropic expansion of the fluid produces a characteristic profile given by a closed algebraic expression [28] ;

– the triple point shock tube [4] : this test case corresponds to a three-state Riemann problem with different densities, pressures, and isentropic coefficients in a rectangular domain. With these initial conditions, two shocks appear and propagate with different speeds. This creates a shearing along the initial horizontal contact discontinuity and a vortex at the triple point. Initial conditions for densities, pressures, and isentropic coefficients are given in Figure 3.2 ;

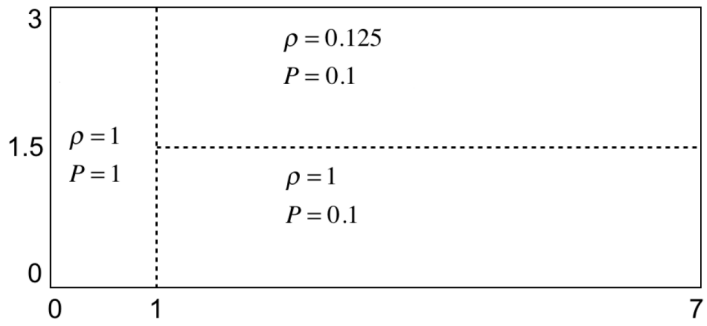

FIGURE 3.2 – Density and pressure initialization for the triple point shock tube.

– Woodward–Colella's double shock tube [65] : this one-dimensional test problem involves multiple interactions between strong shocks, rarefaction waves, and contact discontinuities. Initial conditions consist of three constant states with two interfaces located at $x = 0.1$ and 0.9. Density is equal to one everywhere and pressure is equal to 1000 in the leftmost tenth of the volume, 100 in the rightmost of the volume, and 0.01 in between. The isentropic coefficient is $\gamma = 7/5$. Two strong shock waves develop and collide, producing a new contact discontinuity. As much of the important flow features takes place in a small volume, this

test is difficult to compute on purely Eulerian grids due to numerical diffusion, although it poses no particular difficulty for Lagrangian calculations. The use of an ALE approach allows to combine advantages of both Eulerian and Lagrangian methods.

For all test cases, the fluid is supposed to be a perfect gas with $P = (\gamma - 1)\rho e$ where γ is the isentropic coefficient.

Results of numerical tests are organized as follows :

- in order to determine the convergence rate of GEECS, the isentropic vortex is performed in Eulerian, Lagrangian, and half-Lagrangian limits in Section 3.5.1. Errors between numerical and exact solutions are computed using the L^2-norm for both density and entropy fields at four mesh resolutions ;
- in order to test the indifference to implicit or explicit character of the advection, the behavior of iGEECS and GEECS is compared on both Sod's shock tube and Sedov's plane blast wave in Section 3.5.2 using uniform and constant grid velocities over the entire numerical domain. Three grid velocities are tested : i) Eulerian with fixed nodes or $\boldsymbol{w} = \mathbf{0}$; ii) the fluid velocity of the fastest rightward sonic wave in the domain (which is faster than the shock wave) ; and iii) the fluid velocity of the slowest leftward sonic wave in the domain. In the last two configurations, the grid evolves in a supersonic motion relative to the fluid flow ;
- in order to allow comparison with results from literature, both Sod's shock tube and Sedov's plane blast wave are performed in Section 3.5.3 with coarse meshes in one dimension using three grid motion strategies : i) Eulerian with fixed nodes or $\boldsymbol{w} = \mathbf{0}$, ii) "half-Lagrangian", and iii) "near-Lagrangian" where the grid velocity formulation is given in Appendix .2 ;
- in order to verify the indifference to grid velocity, two new variants of Sod's shock tube are proposed in Sections 3.5.4 and 3.5.5 where the grid is sheared across the x or y directions. The total number of mesh cells is chosen so that initial cells are perfect squares and final cells are exact parallelograms with a $\pi/4$ angle relative to the initial mesh. These variants test the ability of GEECS to handle : i) significant grid deformations, ii) tilting of flow characteristics, and iii) inprint of mesh distortions on fluid motions. Results of Sedov's

plane blast wave performed using two-dimensional sheared grid and dynamically randomly distorted meshes are also presented ;

– in order to verify the versatility to grid motion strategy, Sedov's cylindrical blast wave is performed in Section 3.5.6 using two grid motion strategies : i) Eulerian mesh with fixed nodes or $\boldsymbol{w} = \boldsymbol{0}$ thus leading to quite diffusive results, and ii) near-Lagrangian mesh in order to best follow fluid motions and preserve a sharp and accurate capture of the exact solution for a small number of cells. The triple point shock tube is performed in Section 3.5.7 using two grid motions strategies : i) Eulerian mesh with fixed nodes or $\boldsymbol{w} = \boldsymbol{0}$, and ii) a prescribed ALE mesh evolving in both x and y directions, in order to obtain less diffusive results and a more accurate capture of the flow features ;

– in order to demonstrate the usability of the scheme with ALE grid motions aiming at following material interfaces, both Sod's shock tube and Woodward–Colella's double shock tube are performed in Section 3.5.8 with two grid motion strategies : i) Eulerian grid with fixed nodes or $\boldsymbol{w} = \boldsymbol{0}$, and ii) grid velocity is linearly interpolated from fixed Eulerian edges to Lagrangian contact discontinuities.

3.5.1 Isentropic vortex

In this section, the convergence rates of GEECS are measured on the smooth isentropic vortex flow over four meshes of 25×25, 50×50, 100×100, and 200×200 cells. In order to obtain accuracy orders of GEECS in both Eulerian and Lagrangian limits, three grid motion strategies are used : i) Eulerian grid with fixed nodes or $\boldsymbol{w} = \boldsymbol{0}$; ii) Lagrangian grid where $\boldsymbol{w} = \boldsymbol{\mu}$ where $\boldsymbol{\mu}$ is the analytical vortex velocity given by (3.43) ; and iii) "half-Lagrangian" grid where $\boldsymbol{w} = 0.5\boldsymbol{\mu}$ where $\boldsymbol{\mu}$ is given by (3.43).

For this purely isentropic test, the artificial viscosity is cancelled due to the fact that : i) it affects the scheme order ; and ii) the shock sensor used in the present work (3.41) is rudimentary and needs further developments in order to be able to properly detect shocks and isentropic compressions.

Errors between numerical and exact solutions ϵ_{L2} are computed with the L^2-norm for both

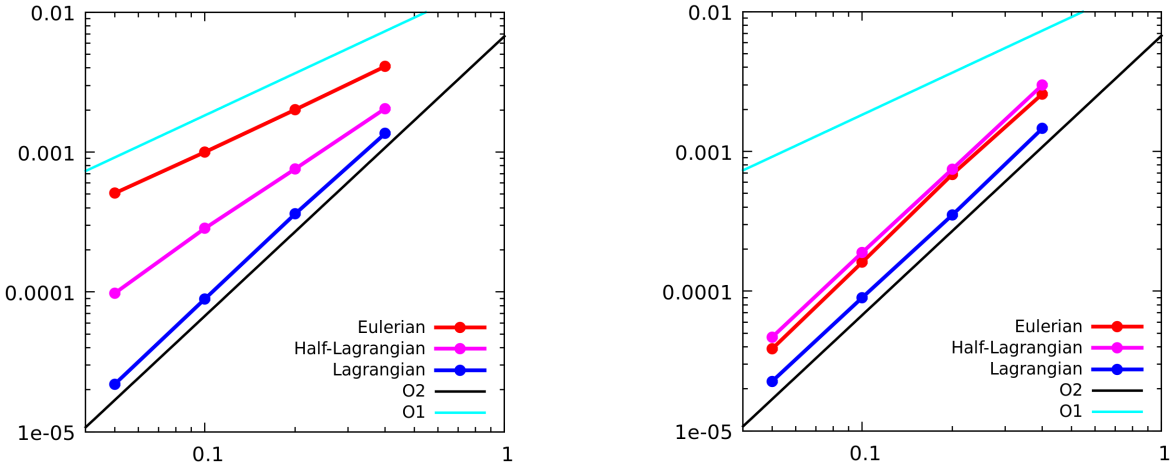

(a) Density errors (b) Entropy errors

FIGURE 3.3 – L^2-errors and convergence rates for both density (left) and entropy fields (right) on the isentropic vortex problem performed on Eulerian, "half-Lagrangian", and Lagrangian grids using the GEECS method. Computations are done with $I = 25 \times 25$, 50×50, 100×100, and 200×200 cells, final time $t = 1$, and CFL $= 0.8$.

density and entropy fields, and the convergence rate for each quantity is obtained by computing the ratio $\log(r)/\log(2)$ where r is the ratio between errors associated with two successive meshes. Results of the convergence rate for the three grid motion strategies are displayed on Figures 3.3 and in Table 3.1. As expected, GEECS is second-order accurate in the Lagrangian limit and first-order accurate in the Eulerian limit.

Less trivially however, computations of L^2-errors for the entropy field with Eulerian, half-Lagrangian, and Lagrangian mesh show that the thermodynamic consistency of the pressure work remains ensured to second-order regardless of mesh motions. Even if GEECS is first-order accurate for advection, entropy is still preserved at second-order. Due to the use of a variational approach in the generic GEEC procedure developed in the present work, entropy compatibility is naturally ensured and improves both accuracy and robustness.

3.5.2 One-dimensional tests of indifference to implicit or explicit advection

The indifference to implicit or explicit character of advection is tested in one dimension on both Sod's shock tube and Sedov's plane blast wave. For these tests, the grid velocity is uniform

TABLE 3.1 – L^2-errors and convergence rates for both density and entropy fields on the isentropic vortex problem performed with three grid motion strategies using the GEECS method.

	Density					
Grid motion	Eulerian		Half-Lagrangian		Lagrangian	
Mesh size	ϵ_{L2}		ϵ_{L2}		ϵ_{L2}	
25×25	$4.10.10^{-3}$	–	$2.05.10^{-3}$	–	$1.36.10^{-3}$	–
50×50	$2.01.10^{-3}$	1.03	$7.58.10^{-4}$	1.43	$3.61.10^{-4}$	1.92
100×100	$1.00.10^{-3}$	1.01	$2.85.10^{-4}$	1.41	$8.92.10^{-5}$	2.01
200×200	$5.08.10^{-4}$	0.98	$9.79.10^{-5}$	1.54	$2.19.10^{-5}$	2.02
	Entropy					
Grid motion	Eulerian		Half-Lagrangian		Lagrangian	
Mesh size	ϵ_{L2}		ϵ_{L2}		ϵ_{L2}	
25×25	$2.58.10^{-3}$	–	$2.99.10^{-3}$	–	$1.46.10^{-3}$	–
50×50	$6.86.10^{-4}$	1.91	$7.48.10^{-4}$	2.00	$3.51.10^{-4}$	2.05
100×100	$1.61.10^{-4}$	2.01	$1.89.10^{-4}$	1.98	$8.99.10^{-5}$	1.97
200×200	$3.86.10^{-5}$	2.06	$4.68.10^{-5}$	2.01	$2.26.10^{-5}$	2.00

and constant over the whole computational area. The two test cases are performed using fine meshes of 600 cells in order to find a compromise between numerical diffusion and possibly numerical artifact or oscillation.

All density profiles in Figures 3.4 and 3.5 display an accurate capture of the exact solution for both Sod's shock tube and Sedov's plane blast wave. Results obtained with supersonic grids—the grid velocity is faster or slower than all waves across the domain—demonstrate the robustness and stability of both iGEECS and GEECS as no numerical artifact or oscillation appears in the density profiles, despite a CFL number close to one.

Density profiles shown in Figures 3.4 and 3.5 display numerical diffusion due to the first-order feature of transport of conserved quantities. The amount of numerical diffusion is larger when the mesh evolves faster than the fastest wave across the domain (shock included). It can be noticed that for Sod's shock tube, the implicit version of GEECS diplays more numerical diffusion at the contact discontinuity because the CFL number is close to one.

For all tests performed in the course of the present work, differences between iGEECS and GEECS remain marginal and due to non pre-conditionned LU decompositions, iGEECS is more time consuming than GEECS. As a consequence, only the cheaper explicit scheme GEECS is used for the results displayed in the following sections.

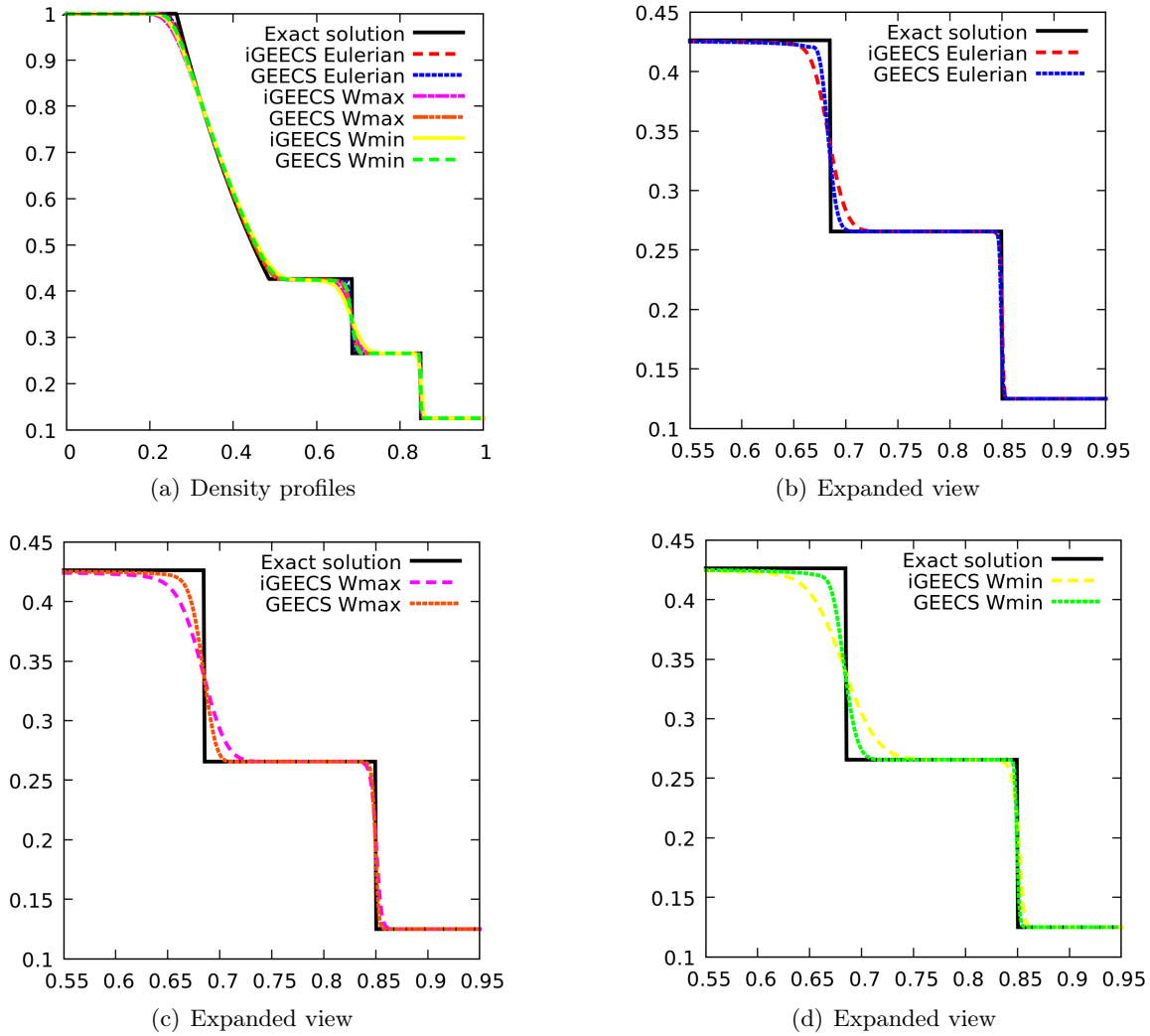

(a) Density profiles

(b) Expanded view

(c) Expanded view

(d) Expanded view

FIGURE 3.4 – Density profiles for one-dimensional Sod's shock tube for both iGEECS and GEECS with three different grid motion strategies : $w = 0$, $= 2.2$, and $= -1.2$ (top left). The two last configurations correspond to supersonic motions relative to the flow where the grid velocity is the highest (respectively lowest) sonic wave across the domain. Expanded view of the density profiles for iGEECS and GEECS with $w = 0$ (top right), $w = 2.2$ (bottom left), and $w = -1.2$ (bottom right). Computations are done with $I = 600$ cells, final time $t = 0.2$, and CFL $= 0.9$.

3.5.3 One-dimensional Sod's shock tube and Sedov's plane blast wave

In order to verify the conservation properties in test cases involving shocks, both Sod's shock tube and Sedov's plane blast wave are performed in one dimension using three grid motions strategies : i) Eulerian grid with fixed nodes or $\boldsymbol{w} = \mathbf{0}$; ii) near-Lagrangian grid or $\boldsymbol{w} = 0.99\boldsymbol{w}^{NL}$

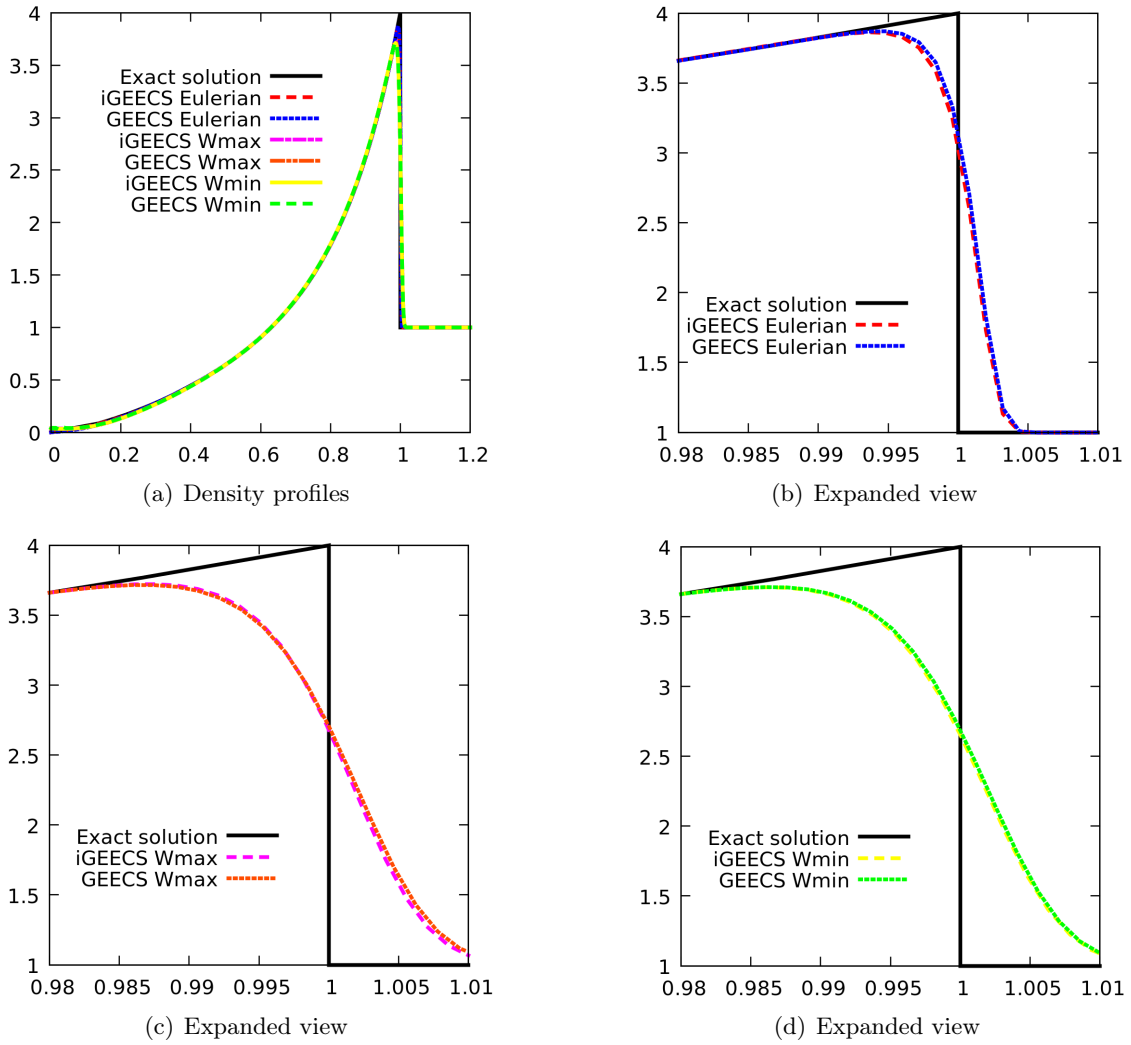

(a) Density profiles

(b) Expanded view

(c) Expanded view

(d) Expanded view

FIGURE 3.5 – Density profiles for one-dimensional Sedov's plane blast wave for both iGEECS and GEECS with three different grid motion strategies : $w = 0$, $= 2$, and $= -2$ (top left). The two last configurations correspond to supersonic motions relative to the flow where the grid velocity is the highest (respectively lowest) sonic wave across the domain. Expanded view of the density profiles for iGEECS and GEECS with $w = 0$ (top right), $w = 2$ (bottom left), and $w = -2$ (bottom right). Computations are done with $I = 600$ cells, final time $t = 1$, and CFL $= 0.9$.

where $\boldsymbol{w}^{NL}$ is the near-Lagrangian grid velocity computed by the scheme (see Appendix .2) ; and iii) half-Lagrangian grid or $\boldsymbol{w} = 0.5\boldsymbol{w}^{NL}$.

These two tests are performed using relatively coarse one-dimensional grids of 200 cells for Sod's and 100 cells for Sedov's. Figure 3.6 displays density profiles (and expanded views) for

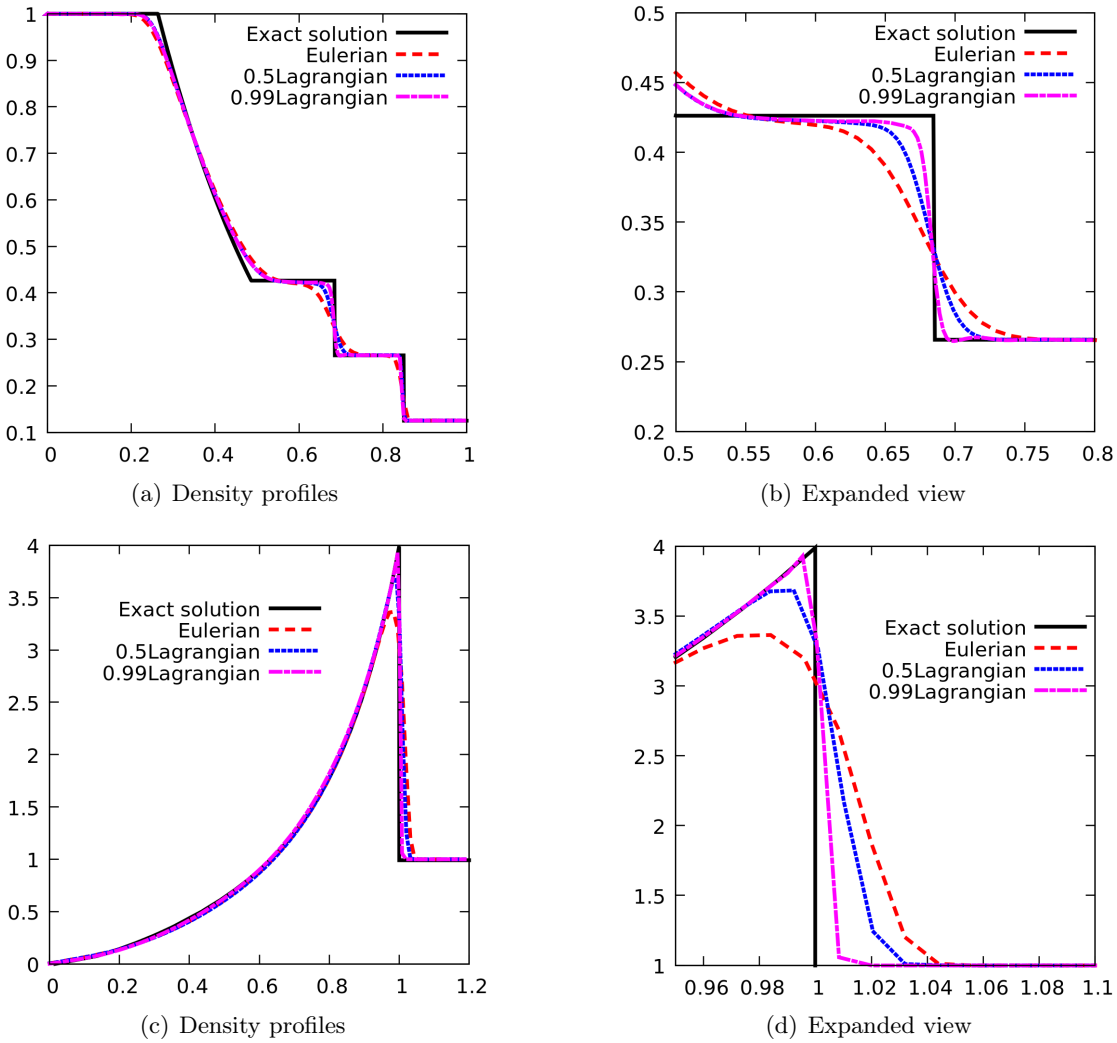

(a) Density profiles

(b) Expanded view

(c) Density profiles

(d) Expanded view

FIGURE 3.6 – Density profiles (left) and expanded view (right) for one-dimensional Sod's shock tube (top) and Sedov's plane blast wave (bottom) for GEECS with three different grid motion strategies : Eulerian with fixed nodes, near-Lagrangian, and half-Lagrangian. Computations are done with 200 cells (top) and 100 cells (bottom), final time $t = 0.2$ (top) and $t = 1$ (bottom), and CFL $= 0.9$.

the plane Sod's shock tube and Sedov's blast wave respectively. All density profiles show a proper capture of the exact solutions for both Sod's shock tube and Sedov's blast wave. As expected, Eulerian results are more diffusive due to the first-order character of transport of conserved quantities. The use of half- and near-Lagrangian grids reduce the amount of numerical diffusion at contact discontinuity and shocks without numerical artefact or oscillation. The three

configurations display an accurate capture of shock levels and shock velocities, confirming the conservative property of the scheme.

3.5.4 Two-dimensional Sod's shock tube

In order to verify the ability of GEECS to handle large grid distortions, two variants of Sod's shock tube [53] performed on sheared grids are proposed in this section. Figures 3.7(a) and 3.7(b) display the density map and profile for Sod's shock tube performed on a two-dimensional sheared grid across the x direction. The initial domain is $[0;1] \times [-0.3;0.6]$ and the (non-uniform) grid velocity is $\boldsymbol{w} = (w_x; w_y) = (5y; 0)$. The grid velocity has maximal and minimal values of $w_x = 3$ at $y = 0.6$ and $w_x = -1.5$ at $y = -0.3$ respectively. Grid motions thus shift progressively the fluid characteristics across the y direction—black lines shown in Figure 3.7(a) represent the Lagrangian μ and supersonic fluid velocities computed by $\mu \pm \sqrt{\gamma P/\rho}$.

Figures 3.7(c) and 3.7(d) display the density map and profile for Sod's shock tube performed on a two-dimensional grid sheared across the y direction. The initial domain is $[0;1] \times [0;0.9]$ and the (non-uniform) grid velocity is $\boldsymbol{w} = (w_x; w_y) = (0; 5x - 2.5)$. With this particular grid motion strategy, the shock is not stationary as the tangential grid velocity is not constant along the x direction and eventually becomes supersonic.

Results of both sheared version of the two-dimensional Sod's shock tube are in good agreement with the exact solution. The three waves of this test—expansion fan, contact discontinuity, and shock of medium strength—are properly captured by GEECS. As expected, the contact discontinuity is smeared in both cases due to the first-order feature of transport of conserved quantities but no numerical artefact is observed.

For Sod's shock tube sheared across the x direction, the impact of mesh shearing is seen in the amount of numerical diffusion at the contact discontinuity. In particular, the near-Lagrangian slice of mesh that evolves exactly at the contact discontinuity speed—around $y = 0.2$—shows minimal numerical diffusion as fluxes of conserved quantities are nearly equal to zero during the flow evolution.

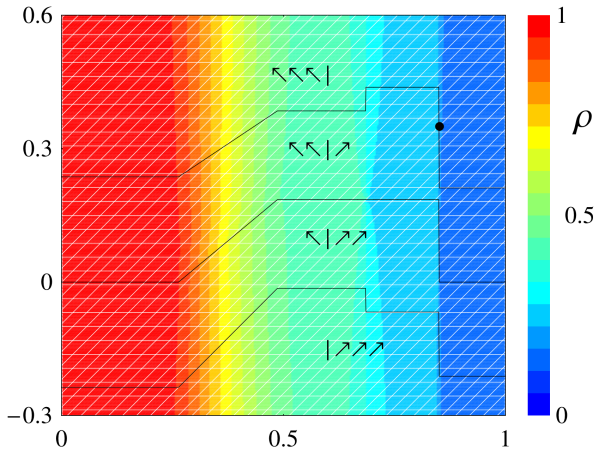

(a) Two-dimensional density map

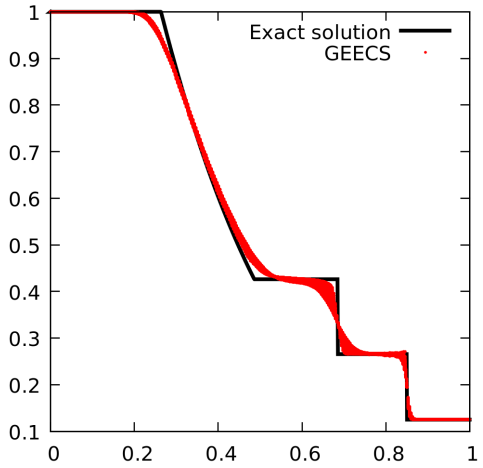

(b) One-dimensional superposition of all points

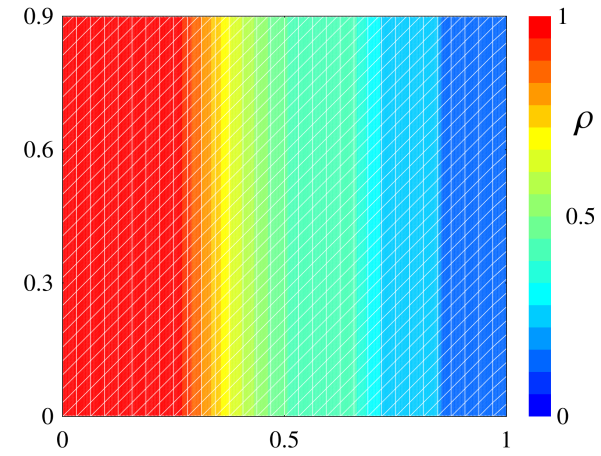

(c) Two-dimensional density map

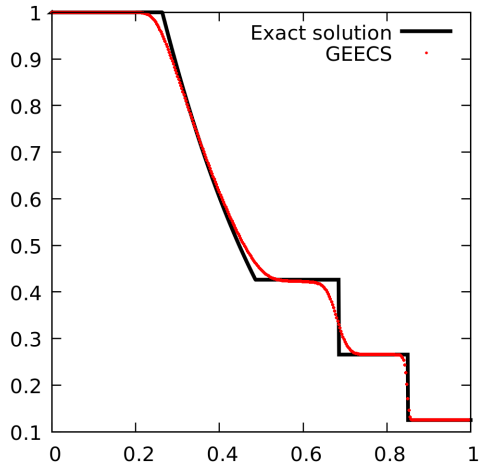

(d) One-dimensional superposition of all points

FIGURE 3.7 – Density maps (left) and profiles (right) for the two-dimensional Sod's shock tube performed on sheared grids across x (top) and y (bottom) directions. Maximums of grid velocity are supersonic relative to the fluid flow. Black lines on the density map (top left) correspond to the Lagrangian fluid velocity μ and supersonic limits $\mu \pm \sqrt{\gamma P/\rho}$. The black dot represents the shock velocity. Computations are done with 320×290 cells, every displayed macro cell (white lines) corresponds to 10×10 numerical cells, final time $t = 0.2$, and CFL $= 0.8$.

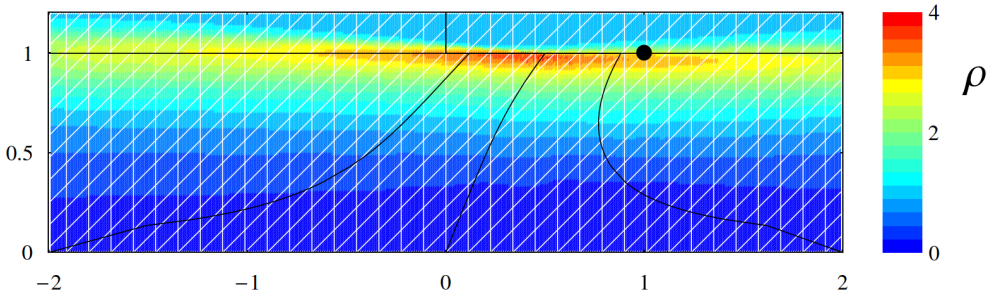

(a) Two-dimensional density map

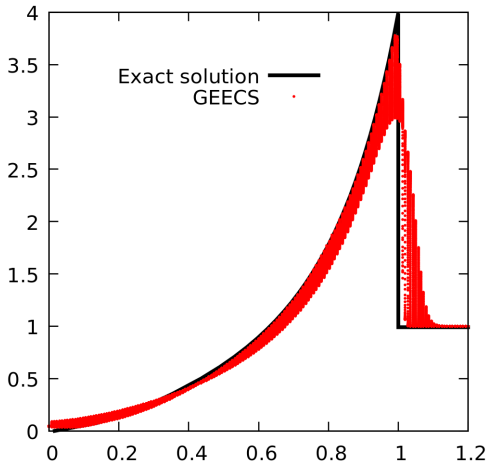

(b) One-dimensional superposition of all points

FIGURE 3.8 – Density maps (top) and profiles (bottom) for the two-dimensional Sedov's plane blast wave performed on sheared grid across the y direction. Black lines on Figure 3.8(a) correspond to the Lagrangian fluid velocity μ and supersonic limits $\mu \pm \sqrt{\gamma P/\rho}$. The black dot represents the shock velocity. Computations are performed with CFL $= 0.8$, final time $t = 1$, and 350×110 cells. Every displayed macro cell (white lines) corresponds to 10×10.

3.5.5 Two-dimensional Sedov's plane blast wave

Two variants of Sedov's plane bast wave performed on sheared and randomly distorted two-dimensional grids are proposed in this section.

Figures 3.8(a) and 3.8(b) display the density map and profile for Sedov's plane blast wave sheared across the x direction. The initial domain is $[-2; 2] \times [0; 1.2]$ and the (non-uniform) grid velocity is given by $\boldsymbol{w} = (w_x; w_y) = (0; x)$. As the shock is stronger in Sedov's blast wave than in

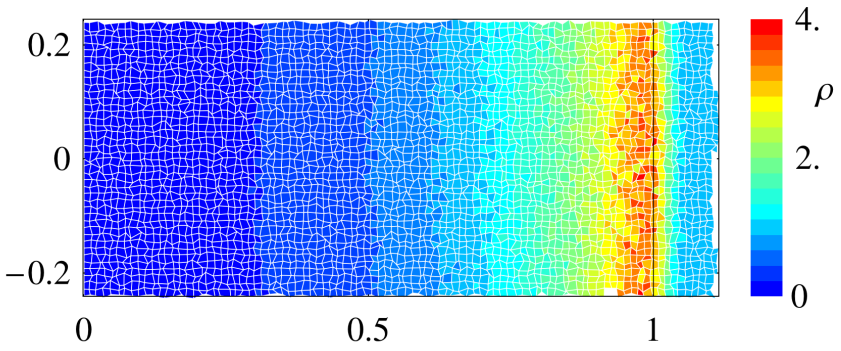

(a) Two-dimensional density map

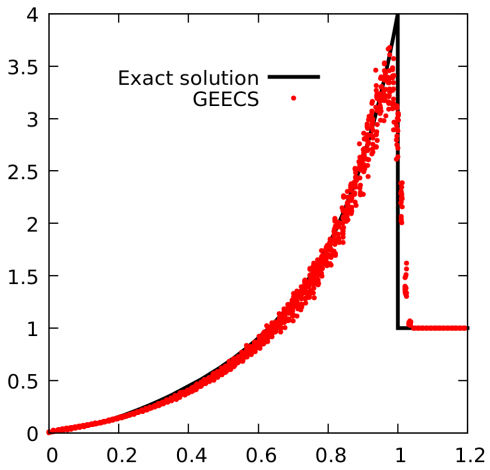

(b) One-dimensional superposition of all points

FIGURE 3.9 – Density maps (top) and profiles (bottom) for the two-dimensional Sedov's plane blast wave performed on randomly distorted grid. Computations are performed with CFL = 0.8, final time $t = 1$, and 100×40 cells. Every displayed macro cell (white lines) corresponds to 1×1 numerical cells (bottom).

Sod's shock tube, this variant tests the ability of the scheme to capture precisely the position of the strong shock despite the distortions of mesh cells and the shifting of characteristics—as for the sheared Sod's shock tube in Section 3.5.4 black lines in Figure 3.8(a) represent the Lagrangian μ and supersonic fluid velocities $\mu \pm \sqrt{\gamma P/\rho}$. The smearing of the results due to grid motions is similar to what is observed in Sod's shock tube sheared across the x direction done in Section 3.5.4.

Figures 3.9(a) and 3.9(b) display the density map and profile for Sedov's plane blast wave performed on dynamically randomly distorted two-dimensional grid. The initial domain $[0; 1.2] \times$

$[-0.24; 0.24]$ is meshed with a uniform coarse Cartesian grid of 100×40 cells which is then dynamically distorted by the grid velocity $\boldsymbol{w} = (w_x, w_y)$ where w_x and w_y are random numbers between ± 0.5. Results are in good agreement with the exact solution of Sedov's blast plane wave. Even with a relatively coarse grid, the shock level and velocity are properly captured. The impact of the distortion of the mesh is only visible on the smearing by numerical diffusion at the shock area but no numerical artefact has been generated.

3.5.6 Sedov's cylindrical blast wave

Figures 3.10(a) and 3.10(b) display the density map and profile for Sedov's cylindrical blast wave on two-dimensional Eulerian fined grid of fixed nodes. Results are fully symmetric and show a good agreement with the exact solution. Even with a large mesh of 240×240 cells, some smearing takes place at the shock area due to the first-order feature of transport of conserved quantities. In order to define a simple ALE grid strategy, close to a Lagrangian tracking, the grid velocity is now chosen to be

$$\boldsymbol{w}_p^{n+1/2} = \eta \; \boldsymbol{w}_p^{\mathrm{NL}} \; , \qquad \text{with} \qquad \eta = (t/t_0)^2 \, / \left(1 + (t/t_0)^2\right) \; , \tag{3.45}$$

where $\boldsymbol{w}_p^{\mathrm{NL}}$ is the near-Lagrangian grid velocity computed by the scheme (computed by mean at nodes of absolute fluid velocities at cells, see Appendix .2), and η is a time increasing factor to produce a smooth Eulerian to Lagrangian transition over the characteristic time t_0. For the present Sedov's blast wave, the Eulerian to Lagrangian transition time is chosen to be $t_0 = 0.1$ so as to reduce the numerical diffusion on the entire computational domain while avoiding critical grid deformations in the first cells of the mesh, especially at early times.

Figures 3.10(c) and 3.10(d) display the density map and profile for the two-dimensional Sedov's cylindrical blast wave performed on near-Lagrangian mesh. Results show an accurate and sharp capture of the shock level and velocity for a relatively small number of mesh cells 40×40 (to be compared to the Eulerian case with 240×240). The radial symmetry of this test is verified on the two-dimensional mesh in Figure 3.10(c). Choosing a grid velocity given by (3.45) ensures that : i) large mesh distortions are avoided at early times ; ii) shock level and shock velocity are

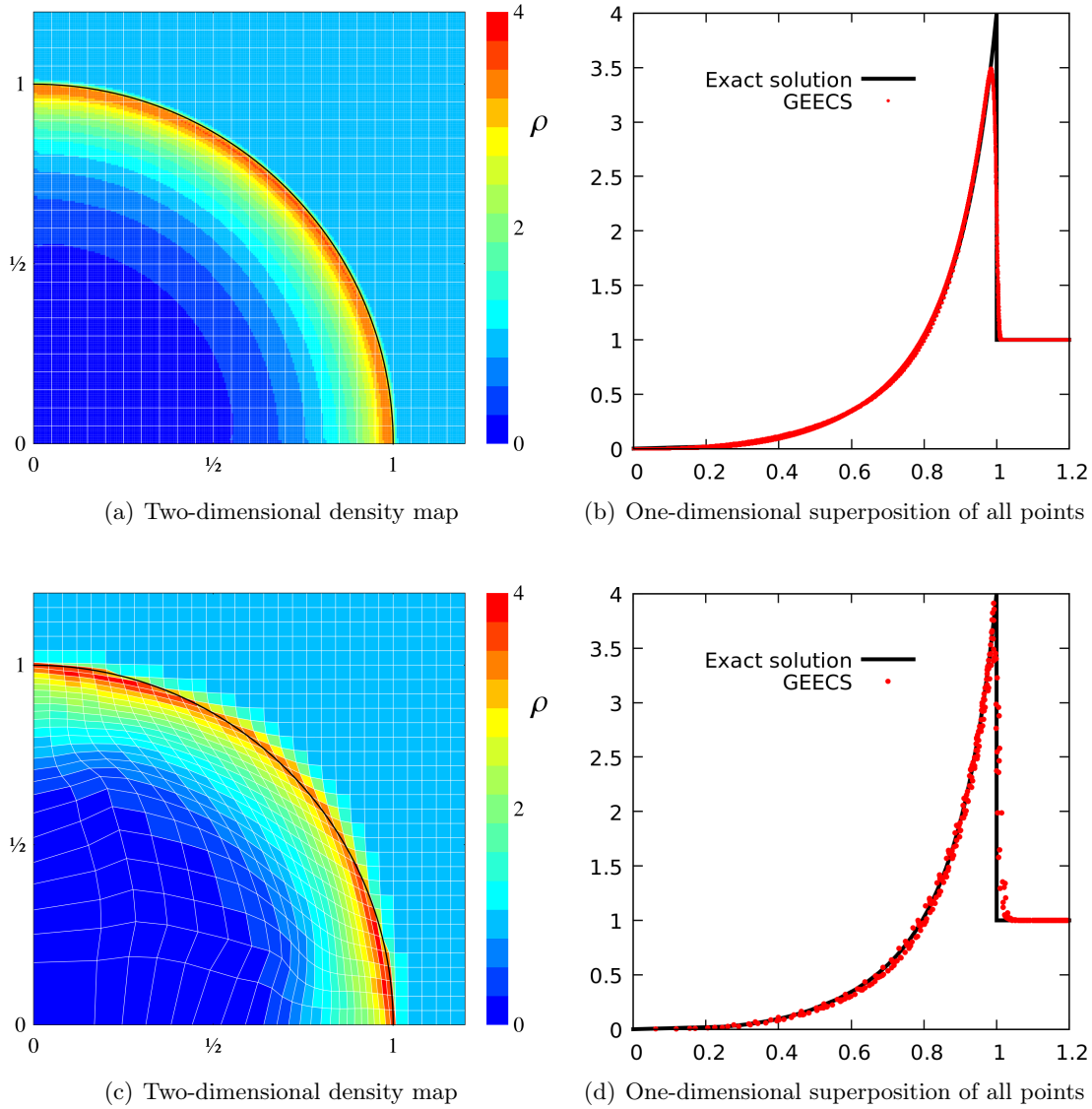

(a) Two-dimensional density map

(b) One-dimensional superposition of all points

(c) Two-dimensional density map

(d) One-dimensional superposition of all points

FIGURE 3.10 – Density maps (left) and profiles (right) for the two-dimensional Sedov's cylindrical blast wave performed on Eulerian (top) and near-Lagrangian (bottom) grids. Computations are done with CFL $= 0.9$, final time $t = 1$, 240×240 cells for the Eulerian case (top), and 40×40 cells for the near-Lagrangian case (bottom). Every displayed macro cell (white lines) corresponds to 10×10 (top) and 1×1 numerical cells (bottom).

accurately captured in a robust way ; and iii) numerical diffusion due to first-order transports is drastically reduced for a smaller number of mesh cells.

3.5.7 Two-dimensional triple point shock tube

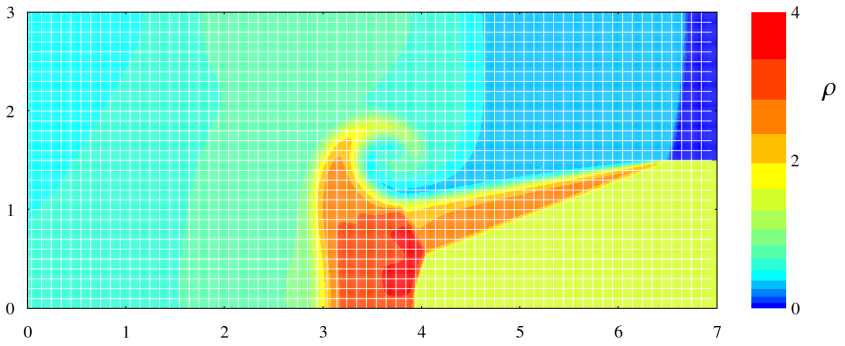

(a) Two-dimensional density map

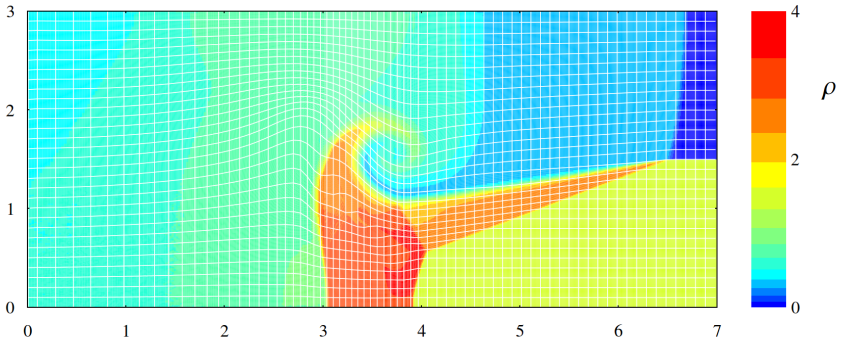

(b) Two-dimensional density map

FIGURE 3.11 – Density maps for the two-dimensional triple point shock tube performed on Eulerian (top) and ALE (bottom) grids. Computations are done with 700×300 cells, final time $t = 3$, and CFL $= 0.9$. Every displayed macro cell (white lines) corresponds to 10×10 numerical cells.

Figure 3.11(a) displays the density map for triple point shock tube performed on two-dimensional Eulerian grid with fixed nodes or $\boldsymbol{w} = \mathbf{0}$. The three different waves in this test are captured but Eulerian results are diffusive due to first-order transport of conserved quantities.

In order to capture the vortex more accurately while avoiding critical mesh tangling, the grid

velocity is now given by : i) in the x direction,

$$w_x^{n+1/2} = \frac{1}{N_y/2} \sum_{N_y/2} w_x^{\mathrm{NL}} \ , \tag{3.46}$$

where $\boldsymbol{w}_p^{\mathrm{NL}}$ corresponds to the near-Lagrangian velocity given by the scheme (see Appendix .2). For each node, it corresponds to the Lagrangian velocity in the x direction, averaged in the y direction over the first half of the domain so as to avoid grid distortions due to vortex effects and to concentrate mesh cells around $x = 3$ at final time ; and ii) in the y direction, near-Lagrangian motions given by (3.45) where the Eulerian to Lagrangian transition time is $t_0 = 1$.

Figure 3.11(b) displays the density map for triple point shock tube performed on the above two-dimensional ALE grid. This moving grid evolves in both x and y directions in order to follow the fluid flow and to obtain less diffusive and more accurate capture of the vortex, shocks, and contact discontinuities of the flow. The purely Lagrangian grid motion could not be used for this test case due to mesh tangling in the vortex area—especially at early times.

This test case shows the ability of GEECS to handle more complex flows with appropriate ALE strategies. For the readers interested on flows dominated by vorticity however, a second-order extension can become necessary but could be obtained from the generic variational GEEC procedure proposed in the present work.

3.5.8 Material interface tracking

In some practical applications, it may be useful to follow contact discontinuities in a Lagrangian way in order to remove numerical diffusion and track accurately the material interfaces. In order to obtain such ALE grid strategy, linearly interpolated meshes are used for both Sod's shock tube and Woodward–Colella's double shock tube. This grid strategy corresponds to completely regularized meshes between material interfaces, as a limit case of geometric regularizing strategies used in indirect ALE solvers.

Figures 3.12(a) and 3.12(b) display the density profiles and an expanded views for Sod's shock tube and Woodward–Colella's double shock tube performed on one-dimensional ALE grids.

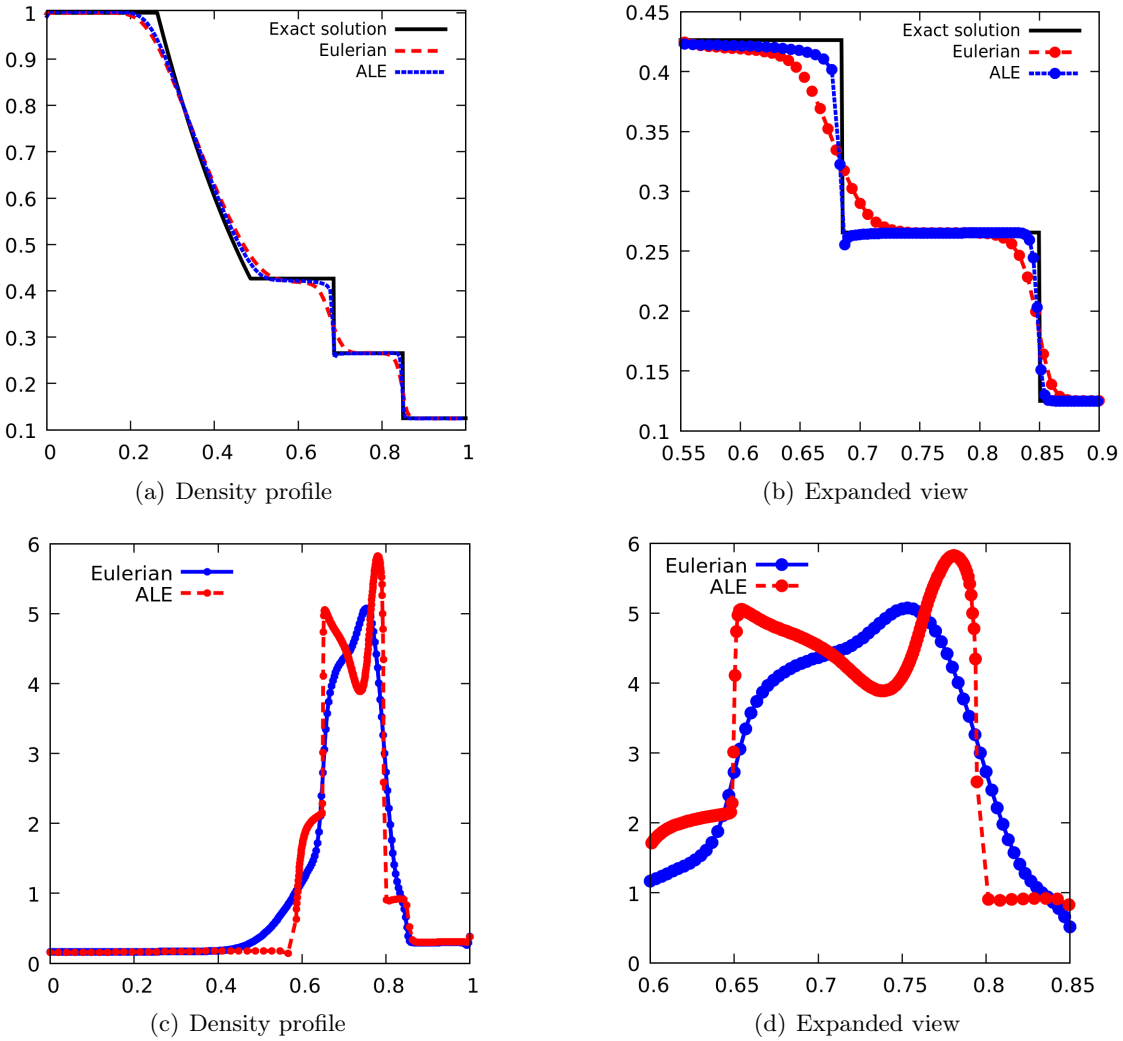

(a) Density profile (b) Expanded view

(c) Density profile (d) Expanded view

FIGURE 3.12 – Density profiles (left) and expanded view (right) for Sod's shock tube (top) and Woodward–Colella's double shock tube (bottom). For these tests, the grid velocity is linearly interpolated from Lagrangian contact discontinuities to fixed Eulerian domain boundaries. Computations are done with 300 cells, final time $t = 0.2$ (top) and $t = 0.038$ (bottom), and CFL $= 0.8$.

In order to almost completely remove the numerical diffusion at the contact discontinuity, the grid velocity is given by the following procedure : i) the node initially at the interface ($x = 0.5$) evolves exactly at the flow speed given by the scheme ; and ii) the velocities of other nodes are computed so as to produce even-spaced meshings over intervals bounded by domain limits and Lagrangian nodes. No disturbances are seen in the entire numerical area and the contact

discontinuity presents almost no numerical diffusion—only two nodes in the contact discontinuity area. A slight undershoot is observed downstream of the discontinuity on the expanded view which is commonly observed with Lagrangian codes [35] and is attributed to wall heating effects.

Figures 3.12(c) and 3.12(d) show that ALE results are less diffusive than Eulerian results for the same number of mesh cells. Both contact discontinuities are accurately captured—only two nodes for each of the discontinuity—without distortion nor oscillation.

General linear interpolation strategies used in this section do not require a priori knowledge of the solution to the flow equation : mesh velocities are computed “on the fly". For tests having exact solutions, the linear interpolation procedure can be modified so that nodes at interfaces evolve exactly at analytical Lagrangian velocities. For Sod's shock tube, the two linear interpolation procedures provide similar results with marginal differences.

3.6 Conclusion

The present work has developed a novel generic GEEC (Geometry, Energy, and Entropy Compatible) procedure for the derivation of physics-compatible numerical scheme ensuring geometric, energetic, and entropic compatibility. This GEEC procedure is addressed over a three-step mimicking derivation : i) a variational least action principle is used in order to ensure the thermodynamic consistency to second-order regardless of mesh motions ; ii) a tally is performed in order to ensure total energy conservation at discrete level (up to round-off errors) ; and iii) an artificial viscosity stress is added in the evolution equations in order to capture shocks and to stabilize the scheme.

As a proof of concept, the GEEC procedure is tested on a novel direct ALE scheme (named GEECS) for the simulation of unsteady and compressible single-fluid flows. The resulting scheme displays the following features : i) both relative and absolute velocities are defined at half time steps and cell centers, while the grid velocity is discretized at half time steps and at nodes ; ii) discrete mass, momentum and internal energy evolution equations are derived without any constraint on structure or spatial dimension—however, all test cases reported in Section 3.5 are restricted to structured meshes of quadrangles in one and two dimensions ; iii) both kinetic and

internal energies are discretized to second-order in both space-and-time, while for simplicity mass and Lagrangian coordinates transports are only discretized to first-order in space and time using a simple upwind scheme ; and iv) an internal energy correction at half time steps is introduced in the internal energy evolution equation—which corresponds to a Strang splitting of the pressure work over half time steps—in order to solve only a linearly implicit evolution equation for the internal energy ;

Space-and-time localisations of thermodynamic variables and velocities—along with the artificial viscosity term—ensure a continuity with the spirit of CEA/DAM purely Lagrangian schemes [42, 64]. The first-order discretization of mass transport may appear inconsistent with the second-order discretization of grid velocity and energies in the Lagrangian limit but it is acceptable as a proof of concept provided that thermodynamic consistency is always at second-order regardless of mesh motions. The second-order extension for the advective part of the scheme can be achieved using the same variational approach but yields more complex schemes. The Strang splitting of the pressure work (see Equation (3.31)) is introduced for both the implicit iGEECS and explicit version of GEECS—although for GEECS this change of variable is not mandatory as the internal energy equation is already fully explicit—in order to obtain a better control of the internal energy transport when the simulated flow involves large and fast—supersonic—advections. The use of a variational principle for the discrete derivation of the momentum evolution equation ensures a rigorous thermodynamic consistency at second-order and leads to a non standard formulation of the pressure gradient—and thus of the pressure work in the internal energy equation.

Finally, results of the isentropic vortex, Sod's shock tube, Sedov's blast wave, Woodward–Colella's double shock tube, and the triple point shock tube are presented in Eulerian, Lagrangian, or ALE formalisms confirming the different built-in properties of the scheme. Expected convergence rates for the advective part of the scheme—second-order in Lagrangian limit and first-order in Eulerian limit—are verified with the isentropic vortex. Thermodynamic consistency to second-order is also verified regardless of mesh motions—even if the advective terms of the scheme are only first-order accurate. Exact conservation of mass, momentum and total energy up to round-off errors is verified and makes the scheme able to capture proper shock levels and shock velocities.

These test cases are also performed using strenuous grid motion in ALE frameworks in order to illustrate the indifference and versatility towards grid displacements. Particularly straining are the sheared test cases of Sod's shock tube and Sedov's blast wave which were introduced in the present work : they involve both supersonic motions and large but regular grid deformations in order to demonstrate the ability of the scheme to handle all configurations of flow characteristics with respect to grid motion, yet with CFL numbers close to one.

GEECS is physics-compatible, simple, and robust. It represents a proof of concept and as such a starting point to apply this novel generic GEEC procedure for the discrete derivation of mimetic schemes describing more complex flows. Extensions to multiphase flows, second-order accuracy for advective terms, and detailed analysis of boundary conditions are planned for later publications.

.1 Notations

n,$n+1/2$	labels of integer and half integer times t^n and $t^{n+1/2}$
$\Delta t^{n+1/2}$	$= t^{n+1} - t^n$, time step $n+1/2$
Δt^n	$= 1/2(\Delta t^{n+1/2} + \Delta t^{n-1/2})$, time step n
c, d	labels of cells
$\mathcal{D}(c)$	set of cell labels neighboring cell c (connected by a common node in one dimension, edge in two dimensions, or face in three dimensions)
$\mathcal{P}(c)$	set of node labels around of cell c
V_c^n	volume of cell c at time t^n
$\boldsymbol{s}_{cd}^n$	outward pointing vector to boundary between cells c and d at time t^n (oriented outwards from c, or from c to d, $\boldsymbol{s}_{cd}^n = -\boldsymbol{s}_{dc}^n$; amplitude given by area of boundary element)
ρ_c^n	mass density in cell c at time t^n
e_c^n	internal energy in cell c at time t^n
$\boldsymbol{w}_p^{n+1/2}$	grid velocity of node p at time $t^{n+1/2}$, externally defined by user
$\boldsymbol{w}_c^{n+1/2}$	$= \sum_{\mathcal{P}(c)} \boldsymbol{w}_p^{n+1/2} / \lvert\mathcal{P}(c)\rvert$, interpolated grid velocity at cell c and time $t^{n+1/2}$
$\boldsymbol{u}_c^{n+1/2}$	relative-to-grid fluid velocity in cell c at time $t^{n+1/2}$
$\boldsymbol{\mu}_c^{n+1/2}$	$= \boldsymbol{u}_c^{n+1/2} + \boldsymbol{w}_c^{n+1/2}$, absolute fluid velocity in cell c at time $t^{n+1/2}$
$\sigma_{cd}^{n+1/2}$	$= \frac{1}{2}\big(1 + \mathrm{sign}(\boldsymbol{s}_{cd}^{n+1/2} \cdot \boldsymbol{u}_c^{n+1/2})\big)$, transport off-centering factor from cell c to cell d at time $t^{n+1/2}$
χ_c^n	Lagrangian coordinate in cell c and time t^n
$\phi_c^{n+1/2}$	Lagrange multiplier of mass transport equation in cell c and time $t^{n+1/2}$
$\lambda_c^{n+1/2}$	Lagrange multiplier of Lagrangian coordinate equation in cell c and time $t^{n+1/2}$

.2 Near-Lagrangian grid velocity

As relative-to-grid $\boldsymbol{u}$, and absolute fluid $\boldsymbol{\mu}$ velocities are not discretized over identical space cells, an interpolation procedure must be applied in order to compute a near-Lagrangian grid velocity (as close as posible to the theoritical Lagrangian fluid velocity).

The simplest interpolation procedure consists in taking the arithmetic average of the absolute velocity in the neighboring cells c for each node p at the same time

$$\boldsymbol{w}_p^{n+1/2} = \sum_{\mathcal{D}(c)} \boldsymbol{\mu}_c^{n+1/2} / |\mathcal{P}(c)| \ , \tag{47}$$

where $\boldsymbol{\mu}_c^{n+1/2}$ is the absolute fluid velocity given by the scheme. This rudimentary interpolation has been tested on the two-dimensional Sedov's blast wave, giving accurate but still diffusive results.

Another more consistent near-Lagrangian grid motion can be obtained by minimizing the mean square of mass fluxes at each of the neighboring cell-edges (c,d) of each node p of the mesh

$$\boldsymbol{w}_p^{n+1/2} = \min \sum_{c,d\in(p)} \left(\rho_c^n \boldsymbol{s}_{cd}^{n+1/2} \cdot \left(\boldsymbol{\mu}_c^{n+1/2} - \boldsymbol{w}_p^{n+1/2} \right) \right)^2 \ , \tag{48}$$

where $\boldsymbol{\mu}_c^{n+1/2}$ is the absolute fluid velocity given by the scheme.

The minimization of (48) leads to

$$\sum_{c,d\in(p)} (\rho_c^n)^2 \boldsymbol{s}_{cd}^{n+1/2} \otimes \boldsymbol{s}_{cd}^{n+1/2} \cdot \left(\boldsymbol{\mu}_c^{n+1/2} - \boldsymbol{w}_p^{n+1/2} \right) = 0 \ , \tag{49}$$

which can be solved as

$$\boldsymbol{w}_p^{\mathrm{NL}} = \boldsymbol{w}_p^{n+1/2} = \left(\sum_{c,d\in(p)} (\rho_c^n)^2 \left(\boldsymbol{s}_{cd}^{n+1/2} \otimes \boldsymbol{s}_{cd}^{n+1/2} \right) \right)^{-1} \cdot \sum_{c,d\in(p)} (\rho_c^n)^2 \left(\boldsymbol{s}_{cd}^{n+1/2} \otimes \boldsymbol{s}_{cd}^{n+1/2} \right) \cdot \boldsymbol{\mu}_c^{n+1/2} \ . \tag{50}$$

.3 Discrete derivation of variational absolute velocity and momentum equations

Following a similar path as the continuous Eulerian derivation (see Section 3.3.1), the absolute velocity and momentum equations can be derived in the discrete case from the discrete Euler–

Lagrange equations

$$V_c^{n+1}\rho_c^{n+1} - V_c^n\rho_c^n + \Delta t^{n+1/2}\sum_{d\in\mathcal{D}(c)}\left(\dot{V}_{cd}^{n+1/2}\rho_c^{n+1} - \dot{V}_{dc}^{n+1/2}\rho_d^{n+1}\right) = 0\ , \tag{51a}$$

$$V_c^{n+1}\rho_c^{n+1}\chi_c^{n+1} - V_c^n\rho_c^n\chi_c^n + \Delta t^{n+1/2}\sum_{d\in\mathcal{D}(c)}\left(\dot{V}_{cd}^{n+1/2}\rho_c^{n+1}\chi_c^{n+1} - \dot{V}_{dc}^{n+1/2}\rho_d^{n+1}\chi_d^{n+1}\right) = 0\ , \tag{51b}$$

$$V_c^n\boldsymbol{\mu}_c^{n-1/2} = \sum_{d\in\mathcal{D}(c)}[\sigma\boldsymbol{s}]_{cd}^{n-1/2}\left(\phi_d^{n-1/2} - \phi_c^{n-1/2}\right) + \chi_c^n\sum_{d\in\mathcal{D}(c)}[\sigma\boldsymbol{s}]_{cd}^{n-1/2}\left(\lambda_d^{n-1/2} - \lambda_c^{n-1/2}\right)\ , \tag{51c}$$

$$\begin{aligned} V_c^n\left(\phi_c^{n+1/2} - \phi_c^{n-1/2}\right) &= \tfrac{1}{2}\Delta t^{n-1/2}V_c^n\left(\boldsymbol{\mu}_c^{n-1/2}\right)^2 - \Delta t^n V_c^n\left(e_c^n + P_c^n/\rho_c^n\right) \\ &+ V_c^n\chi_c^n\left(\lambda_c^{n-1/2} - \lambda_c^{n+1/2}\right) - \Delta t^{n-1/2}\sum_{d\in\mathcal{D}(c)}\dot{V}_{cd}^{n-1/2}\left(\phi_d^{n-1/2} - \phi_c^{n-1/2}\right) \\ &- \Delta t^{n-1/2}\chi_c^n\sum_{d\in\mathcal{D}(c)}\dot{V}_{cd}^{n-1/2}\left(\lambda_d^{n-1/2} - \lambda_c^{n-1/2}\right)\ , \end{aligned} \tag{51d}$$

$$V_c^n\left(\lambda_c^{n+1/2} - \lambda_c^{n-1/2}\right) + \Delta t^{n-1/2}\sum_{d\in\mathcal{D}(c)}\dot{V}_{cd}^{n-1/2}\left(\lambda_d^{n-1/2} - \lambda_c^{n-1/2}\right) = 0\ . \tag{51e}$$

.3.1 Absolute velocity equation

The evolution in time of the absolute velocity is obtained from the combination $(51c)^{n+1/2} - (51c)^{n-1/2}$ yielding

$$\begin{aligned}\boldsymbol{\mu}_c^{n+1/2} - \boldsymbol{\mu}_c^{n-1/2} = &\sum_{d\in\mathcal{D}(c)} \frac{[\sigma \boldsymbol{s}]_{cd}^{n-1/2}}{V_c^n}\left(\phi_d^{n+1/2} - \phi_d^{n-1/2} - \phi_c^{n+1/2} + \phi_c^{n-1/2}\right) \\ &+ (\chi_c^{n+1} - \chi_c^n) \sum_{d\in\mathcal{D}(c)} \frac{[\sigma \boldsymbol{s}]_{cd}^{n+1/2}}{V_c^{n+1}}\left(\lambda_d^{n+1/2} - \lambda_c^{n+1/2}\right) \\ &+ \chi_c^n \sum_{d\in\mathcal{D}(c)} \frac{[\sigma \boldsymbol{s}]_{cd}^{n-1/2}}{V_c^n}\left(\lambda_d^{n+1/2} - \lambda_d^{n-1/2} - \lambda_c^{n+1/2} + \lambda_c^{n-1/2}\right) \\ &+ \sum_{d\in\mathcal{D}(c)} \left(\frac{[\sigma \boldsymbol{s}]_{cd}^{n+1/2}}{V_c^{n+1}} - \frac{[\sigma \boldsymbol{s}]_{cd}^{n-1/2}}{V_c^n}\right)\left(\phi_d^{n+1/2} - \phi_c^{n+1/2} + \chi_c^n\left(\lambda_d^{n+1/2} - \lambda_c^{n+1/2}\right)\right) . \quad (52)\end{aligned}$$

In a similar way, combining (51e) and (51d) leads to

$$\begin{aligned}\phi_c^{n+1/2} - \phi_c^{n-1/2} = &\tfrac{1}{2}\Delta t^{n-1/2}\left(\boldsymbol{\mu}_c^{n-1/2}\right)^2 - \Delta t^n\left(e_c^n + P_c^n/\rho_c^n\right) \\ &- \Delta t^{n-1/2} \sum_{d\in\mathcal{D}(c)} \frac{\dot{V}_{cd}^{n-1/2}}{V_c^n}\left(\phi_d^{n-1/2} - \phi_c^{n-1/2}\right) . \quad (53)\end{aligned}$$

Inserting $(53)_d - (53)_c$ into (52) leads to

$$\begin{aligned}
\boldsymbol{\mu}_c^{n+1/2} - \boldsymbol{\mu}_c^{n-1/2} = &-\Delta t^n \sum_{d\in\mathcal{D}(c)} \frac{[\sigma \boldsymbol{s}]_{cd}^{n-1/2}}{V_c^n} \left(e_d^n - e_c^n + P_d^n/\rho_d^n - P_c^n/\rho_c^n\right) \\
&+ \tfrac{1}{2}\Delta t^{n-1/2} \sum_{d\in\mathcal{D}(c)} \frac{[\sigma \boldsymbol{s}]_{cd}^{n-1/2}}{V_c^n} \left(\left(\boldsymbol{\mu}_d^{n-1/2}\right)^2 - \left(\boldsymbol{\mu}_c^{n-1/2}\right)^2\right) \\
-\Delta t^{n-1/2} \sum_{d\in\mathcal{D}(c)} \frac{[\sigma \boldsymbol{s}]_{cd}^{n-1/2}}{V_c^n} &\left(\sum_{d'\in\mathcal{D}(d)} \frac{\dot{V}_{dd'}^{n-1/2}}{V_d^n} \left(\phi_{d'}^{n-1/2} - \phi_d^{n-1/2}\right) - \sum_{d\in\mathcal{D}(c)} \frac{\dot{V}_{cd}^{n-1/2}}{V_c^n} \left(\phi_d^{n-1/2} - \phi_c^{n-1/2}\right)\right) \\
&+ \left(\chi_c^{n+1} - \chi_c^n\right) \sum_{d\in\mathcal{D}(c)} \frac{[\sigma \boldsymbol{s}]_{cd}^{n+1/2}}{V_c^{n+1}} \left(\lambda_d^{n+1/2} - \lambda_c^{n+1/2}\right) \\
&+ \chi_c^n \sum_{d\in\mathcal{D}(c)} \frac{[\sigma \boldsymbol{s}]_{cd}^{n-1/2}}{V_c^n} \left(\lambda_d^{n+1/2} - \lambda_d^{n-1/2} - \lambda_c^{n+1/2} + \lambda_c^{n-1/2}\right) \\
&+ \sum_{d\in\mathcal{D}(c)} \left(\frac{[\sigma \boldsymbol{s}]_{cd}^{n+1/2}}{V_c^{n+1}} - \frac{[\sigma \boldsymbol{s}]_{cd}^{n-1/2}}{V_c^n}\right) \left(\phi_d^{n+1/2} - \phi_c^{n+1/2} + \chi_c^n \left(\lambda_d^{n+1/2} - \lambda_c^{n+1/2}\right)\right) . \quad (54)
\end{aligned}$$

Substituting $\left(\lambda_d^{n+1/2} - \lambda_d^{n-1/2} - \lambda_c^{n+1/2} + \lambda_c^{n-1/2}\right)$ from $(51e)_d - (51e)_c$ into (54) leads to

$$\begin{aligned}
\boldsymbol{\mu}_c^{n+1/2} - \boldsymbol{\mu}_c^{n-1/2} = &-\Delta t^n \sum_{d\in\mathcal{D}(c)} \frac{[\sigma \boldsymbol{s}]_{cd}^{n-1/2}}{V_c^n} \left(e_d^n - e_c^n + P_d^n/\rho_d^n - P_c^n/\rho_c^n\right) \\
&+ \tfrac{1}{2}\Delta t^{n-1/2} \sum_{d\in\mathcal{D}(c)} \frac{[\sigma \boldsymbol{s}]_{cd}^{n-1/2}}{V_c^n} \left(\left(\boldsymbol{\mu}_d^{n-1/2}\right)^2 - \left(\boldsymbol{\mu}_c^{n-1/2}\right)^2\right) \\
-\Delta t^{n-1/2} \sum_{d\in\mathcal{D}(c)} \frac{[\sigma \boldsymbol{s}]_{cd}^{n-1/2}}{V_c^n} &\left(\sum_{d'\in\mathcal{D}(d)} \frac{\dot{V}_{dd'}^{n-1/2}}{V_d^n} \left(\phi_{d'}^{n-1/2} - \phi_d^{n-1/2}\right) - \sum_{d\in\mathcal{D}(c)} \frac{\dot{V}_{cd}^{n-1/2}}{V_c^n} \left(\phi_d^{n-1/2} - \phi_c^{n-1/2}\right)\right) \\
-\Delta t^{n-1/2}\chi_c^n \sum_{d\in\mathcal{D}(c)} \frac{[\sigma \boldsymbol{s}]_{cd}^{n-1/2}}{V_c^n} &\left(\sum_{d'\in\mathcal{D}(d)} \frac{\dot{V}_{dd'}^{n-1/2}}{V_d^n} \left(\lambda_{d'}^{n-1/2} - \lambda_d^{n-1/2}\right) - \sum_{d\in\mathcal{D}(c)} \frac{\dot{V}_{cd}^{n-1/2}}{V_c^n} \left(\lambda_d^{n-1/2} - \lambda_c^{n-1/2}\right)\right) \\
&+ \left(\chi_c^{n+1} - \chi_c^n\right) \sum_{d\in\mathcal{D}(c)} \frac{[\sigma \boldsymbol{s}]_{cd}^{n+1/2}}{V_c^{n+1}} \left(\lambda_d^{n+1/2} - \lambda_c^{n+1/2}\right) \\
&+ \sum_{d\in\mathcal{D}(c)} \left(\frac{[\sigma \boldsymbol{s}]_{cd}^{n+1/2}}{V_c^{n+1}} - \frac{[\sigma \boldsymbol{s}]_{cd}^{n-1/2}}{V_c^n}\right) \left(\phi_d^{n+1/2} - \phi_c^{n+1/2} + \chi_c^n \left(\lambda_d^{n+1/2} - \lambda_c^{n+1/2}\right)\right) . \quad (55)
\end{aligned}$$

Inserting $(51c)_c$ and $(51c)_d$ into the third and fourth terms of (55) gives

$$\begin{aligned}
\boldsymbol{\mu}_c^{n+1/2} - \boldsymbol{\mu}_c^{n-1/2} = &-\Delta t^n \sum_{d\in\mathcal{D}(c)} \frac{[\sigma \boldsymbol{s}]_{cd}^{n-1/2}}{V_c^n} \left(e_d^n - e_c^n + P_d^n/\rho_d^n - P_c^n/\rho_c^n\right) \\
&+ \tfrac{1}{2}\Delta t^{n-1/2} \sum_{d\in\mathcal{D}(c)} \frac{[\sigma \boldsymbol{s}]_{cd}^{n-1/2}}{V_c^n} \left(\left(\boldsymbol{\mu}_d^{n-1/2}\right)^2 - \left(\boldsymbol{\mu}_c^{n-1/2}\right)^2\right) \\
&+ \Delta t^{n-1/2} \sum_{d\in\mathcal{D}(c)} \frac{[\sigma \boldsymbol{s}]_{cd}^{n-1/2} \cdot \boldsymbol{u}_c^{n-1/2}}{V_c^n} \boldsymbol{\mu}_c^{n-1/2} - \frac{[\sigma \boldsymbol{s}]_{cd}^{n-1/2} \cdot \boldsymbol{u}_d^{n-1/2}}{V_c^n} \boldsymbol{\mu}_d^{n-1/2} \\
&- \Delta t^{n-1/2} \sum_{d\in\mathcal{D}(c)} (\chi_c^n - \chi_d^n) \frac{[\sigma \boldsymbol{s}]_{cd}^{n-1/2}}{V_c^n} \cdot \frac{\boldsymbol{u}_d^{n-1/2}}{V_d^n} \sum_{d'\in\mathcal{D}(d)} [\sigma \boldsymbol{s}]_{dd'}^{n-1/2} (\lambda_{d'}^{n-1/2} - \lambda_d^{n-1/2}) \\
&+ \left(\chi_c^{n+1} - \chi_c^n\right) \sum_{d\in\mathcal{D}(c)} \frac{[\sigma \boldsymbol{s}]_{cd}^{n+1/2}}{V_c^{n+1}} \left(\lambda_d^{n+1/2} - \lambda_c^{n+1/2}\right) \\
&+ \sum_{d\in\mathcal{D}(c)} \left(\frac{[\sigma \boldsymbol{s}]_{cd}^{n+1/2}}{V_c^{n+1}} - \frac{[\sigma \boldsymbol{s}]_{cd}^{n-1/2}}{V_c^n}\right) \left(\phi_d^{n+1/2} - \phi_c^{n+1/2} + \chi_c^n \left(\lambda_d^{n+1/2} - \lambda_c^{n+1/2}\right)\right) . \quad (56)
\end{aligned}$$

Making algebraic manipulations and development of $\chi_c^{n+1} - \chi_c^n$ using (51a) and (51b) eventually provides the discrete absolute velocity equation

$$\begin{aligned}
\boldsymbol{\mu}_c^{n+1/2} - \boldsymbol{\mu}_c^{n-1/2} = &-\Delta t^n \sum_{d\in\mathcal{D}(c)} \frac{[\sigma \boldsymbol{s}]_{cd}^{n-1/2}}{V_c^n} \left(e_d^n - e_c^n + P_d^n/\rho_d^n - P_c^n/\rho_c^n\right) \\
&- \tfrac{1}{2}\Delta t^{n-1/2} \sum_{d\in\mathcal{D}(c)} \frac{[\sigma \boldsymbol{s}]_{cd}^{n-1/2}}{V_c^n} \left(\left(\boldsymbol{u}_d^{n-1/2}\right)^2 - \left(\boldsymbol{u}_c^{n-1/2}\right)^2 - \left(\boldsymbol{w}_d^{n-1/2}\right)^2 + \left(\boldsymbol{w}_c^{n-1/2}\right)^2\right) \\
&- \Delta t^{n-1/2} \sum_{d\in\mathcal{D}(c)} (\chi_c^n - \chi_d^n) \frac{[\sigma \boldsymbol{s}]_{cd}^{n-1/2}}{V_c^n} \cdot \frac{\boldsymbol{u}_d^{n-1/2}}{V_d^n} \sum_{d'\in\mathcal{D}(d)} [\sigma \boldsymbol{s}]_{dd'}^{n-1/2} \left(\lambda_{d'}^{n-1/2} - \lambda_d^{n-1/2}\right) \\
&+ \Delta t^{n+1/2} \sum_{d\in\mathcal{D}(c)} \left(\chi_c^{n+1} - \chi_d^{n+1}\right) \frac{[\sigma \boldsymbol{s}]_{dc}^{n+1/2}}{\rho_c^n V_c^n} \cdot \frac{\boldsymbol{u}_d^{n+1/2} \rho_d^{n+1}}{V_c^{n+1}} \sum_{d'\in\mathcal{D}(d)} [\sigma \boldsymbol{s}]_{dd'}^{n+1/2} \left(\lambda_{d'}^{n+1/2} - \lambda_d^{n+1/2}\right) \\
&+ \sum_{d\in\mathcal{D}(c)} \left(\frac{[\sigma \boldsymbol{s}]_{cd}^{n+1/2}}{V_c^{n+1}} - \frac{[\sigma \boldsymbol{s}]_{cd}^{n-1/2}}{V_c^n}\right) \left(\phi_d^{n+1/2} - \phi_c^{n+1/2} + \chi_c^n \left(\lambda_d^{n+1/2} - \lambda_c^{n+1/2}\right)\right) . \quad (57)
\end{aligned}$$

.3.2 Momentum equation

As in the continuous derivation Section 3.3.1, the momentum conservation equation is obtained from the following combination (51a) $\times\ \boldsymbol{\mu}_c^{n+1/2} +$ (57) $\times\ \rho_c^n V_c^n$ thus yielding

$$
\begin{aligned}
V_c^{n+1}\rho_c^{n+1}\boldsymbol{\mu}_c^{n+1/2} - V_c^n\rho_c^n\boldsymbol{\mu}_c^{n-1/2} = &-\Delta t^n \rho_c^n \sum_{d\in\mathcal{D}(c)} [\sigma \boldsymbol{s}]_{cd}^{n-1/2} \left(e_d^n - e_c^n + P_d^n/\rho_d^n - P_c^n/\rho_c^n\right) \\
&- \Delta t^{n+1/2}\boldsymbol{\mu}_c^{n+1/2} \sum_{d\in\mathcal{D}(c)} \left(\dot{V}_{cd}^{n+1/2}\rho_c^{n+1} - \dot{V}_{dc}^{n+1/2}\rho_d^{n+1}\right) \\
&- \tfrac{1}{2}\rho_c^n \Delta t^{n-1/2} \sum_{d\in\mathcal{D}(c)} [\sigma \boldsymbol{s}]_{cd}^{n-1/2} \left(\left(\boldsymbol{u}_d^{n-1/2}\right)^2 - \left(\boldsymbol{u}_c^{n-1/2}\right)^2 - \left(\boldsymbol{w}_d^{n-1/2}\right)^2 + \left(\boldsymbol{w}_c^{n-1/2}\right)^2\right) \\
&- \Delta t^{n-1/2}\rho_c^n \sum_{d\in\mathcal{D}(c)} [\sigma \boldsymbol{s}]_{cd}^{n-1/2} \left(\chi_c^n - \chi_d^n\right) \frac{\boldsymbol{u}_d^{n-1/2}}{V_d^n} \sum_{d'\in\mathcal{D}(d)} [\sigma \boldsymbol{s}]_{dd'}^{n-1/2} \left(\lambda_{d'}^{n-1/2} - \lambda_d^{n-1/2}\right) \\
&+ \Delta t^{n+1/2} \sum_{d\in\mathcal{D}(c)} [\sigma \boldsymbol{s}]_{dc}^{n+1/2} \left(\chi_c^{n+1} - \chi_d^{n+1}\right) \frac{\boldsymbol{u}_d^{n+1/2}\rho_d^{n+1}}{V_c^{n+1}} \sum_{d'\in\mathcal{D}(d)} [\sigma \boldsymbol{s}]_{dd'}^{n+1/2} \left(\lambda_{d'}^{n+1/2} - \lambda_d^{n+1/2}\right) \\
&+ \rho_c^n V_c^n \sum_{d\in\mathcal{D}(c)} \left(\frac{[\sigma \boldsymbol{s}]_{cd}^{n+1/2}}{V_c^{n+1}} - \frac{[\sigma \boldsymbol{s}]_{cd}^{n-1/2}}{V_c^n}\right) \left(\phi_d^{n+1/2} - \phi_c^{n+1/2} + \chi_c^n \left(\lambda_d^{n+1/2} - \lambda_c^{n+1/2}\right)\right) . \quad (58)
\end{aligned}
$$

The momentum evolution equation (58) is not fully conservative due to both pressure gradient and momentum transport terms and requires further corrections (see Section 3.3.3).

Bibliographie

[1] C.E. Anderson, An overview of the theory of hydrocodes History and application of hydrocodes in hypervelocity impact, Internat. J. Impact Engrg., 5 (1987), 33-59.

[2] D.J. Benson, Computational methods in Lagrangian and Eulerian hydrocodes, Comput. Methods Appl. Mech. Engrg., 99 (1992), 235-394.

[3] W. Boscheri, M. Dumbser, A direct Arbitrary-Lagrangian-Eulerian ADER-WENO finite volume scheme on unstructured tetrahedral meshes for conservative and non-conservative hyperbolic systems in 3D, J. Comput. Phys., 275 (2014), 484-523.

[4] J. Breil, S. Galera, P.H. Maire, A two dimensional VOF interface reconstruction in a multi-material cell-centered ALE scheme, Int. J. Numer. Meth. Fluids, 65 (2011), 1351-1364.

[5] T.J. Bridges, S. Reich, Numerical methods for Hamiltonian PDEs, J. Phys. A : Math. Gen., 39 (2006), 5287-5326.

[6] K.G. Budge, J.S. Peery, RHALE : a MMALE shock physics code written in C++, Internat. J. Impact Engrg., 14 (1993), 107-120.

[7] D.E. Burton, Exact conservation of energy and momentum in staggered-grid hydrodynamics with arbitrary connectivity, Lect. Notes Phys., 395, 1991.

[8] N.M. Chhay, A. Hamdouni, Lie symmetry preservation by finite difference schemes for the Burgers equation, Symmetry, 2 (2010), 868-883.

[9] P.H. Cournede, Un schéma bi-Lagrange plus projection pour la simulation bifluide des instabilités de mélanges, PhD dissertation École Centrale Paris, 2001.

[10] C.J. Cotter, D.D. Holm, P.E. Hydon, Multisymplectic formulation of fluid dynamics using the inverse map, Proc. R. Soc. A., 463 (2007), 2671-2687.

[11] Q. Duan, X. Li, An ALE based iterative CBS algorithm for non-isothermal non-Newtonian flow with adaptative coupled finite element and meshfree method, Comput. Methods Appl. Mech. Engrg., 196 (2007), 4911-4933.

[12] V. Daru, P. Le Quéré, M.C. Duluc, O. Le Maître, A numerical method for the simulation of low Mach number liquid–gas flows, J. Comput. Phys., 229 (2010), 8844-8867.

[13] R. DeBar, Fundamentals of KRAKEN code, LLNL report, 1974.

[14] C. Eckart, Phys. Rev., 54 (1938).

[15] E.P. Fahrenthold, J.C. Koo, Discrete Hamilton's equations for viscous compressible fluid dynamics, Comput. Methods Appl. Mech.Engrg, 178 (1999), 1-22.

[16] D.P. Flanagan, T. Belytschko, A uniform strain hexahedron and quadrilateral with orthogonal hourglass control, Int. J. Numer. Meth. Eng., 17 (1981), 679-706.

[17] Z. Ge, J.E. Marsden, Lie–Poisson integrators and Lie–Poisson Hamilton–Jacobi theory, Phys. Lett. A., 133 (1988), 134-139.

[18] J.F. Gerbeau, T. Lelievre, Generalized navier boundary condition and geometric conservation lawfor surface tension, Comput. Methods Appl. Mech. Engrg., 198 (2009), 644-656.

[19] S.K. Godunov, Finite difference method for numerical computation of discontinuous solutions of the equations of fluid dynamics, Matematicheskii Sbornik, 47 (1959), 271-306.

[20] H. Goldstein, C. Poole, J. Safko, Classical mechanics, Addison–Wesley, 2002.

[21] E. Hairer, C. Lubich, G. Wanner, Geometrical integration illustrated by the Stormer/Verlet method, Acta Numer., 12 (2003), 399-450.

[22] J.W. Herivel, The derivation of the equations of motion of an ideal flow by Hamilton principle, Proc. Camb. Phil. Soc., 51 (1955).

[23] C.W. Hirt, A.A. Amsden, J.L. Cook, An Arbitrary Lagrangian–Eulerian Computing Method for All Flow Speeds, J. Comput. Phys., 135 (1974), 203-216.

[24] J. Comput. Phys., 257 Part B (2014).

[25] W.E. Johnson, C.E. Anderson, History and application of hydrocodes in hypervelocity impact, Internat. J. Impact Engrg., 5 (1987), 423-439.

[26] J.V. Jose, E.J. Saletan, Classical dynamics : a contemporary approach, Cambridge University Press, 1998.

[27] J.R. Kamm, Evaluation of the Sedov-von Neumann-Taylor blast wave solution, LANL, Report LA-UR-00-6055, (2000).

[28] J.R. Kamm, F.X. Timmes, On efficient generation of numerically robust Sedov solutions, LANL, Report LA-UR-07-2849 (2007).

[29] J.C. Koo, E.P. Fahrenthold, Discrete Hamilton's equations for Arbitrary Lagrangian–Eulerian dynamics of viscous compressible flow, Comput. Methods Appl. Mech.Engrg, 189 (2000), 875-900.

[30] M. Kucharik, M. Shashkov, Conservative multi-material remap for staggered multi-material Arbitrary Lagrangian–Eulerian methods, J. Comput. Phys., 258 (2014), 268-304.

[31] R. Landshoff, A numerical method for treating fluid flow in the presence of shocks, LANL Report LA-1930, (1955).

[32] A. Lew, J.E. Marsden, M. Ortiz, M. West, An overview of variational integrators, Finite elements methods : 1970's and beyond, Theory and Engineering Applications of Computational Methods, CIMNE Spain, 2003.

[33] C.C. Lin, Hydrodynamics of liquid Helium II, Phys. Rev. Lett., 2 (1959), 245-246.

[34] W.K. Liu, J.S. Chen, T., Belytschko, Y.F. Zhang, Adaptative ALE finite elements with particular reference to external work rate on frictional interface, Comput. Methods Appl. Mech. Engrg., 93 (1991), 189-216.

[35] A. Llor, A. Claisse, C. Fochesato, Energy preservation and entropy in Lagrangian space- and time-staggered hydrodynamic schemes, J. Comput. Phys., 309 (2016), 324-349.

[36] R. Loubere, Contribution to Lagrangian and Arbitrary-Lagrangian-Eulerian numerical schemes, Habilitation à diriger des recherches, Université de Toulouse Paul-Sabatier, 2013.

[37] R. Loubere, P.H Maire, M. Shashkov, J. Breil, S. Galera, ReALE : A Reconnection-based Arbitrary-Lagrangian-Eulerian method, J. Comput. Phys., 229 (2011), 4724-4761.

[38] L.G. Margolin, Arbitrary Lagrangian–Eulerian (ALE) methods a personal perspective, LA-UR-13-24124, 2013.

[39] J.E. Marsden, M. West, Discrete mechanics and variational integrators, Acta Numer., 10 (2001), 357-514.

[40] P.J. Morrison, Hamiltonian description of the ideal fluid, Rev. Mod. Physics, 70 (1998), 467-521.

[41] J. von Neumann, Proposal and analysis of a new numerical method for the treatment of hydrodynamical shock problems, Institute of Advanced Study, Princeton, AMP Report 108 (1944).

[42] J. von Neumann, R.D. Richtmyer, A method for the numerical calculation of hydrodynamic shocks, J. Appl. Phys., 21 (1950), 232-237.

[43] G. Ni, S. Jiang, K. Xu, Remapping-free ALE-type kinetic method for flow computations, J. Comput. Phys., 228 (2009), 3154-3171.

[44] S.E. Norris, C.J. Were, P.J. Richards, G.D. Mallinson, A Voronoi-based ALE solver for the calculation of incompressible flow on deforming unstructured meshes, Int. J. Numer. Meth. Fluids, 65 (2011), 1160-1179.

[45] D. Pavlov, P. Mullen, Y. Tong, E. Kanso, J.E. Marsden, M. Desbrun, Structure-preserving discretization of incompressible fluids, Physica D, 240 (2011), 443-458.

[46] G. Pijaudier-Cabot, L. Bode, A. Huerta, Arbitrary Lagrangian–Eulerian finite element analysis of strain localization in transient problems, Int. J. Numer. Methods Eng., 38 (1995), 4174-4191.

[47] B. Ramaswamy, Numerical solution of unsteady viscous free surface flow, J. Comput. Phys., 90 (1990), 396-430.

[48] W.J. Rider, E. Love, M.K. Wong, O.E. Strack, S.V. Petney, D.A. Labreche, Adaptative methods for multi-materials ALE hydrodynamics, Int. J. Numer. Meth. Fluids, 65 (2011), 1325-1337.

[49] A.C. Robinson, J.H.J. Niederhaus, V.G. Weirs, E. Love, Arbitrary Lagrangian–Eulerian 3D ideal MHD algorithms, Int. J. Numer. Meth. Fluids, 65 (2011), 1438-1450.

[50] L.I. Sedov, Similarity and dimensional methods in mechanics, Academic Press, 1959.

[51] J. Serrin, Mathematical principles of classical mechanics, Handbuch der physik, Springer, 1959.

[52] C.W. Shu, Essentially non-oscillatory and weighted essentially non-oscillatory schemes for hyperbolic conservation laws, Advanced Numerical Approximation of Nonlinear Hyperbolic Equations, Lectures Notes in Mathematics, Springer, 1697 (1998), 325-432.

[53] G.A. Sod, A survey of several finite difference methods for system of nonlinear hyperbolic conservation laws, J. Comput. Phys., 27 (1978).

[54] A. Stern, Y. Tong, M. Desbrun, J. Marsden, Geometric computational electrodynamics with variational integrators and discrete differential forms, Springer New York, 2015.

[55] W.G. Strang, SIAM J.Numer. Anal.,5 (1968).

[56] E. Tonti, Why starting from differential equations for computational physics ?, J. Comput. Phys., 257 (2014), 1260-1290.

[57] J.G. Trulio, K.R. Trigger, Numerical solution of the one–dimensional Lagrangian hydrodynamic equations, UC-LRL Report, 1966.

[58] T.M. Tyranowski, Geometric integration applied to moving mesh methods and degenerate Lagrangians, PhD thesis, California Institute of Technology, 2014.

[59] M.M. Vainberg, Variational methods for the study of nonlinear operators, Holden-Day, San Francisco, 1964.

[60] A. Velghe, N. Gillet, J. Bohbot, A high efficiency parallel unstructured solver dedicated to internal combustion engine simulations, Comput. Fluids, 45 (2011), 116-121.

[61] L. Verlet, Computer “experiments" on classical fluids. I. Thermodynamical properties of Lennard–Jones molecules, Phys. Rev. Lett., 159 (1967), 98-104.

[62] D.H. Wagner, Equivalence of Euler and Lagrangian equations of gas dynamics for weak solutions, J. Diff. Eq., 68 (1987), 118-136.

[63] J.M. Wendlandt, J.E. Marsden, Mechanical integrators derived from a discrete variational principle, Physica D, 106 (1997), 223-246.

[64] M. Wilkins, Calculation of elastic–plastic flow, Methods in computational physics : advances in research and applications, Vol.3, Fundamentals methods in hydrodynamics, Academic Press, 1964.

[65] P. Woodward, P. Colella, The numerical simulation of two-dimensional fluid flow with strong shocks, J. Comput. Phys., 54 (1984), 115-173.

Chapitre 4

Procédure générique de dérivation de schémas ALE direct mimétiques : application aux écoulements multiphasiques

Le corps de ce chapitre est constitué d'un article prêt à être soumis pour publication : A multiphase flow mimetic numerical scheme with thermodynamic and geometric compatibility on an arbitrary moving grid, T. Vazquez-Gonzalez, A. Llor, C. Fochesato, in preparation.

4.1 Abstract

The simulation of transient and compressible multiphase flows in practical applications is one of the most challenging area of Computational Fluid Dynamics (CFD). This is due to the presence of numerous constraints at the same time such as (and non limitatively) : large number of fluids, both isentropic and strongly shocked compressible evolution, highly variable or contrasted equation of state (EOS) stiffnesses, large heat sources, large deformations, and transport over

large distances. Multiphase models that are available for dealing with such constraints comes in a wealth of types and flavours but they all share a common “backbone" structure of mass, momentum, and energy evolution equations with advective terms and coupled through pressure forces and their associated pressure work terms.

In order to fulfill the above mentioned constraints, the present work aims at discretizing the backbone model with a novel multiphase numerical scheme. The discretization of the new scheme is addressed over an arbitrary moving grid (ALE or Arbitrary Lagrangian–Eulerian) approach by a three-steps mimicking derivation : i) a variational least action principle is used to generate the proper pressure forces in the momentum equations—thus ensuring a compatible exchange between kinetic and internal energies under isentropic conditions ; — ii) a tally is performed to match the kinetic and internal energies—thus generating internal energy evolution equations for each phases that respect total energy conservation ; —and iii) an artificial viscosity term is added in the evolution equations—thus stabilizing the scheme. This mimicking derivation GEEC (Geometry, Energy, and Entropy Compatible) procedure has been developed by the authors in "A novel GEEC (Geometry, Energy, and Entropy Compatible) procedure applied to a staggered direct-ALE scheme for hydrodynamics" and applied as a proof of concept on a single-fluid direct ALE scheme.

The resulting numerical scheme named multiGEECS (Geometry, Energy, and Entropy Compatible multiphase Scheme) involves the following features : i) full conservation of mass, momentum, and total energy of the system at discrete level ; ii) a direct ALE formalism where mass, momentum, and internal energy fluxes are taken into account directly into the discrete evolution equations—without separation between Lagrangian evolution and remapping procedure ; iii) thermodynamical consistency of the pressure work obtained by application of a variational principle ; iv) the pressure equilibrium through a *simple* and *local* (to the cells) procedure ; and v) a generic set of evolution equations written for an arbitrary number of fluids and derived without any constraint on structure or spatial dimension in order to simulate a broad category of multiphase flows.

Multiphase numerical test cases—including Sod’s shock tube, water–air shock tube, triple

point test, and Ransom's water faucet—are performed in two dimensions using various strenuous grid motion strategies. The results confirm the following properties : i) exact conservation at discrete level (proper capture of shock levels and shock velocities) ; ii) robust multi-material like behavior with small residual volume fractions ; iii) stable multiphase behavior where each fluid has its own velocity in order to obtain drifting between fluids ; iv) preservation of isentropic flows ; and v) versatility regarding grid motions (including supersonic shearing, linear interpolation of contact discontinuity, or randomly distorted mesh).

4.2 Introduction

4.2.1 Motivations

In many industrial (combustion, nuclear, propulsion, health, and pharmaceutical) and academic fields (astrophysics, geophysics, and meteorology), flows often appear in state of dispersed multiple phases—liquid–gas, solid–gas, gas–liquid, and liquid–liquid phases—or components—individual particles, droplets, and bubbles. Due to the coexistence of these multiple phases with mutual interactions—along with widely disparate gradients of pressure, flow speed, and material properties—the detailed full-system modeling of such systems remains open or merely adressed for specific flow types depending on nature, strength, boundaries, sources, etc. So far, multiphase flows modeling has been widely used in computer codes for simulating, among others bubble flows in vertical columns[24, 12], cooling circuit problems in nuclear industry [38, 3, 2], propagation of evaporation fronts and cavitation problems [41], deflagration-to-detonation transition [1], propagation of detonation waves in heterogeneous media [7], primary and second atomization problems in combustion problems [47, 26], and sloshing problems in fuel tank [6].

One widely used approach for modeling flows containing multiple components is through the so-called multiphase model in which time, space, or ensemble averaging is applied to each phase through a phase-conditioned average (details can be found in [13, 32]). The conditioned averaging operators are thus applied directly to the single-phase mass, momentum, and energy equations thus yielding a broad variety of model types—depending on fluid characteristics, dispersion

geometry, flow regime, dissipation processes, source terms, or boundary conditions. However, all these averaged models display a common structure of coupled Euler-type evolution equations for their non-dissipative terms : when stripped away of all exchange terms and dissipation effects they reduce to the same “backbone" model of mass, momentum, and energy equations with advective terms and coupled through pressure forces and their related pressure work terms. This backbone model corresponds to the convective part of general multi-fluid models. For two-phase flows this backbone is often designated as the “single-pressure six equation model" [48, and references therein].

The numerical resolution of N-phase flow equations is still challenging because of several factors which are already present in the backbone model of $3N$ evolution equations : i) they cannot be expressed in fully conservative forms because of pressure gradients ; ii) they can involve stiff terms when the fluid properties are strongly contrasted (for example highly variable or different EOS stiffnesses) ; iii) they may couple into an elliptic system ; and iv) their thermodynamic consistency—compliance with the second law of thermodynamics which forbids entropy reduction in a closed system and ensures entropy preservation for isentropic flows,—can be challenged by possibly inconsistent calculations of the pressure work in the numerical integration techniques, especially when solving with respect to an arbitrary moving grid. In that case, entropy errors may come from numerical residues on cell volume variations, relative-to-grid advections, and volume fraction coupling between drifting fluids.

In the present work, a novel numerical scheme is developed to simulate multiphase flows involving the following constraints : i) large number of compressible fluids (up to a few dozens in order to modelize polydisperse flows by multi-size approaches [35, and references therein]) ; ii) both isentropic or strongly shocked fluid evolutions ; iii) highly variable and contrasted EOS stiffnesses (such as water and air in which the acoustic impedance differ by a factor of 4000) ; and iv) large deformations and advection over possibly large distances. The present developments also apply to numerical interfaces between fluids—either captured by interface reconstructions on mixed cells or artificially spread over a few cells—which follow formally identical multiphase equations.

The above mentioned constraints mirror into fundamental algebraic properties for the multiphase numerical scheme according to : i) exact conservation of masses, momentum, and total energy at discrete level up to round-off errors in order to ensure the proper capture of shock levels and shock velocities ; ii) & iii) thermodynamic consistency of the pressure work at second-order regardless of mesh motions ; and iv) arbitrarily evolving computational mesh where grid motions can be either given by the user or adaptatively adjusted by the flow constraints.

This last point is further developed into an arbitrary moving grid method. This kind of method—known in the case of single-fluid flow by ALE (Arbitrary Lagrangian–Eulerian) designed by [46, 23]—introduced the idea that single-fluid motion can be computed with respect to a moving grid in order to retain the advantages of both Eulerian—employ fixed meshes—and Lagrangian approaches—use meshes that follow fluid motion. Numerous ALE strategies have been designed for multi-material applications [5, 4, 34, 39, and references therein], and multiphase application [27, 10]. In most of these works, strict thermodynamical consistency appears to have been a relatively minor concern. However, it will be at the core of the present work which emphases the proper capture of the pressure work in the multiphase context.

Two broad categories of ALE strategies exist [49, and references therein] : *indirect* and *direct*. Indirect ALE approaches perform a separation between Lagrangian evolution phases and a remapping procedure after an arbitrary number of time steps. In contrast, no remap step is used in direct ALE approaches as mass, momentum and energy fluxes at moving cell boundaries are directly taken into account in the discrete evolution equations. Indirect ALE approaches have been used for multi-phases multi-velocities flows [9], but the remap step become computationally expensive for multiphase flow systems in two or three dimensions [30]. In this case, direct ALE methods appear more computationally efficient as they do not involve remap steps. However, direct ALE approaches can be challenged by the capture of the pressure work in a thermodynamically consistent way.

4.2.2 Variational approach

Ensuring the consistency and the compliance to the set of specifications mentioned above in the direct ALE context for a multiphase system can be achieved through the use of so-called mimetic approaches which consist in transposing some critically important physical constraints into discrete equations [25]. In the present work, mimetic approach is applied to the critical ingredient of the thermodynamic consistency of the pressure work and pressure forces. The mimetic approach will be applied here not directly to the PDEs but to their underlying least action variational principle [45]. The least action principle is a fundamental ingredient of mathematical physics which allows to find equations of motion which are geometrically and energetically consistent for many systems from a wide range of fields [21].

For systems with discrete numbers of coordinates, variational integrators are based on a discrete version of Hamilton's least action principle and they provide a systematic way to derive numerical methods. However, variational integrators can only retain two out of the three following properties [17, 50] : exact symplecticity, exact conservation of momentum, and exact conservation of total energy. As a consequence, discrete variational integrators are naturally divided into three broad categories : momentum–energy, momentum–symplectic, and energy–symplectic. For CFD applications where emphasis is set on exact conservation of momentum and total energy, only momentum–energy integrators are of practical interest in order to properly capture shock levels and velocities.

For continuous hydrodynamics, the application of variational approaches for describing the motion of a compressible fluid has been an area of increasing interest over the past decades. Valuable sources of variational approaches for single-phase flow problems can be found in the classical works of Eckart [15], Herivel [22], and Lin [31]. In these works, a set of Euler–Lagrange equations is derived directly from a variational principle in Eulerian or Lagrangian frameworks. However, Lin and Serrin showed that in order to recover the Eulerian variational description without an irrotational restriction, it is necessary to add an additional constraint to the Lagrangian. This additional constraint is taken by by means of a Lagrange multiplier in order to force the existence of conserved Lagrangian coordinates for all fluid elements. The application of Hamilton's principle

to multiphase mixtures may be considered as a generalization of Hamilton's principle for a single-phase flow. It was first initiated by Geurst [18] who used a variational principle for the derivation of the one-dimensional two-phase equations of superfluid Helium in the Eulerian framework. The extension to Lagrangian framework was later performed by Bedford and Drumheller [14] for both incompressible and compressible mixtures whose materials occupy the entire volume (for example mixtures of immiscible liquids, or a fluid containing a distribution of particles, droplets, or bubbles).

For compressible—or non-uniform density—CFD applications, the mimicking of these continuous variational approaches has been severely restricted by a major impediment : a discretization of the group of non volume-preserving diffeomorphisms is still to be found and appears particularly complex—as mass and entropy advections cannot be *a priori* simultaneously holonomic and monotonic. A rigorous approach but restricted to incompressible single-fluid flows can be found in [37]. In this work, Pavlov et al. introduced the idea of approximating—in a weak sense—the infinite-dimensional Lie group of volume-preserving diffeomorphisms with an approximate grid-dependent finite-dimensional Lie group. In this framework, mass and volume preserving transport are captured by strictly holonomic constraints which make the fluid evolve over a mimicked symplectic though non-monotonic structure.

4.2.3 Present approach

In the present work, a combination of a fully discrete variational approach and direct ALE formalism is proposed for simulating compressible multiphase flows. The derivation of the numerical scheme is done using the mimicking GEEC (Geometry, Energy, and Entropy Compatible) derivation procedure developed by the authors in [49] which ensured geometric, energetic, and entropic compatibility at discrete level. The discrete derivation of the variational direct ALE numerical scheme proceeds through the following steps : i) in Section 4.3.1, the continuous multiphase Euler–Lagrange equations are derived from the application of the continuous least action principle. A continuous internal energy equation is then derived using thermodynamic relationships. The form of this continuous internal energy equation separates and makes visible

the different processes associated with the pressure work in a thermodynamically consistent way. This continuous derivation—done in the Eulerian framework for simplicity—provides a mimicking guideline for the derivation of the momentum and internal energy evolution equations in the discrete case ; ii) in Section 4.3.2, the space-and-time discretization of fields, mass transport of each fluid, and action integral is presented. This discretization ensures a continuity with purely Lagrangian schemes used at CEA/DAM [36, 51] where staggered velocity fields are naturally compatible with Lagrangian geometry displacements. Then the discrete Euler–Lagrange equations for the multiphase system are obtained by application of the least action principle to the discrete action integral ; iii) in Section 4.3.3, corrections on numerical residues and “flux-in-time" terms are introduced in the variational momentum equation for each fluid in order to bring back the conservation of total momentum at the discrete level ; iv) in Section 4.3.4, an internal energy equation is derived for each fluid by following the continuous Eulerian derivation done in Section 4.3.1 ; and v) in Section 4.3.5, a simple and local to the cells procedure is presented in order to obtain the pressure equilibrium at the end of each time step.

Readers who are not interested in the step-by-step derivation of the evolution equations of the scheme can refer to Section 4.4 where a summary of the multiGEECS algorithm is presented, along with the time step definition and the artificial viscosity formulation. Finally, results of several tests including variants of the Sod’s shock tube, water–air shock tube, Ransom’s water faucet problem, and triple point test are presented in Section 4.5 in order to verify the different built-in properties of the scheme in terms of energetic, geometric, and entropic compatibility.

4.3 Discrete derivation of the direct multiphase ALE scheme

Notation and definitions of the variables used for the discrete derivation are given in Appendix .1. In Section 4.3.1, the derivation of the multiphase Euler–Lagrange equations and the internal energy equation is done in the continuous Eulerian case in order to provide a guideline for the discrete derivation. In Section 4.3.2, the main steps of the discrete derivation of the multiphase evolution equations are presented in the direct ALE framework—for clarity, the detailed step-by-step discrete derivation is postponed to Appendix .4.

4.3.1 Derivation of continuous Eulerian hydrodynamic equations

In this paper, Geurst's variational approach for two-fluid mixtures [18] is extended to a N-phase representation for a general derivation of compressible Euler–Lagrange equations. In order to derive a multiphase system of equations without any irrotational restriction, Lin's constraints are added for all fluids into the variational principle through Lagrange multipliers associated with the conservation of Lagrangian coordinates. As already presented by Drumheller and Bedford [14], we assume here that the materials occupy the entire volume—there are no "voids" in the system. This assumption is introduced into the variational principle through the use of an additional Lagrange multiplier—this volume constraint is thus simply that the sum of the material volume fractions at each point is equal to one. The continuous variational derivation is performed in the Eulerian framework [49]. This does not match the discrete variational ALE derivation to follow which is referenced with respect to grid coordinates but it represents a simple step by step guideline for the discrete derivation of the evolution equations.

In Section 4.3.1.1, the fields, transports, and action integral are presented in the continuous Eulerian framework. In Section 4.3.1.2, the Euler–Lagrange equations are obtained by applying the least action principle to the continuous action integral. In Sections 4.3.1.3, 4.3.1.4, and 4.3.1.5, the velocity and momentum evolution equations are obtained by proceeding through the same algebraic manipulations as in [49]. In Section 4.3.1.6, an internal energy evolution equation is first derived in the continuous Eulerian case then in the ALE case which separates and shows the various processes associated with the pressure work in a rigorous and thermodynamically consistent way. In Section 4.3.1.7, the introduction of artificial viscosity processes into the momentum and internal energy evolution equations is presented in the multiphase context.

4.3.1.1 Fields, transports, and action integral

Considering the isentropic flow of a system of M compressible fluids with polytropic properties $e^\varphi = e^\varphi(\rho^\varphi)$—the geometric evolution of e is thus linked to the evolution of ρ, —the continuous

Lagrangian of hydrodynamics in the Eulerian framework is

$$\mathcal{L} = \sum_{\varphi} \left(\tfrac{1}{2}[\alpha\rho]^{\varphi} v_i^{\varphi} v_i^{\varphi} - [\alpha\rho]^{\varphi} e^{\varphi}(\rho^{\varphi}) + \phi^{\varphi} \left(\partial_t [\alpha\rho]^{\varphi} + ([\alpha\rho]^{\varphi} v_i^{\varphi})_{,i}\right) \right.$$
$$\left. + \lambda^{\varphi} \left(\partial_t([\alpha\rho]^{\varphi}\chi^{\varphi}) + ([\alpha\rho]^{\varphi}\chi^{\varphi} v_i^{\varphi})_{,i}\right) \right) + \mathit{\Pi} \left(\sum_{\varphi} \alpha^{\varphi} - 1 \right) , \quad (4.1)$$

where φ, α^{φ}, ρ^{φ}, e^{φ}, and $\boldsymbol{v}^{\varphi}$ are respectively the label, volume fraction, density, isentropic internal energy, and Eulerian velocity of the fluid φ. Einstein's notation of implicit summation on repeated indices is assumed—$\boldsymbol{\nabla} \cdot \boldsymbol{a} = a_{i,i}$ and $\boldsymbol{\nabla} b = b_{,i}$.

The Lagrangian (4.1) consists in the difference between the total kinetic and total internal energies of the system. Three additional constraints are added in the form of Lagrange multipliers : i) ϕ^{φ} for the mass transport of fluid φ relating velocity and density fields ; ii) λ^{φ} for Lin's constraint associated with the conservation of a Lagrangian coordinate χ^{φ} of fluid φ ; and iii) $\mathit{\Pi}$ for the volume conservation of the system.

4.3.1.2 Euler–Lagrange equations

The continuous form of the Euler–Lagrange equations may be obtained by performing independent variations of the dependent variables. As already mentioned in [18], several choices are available for the independent variations of the dependent variables, for example : i) one can choose the thermodynamic variables (pressure and temperature of the mixture) along with the relative velocity $\boldsymbol{v}_i^{\varphi}$ of fluid φ ; or ii) one can choose the combined variables ρ^{φ}, α^{φ} along with $\boldsymbol{v}_i^{\varphi}$. The former choice involves complicated thermodynamic derivatives of density and entropy. Therefore, the latter choice is used in the present work. Variations of the continuous action of the system (4.1) in function of the variable variations $\delta\phi^{\varphi}$, $\delta\lambda^{\varphi}$, δv_i^{φ}, $\delta\rho^{\varphi}$, $\delta\alpha^{\varphi}$, $\delta\chi^{\varphi}$, and $\delta\mathit{\Pi}$ are

$$\delta\mathcal{A} = \iint \left(\frac{\partial\mathcal{L}}{\partial\phi^{\varphi}}\delta\phi^{\varphi} + \frac{\partial\mathcal{L}}{\partial\lambda^{\varphi}}\delta\lambda^{\varphi} + \frac{\partial\mathcal{L}}{\partial v_i^{\varphi}}\delta v_i^{\varphi} \right.$$
$$\left. + \frac{\partial\mathcal{L}}{\partial\rho^{\varphi}}\delta\rho^{\varphi} + \frac{\partial\mathcal{L}}{\partial\alpha^{\varphi}}\delta\alpha^{\varphi} + \frac{\partial\mathcal{L}}{\partial\chi^{\varphi}}\delta\chi^{\varphi} + \frac{\partial\mathcal{L}}{\partial\mathit{\Pi}}\delta\mathit{\Pi} \right) \mathrm{d}^3\,\boldsymbol{x}\,\mathrm{d}\,t\ . \quad (4.2)$$

It is assumed that the allowed variations in ϕ^φ, λ^φ, v_i^φ, ρ^φ, α^φ, χ^φ, and Π are independent, continuously differentiable and vanish for x and t at domain boundaries. Using the least action principle $\delta\mathcal{A} = 0$ over (4.2) yields the per-fluid Euler–Lagrange equations

$$\partial_t[\alpha\rho]^\varphi + \left([\alpha\rho]^\varphi v_i^\varphi\right)_{,i} = 0 \ , \tag{4.3a}$$

$$\partial_t\left([\alpha\rho]^\varphi \chi^\varphi\right) + \left([\alpha\rho]^\varphi \chi^\varphi v_i^\varphi\right)_{,i} = 0 \ , \tag{4.3b}$$

$$v_i^\varphi - \phi_{,i}^\varphi - \chi^\varphi \lambda_{,i}^\varphi = 0 \ , \tag{4.3c}$$

$$\tfrac{1}{2} v_j^\varphi v_j^\varphi - \left(e^\varphi + \frac{P^\varphi}{\rho^\varphi}\right) - \partial_t\phi^\varphi - v_j^\varphi \phi_{,j}^\varphi - \chi^\varphi \partial_t\lambda^\varphi - \chi^\varphi v_j^\varphi \lambda_{,j}^\varphi = 0 \ , \tag{4.3d}$$

$$\tfrac{1}{2} v_j^\varphi v_j^\varphi - e^\varphi - \partial_t\phi^\varphi - v_j^\varphi \phi_{,j}^\varphi - \chi^\varphi \partial_t\lambda^\varphi - \chi^\varphi v_j^\varphi \lambda_{,j}^\varphi + \frac{\Pi}{\rho^\varphi} = 0 \ , \tag{4.3e}$$

$$\partial_t\lambda^\varphi + v_j^\varphi \lambda_{,j}^\varphi = 0 \ , \tag{4.3f}$$

$$\sum_\varphi \alpha^\varphi = 1 \ , \tag{4.3g}$$

with P^φ the pressure field of the fluid φ. The per-fluid Euler–Lagrange equations (4.3) display the following features : i) Equations (4.3a) and (4.3b) represent respectively the per-fluid mass and Lagrangian coordinates conservation equations ; ii) Equation (4.3c) shows that adding the Lin's constraint into the Lagrangian (4.1) lifts the irrotational restriction (visible when $\chi^\varphi = 0$) ; iii) Equations (4.3d) and (4.3e) are obtained with variations on ρ^φ and α^φ respectively and link the per-fluid pressure of the system P^φ to the Lagrange multiplier Π ; iv) Equation (4.3f) represents the evolution equation of the Lagrange multiplier λ^φ ; and v) Equation (4.3g) ensures the volume conservation for the system of M fluids.

4.3.1.3 Elimination of the Lagrange multiplier Π

Substracting (4.3d) from (4.3e) leads to

$$\Pi = -P^\varphi \ . \tag{4.4}$$

If one imposes in the Lagrangian that mixtures occupy the entire volume—through the use of a Lagrange multiplier Π which is the same for all fluids, —the conservation of volume inevitably

implies the equality of the fluid pressures, i.e. instantaneous pressure relaxation between fluids. Therefore, only one pressure P is considered for all the fluids of the system $P^\varphi = P$.

4.3.1.4 Velocity equation

The derivation of the evolution equation for the velocity of fluid φ will proceed through the same algebraic manipulations presented in [49]. First, substituting ∂_t(4.3c) and (4.3d)$_{,i}$ yields

$$\partial_t v_i^\varphi = -\left(e^\varphi + \frac{P}{\rho^\varphi}\right)_{,i} + v_j^\varphi v_{j,i}^\varphi - v_{j,i}^\varphi \phi_{,j}^\varphi - v_j^\varphi \phi_{,ji}^\varphi + \lambda_{,i}^\varphi \partial_t \chi^\varphi + \chi^\varphi \partial_t \lambda_{,i}^\varphi \ , \tag{4.5}$$

where $\rho^\varphi(e^\varphi + P/\rho^\varphi)_{,i} = P_{,i}$ for a polytropic fluid. Inserting the expressions of $\partial\chi^\varphi$ and $\partial\lambda^\varphi$ from (4.3b) and (4.3f) respectively gives

$$\partial_t v_i^\varphi = -\frac{P_{,i}}{\rho^\varphi} - v_j^\varphi(\phi_{,ji}^\varphi + \chi^\varphi \lambda_{,ij}^\varphi) - \lambda_{,i}^\varphi v_j^\varphi \chi_{,j}^\varphi \ . \tag{4.6}$$

Using the algebraic identities $(\chi^\varphi \lambda_{,i}^\varphi)_{,j} = \chi^\varphi \lambda_{,ij}^\varphi + \lambda_{,i}^\varphi \chi_{,j}^\varphi$ and $\phi_{,ji}^\varphi = \phi_{,ij}^\varphi$ from (4.3c), provides the velocity equation of fluid φ

$$\partial_t v_i^\varphi = -\frac{P_{,i}}{\rho^\varphi} - v_j^\varphi v_{i,j}^\varphi \ . \tag{4.7}$$

4.3.1.5 Conservative momentum equation

The momentum evolution equation of fluid φ is obtained from $[\alpha\rho]^\varphi \times$ (4.7) + (4.3a) $\times\, v_i^\varphi$, thus yielding

$$\partial_t([\alpha\rho]^\varphi v_i^\varphi) = -\alpha^\varphi P_{,i} - [\alpha\rho]^\varphi v_j^\varphi v_{i,j}^\varphi - v_i^\varphi([\alpha\rho]^\varphi v_j^\varphi)_{,j} \tag{4.8a}$$

$$= -\alpha^\varphi P_{,i} - ([\alpha\rho]^\varphi v_i^\varphi v_j^\varphi)_{,j} \ . \tag{4.8b}$$

A conservative momentum transport term is added in (4.8a) consistently with the mass transport equation of fluid φ (4.3a), yielding the conservative momentum evolution equation of fluid φ. The continuous rearrangements from (4.8a) to (4.8b) appear trivial in the continuous Eulerian case but are a source of numerical residues in the discrete derivation.

4.3.1.6 Internal energy equation

In the isentropic case, the evolution of the internal energy is linked to the geometrical evolution of the density through the polytropic property $e^\varphi = e^\varphi(\rho^\varphi)$. However, in the entropic case where entropy is generated by shocks or numerical residues on pressure work, the evolution of internal energy must be taken into account by an evolution equation. In the present work, such equation is derived in the continuous Eulerian case using the thermodynamic relationships

$$\mathrm{d}\, e^\varphi = -P\, \mathrm{d}\, V^\varphi + \delta W^\varphi \ , \tag{4.9a}$$

$$\mathrm{d}\, P = -\gamma^\varphi P \rho^\varphi\, \mathrm{d}\, V^\varphi + \Gamma^\varphi \rho^\varphi \delta W^\varphi \ , \tag{4.9b}$$

where P is the common pressure of the fluids and e^φ, V^φ, Γ^φ, and δW^φ are the internal energy, mass volume, Grüneisen coefficient, and irreversible work of entropy of the fluid φ respectively.

The detailed step-by-step derivation of the continuous Eulerian internal energy evolution equation is postponed to Appendix .2.1. Using the “Lagrangian" and “Eulerian" derivative operators along Eulerian velocities of fluid φ defined as

$$\mathrm{d}_t^\varphi \bullet = \partial_t \bullet + \boldsymbol{v}_i^\varphi (\bullet)_{,i} \ , \tag{4.10a}$$

$$\mathrm{D}_t^\varphi \bullet = \partial_t \bullet + (\bullet \boldsymbol{v}_i^\varphi)_{,i} \ . \tag{4.10b}$$

The evolution equation for the internal energy of the fluid φ is

$$\begin{aligned} \mathrm{D}_t^\varphi \left(\alpha^\varphi \rho^\varphi e^\varphi\right) = -P\beta^\varphi \bar{v}_{i,i} + P_{,i} \sum_\phi \mu^{\varphi\phi} \left(v_i^\varphi - v_i^\phi\right) \\ + \sum_\phi \mu^{\varphi\phi} \left(\Gamma^\phi \rho^\phi \dot{W}^\phi - \Gamma^\varphi \rho^\varphi \dot{W}^\varphi\right) + \alpha^\varphi \rho^\varphi \dot{W}^\varphi \ , \end{aligned} \tag{4.11}$$

where $\sum_\phi \bullet^\phi$ is the summation operator over all fluids, $\bar{\boldsymbol{v}}$ is the volume averaged Eulerian velocity, β^φ are the relative compressibility coefficients of the fluids, and $\mu^{\varphi\phi}$ is the scalar coupling coefficient under along-pressure-gradient drift (not to be confused with the vector of absolute velocity $\boldsymbol{\mu}^\varphi$ of the fluid φ to be defined in Section 4.3.2.1 at Equation (4.21)). These three

quantities are defined by

$$\bar{v}_i = \sum_\phi \alpha^\phi v_i^\phi \ , \tag{4.12a}$$

$$\beta^\varphi = \frac{\alpha^\varphi/\gamma^\varphi}{\sum_\phi \alpha^\phi/\gamma^\phi} \ , \tag{4.12b}$$

$$\mu^{\varphi\phi} = \mu^{\phi\varphi} = \frac{\alpha^\varphi\alpha^\phi/\gamma^\varphi\gamma^\phi}{\sum_\Phi \alpha^\Phi/\gamma^\Phi} \ . \tag{4.12c}$$

The form of the internal energy evolution equation (4.11) separates and shows the three processes associated with the pressure work in a thermodynamically consistent way : i) $-P\beta^\varphi\bar{v}_{i,i}$ is the internal energy production through the overall volume change ; ii) $+P_{,i}\sum_\phi \mu^{\varphi\phi}\left(v_i^\varphi - v_i^\phi\right)$ is the internal energy exchange between fluids through the relative drift in pressure gradient ; iii) $+\sum_\phi \mu^{\varphi\phi}\left(\Gamma^\phi\rho^\phi\dot{W}^\phi - \Gamma^\varphi\rho^\varphi\dot{W}^\varphi\right)$ is the internal energy transfer due to differential heating between fluids ; and iv) $+\alpha^\varphi\rho^\varphi\dot{W}^\varphi$ is the *reversible* driving source of entropy production.

As it will be seen in Section 4.3.4, Equation (4.11) avoids implicit closure by making visible the explicit pressure work terms but these terms cannot be easily discretized in a consistent way in the ALE framework. In order to obtain an explicit expression for the internal energy equation in the ALE framework, (4.11) can be transformed by algebraic manipulations using the "Lagrangian" and "Eulerian" derivative operators along ALE velocities of fluid φ defined as

$$\mathrm{d}_t^\varphi \bullet = \partial_t \bullet + \boldsymbol{u}_i^\varphi(\bullet)_{,i} + \boldsymbol{w}_i(\bullet)_{,i} \ , \tag{4.13a}$$

$$\mathrm{D}_t^\varphi \bullet = \partial_t \bullet + (\bullet\boldsymbol{u}_i^\varphi)_{,i} + (\bullet\boldsymbol{w}_i)_{,i} \ , \tag{4.13b}$$

where $\boldsymbol{u}^\varphi$ is the velocity of the fluid φ relative to the grid and $\boldsymbol{w}$ is the grid velocity. Inserting the expressions (4.13) into (4.11) and making algebraic manipulations yields (the step-by-step derivation of the internal energy equation in the ALE framework—including the irreversible

terms—is postponed to Appendix .2.2)

$$\partial_t \left(\alpha^\varphi \rho^\varphi e^\varphi\right) + \left(\alpha^\varphi \rho^\varphi e^\varphi w_i\right)_{,i} = \beta^\varphi P_{,i} \bar{u}_i - \beta^\varphi P w_{i,i} - \beta^\varphi \sum_\phi \left(\alpha^\phi \left(\rho^\phi e^\phi + P\right) u_i^\phi\right)_{,i} - \sum_\phi \left(e^\varphi \left(\alpha^\varphi \rho^\varphi u_i^\varphi\right)_{,i} - \beta^\varphi e^\phi \left(\alpha^\phi \rho^\phi u_i^\phi\right)_{,i}\right) , \quad (4.14)$$

where the expression of the volume averaged velocity (4.12a) in the ALE framework becomes

$$\bar{u}_i = \sum_\phi \alpha^\phi u_i^\phi \ . \quad (4.15)$$

Equation (4.14) displays several important features : i) the first and second terms on the right hand side are the work of pressure forces–through overall volume changes—of relative-to-grid $\boldsymbol{u}^\phi$ and grid $\boldsymbol{w}$ velocities respectively ; ii) the third term on the right hand side is associated with enthalpy advection ; and iii) the fourth term on the right hand side correspond to exchange terms of internal energy through relative drifting between fluids. As it will be shown in Section 4.3.4, all the terms of (4.15) can be consistently discretized in the ALE framework using both available quantities and prescribed transport equations. For simplicity and as the test cases performed in the present work are mostly isentropic, the irreversible source terms are not included from there on but are kept for references in the step-by-step derivation in Appendix .2.

4.3.1.7 Artificial dissipation in a multiphase medium

Shocks in heterogeneous mixtures can convert kinetic energy into entropy through basically four physical effects [32] : intra-species viscosity and thermal conduction, inter-species friction and heat transfer. The modeling of the interaction between a shock and a multiphase medium must thus include the details of the dissipative mechanisms—a weak solution of the conservation equations cannot yield the jump relations. Shocks can be stabilized by viscous forces alone, but not by thermal conduction alone. Furthermore, multiphase systems considered here are assumed to be dispersed to mesoscopic scales, large enough so as to make drag forces and thermal conduction negligible—over typical time scales of shocks—even if spread by diffraction and dispersion due to

heterogeneities. In the present work, the artificial viscosity for each fluid φ is controlled by the per-fluid compression and is thus given by

$$\mathrm{D}_t^\varphi(\alpha^\varphi\rho^\varphi e^\varphi) = (4.11) + \alpha^\varphi\rho^\varphi W^\varphi \ , \qquad \text{with} \qquad \alpha^\varphi\rho^\varphi W^\varphi = -Q^\varphi\beta^\varphi\bar{v}_{i,i} \ , \tag{4.16}$$

where $\bar{v}_i$ is given by (4.12a) and Q^φ is the artificial viscosity stress of fluid φ expressed as a combination of linear and quadratic functions of the compressions in each fluid

$$Q^\varphi = -a_1\rho^\varphi C^\varphi\left(\frac{\beta^\varphi}{\alpha^\varphi}\left(\sum_\phi \alpha^\phi v_i^\phi\right)_{,i} L\right) + a_2\rho^\varphi\left(\frac{\beta^\varphi}{\alpha^\varphi}\min\left(0, \left(\sum_\phi \alpha^\phi v_i^\phi\right)_{,i} L\right)\right)^2 \ , \tag{4.17}$$

where L is the characteristic cell size, a_1 and a_2 are dimensionless coefficients, C^φ is the sound velocity of fluid φ, and β^φ is the compressibility coefficients for fluid φ defined by (4.12b).

Positivity of per-fluid entropy production is thus ensured by closing Q^φ with positive viscosity, i.e. $Q^\varphi\bar{v}_{i,i} \leq 0$. Cross work of pressure between fluids is produced by these entropy productions according to the usual $\Gamma^\phi\rho^\phi W^\phi - \Gamma^\varphi\rho^\varphi W^\varphi$ terms. The overall production involves the total artificial stress Q

$$\textstyle\sum_\phi \alpha^\phi\rho^\phi W^\phi = -Q\bar{v}_{i,i} \ , \qquad \text{with} \qquad Q = \sum_\phi \beta^\phi Q^\phi \ . \tag{4.18}$$

Total energy conservation thus requires that viscous stress terms must be added to the momentum equations according to

$$\mathrm{D}_t^\varphi(\alpha^\varphi\rho^\varphi v_i^\varphi) = (4.8b) - \alpha^\varphi Q_{,i} \ . \tag{4.19}$$

4.3.2 Discrete variational derivation of the evolution equations

In Section 4.3.2.1, the discretization of the mesh, fields, transports, and action integral is performed. Then in Section 4.3.2.2, the discrete version of the per-fluid Euler–Lagrange equations is obtained by applying the least action principle to the action integral discretized in both space and time. Following a similar path stated in [49], an approximation of explicit mass transport is presented for performance purposes in Section 4.3.2.3.

4.3.2.1 Discretization of fields, transports, and action integral

In the present multiphase ALE framework, accuracy in both space-and-time is sought on the action integral to second-order for all terms except for the relative transport of mass and Lagrangian coordinate of fluid φ which will be first-order in space and time. This first-order feature may appear inconsistent with the second-order discretization of grid velocity and energies in the Lagrangian limit, but it is acceptable as a proof of concept provided that thermodynamic consistency is ensured as discussed below after (4.26).

In addition to the discretization choices already explained in the single-fluid case of [49], several discretization choices specific to the multiphase case can be presented : i) mesh is defined at integer time steps t^n by node p at positions $\boldsymbol{x}_p^n$; ii) grid velocity $\boldsymbol{w}$ is discretized at half time steps and at nodes as

$$\boldsymbol{w}_p^{n+1/2} = \left(\boldsymbol{x}_p^{n+1} - \boldsymbol{x}_p^n\right) / \Delta t^{n+1/2} \ , \tag{4.20}$$

where $\Delta t^{n+1/2} = t^{n+1} - t^n$; iii) each fluid possesses its own relative (to the grid) velocity $\boldsymbol{u}^\varphi$ and absolute (in the laboratory frame) velocity $\boldsymbol{\mu}^\varphi$ defined at half time steps and at cell centers ; iv) grid velocity is common for all fluids yielding the discrete relationship

$$\boldsymbol{\mu}_c^{\varphi n+1/2} = \boldsymbol{u}_c^{\varphi n+1/2} + \boldsymbol{w}_c^{n+1/2} \ , \tag{4.21}$$

where $\boldsymbol{w}_c^{n+1/2}$ is computed using the simplest arithmetic interpolation strategy of the grid velocity at cell centers ; and v) as well as for the density $\rho_c^{\varphi n}$ and internal energy $e_c^{\varphi n}$, the finite volume approach is used for the volume fraction $\alpha_c^{\varphi n}$ defined at integer time steps and cell centers—the mass of the fluid φ contained in each cell c at time t^n is thus $[\alpha\rho]_c^{\varphi n} V_c^n$.

As a natural extension of the single-fluid case of [49], the mass balance of each fluid φ is

computed using a first-order in space-and-time upwind implicit scheme

$$
\begin{aligned}
&V_c^{n+1}[\alpha\rho]_c^{\varphi n+1} - V_c^n[\alpha\rho]_c^{\varphi n} \\
&= \Delta t^{n+1/2} \sum_{d\in\mathcal{D}(c)} \left(\sigma_{dc}^{\varphi n+1/2} \boldsymbol{s}_{dc}^{n+1/2} \cdot \boldsymbol{u}_d^{\varphi n+1/2} [\alpha\rho]_d^{\varphi n+1} - \sigma_{cd}^{\varphi n+1/2} \boldsymbol{s}_{cd}^{n+1/2} \cdot \boldsymbol{u}_c^{\varphi n+1/2} [\alpha\rho]_c^{\varphi n+1}\right) \quad (4.22a) \\
&= \Delta t^{n+1/2} \sum_{d\in\mathcal{D}(c)} \left(\dot{V}_{dc}^{\varphi n+1/2} [\alpha\rho]_d^{\varphi n+1} - \dot{V}_{cd}^{\varphi n+1/2} [\alpha\rho]_c^{\varphi n+1}\right) , \quad (4.22b)
\end{aligned}
$$

where $\dot{V}_{cd}^{\varphi n+1/2} = \sigma_{cd}^{\varphi n+1/2} \boldsymbol{s}_{cd}^{n+1/2} \cdot \boldsymbol{u}_c^{\varphi n+1/2}$ is the rate of volume transfer of fluid φ from cell c to cell d and $\boldsymbol{s}_{cd}^{n+1/2}$ is the outward pointing normal vector to the boundary between adjacent cells c and d at time $t^{n+1/2}$ of magnitude given by the area of the $c-d$ boundary element. The off-centering factor $\sigma_{cd}^{\varphi n+1/2}$ of fluid φ is computed with

$$
\sigma_{cd}^{\varphi n+1/2} = \tfrac{1}{2}\left(1 + \operatorname{sign}\left(\boldsymbol{s}_{cd}^{n+1/2} \cdot \boldsymbol{u}_c^{\varphi n+1/2}\right)\right) . \quad (4.23)
$$

For a given cell c and a given fluid φ, one mass transport equation is discretized—and thus one Lagrange multiplier field ϕ discretized as $\phi_c^{\varphi n+1/2}$.

In order to lift the irrotational restriction, a Lin's constraint must be added for each fluid in the discrete action integral through a Lagrange multiplier field λ of fluid φ discretized as $\lambda_c^{\varphi n+1/2}$. The Lagrangian coordinate conservation equation of fluid φ is discretized consistently with the first-order in space-and-time upwind implicit mass transport

$$
\begin{aligned}
&V_c^{n+1}[\alpha\rho]_c^{\varphi n+1}\chi_c^{\varphi n+1} - V_c^n[\alpha\rho]_c^{\varphi n}\chi_c^{\varphi n} \\
&\qquad = \Delta t^{n+1/2} \sum_{d\in\mathcal{D}(c)} \left(\dot{V}_{dc}^{\varphi n+1/2} [\alpha\rho]_d^{\varphi n+1}\chi_d^{\varphi n+1} - \dot{V}_{cd}^{\varphi n+1/2} [\alpha\rho]_c^{\varphi n+1}\chi_c^{\varphi n+1}\right) . \quad (4.24)
\end{aligned}
$$

The constraint of volume conservation is discretized at each cell c using the standard finite volume representation thus yielding

$$
\sum_{\varphi} \alpha_c^{\varphi n} = 1 . \quad (4.25)
$$

Mimicking the continuous Lagrangian (4.1), the volume conservation is embedded in the variational

approach through a Lagrange multiplier field Π discretized as Π_c^n.

Finally, the discrete multiphase action integral of the system with its additional constraints is

$$\begin{aligned}\mathcal{A} = \sum_{n,c,\varphi} \Bigg(& \Delta t^{n-1/2} V_c^n \, \tfrac{1}{2} \, [\alpha\rho]_c^{\varphi n} \left(\boldsymbol{\mu}_c^{\varphi n-1/2} \right)^2 - \Delta t^n V_c^n [\alpha\rho]_c^{\varphi n} e_c^{\varphi n} \\ & + \phi_c^{\varphi n+1/2} \Bigg(V_c^{n+1} [\alpha\rho]_c^{\varphi n+1} - V_c^n [\alpha\rho]_c^{\varphi n} \\ & - \Delta t^{n+1/2} \sum_{d \in \mathcal{D}(c)} \left(\dot{V}_{dc}^{\varphi n+1/2} [\alpha\rho]_d^{\varphi n+1} - \dot{V}_{cd}^{\varphi n+1/2} [\alpha\rho]_c^{\varphi n+1} \right) \Bigg) \\ & + \lambda_c^{\varphi n+1/2} \Bigg(V_c^{n+1} [\alpha\rho]_c^{\varphi n+1} \chi_c^{\varphi n+1} - V_c^n [\alpha\rho]_c^{\varphi n} \chi_c^{\varphi n} \\ & - \Delta t^{n+1/2} \sum_{d \in \mathcal{D}(c)} \left(\dot{V}_{dc}^{\varphi n+1/2} [\alpha\rho]_d^{\varphi n+1} \chi_d^{\varphi n+1} - \dot{V}_{cd}^{\varphi n+1/2} [\alpha\rho]_c^{\varphi n+1} \chi_c^{\varphi n+1} \right) \Bigg) \Bigg) \\ & + \sum_{n,c} \Pi_c^n \left(\sum_{\varphi} \alpha_c^{\varphi n} - 1 \right) . \end{aligned} \tag{4.26}$$

This action integral involves several features : i) the mass and Lagrangian coordinate equations in the ALE framework are embedded into transport equations advected by the relative-to-grid velocity $\boldsymbol{u}^{\varphi}$ (in contrast with (4.1) where conserved quantities are advected by the Eulerian velocity of the fluid) ; ii) the first-order feature of both mass and Lagrangian coordinate transports of fluid φ is acceptable as a proof of concept for the study of variational multiphase schemes provided that thermodynamic consistency remains ensured at least to second-order regardless of mesh motions—it also guarantees a positive formulation without resorting to limiters ; — iii) the density must be $\Delta t^{n-1/2}/2$ ahead of absolute velocity in both kinetic energy and transport equations in order to obtain an explicit equation for the asbolute velocity ; and iv) the discretization of kinetic energy–and thus momentum—at cell centers is made without nodal masses and thus complies with the so-called DeBar condition [11]—a uniform self-advecting velocity field must remain uniform regardless of density gradients. Positivity and DeBar condition are of fundamental interest for multiphase flow simulations [48].

4.3.2.2 Euler–Lagrange equations of fluid φ

The derivation of the continuous Euler–Lagrange equations (4.3) is mimicked in the ALE framework by applying the variational least action principle to the discrete action integral (4.26). The resulting variations of $\mathcal{A}$ under variations of Lagrange multipliers, relative velocity, density, volume fraction, and Lagrangian coordinate of fluid φ can be written

$$\delta\mathcal{A} = \sum_{n,c,\varphi} \left(\frac{\partial \mathcal{A}}{\partial \phi_c^{\varphi n+1/2}} \delta\phi_c^{\varphi n+1/2} + \frac{\partial \mathcal{A}}{\partial \lambda_c^{\lambda n+1/2}} \delta\lambda_c^{\lambda n+1/2} + \frac{\partial \mathcal{A}}{\partial \boldsymbol{u}_c^{\varphi n-1/2}} \cdot \delta\boldsymbol{u}_c^{\varphi n-1/2} \right.$$
$$\left. + \frac{\partial \mathcal{A}}{\partial \rho_c^{\varphi n}} \delta\rho_c^{\varphi n} + \frac{\partial \mathcal{A}}{\partial \alpha_c^{\varphi n}} \delta\alpha_c^{\varphi n} + \frac{\partial \mathcal{A}}{\partial \chi_c^{\varphi n}} \delta\chi_c^{\varphi n} + \frac{\partial \mathcal{A}}{\partial \Pi_c^{n}} \delta\Pi_c^{n} \right) = 0 \ . \quad (4.27)$$

Substituting (4.26) into (4.27) leads to the following discrete Euler–Lagrange equations of fluid φ

$$V_c^{n+1}[\alpha\rho]_c^{\varphi n+1} - V_c^n[\alpha\rho]_c^{\varphi n} = \Delta t^{n+1/2} \sum_{d\in\mathcal{D}(c)} \left(\dot{V}_{dc}^{\varphi n+1/2}[\alpha\rho]_d^{\varphi n+1} - \dot{V}_{cd}^{\varphi n+1/2}[\alpha\rho]_c^{\varphi n+1} \right) \ , \quad (4.28a)$$

$$V_c^{n+1}[\alpha\rho]_c^{\varphi n+1}\chi_c^{\varphi n+1} - V_c^n[\alpha\rho]_c^{\varphi n}\chi_c^{\varphi n}$$
$$= \Delta t^{n+1/2} \sum_{d\in\mathcal{D}(c)} \left(\dot{V}_{dc}^{\varphi n+1/2}[\alpha\rho]_d^{\varphi n+1}\chi_d^{\varphi n+1} - \dot{V}_{cd}^{\varphi n+1/2}[\alpha\rho]_c^{\varphi n+1}\chi_c^{\varphi n+1} \right) \ , \quad (4.28b)$$

$$V_c^n \boldsymbol{\mu}_c^{\varphi n-1/2} - \sum_{d\in\mathcal{D}(c)} \sigma_{cd}^{\varphi n-1/2} \boldsymbol{s}_{cd}^{n-1/2} \left(\phi_d^{\varphi n-1/2} - \phi_c^{\varphi n-1/2} \right)$$
$$- \chi_c^{\varphi n} \sum_{d\in\mathcal{D}(c)} \sigma_{cd}^{\varphi n-1/2} \boldsymbol{s}_{cd}^{n-1/2} \left(\lambda_d^{\varphi n-1/2} - \lambda_c^{\varphi n-1/2} \right) = 0 \ , \quad (4.28c)$$

$$\Delta t^{n-1/2} V_c^n \ \frac{1}{2} \left(\boldsymbol{\mu}_c^{\varphi n-1/2} \right)^2 - \Delta t^n V_c^n \left(e_c^{\varphi n} + P_c^{\varphi n}/\rho_c^{\varphi n} \right)$$
$$+ V_c^n \left(\phi_c^{\varphi n-1/2} - \phi_c^{\varphi n+1/2} \right) + V_c^n \chi_c^{\varphi n} \left(\lambda_c^{\varphi n-1/2} - \lambda_c^{\varphi n+1/2} \right)$$
$$- \Delta t^{n-1/2} \sum_{d\in\mathcal{D}(c)} \dot{V}_{cd}^{\varphi n-1/2} \left(\phi_d^{\varphi n-1/2} - \phi_c^{\varphi n-1/2} + \chi_c^{\varphi n} \left(\lambda_d^{\varphi n-1/2} - \lambda_c^{\varphi n-1/2} \right) \right) = 0 \ , \quad (4.28d)$$

$$\Delta t^{n-1/2} V_c^n \tfrac{1}{2} \left(\boldsymbol{\mu}_c^{\varphi n-1/2}\right)^2 - \Delta t^n V_c^n e_c^{\varphi n} + \Pi_c^n / \rho_c^{\varphi n} + V_c^n \left(\phi_c^{\varphi n-1/2} - \phi_c^{\varphi n+1/2}\right) + V_c^n \chi_c^{\varphi n} \left(\lambda_c^{\varphi n-1/2} - \lambda_c^{\varphi n+1/2}\right) - \Delta t^{n-1/2} \sum_{d\in\mathcal{D}(c)} \dot{V}_{cd}^{\varphi n-1/2} \left(\phi_d^{\varphi n-1/2} - \phi_c^{\varphi n-1/2} + \chi_c^{\varphi n} \left(\lambda_d^{\varphi n-1/2} - \lambda_c^{\varphi n-1/2}\right)\right) = 0 \ , \tag{4.28e}$$

$$V_c^n \left(\lambda_c^{\varphi n+1/2} - \lambda_c^{\varphi n-1/2}\right) + \Delta t^{n-1/2} \sum_{d\in\mathcal{D}(c)} \dot{V}_{cd}^{\varphi n-1/2} \left(\lambda_d^{\varphi n-1/2} - \lambda_c^{\varphi n-1/2}\right) = 0 \ , \tag{4.28f}$$

$$\sum_{\varphi} \alpha_c^{\varphi n} - 1 = 0 \ . \tag{4.28g}$$

The system (4.28) mimics the continuous Euler–Lagrange equations (4.3) but here it is directly written in grid coordinates : i) Equations (4.28a) and (4.28b) are the mass and Lagrangian coordinate transports of fluid φ ; ii) Equation (4.28c) gives the evolution of the absolute velocity of fluid φ and shows that the presence of the Lin's constraint lifts the irrotational restriction— visible when $\chi_c^{\varphi n} = 0$; — iii) Equations (4.28d) and (4.28e) relate the pressure field to the Lagrange multiplier Π ; iv) Equations (4.28f) are the evolution equations for the Lagrange multipliers $\lambda_c^{\varphi n+1/2}$; and v) Equation (4.28g) ensures the volume conservation in every cell of the mesh.

Velocity variations $\delta \boldsymbol{u}_c^{\varphi n-1/2}$ of fluid φ do not affect off-centering factors $\sigma_{cd}^{\varphi n-1/2}$—they are almost everywhere independent of the relative velocity of fluid φ except in the singular Lagrangian limit where $\boldsymbol{u}^{\boldsymbol{\varphi}} = \mathbf{0}$. The system of equations (4.28) cannot be used in practice because the momentum is only approximately conserved and the pressure gradient in (4.28d) involves external entropy forces (already observed in the single fluid case of [49]). Thus the methodology of the discrete derivation of momentum equations consists in adding corrections on numerical residues and "flux-in-time" terms in order to bring back the conservation of momentum at discrete level, while at the same time preserving the explicit character of velocity equations.

4.3.2.3 Explicit approximation for mass transports

Due to the implicit nature of mass transport, deriving the evolution equations with the discrete version of the Euler–Lagrange equations (4.28) implies solving a *non-local* and *non-linear* set of equations—for each time step and for each fluid. In the single-fluid case of [49], taking an explicit version of the implicit mass transport equation provides similar results than the fully implicit scheme while reducing the computational cost of the simulations. An explicit version of (4.28a) is thus taken by following the principles stated in [49, §2.6] thus yielding

$$V_c^{n+1}[\alpha\rho]_c^{\varphi n+1} - V_c^n[\alpha\rho]_c^{\varphi n} = \Delta t^{n+1/2} \sum_{d\in\mathcal{D}(c)} \left(\dot{V}_{dc}^{\varphi n+1/2}[\alpha\rho]_d^{\varphi n} - \dot{V}_{cd}^{\varphi n+1/2}[\alpha\rho]_c^{\varphi n}\right) . \tag{4.29}$$

From now on, the mass transport of fluid φ is described by the explicit version of mass transport of fluid φ (4.29).

4.3.3 Correction of Euler–Lagrange equations into conservative and explicit equations

The derivation of the momentum evolution equation of fluid φ in the local ALE grid frame is mimicked in an analogous way to the continuous Eulerian derivation done in Section 4.3.1 : i) in Section 4.3.3.1, the Lagrange multiplier associated with volume conservation is substituted by the pressure of the system ; ii) in Section 4.3.3.2, the discrete mimetic momentum evolution equation of fluid φ is derived—for clarity, details of all the algebraic manipulations are postponed to Appendix .4 ; — iii) in Sections 4.3.3.3 and 4.3.3.4, corrections on numerical residues, pressure gradient, and momentum transport term are performed in order to bring back the conservativity and consistency of the momentum equation of fluid φ ; iv) in Section 4.3.3.5, an explicit absolute velocity equation for fluid φ is reconstructed from the conservative momentum equation of fluid φ ; and v) in Section 4.3.3.6, a kinetic energy evolution equation of fluid φ is derived from its conservative momentum evolution equation.

4.3.3.1 Elimination of the Lagrange multiplier Π

The Lagrange multiplier Π is eliminated by substituting (4.28d) into (4.28e) thus yielding

$$\Pi_c^n = -V_c^n \Delta t^n P_c^{\varphi n} \ . \tag{4.30}$$

As in the continuous Eulerian case (4.4), imposing the conservation of volume in the action integral (4.26) automatically leads to the pressure equality between fluids. From now on, only one pressure is considered for the system $P_c^{\varphi n} = P_c^n$.

4.3.3.2 Non-conservative variational momentum equation

The discrete variational momentum equation of fluid φ in the local grid frame is derived by mimicking the continuous Eulerian derivation in Section 4.3.1 in the grid coordinates. All the algebraic manipulations of the derivation are provided in Appendix .4. Starting from the discrete Euler-Lagrange equations in the ALE framework (4.28)—with the explicit mass transport

equation (4.29)—the discrete variational momentum equation of fluid φ is

$$
\begin{aligned}
V_c^{n+1}[\alpha\rho]_c^{\varphi n+1}\boldsymbol{\mu}_c^{\varphi n+1/2} - V_c^{n}[\alpha\rho]_c^{\varphi n}\boldsymbol{\mu}_c^{\varphi n-1/2} = \\
&- \Delta t^n[\alpha\rho]_c^{\varphi n}\sum_{d\in\mathcal{D}(c)}\sigma_{cd}^{\varphi n-1/2}\boldsymbol{s}_{cd}^{n-1/2}\left(e_d^{\varphi n} - e_c^{\varphi n} + P_d^n/\rho_d^{\varphi n} - P_c^n/\rho_c^{\varphi n}\right)\\
&- \Delta t^{n+1/2}\boldsymbol{\mu}_c^{\varphi n+1/2}\sum_{d\in\mathcal{D}(c)}\left(\dot{V}_{cd}^{\varphi n+1/2}[\alpha\rho]_c^{\varphi n} - \dot{V}_{dc}^{\varphi n+1/2}[\alpha\rho]_d^{\varphi n}\right)\\
&- \tfrac{1}{2}\Delta t^{n-1/2}[\alpha\rho]_c^{\varphi n}\sum_{d\in\mathcal{D}(c)}\sigma_{cd}^{\varphi n-1/2}\boldsymbol{s}_{cd}^{n-1/2}\left((\boldsymbol{u}_d^{\varphi n-1/2})^2 - (\boldsymbol{u}_c^{\varphi n-1/2})^2 - (\boldsymbol{w}_d^{\varphi n-1/2})^2 + (\boldsymbol{w}_c^{\varphi n-1/2})^2\right)\\
&- \Delta t^{n-1/2}[\alpha\rho]_c^{\varphi n}\sum_{d\in\mathcal{D}(c)}(\chi_c^{\varphi n} - \chi_d^{\varphi n})\sigma_{cd}^{\varphi n-1/2}\boldsymbol{s}_{cd}^{n-1/2}\\
&\times\frac{\boldsymbol{u}_d^{\varphi n-1/2}}{V_d^n}\sum_{d'\in\mathcal{D}(c)}\sigma_{dd'}^{\varphi n-1/2}\boldsymbol{s}_{dd'}^{n-1/2}(\lambda_{d'}^{\varphi n-1/2} - \lambda_d^{\varphi n-1/2})\\
&+ \Delta t^{n+1/2}\sum_{d\in\mathcal{D}(c)}(\chi_c^{\varphi n+1} - \chi_d^{\varphi n+1})[\alpha\rho]_d^{\varphi n+1}\sigma_{dc}^{\varphi n+1/2}\boldsymbol{s}_{dc}^{n+1/2}\\
&\times\frac{\boldsymbol{u}_d^{\varphi n+1/2}}{V_c^{n+1}}\sum_{d'\in\mathcal{D}(d)}\sigma_{dd'}^{\varphi n+1/2}\boldsymbol{s}_{dd'}^{n+1/2}\left(\lambda_{d'}^{\varphi n+1/2} - \lambda_d^{\varphi n+1/2}\right)\\
&+ V_c^n[\alpha\rho]_c^{\varphi n}\sum_{d\in\mathcal{D}(c)}\left(\frac{\sigma_{cd}^{\varphi n+1/2}\boldsymbol{s}_{cd}^{n+1/2}}{V_c^{n+1}} - \frac{\sigma_{cd}^{\varphi n-1/2}\boldsymbol{s}_{cd}^{n-1/2}}{V_c^n}\right)\\
&\times\left((\phi_d^{\varphi n+1/2} - \phi_c^{\varphi n+1/2}) + \chi_c^{\varphi n}(\lambda_d^{\varphi n+1/2} - \lambda_c^{\varphi n+1/2})\right)\ . \qquad (4.31)
\end{aligned}
$$

The first and second terms on the right hand side of (4.31) contain respectively the variational pressure gradient and momentum transport terms. All the other terms are produced by the discrete variational derivation, and are expected to cancel at the scheme order. The discrete momentum evolution equation of fluid φ must be consistent with its continuous form (4.8b) in the grid coordinates—only a conservative pressure gradient and momentum transport terms are left.

Further corrections must be made in (4.31) in order to ensure several features : i) elimination of Lagrange multipliers ϕ^φ and λ^φ ; ii) conservativity of total momentum—when summing over the fluids—at the discrete level ; and iii) no entropy driven impulse as only pressure forces are retained. The global strategy of the present work is thus to cancel numerical residues at the

scheme order in order to comply with the properties mentioned above.

4.3.3.3 Elimination of entropy residues and conservative pressure gradient

In contrast with the continuous derivation in Section 4.3.1, the discrete variational pressure gradient indirectly appears in the first term of the right hand side of (4.31). It may be separated into

$$
\begin{aligned}
&-\Delta t^n \sum_{d\in\mathcal{D}(c)} \sigma_{cd}^{\varphi n-1/2} \boldsymbol{s}_{cd}^{n-1/2} [\alpha\rho]_c^{\varphi n} \left(e_d^{\varphi n} - e_c^{\varphi n} + P_d^n/\rho_d^{\varphi n} - P_c^n/\rho_c^{\varphi n}\right) \\
&\qquad = -\Delta t^n \sum_{d\in\mathcal{D}(c)} \sigma_{cd}^{\varphi n-1/2} \boldsymbol{s}_{cd}^{n-1/2} \alpha_c^{\varphi n} \left(P_d^n - P_c^n\right) + \mathcal{O}\left[\Delta_x \left(e + P/\rho\right) - \Delta_x P/\rho\right] \ , \quad (4.32)
\end{aligned}
$$

where $\mathcal{O}\left[\Delta_x(e + P/\rho) - \Delta_x P/\rho\right]$ is a numerical entropy residue. This residue is : i) negligible in off shock areas where the flow is mostly isentropic ; and ii) non-negligible elsewhere but dominated by the artificial viscosity stress Q added in the evolution equations in order to stabilize the scheme and capture shocks. In the following $\tilde{P}$ will designate $P + Q$ where the expression of Q is given in Section 4.4.

The pressure gradient in the first term of the right hand side of (4.32) is not yet conservative—it is not written using only flux terms—due to the off-centering factor $\sigma_{cd}^{\varphi n-1/2}$ and the volume fraction term $\alpha_c^{\varphi n}$ of fluid φ. In order to be consistent with the Eulerian continuous pressure gradient in the grid coordinates, the total pressure gradient must be conservative at the discrete level. Following the solution presented in [49], this total pressure gradient can be made conservative by separating the centered and off-centered contributions of σ^{φ}. The centered contribution is already conservative and does not require corrections. The off-centered contribution from cell c to

d and from cell d to c are averaged over their common edge yielding

$$
\begin{aligned}
&c \to d \text{ in } (4.32)_c^{\varphi},\\
&\quad \sigma_{cd}^{\varphi n-1/2} \boldsymbol{s}_{cd}^{n-1/2} \alpha_c^{\varphi n} \left(\tilde{P}_d^n - \tilde{P}_c^n\right)\\
&\quad = \left(\tfrac{1}{2}\alpha_c^{\varphi n} + \alpha_c^{\varphi n}\left(\sigma_{cd}^{\varphi n-1/2} - \tfrac{1}{2}\right)\right) \boldsymbol{s}_{cd}^{n-1/2} \left(\tilde{P}_d^n - \tilde{P}_c^n\right)\\
&\quad = \left(\tfrac{1}{2}\alpha_c^{\varphi n} + \tfrac{1}{2}\alpha_c^{\varphi n}\left(\sigma_{cd}^{\varphi n-1/2} - \tfrac{1}{2}\right) - \tfrac{1}{2}\alpha_d^{\varphi n}\left(\sigma_{dc}^{\varphi n-1/2} - \tfrac{1}{2}\right)\right) \boldsymbol{s}_{cd}^{n-1/2} \left(\tilde{P}_d^n - \tilde{P}_c^n\right)\\
&\qquad\qquad + \mathcal{O}\left[\Delta_x(\alpha^{\varphi}\sigma^{\varphi}s)\Delta_x(\tilde{P})\right]\\
&\quad = \tfrac{1}{2}\left(\frac{\alpha_c^{\varphi n} + \alpha_d^{\varphi n}}{2} + \alpha_c^{\varphi n}\sigma_{cd}^{\varphi n-1/2} - \alpha_d^{\varphi n}\sigma_{dc}^{\varphi n-1/2}\right) \boldsymbol{s}_{cd}^{n-1/2} \left(\tilde{P}_d^n - \tilde{P}_c^n\right)\\
&\qquad\qquad + \mathcal{O}\left[\Delta_x(\alpha^{\varphi}\sigma^{\varphi}s)\Delta_x(\tilde{P})\right] \quad , \qquad (4.33a)\\
&d \to c \text{ in } (4.32)_d^{\varphi},\\
&\quad \sigma_{dc}^{\varphi n-1/2} \boldsymbol{s}_{dc}^{n-1/2} \alpha_d^{\varphi n} \left(\tilde{P}_c^n - \tilde{P}_d^n\right)\\
&\quad = \tfrac{1}{2}\left(\frac{\alpha_d^{\varphi n} + \alpha_c^{\varphi n}}{2} + \alpha_d^{\varphi n}\sigma_{dc}^{\varphi n-1/2} - \alpha_c^{\varphi n}\sigma_{cd}^{\varphi n-1/2}\right) \boldsymbol{s}_{dc}^{n-1/2} \left(\tilde{P}_c^n - \tilde{P}_d^n\right)\\
&\qquad\qquad + \mathcal{O}\left[\Delta_x(\alpha^{\varphi}\sigma^{\varphi}s)\Delta_x(\tilde{P})\right] \quad . \qquad (4.33b)
\end{aligned}
$$

Off-centered contributions in (4.33a) and (4.33b) are exactly opposite up to numerical residues which cancel almost everywhere if $\boldsymbol{u}^{\boldsymbol{\varphi}} \neq \mathbf{0}$ for $\Delta x \longrightarrow 0$. The approximation done on the pressure gradient is actually exact at edges where transport has constant direction. The total pressure gradient in cell c—given by $\sum_{\varphi}$ (4.33a)—is now fully conservative at discrete level up to round-off errors.

4.3.3.4 Momentum evolution equation of fluid φ

Mimicking the continuous derivation for (4.8b) in the grid coordinates, a conservative momentum transport term of fluid φ that mirrors mass advection is obtained by performing a discrete integration by parts of the second term on the right hand side of (4.31). Inserting the corrected pressure gradient of fluid φ from (4.33a), the conservative momentum transport term of fluid φ and neglecting all the numerical residues coming from the discrete variational derivation, (4.31)

becomes

$$
\begin{aligned}
&V_c^{n+1}[\alpha\rho]_c^{\varphi n+1}\boldsymbol{\mu}_c^{\varphi n+1/2} - V_c^{n}[\alpha\rho]_c^{\varphi n}\boldsymbol{\mu}_c^{\varphi n-1/2} \\
&\qquad = -\Delta t^n \sum_{d\in\mathcal{D}(c)} \tfrac{1}{2}\boldsymbol{s}_{cd}^{n-1/2}\left(\frac{\alpha_c^{\varphi n}+\alpha_d^{\varphi n}}{2} + \alpha_c^{\varphi n}\sigma_{cd}^{\varphi n-1/2} - \alpha_d^{\varphi n}\sigma_{dc}^{\varphi n-1/2}\right)\left(\tilde{P}_d^n - \tilde{P}_c^n\right) \\
&\qquad\qquad - \Delta t^{n+1/2}\sum_{d\in\mathcal{D}(c)}\left(\dot{V}_{cd}^{\varphi n+1/2}\boldsymbol{\mu}_c^{\varphi n+1/2}[\alpha\rho]_c^{\varphi n} - \dot{V}_{dc}^{\varphi n+1/2}\boldsymbol{\mu}_d^{\varphi n+1/2}[\alpha\rho]_d^{\varphi n}\right) . \quad (4.34)
\end{aligned}
$$

The momentum equation of fluid φ (4.34) is consistent with the continuous momentum equation (4.8b) in the grid coordinates and conservative at the discrete level when summing over all the fluids. Discrete variational integrators can be either symplectic–momentum or energy–momentum [49]. In the present paper, emphasis is set on *exact* conservation, numerical residues coming from the discrete derivation of absolute and momentum evolution equations must thus be cancelled in order to bring back the conservative property of the momentum. The discrete derivation of the scheme is thus variational but not exactly symplectic. However, the discrete symplectic derivation, if not fully pursued, has given the needed compatibility of the main terms, notably between mass and momentum transports and pressure gradient term. Indeed, advection of both mass and momentum is computed with the same *upwind* discretization but the pressure gradient possesses a *downwind* structure when fluids are advected with a uniform velocity. A similar dual structure is found for the single-fluid variational GEECS method [49, eq. 23].

4.3.3.5 Explicit absolute velocity equation and compatible momentum equation of fluid φ

The momentum evolution equation of fluid φ (4.34) cannot be easily solved due to the implicit factor $[\alpha\rho]_c^{\varphi n+1}$ on its left hand side. One solution consists in solving the absolute velocity equation of fluid φ instead. Equation (86) must thus be reconstructed from the combination (4.34) $-\ \boldsymbol{\mu}_c^{\varphi n+1/2} \times$ (4.29) so as to include the corrections on pressure gradient and residual terms

performed in Sections 4.3.3.4 and 4.3.3.3 yielding

$$
\begin{aligned}
&V_c^n[\alpha\rho]_c^{\varphi n}\left(\boldsymbol{\mu}_c^{\varphi n+1/2}-\boldsymbol{\mu}_c^{\varphi n-1/2}\right)\\
&\quad=-\Delta t^n\sum_{d\in\mathcal{D}(c)}\tfrac{1}{2}\boldsymbol{s}_{cd}^{n-1/2}\left(\frac{\alpha_c^{\varphi n}+\alpha_d^{\varphi n}}{2}+\alpha_c^{\varphi n}\sigma_{cd}^{\varphi n-1/2}-\alpha_d^{\varphi n}\sigma_{dc}^{\varphi n-1/2}\right)\left(\tilde{P}_d^n-\tilde{P}_c^n\right)\\
&\qquad+\Delta t^{n+1/2}\sum_{d\in\mathcal{D}(c)}\dot{V}_{dc}^{\varphi n+1/2}[\alpha\rho]_d^{\varphi n}\left(\boldsymbol{\mu}_d^{\varphi n+1/2}-\boldsymbol{\mu}_c^{\varphi n+1/2}\right)\ . \qquad (4.35)
\end{aligned}
$$

The equation (4.35) is explicit except for the last off-centered gradient of $\boldsymbol{\mu}^{\varphi}$. A fully explicit absolute velocity equation of fluid φ is then obtained by using the solution elaborated in [33, 49] which consists in transforming the last term of (4.35) into a time flux term. The resulting explicit absolute velocity equation is then

$$
\begin{aligned}
&V_c^n[\alpha\rho]_c^{\varphi n}\left(\boldsymbol{\mu}_c^{\varphi n+1/2}-\boldsymbol{\mu}_c^{\varphi n-1/2}\right)\\
&\quad=-\Delta t^n\sum_{d\in\mathcal{D}(c)}\tfrac{1}{2}\boldsymbol{s}_{cd}^{n-1/2}\left(\frac{\alpha_c^{\varphi n}+\alpha_d^{\varphi n}}{2}+\alpha_c^{\varphi n}\sigma_{cd}^{\varphi n-1/2}-\alpha_d^{\varphi n}\sigma_{dc}^{\varphi n-1/2}\right)\left(\tilde{P}_d^n-\tilde{P}_c^n\right)\\
&\qquad+\Delta t^{n-1/2}\sum_{d\in\mathcal{D}(c)}\dot{V}_{dc}^{n-1/2}[\alpha\rho]_d^{\varphi n-1}\left(\boldsymbol{\mu}_d^{\varphi n-1/2}-\boldsymbol{\mu}_c^{\varphi n-1/2}\right)\ , \qquad (4.36)
\end{aligned}
$$

where (4.36) $=$ (4.35) $+\,\theta^{\varphi n+1}-\theta^{\varphi n}$ with $\theta^n=\Delta t^{n-1/2}\sum_{d\in\mathcal{D}(c)}\dot{V}_{dc}^{n-1/2}[\alpha\rho]_d^{\varphi n-1}\left(\boldsymbol{\mu}_d^{\varphi n-1/2}-\boldsymbol{\mu}_c^{\varphi n-1/2}\right)$. It can be observed that $\theta^{n+1}-\theta^n$ is a correction at the scheme order. The absolute velocity equation of fluid φ (4.36) is now fully explicit and can be easily discretized for each fluid φ. The time flux term $\theta^{\varphi n+1}-\theta^{\varphi n}$ can now be inserted into the momentum equation of fluid φ (4.34) in order to keep a consistent link between the absolute velocity and momentum equations of fluid φ.

Equation (4.34) thus becomes

$$
\begin{aligned}
&V_c^{n+1}[\alpha\rho]_c^{\varphi n+1}\boldsymbol{\mu}_c^{\varphi n+1/2} - V_c^{n}[\alpha\rho]_c^{\varphi n}\boldsymbol{\mu}_c^{\varphi n-1/2} \\
&\quad = -\Delta t^n \sum_{d\in\mathcal{D}(c)} \tfrac{1}{2}\boldsymbol{s}_{cd}^{n-1/2}\left(\frac{\alpha_c^{\varphi n}+\alpha_d^{\varphi n}}{2} + \alpha_c^{\varphi n}\sigma_{cd}^{\varphi n-1/2} - \alpha_d^{\varphi n}\sigma_{dc}^{\varphi n-1/2}\right)\left(\tilde{P}_d^n - \tilde{P}_c^n\right) \\
&\qquad - \Delta t^{n+1/2}\sum_{d\in\mathcal{D}(c)}\left(\dot{V}_{cd}^{\varphi n+1/2}\boldsymbol{\mu}_c^{\varphi n+1/2}[\alpha\rho]_c^{\varphi n} - \dot{V}_{dc}^{\varphi n+1/2}\boldsymbol{\mu}_d^{\varphi n+1/2}[\alpha\rho]_d^{\varphi n}\right) \\
&\qquad\quad - \Delta t^{n+1/2}\sum_{d\in\mathcal{D}(c)}\dot{V}_{dc}^{\varphi n+1/2}[\alpha\rho]_d^{\varphi n+1}\left(\boldsymbol{\mu}_d^{\varphi n+1/2} - \boldsymbol{\mu}_c^{\varphi n+1/2}\right) \\
&\qquad\quad + \Delta t^{n-1/2}\sum_{d\in\mathcal{D}(c)}\dot{V}_{dc}^{\varphi n-1/2}[\alpha\rho]_d^{\varphi n-1}\left(\boldsymbol{\mu}_d^{\varphi n-1/2} - \boldsymbol{\mu}_c^{\varphi n-1/2}\right) . \qquad (4.37)
\end{aligned}
$$

4.3.3.6 Kinetic energy evolution equation of fluid φ

The kinetic energy evolution equation of fluid φ is obtained from (4.37)$\times\frac{1}{2}\left(\boldsymbol{\mu}_c^{\varphi n+1/2}+\boldsymbol{\mu}_c^{\varphi n-1/2}\right)$− (4.29) $\times\ \frac{1}{2}\left(\boldsymbol{\mu}_c^{\varphi n+1/2}\cdot\boldsymbol{\mu}_c^{\varphi n-1/2}\right)$ as

$$
\begin{aligned}
&\tfrac{1}{2}V_c^{n+1}[\alpha\rho]_c^{\varphi n+1}\left(\boldsymbol{\mu}_c^{\varphi n+1/2}\right)^2 - \tfrac{1}{2}V_c^{n}[\alpha\rho]_c^{\varphi n}\left(\boldsymbol{\mu}_c^{\varphi n-1/2}\right)^2 \\
&= -\tfrac{1}{2}\Delta t^n\sum_{d\in\mathcal{D}(c)}\tfrac{1}{2}\boldsymbol{s}_{cd}^{n-1/2}\cdot\left(\boldsymbol{\mu}_c^{\varphi n+1/2}+\boldsymbol{\mu}_c^{\varphi n-1/2}\right)\left(\tfrac{\alpha_c^{\varphi n}+\alpha_d^{\varphi n}}{2} + \alpha_c^{\varphi n}\sigma_{cd}^{\varphi n-1/2} - \alpha_d^{\varphi n}\sigma_{dc}^{\varphi n-1/2}\right)\left(\tilde{P}_d^n - \tilde{P}_c^n\right) \\
&\qquad - \tfrac{1}{2}\Delta t^{n+1/2}\sum_{d\in\mathcal{D}(c)}\left(\dot{V}_{cd}^{\varphi n+1/2}\left(\boldsymbol{\mu}_c^{\varphi n+1/2}\right)^2[\alpha\rho]_c^{\varphi n} - \dot{V}_{dc}^{\varphi n+1/2}\left(\boldsymbol{\mu}_d^{\varphi n+1/2}\right)^2[\alpha\rho]_d^{\varphi n}\right) \\
&\qquad - \tfrac{1}{2}\Delta t^{n+1/2}\sum_{d\in\mathcal{D}(c)}\dot{V}_{dc}^{\varphi n+1/2}[\alpha\rho]_d^{\varphi n}\left(\boldsymbol{\mu}_d^{\varphi n+1/2}+\boldsymbol{\mu}_c^{\varphi n+1/2}\right)\cdot\left(\boldsymbol{\mu}_d^{\varphi n+1/2}-\boldsymbol{\mu}_c^{\varphi n+1/2}\right) \\
&\qquad + \tfrac{1}{2}\Delta t^{n-1/2}\sum_{d\in\mathcal{D}(c)}\dot{V}_{dc}^{\varphi n-1/2}[\alpha\rho]_d^{\varphi n-1}\left(\boldsymbol{\mu}_c^{\varphi n+1/2}+\boldsymbol{\mu}_c^{\varphi n-1/2}\right)\cdot\left(\boldsymbol{\mu}_d^{\varphi n-1/2}-\boldsymbol{\mu}_c^{\varphi n-1/2}\right) . \qquad (4.38)
\end{aligned}
$$

This equation displays the following features : i) the first term on the right hand side is the work of the pressure forces for the fluid φ in its momentum equation (4.37) ; ii) the second term on the right hand side is a conservative kinetic energy transport term obtained by a discrete integration by parts similarly to what was performed in Section 4.3.3.4 for the momentum transport term in (4.34) ; and iii) the last two terms of (4.38) represent numerical residues produced by discrete integration by parts and time-flux terms.

4.3.4 Internal energy evolution equation of fluid φ

As already presented in Section 4.3.1.6, the continuous version of the continuous Eulerian internal energy evolution equation (4.11) makes explicitly visible the processes associated with the pressure work in a thermodynamically consistent way. However, the form of (4.11) cannot be consistently discretized in the ALE framework. In Section 4.3.1.6, another expression of (4.11) has been derived in the continuous case which can be easily discretized in the ALE framework

$$\begin{aligned}\partial_t\left(\alpha^\varphi\rho^\varphi e^\varphi\right)+\left(\alpha^\varphi\rho^\varphi e^\varphi w_i\right)_{,i}&=\beta^\varphi P_{,i}\left(\sum_\phi \alpha^\phi u_i^\phi\right)-\beta^\varphi P w_{i,i}\\&-\beta^\varphi\sum_\phi\left(\alpha^\phi\left(\rho^\phi e^\phi+P\right)u_i^\phi\right)_{,i}-\sum_\phi\left(e^\varphi\left(\alpha^\varphi\rho^\varphi u_i^\varphi\right)_{,i}-\beta^\varphi e^\phi\left(\alpha^\phi\rho^\phi u_i^\phi\right)_{,i}\right)\ .\end{aligned}\tag{4.39}$$

In the present work, each term of (4.39) has to be consistently discretized using the mass transport operator and the expression of pressure forces in the kinetic energy equation (4.38).

4.3.4.1 Pressure work associated with relative velocity

The first term in the right hand side of (4.39) represents the work of pressure forces associated with the relative-to-grid velocity $\boldsymbol{u}^\varphi$. It can be decomposed into two contributions depending on both grid and absolute velocity according to (4.21) as

$$\beta^\varphi P_{,i}\sum_\phi \alpha^\phi u_i^\phi=-\beta^\varphi P_{,i}\sum_\phi \alpha^\phi w_i+\beta^\varphi P_{,i}\sum_\phi \alpha^\phi \mu_i^\phi\ .\tag{4.40}$$

The first term of (4.40) is consistently discretized using the expression of the total kinetic energy equation $\sum_\phi$ (4.38) with $\boldsymbol{\mu^\varphi}=w$—thus implying $\boldsymbol{u}=0$—and with opposite sign for total energy conservation. It comes

$$-\beta^\varphi P_{,i}\sum_\phi \alpha^\phi w_i\ \rightsquigarrow\ -\tfrac{1}{2}\beta_c^{\varphi n}\Delta t^n\sum_{d\in\mathcal{D}(c)}\left(\tilde{P}_d^{\varphi n}-\tilde{P}_c^{\varphi n}\right)\boldsymbol{s}_{cd}^{n-1/2}\cdot\bar{\boldsymbol{w}}_c^n\ ,\tag{4.41}$$

where according to the continuous relationships $\tilde{P}_c^{\varphi n}=P_c^n+Q_c^{\varphi n}$ (see (4.16)). $\bar{\boldsymbol{w}}_c^n$ is the discrete volume averaged grid velocity, and $\beta_c^{\varphi n}$ are the discrete relative compressibility coefficients defined

by

$$\bar{\boldsymbol{w}}_c^n = \tfrac{1}{2}\sum_\phi \left(\frac{\alpha_c^{\phi n} + \alpha_d^{\phi n}}{2} + \alpha_c^{\phi n}\sigma_{cd}^{\phi n-1/2} - \alpha_d^{\phi n}\sigma_{dc}^{\phi n-1/2} \right) \left(\boldsymbol{w}_c^{n+1/2} + \boldsymbol{w}_c^{n-1/2} \right) , \tag{4.42a}$$

$$\beta_c^{\varphi n} = \frac{\alpha_c^{\varphi n}/\gamma^\varphi}{\sum_\phi \alpha_c^{\phi n}/\gamma^\phi} . \tag{4.42b}$$

The second term of (4.40) is consistently discretized using the expression of the total kinetic energy equation $\sum_\varphi$ (4.38) with opposite sign for total energy conservation, which yields

$$\begin{aligned} \beta^\varphi P_{,i} \sum_\phi \alpha^\phi \mu_i^\phi \rightsquigarrow\ & \tfrac{1}{2}\beta_c^{\varphi n}\Delta t^n \sum_{d\in\mathcal{D}(c)} \left(\tilde{P}_d^{\varphi n} - \tilde{P}_c^{\varphi n} \right) \boldsymbol{s}_{cd}^{n-1/2} \cdot \bar{\boldsymbol{\mu}}_c^n \\ & + \tfrac{1}{2}\beta_c^{\varphi n}\Delta t^{n+1/2} \sum_{\phi,d\in\mathcal{D}(c)} \dot{V}_{dc}^{\phi n+1/2} \left(\boldsymbol{\mu}_d^{\phi n+1/2} + \boldsymbol{\mu}_c^{\phi n+1/2} \right) \cdot \left(\boldsymbol{\mu}_d^{\phi n+1/2} - \boldsymbol{\mu}_c^{\phi n+1/2} \right) [\alpha\rho]_d^{\phi n} \\ & - \tfrac{1}{2}\beta_c^{\varphi n}\Delta t^{n-1/2} \sum_{\phi,d\in\mathcal{D}(c)} \dot{V}_{dc}^{\phi n-1/2} \left(\boldsymbol{\mu}_c^{\phi n+1/2} + \boldsymbol{\mu}_c^{\phi n-1/2} \right) \cdot \left(\boldsymbol{\mu}_d^{\phi n-1/2} - \boldsymbol{\mu}_c^{\phi n-1/2} \right) [\alpha\rho]_d^{\phi n-1} , \end{aligned} \tag{4.43}$$

where the discrete volume averaged absolute velocity $\bar{\boldsymbol{\mu}}_c^n$ is defined as

$$\bar{\boldsymbol{\mu}}_c^n = \tfrac{1}{2}\sum_\phi \left(\frac{\alpha_c^{\phi n} + \alpha_d^{\phi n}}{2} + \alpha_c^{\phi n}\sigma_{cd}^{\phi n-1/2} - \alpha_d^{\phi n}\sigma_{dc}^{\phi n-1/2} \right) \left(\boldsymbol{\mu}_c^{\phi n+1/2} + \boldsymbol{\mu}_c^{\phi n-1/2} \right) . \tag{4.44}$$

It must be noted that last two terms on the right hand side of (4.43) are numerical residues coming form the discrete integration by parts of momentum and kinetic energy transport terms. They must be transposed in the internal energy equation of fluid φ in order to ensure total energy conservation at discrete level—only flux terms must remain when summing total kinetic and internal energy equations.

Eventually, the discrete expression of the work of pressure forces associated with the relative-

to-grid velocity $\boldsymbol{u}^{\varphi}$ (4.40) is obtained by summing (4.41) and (4.43) yielding

$$\begin{aligned}
\beta^{\varphi} P_{,i} \sum_{\phi} \alpha^{\phi} u_i^{\phi} \;\rightsquigarrow\; & \tfrac{1}{2}\beta_c^{\varphi n}\Delta t^n \sum_{d\in\mathcal{D}(c)} \left(\tilde{P}_d^{\varphi n} - \tilde{P}_c^{\varphi n}\right) \boldsymbol{s}_{cd}^{n-1/2} \cdot \bar{\boldsymbol{u}}_c^n \\
& + \tfrac{1}{2}\beta_c^{\varphi n}\Delta t^{n+1/2} \sum_{\phi, d\in\mathcal{D}(c)} \dot{V}_{dc}^{\phi n+1/2} \left(\boldsymbol{\mu}_d^{\phi n+1/2} + \boldsymbol{\mu}_c^{\phi n+1/2}\right) \cdot \left(\boldsymbol{\mu}_d^{\phi n+1/2} - \boldsymbol{\mu}_c^{\phi n+1/2}\right) [\alpha\rho]_d^{\phi n} \\
& - \tfrac{1}{2}\beta_c^{\varphi n}\Delta t^{n-1/2} \sum_{\phi, d\in\mathcal{D}(c)} \dot{V}_{dc}^{\phi n-1/2} \left(\boldsymbol{\mu}_c^{\phi n+1/2} + \boldsymbol{\mu}_c^{\phi n-1/2}\right) \cdot \left(\boldsymbol{\mu}_d^{\phi n-1/2} - \boldsymbol{\mu}_c^{\phi n-1/2}\right) [\alpha\rho]_d^{\phi n-1} \;, \qquad (4.45)
\end{aligned}$$

where the discrete volume averaged relative velocity $\bar{\boldsymbol{u}}_c^n$ is defined as

$$\bar{\boldsymbol{u}}_c^n = \tfrac{1}{2} \sum_{\phi} \left(\frac{\alpha_c^{\phi n} + \alpha_d^{\phi n}}{2} + \alpha_c^{\phi n}\sigma_{cd}^{\phi n-1/2} - \alpha_d^{\phi n}\sigma_{dc}^{\phi n-1/2} \right) \left(\boldsymbol{u}_c^{\phi n+1/2} + \boldsymbol{u}_c^{\phi n-1/2}\right) \;. \qquad (4.46)$$

4.3.4.2 Pressure work associated with grid velocity

The second term of (4.39) represents the internal energy production through volume changes associated with the grid velocity $\boldsymbol{w}$. This term is discretized as a geometric gradient between cells c and d yielding

$$-\beta^{\varphi} P w_{i,i} \;\rightsquigarrow\; -\tfrac{1}{4}\beta_c^{\varphi n}\Delta t^n P_c^n \sum_{d\in\mathcal{D}(c)} \boldsymbol{s}_{cd}^{n-1/2} \cdot \left(w_c^{n+1/2} + w_c^{n-1/2} + w_d^{n+1/2} + w_d^{n-1/2}\right) \;. \qquad (4.47)$$

4.3.4.3 Conservative enthalpy advection

The third term of (4.39) is the enthalpy transport term. The expression of this transport term must be consistent with the swept-flux volume transfers in the mass transport operator of fluid φ (4.29) because internal energy transport operators must match entropy operators—with are

identical to mass transport operators. It yields

$$
\begin{aligned}
-\beta^{\varphi}\sum_{\phi}\left(\alpha^{\phi}(\rho^{\phi}e^{\phi}+P)u_i^{\phi}\right)_{,i} \rightsquigarrow \\
-\beta_c^{\varphi n}\Delta t^{n+1/2}\sum_{\phi,d\in\mathcal{D}(c)}\Big(\dot{V}_{cd}^{\phi n+1/2}\left(\alpha_c^{\phi n}\left(\rho_c^{\phi n}e_c^{\phi n}+P_c^n\right)\right) \\
-\dot{V}_{dc}^{\phi n+1/2}\left(\alpha_d^{\phi n}\left(\rho_d^{\phi n}e_d^{\phi n}+P_d^n\right)\right)\Big) \quad . \quad (4.48)
\end{aligned}
$$

4.3.4.4 Exchange terms between fluids

The last two terms of (4.39) correspond to internal energy exchanges between fluids through relative drift. These terms are consistently discretized using the expression of the conservative discrete divergence operators for mass, momentum and internal energy thus yielding

$$
\begin{aligned}
-\sum_{\phi}\left(e^{\varphi}(\alpha^{\varphi}\rho^{\varphi}u_i^{\varphi})_{,i}-\beta^{\varphi}e^{\phi}(\alpha^{\phi}\rho^{\phi}u_i^{\phi})_{,i}\right) \\
\rightsquigarrow -\Delta t^{n+1/2}\sum_{\phi,d\in\mathcal{D}(c)}\Big(e_c^{\varphi n}\left(\dot{V}_{cd}^{\varphi n+1/2}[\alpha\rho]_c^{\varphi n}-\dot{V}_{dc}^{\varphi n+1/2}[\alpha\rho]_d^{\varphi n}\right) \\
-\beta_c^{\varphi n}e_c^{\phi n}\left(\dot{V}_{cd}^{\phi n+1/2}[\alpha\rho]_c^{\phi n}-\dot{V}_{dc}^{\phi n+1/2}[\alpha\rho]_d^{\phi n}\right)\Big) \quad . \quad (4.49)
\end{aligned}
$$

4.3.4.5 Internal energy equation of fluid φ

Eventually, an internal energy evolution equation of fluid φ is obtained using the expressions derived in Sections 4.3.4.1, 4.3.4.2, 4.3.4.3, and 4.3.4.4 yielding

$$
\begin{aligned}
V_c^{n+1}[\alpha\rho]_c^{\varphi n+1}e_c^{\varphi n+1} - V_c^{n}[\alpha\rho]_c^{\varphi n}e_c^{\varphi n} = & \underbrace{\tfrac{1}{2}\beta_c^{\varphi n}\Delta t^n \sum_{d\in\mathcal{D}(c)} \left(\tilde{P}_d^{\varphi n} - \tilde{P}_c^{\varphi n}\right) \boldsymbol{s}_{cd}^{n-1/2}\cdot\bar{\boldsymbol{u}}_c^n}_{\text{Pressure work associated with the relative velocity}} \\
& \underbrace{-\tfrac{1}{4}\beta_c^{\varphi n}\Delta t^n P_c^n \sum_{d\in\mathcal{D}(c)} \boldsymbol{s}_{cd}^{n-1/2}\cdot\left(w_c^{n+1/2} + w_c^{n-1/2} + w_d^{n+1/2} + w_d^{n-1/2}\right)}_{\text{Pressure work associated with the grid velocity}} \\
& \underbrace{-\beta_c^{\varphi n}\Delta t^{n+1/2} \sum_{\phi,d\in\mathcal{D}(c)} \left(\dot{V}_{cd}^{\phi n+1/2}\alpha_c^{\phi n}\left(\rho_c^{\phi n}e_c^{\phi n} + P_c^n\right) - \dot{V}_{dc}^{\phi n+1/2}\alpha_d^{\phi n}\left(\rho_d^{\phi n}e_d^{\phi n} + P_d^n\right)\right)}_{\text{Enthalpy advection}} \\
& \underbrace{+\tfrac{1}{2}\beta_c^{\varphi n}\Delta t^{n+1/2} \sum_{\phi,d\in\mathcal{D}(c)} \dot{V}_{dc}^{\phi n+1/2}\left(\boldsymbol{\mu}_d^{\phi n+1/2} + \boldsymbol{\mu}_c^{\phi n+1/2}\right)\cdot\left(\boldsymbol{\mu}_d^{\phi n+1/2} - \boldsymbol{\mu}_c^{\phi n+1/2}\right)[\alpha\rho]_d^{\phi n}}_{\text{Residue from kinetic energy}} \\
& \underbrace{-\tfrac{1}{2}\beta_c^{\varphi n}\Delta t^{n-1/2} \sum_{\phi,d\in\mathcal{D}(c)} \dot{V}_{dc}^{\phi n-1/2}\left(\boldsymbol{\mu}_c^{\phi n+1/2} + \boldsymbol{\mu}_c^{\phi n-1/2}\right)\cdot\left(\boldsymbol{\mu}_d^{\phi n-1/2} - \boldsymbol{\mu}_c^{\phi n-1/2}\right)[\alpha\rho]_d^{\phi n-1}}_{\text{Residue from kinetic energy}} \\
& \underbrace{+\beta_c^{\varphi n}\Delta t^{n+1/2} \sum_{\phi,d\in\mathcal{D}(c)} e_c^{\phi n}\left(\dot{V}_{cd}^{\phi n+1/2}[\alpha\rho]_c^{\phi n} - \dot{V}_{dc}^{\phi n+1/2}[\alpha\rho]_d^{\phi n}\right)}_{\text{Exchange from fluids } \phi \text{ to fluid } \varphi} \\
& \underbrace{-\Delta t^{n+1/2} \sum_{d\in\mathcal{D}(c)} e_c^{\varphi n}\left(\dot{V}_{cd}^{\varphi n+1/2}[\alpha\rho]_c^{\varphi n} - \dot{V}_{dc}^{\varphi n+1/2}[\alpha\rho]_d^{\varphi n}\right)}_{\text{Exchange from fluid } \varphi \text{ to fluids } \phi}, \qquad (4.50)
\end{aligned}
$$

where $\tilde{P}_c^{\varphi n} = P_c^{\varphi n} + Q_c^{\varphi n}$ and the discrete volume averaged relative velocity $\bar{\boldsymbol{u}}_c^n$ is given by (4.46).

4.3.5 Instantaneous pressure equilibrium

At the end of the cycle, both $[\alpha\rho]^{\varphi n+1}$ and $e^{\varphi n+1}$ are available by solving (4.29) and (4.50) respectively, but $\alpha^{\varphi n+1}$ and P^{n+1} need to be computed. These two quantities are simultaneously

obtained by solving the following identities

$$\sum_{\phi} \alpha_c^{\phi n+1} = 1 \ , \tag{4.51a}$$

$$P = P_c^{\varphi n+1} \qquad \forall \varphi \ , \tag{4.51b}$$

where P^{φ} are provided by the equations of state of the fluids. The system (4.51) is *local* and has *explicit* solutions for perfect and stiffened gas equations of state. For example, in the case of perfect gases P^{φ} is linked to ρ^{φ} and e^{φ} through the relationship $P^{\varphi} = (\gamma^{\varphi} - 1)\rho^{\varphi} e^{\varphi}$ where γ^{φ} the isentropic coefficient of the fluid. The solutions of (4.51) are thus

$$\alpha_c^{\varphi n+1} = \frac{(\gamma^{\varphi} - 1)[\alpha\rho]_c^{\varphi n+1} e_c^{\varphi n+1}}{\sum_{\phi}(\gamma^{\phi} - 1)[\alpha\rho]_c^{\phi n+1} e_c^{\phi n+1}} \ , \tag{4.52a}$$

$$P = \sum_{\phi}(\gamma^{\phi} - 1)[\alpha\rho]_c^{\phi n+1} e_c^{\phi n+1} \ . \tag{4.52b}$$

For more elaborated equations of state—which is beyond the goal of this work —(4.51) can be solved using an iterative Newton–Raphson method.

4.4 Summary of the multiGEECS algorithm

For clarity, a summary of the steps of the multiGEECS algorithm, together with definitions of time step and artificial viscosity, is presented in this section.

The time step of the simulation $\Delta t^{n+1/2}$ is bounded by a simple CFL condition involving the mixture sound velocity and the fluid advection velocity according to

$$\Delta t^{n+1/2} = \mathrm{CFL} \times \min_{\varphi,c} \left(\frac{\Delta_c^n}{C_c^n + |\boldsymbol{\mu}_c^{\varphi n-1/2}|} \right) \ , \tag{4.53}$$

where Δ_c^n is a characteristic length scale—here the length of the smallest diagonal and median—of cell c at time t^n, and C_c^n is the sound velocity of the mixture. For a zero drag force, C_c^n is expressed using the relative compressibility coefficients (4.42b) and the sound velocities of the

fluids as

$$(C_c^n)^2 = \sum_\phi \beta_c^{\phi n} \left(C_c^{\phi n}\right)^2 , \qquad \text{with,} \qquad C_c^{\phi n} = \sqrt{\frac{\gamma^\phi P_c^n}{\rho_c^{\phi n}}} . \tag{4.54}$$

As for purely Lagrangian schemes [9, 51, 36], an artificial viscosity term Q is added in the equations in order to stabilize the scheme and to capture shocks. In the present work, this artificial viscosity term must take into account the contrast between the fluid compressibilities. The expression of Q is thus discretized from the continuous formulation of the artificial viscosity stress (4.17) as

$$\begin{aligned} Q_c^{\varphi n} = -a_1 \rho_c^{\varphi n} C_c^{\varphi n} \left(\frac{\beta_c^{\varphi n}}{\alpha_c^{\varphi n}} \left(\sum_{d \in \mathcal{D}(c)} \left(\boldsymbol{s}_{cd}^{n-1/2} \cdot \bar{\boldsymbol{u}}_c^n + \boldsymbol{s}_{cd}^{n-1/2} \cdot \bar{\boldsymbol{u}}_d^n \right) \right) \right) \\ + \tfrac{1}{2} a_2 (\gamma^\varphi + 1) \rho_c^{\varphi n} \left(\frac{\beta_c^{\varphi n}}{\alpha_c^{\varphi n}} \min \left(0, \left(\sum_{d \in \mathcal{D}(c)} \left(\boldsymbol{s}_{cd}^{n-1/2} \cdot \bar{\boldsymbol{u}}_c^n + \boldsymbol{s}_{cd}^{n-1/2} \cdot \bar{\boldsymbol{u}}_d^n \right) \right) \right) \right)^2 , \end{aligned} \tag{4.55}$$

where the discrete volume averaged relative velocity $\bar{\boldsymbol{u}}_c^n$ is given by (4.46).

As in the continuous case (4.18), the total artificial viscosity stress is given by $Q_c^n = \sum_\phi \beta_c^{\phi n} Q_c^{\phi n}$. The shock sensor of (4.55) is based on the relative velocity variables of fluid φ of the cells, which is off-centered with the same structure as for the pressure work term in (4.50). This ensures that the work of $Q_c^{\varphi n}$ always remains positive.

Starting from the main quantities at time t^n, the multiGEECS time step to t^{n+1} consists in the successive applications of the following equations for each fluid φ

At t^n	$\Delta t^{n-1/2}\boldsymbol{\mu}_c^{\varphi n-1/2}$	$\boldsymbol{w}_p^{n-1/2}\boldsymbol{x}_p^n$	$\boldsymbol{u}_c^{\varphi n-1/2}\sigma_{cd}^{\varphi n-1/2}$	$[\alpha\rho]_c^{\varphi n}Q_c^{\varphi n}$	$e_c^{\varphi n}\alpha_c^{\varphi n}$	P_c^n
(4.53)	$\Delta t^{n+1/2}$					
(4.36)	$\boldsymbol{\mu}_c^{\varphi n+1/2}$					
see .3		$\boldsymbol{w}_p^{n+1/2}$				
(4.20)		$\boldsymbol{x}_p^{n+1}$				
(4.21)			$\boldsymbol{u}_c^{\varphi n+1/2}$			
(4.23)			$\sigma_{cd}^{\varphi n+1/2}$			
(4.29)				$[\alpha\rho]_c^{\varphi n+1}$		
(4.55)				$Q_c^{\varphi n+1}$		
(4.50)					$e_c^{\varphi n+1}$	
(4.52)					$\alpha_c^{\varphi n+1}$	P_c^{n+1}

4.5 Two-dimensional numerical results

The behavior of multiGEECS is analyzed by performing several two-dimensional benchmark tests from the literature involving strong shocks, large advections, and large volume effects between fluids. In order to verify the ability of the scheme to handle simple but strenuous grid displacements, all the test results are presented using either Eulerian mesh of fixed nodes, near-Lagrangian grid velocity, or linear interpolation of contact discontinuity. In the latter case, the grid velocity is linearly interpolated from fixed Eulerian edges to Lagrangian contact discontinuity in order to follow artificial interfaces between materials.

In all test cases, perfect gas or stiffened gas equations of state are used for the description of the fluids. The relationship between pressure, density and internal energy for the perfect gas equation of state is given by

$$P = (\gamma - 1)\rho e \ , \qquad T = e/C_v \ , \qquad s = C_v \log\left(P/\rho^{\gamma}\right) \ , \tag{4.56}$$

where γ is the isentropic coefficient, and P [Pa], ρ [kg/m^3], e [J/kg], T [K], C_v [J/K/kg] and s [J/K/kg] are the pressure, density, specific internal energy, temperature, specific heat at constant volume, and specific entropy of the fluid respectively. For air, the perfect gas is supposed to be close to : $\gamma = 1.4$, $P = 10^5$ Pa, $\rho = 1$ kg/m^3, $T = 300$ K and a sound velocity of $C = \sqrt{\gamma P/\rho} = 374.16$ m/s.

For the stiffened gas equation of state, the relationships (4.56) become

$$P = (\gamma_s - 1)\rho e - \pi \ , \qquad T = \frac{1}{C_v}\left(e - \frac{\pi}{\gamma_s \rho}\right) \ , \qquad s = C_v \log\left(\frac{\frac{P+\pi}{\gamma_s - 1} - \frac{\pi}{\gamma_s}}{\rho^{\gamma_s}}\right) \ . \tag{4.57}$$

For water, the stiffened gas is supposed to be close to : $\gamma_s = 7$, $\pi = 21.10^8$ Pa, $P = 10^5$ Pa, $\rho = 1$ kg/m^3, $T = 300$ K and a sound velocity of $C = \sqrt{(\gamma_s P + \pi)/\rho} = 1449.38$ m/s. The coefficient γ_s in (4.57) is only a constant from the stiffened gas equation of state and must not be confused with the isentropic coefficient γ.

In Section 4.5.1, we verify the ability of the scheme to handle artificial interface problems

with nearly pure materials by setting an infinite drag coefficient between fluids—the absolute velocity of the fluids is averaged for each fluid at each time step :

- in Section 4.5.1.1, a two-fluid Sod's shock tube is performed with two grid motion strategies : i) grid sheared across the x direction in order to obtain significant grid deformations as well as the tilting of the characteristics ; and ii) grid linearly interpolated from fixed Eulerian edges to Lagrangian contact discontinuity between the pure materials in order to follow artificial material interfaces with almost no numerical diffusion.
- in Section 4.5.1.2, a two-fluid water–air shock tube is performed on a grid sheared across the x direction. This test represents a more strenuous test than Sod's shock tube due to : i) large discontinuity of densities and pressures at initial time ; and ii) use of stiffened gas equation of state for the water.
- in Section 4.5.1.3, a three-fluid triple point test is performed with two grid motion strategies : i) Eulerian grid with fixed nodes $\boldsymbol{w} = \mathbf{0}$; and ii) near-Lagrangian grid motion in both x and y directions in order to best follow fluid motions.

In Section 4.5.2, no drag force is set between fluids in order to simulate multiphase flow mixtures with drifting fluids :

- in Section 4.5.2.1, a two-fluid advection of a volume fraction discontinuity with two grid motion strategies : i) grid sheared across the x direction ; and ii) grid linearly interpolated from fixed Eulerian edges to Lagrangian volume fraction discontinuity.
- in Section 4.5.2.2, a two-fluid Ransom's water faucet problem with two grid motion strategies : i) Eulerian grid with fixed nodes $\boldsymbol{w} = \mathbf{0}$ in order to study the convergence of the solution ; and ii) grid dynamically distorted by a random grid velocity at each cycle.
- in Section 4.5.2.3, a four-fluid crossing test of three packets of heavy fluids in a surrounding light gas with two grid motions strategies : i) Eulerian with fixed nodes $\boldsymbol{w} = \mathbf{0}$ for reference to evaluate the impact of numerical diffusion ; and ii) grid distorted by a smooth vortex.
- in Section 4.5.2.4, a five-fluid crossing test of four packets of heavy fluids in a surrounding light gas with two grid motions strategies : i) Eulerian with fixed nodes $\boldsymbol{w} = \mathbf{0}$ for reference to evaluate the impact of numerical diffusion ; and ii) shrink-then-stretch grid.

– in Section 4.5.2.5, a nine-fluid crossing test of eight packets of heavy fluids in a surrounding light gas on a shrink-then-stretch swirling grid. This test represents a starting point for the simulation of gas–particles flows using multi-size approaches in CEA applications involving sprays of heavy droplets into light gas.

4.5.1 Multi-material test cases with infinite drag coefficient

The behavior of multiGEECS is tested in two dimensions with an infinite drag force term between fluid velocities, in order to simulate the two-material Sod's shock tube, the two-material water–air shock tube, and the three-material triple point test.

4.5.1.1 Two-dimensional two-fluid Sod's shock tube

A novel variant of the single-fluid Sod's shock tube [44] is proposed in this section. This Riemann problem produces three waves—an expansion fan, a contact discontinuity, and a shock of medium strength. The initial domain is $[0;1]\times[-0.3;0.6]$ with an artificial interface located at $x=0.5$—the states on the left and on the right are constant, —isentropic coefficients of fluids are $\gamma^{\pm}=7/5$ where the two fluids are labeled $+$ and $-$ respectively, and initial conditions for densities, volume fractions, velocities, and pressure are

$$\begin{array}{cccccc} & \rho_{\pm} & \alpha_{+} & \alpha_{-} & \mu_{\pm} & u_{\pm} & P \\ x<0.5 & 1 & 1-10^{-12} & 10^{-12} & 0 & 0 & 1 \\ x>0.5 & 0.125 & 10^{-12} & 1-10^{-12} & 0 & 0 & 0.1 \end{array} \tag{4.58}$$

Results of the two-fluid Sod's shock tube sheared across the x direction is shown on Figures 4.1(a) and 4.1(b) for two-dimensional density map and profile. The grid velocity is $\boldsymbol{w}=(w_x;w_y)=(5y;0)$ with maximal and minimal values of respectively $w_x=3$ at $y=0.6$ and $w_x=-1.5$ at $y=-0.3$. The grid thus undergoes a shearing across the x direction with a shifting of the characteristics. The number of cells in the x and y directions, 320×290, is chosen so that initial cells are perfect squares and at final time $t=0.2$ they are exact parallelograms with a $\pi/4$ angle relative to the initial mesh. The symmetry of the problem is well-respected despite the large

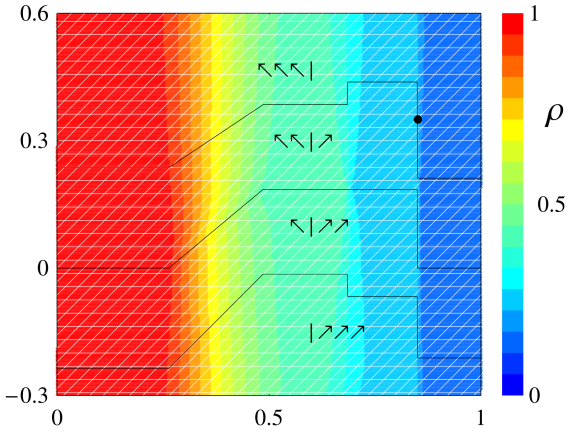

(a) Two-dimensional density map

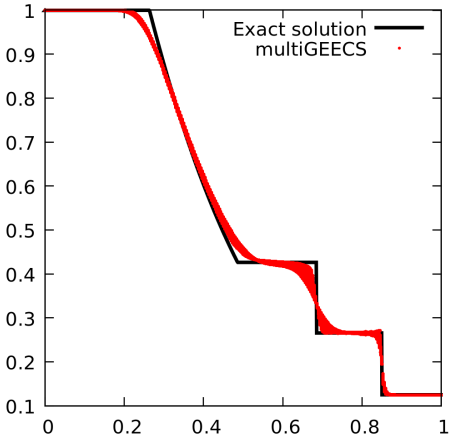

(b) One-dimensional superposition of all density points

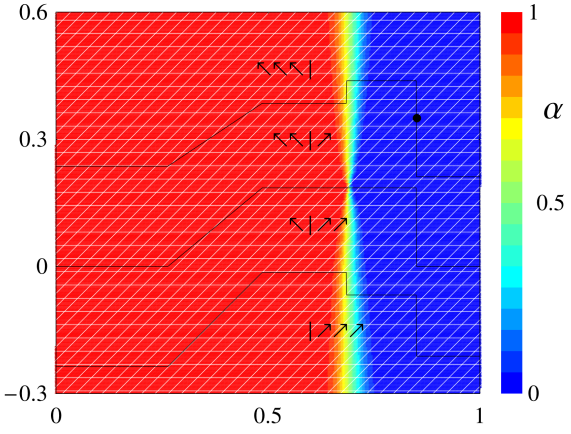

(c) Two-dimensional volume fraction map

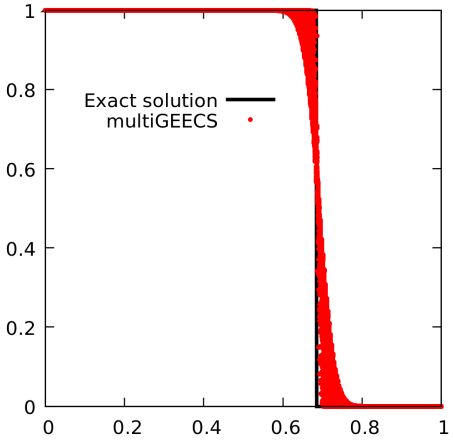

(d) One-dimensional superposition of all volume fraction points

FIGURE 4.1 – Density (top) and volume fraction (bottom) maps and profiles for the two-dimensional two-fluid Sod's shock tube on sheared grid across the x direction. The grid velocity is $\boldsymbol{w} = (w_x; w_y) = (5y; 0)$. Maximums of grid velocity are supersonic relative to the fluid flow. The black lines on the density map correspond to Lagrangian fluid velocity μ and supersonic limits computed by $\mu \pm \sqrt{\gamma P/\rho}$. The black dot represents the shock velocity. Computations are done with CFL $= 0.5$, final time $t = 0.2$, and $I = 320 \times 290$ cells, every displayed macro cell (white lines) corresponds to 10×10 numerical cells.

deformation of the cells. The scheme handles the shifting of the characteristics—Lagrangian and supersonic limits are represented with black lines on the two-dimensional density map—without producing any numerical artifact nor oscillation. The impact of the shearing motion is only visible

on the smearing of the contact discontinuity between the two fluids. Figures 4.1(c) and 4.1(d) display the two-dimensional volume fraction map and profile. The scheme handles nearly single-fluid flow in each area of the tube except in the contact discontinuity region where some numerical diffusion appears. As expected, the slice of mesh evolving exactly at the contact discontinuity velocity at $y \approx 0.2$ shows almost no numerical diffusion as fluxes of conserved quantities are nearly equal to zero during the flow evolution.

Density map and profile displayed on Figures 4.2(a) and 4.2(b) are obtained with a grid velocity linearly interpolated from fixed Eulerian boundaries to Lagrangian artificial interface between fluids in order to almost completely remove the numerical diffusion in the contact discontinuity area. The scheme captures accurately the three waves of Sod's shock tube without disturbance. Results for the volume fraction map and profile are presented on Figures 4.2(c) and 4.2(d). Almost no numerical diffusion can be observed in the contact discontinuity area. A slight undershoot appears downstream of the discontinuity which is commonly observed in Lagrangian hydrocodes and is attributed to wall heating effects. This particular grid motion strategy can be used to accurately follow contact discontinuities in practical applications. It must be noted that in the present work, even if Sod's shock tube has an exact known solution, the grid velocity of the node initially at the interface $x = 0.5$ is not given by the analytical value of the contact discontinuity speed but rather by the fluid velocity given by the scheme at each cyle.

4.5.1.2 Two-dimensional two-fluid water–air shock tube

This two-fluid shock tube, presented in [40], represents a more challenging test than Sod's shock tube done in Section 4.5.1.1. This Riemann problem produces an expansion fan, a contact discontinuity, and a shock of large strength. The initial domain is $[0; 1] \times [-0.4; 0.9]$ with an artificial interface located at $x = 0.7$—the states on the left and on the right are constant. Equations of state for water and air are approximated by stiffened (4.57) and perfect gases (4.56)

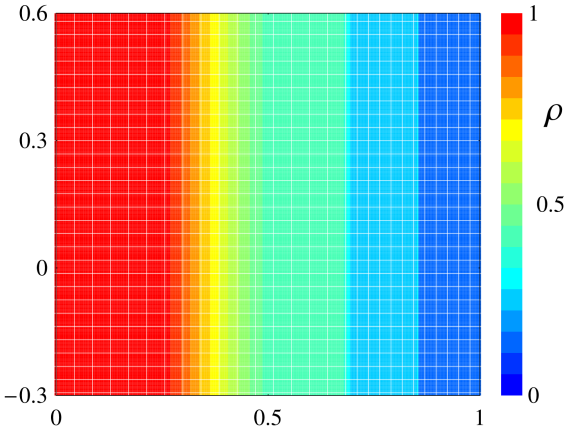

(a) Two-dimensional density map

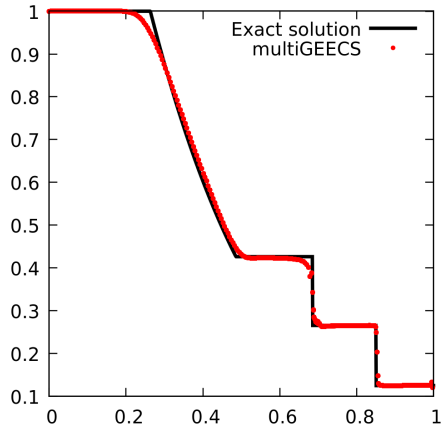

(b) One-dimensional superposition of all density points

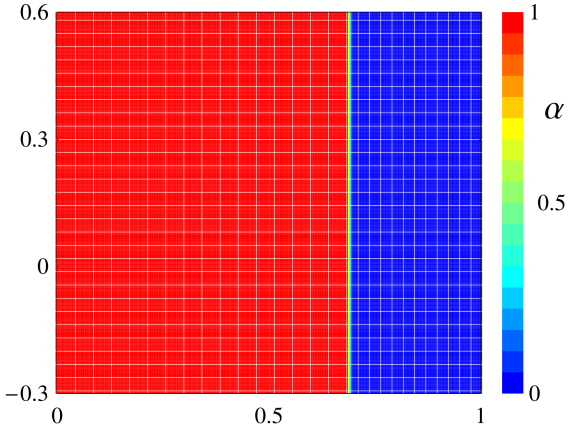

(c) Two-dimensional density map

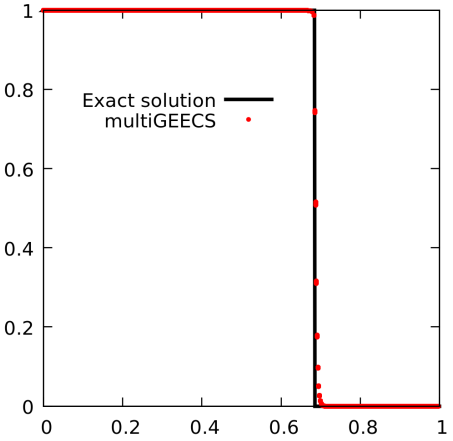

(d) One-dimensional superposition of all volume fraction points

FIGURE 4.2 – Density (top) and volume fraction (bottom) maps and profiles for the two-dimensional two-fluid Sod's shock tube on linearly interpolated grid. Computations are done with CFL $= 0.5$, final time $t = 0.2$, and $I = 320 \times 290$ cells, every displayed macro cell (white lines) corresponds to 10×10 numerical cells.

respectively. Initial conditions for densities, volume fractions, velocities, and pressure are

	$\rho_\pm$	α_+	α_-	$\mu_\pm$	$u_\pm$	P
$x < 0.7$	1000	$1 - 10^{-12}$	10^{-12}	0	0	10^9
$x > 0.7$	1	10^{-12}	$1 - 10^{-12}$	0	0	10^5

(4.59)

The grid velocity is $\boldsymbol{w} = (w_x; w_y) = (4167y; 0)$ with maximal and minimal values of respectively $w_x = 3750$ at $y = 0.9$ and $w_x = -1667$ at $y = -0.4$. The grid thus undergoes a shearing across the x direction with a shifting of the characteristics. The number of cells in the x and y directions, 200×260, is chosen so that initial cells are perfect squares and at final time $t = 0.00024$ they are exact parallelograms with a $\pi/4$ angle relative to the initial mesh.

Results of the two-fluid water–air shock tube sheared across the x direction are shown on Figures 4.3(a) and 4.3(b) for two-dimensional density map and profile. The scheme handles the shifting of the characteristics without producing any numerical artifact nor oscillation. The impact of the shearing motion is only visible on the smearing of the contact discontinuity between the two fluids. Figures 4.3(c) and 4.3(d) display the two-dimensional volume fraction map and profile. The scheme handles nearly single-fluid flow in each area of the tube except in the contact discontinuity region where some numerical diffusion appears in the volume fraction profile. As expected, the slice of mesh evolving exactly at the contact discontinuity velocity at $y \approx 0.12$ shows almost no numerical diffusion as fluxes of conserved quantities are nearly equal to zero during the flow evolution.

4.5.1.3 Two-dimensional three-fluid triple point test

This test case corresponds to a three-state Riemann problem with different densities, pressures, and isentropic coefficients in a rectangular domain. Two shocks appear and propagate with different speeds due to the difference of density and pressure. These two shocks create a shear along initial horizontal contact discontinuity and a vortex. Initial conditions for densities, pressures, and isentropic coefficients are given in Figure 4.4.

Figures 4.5(a) and 4.5(b) display the two-dimensional density and volume fraction maps for the three-fluid triple point test performed on an Eulerian grid with fixed nodes $\boldsymbol{w} = \mathbf{0}$. Due to first-order transport equations, the results are diffusive at the artificial interface between fluids with $\gamma = 1.5$ and the fluid with $\gamma = 1.4$. In order to reduce the numerical diffusion at the artificial interface between fluids, the grid velocity is now set up to : i) in the x direction, near-Lagrangian grid velocity computed using the strategy of Appendix .3, then averaged in the y direction in

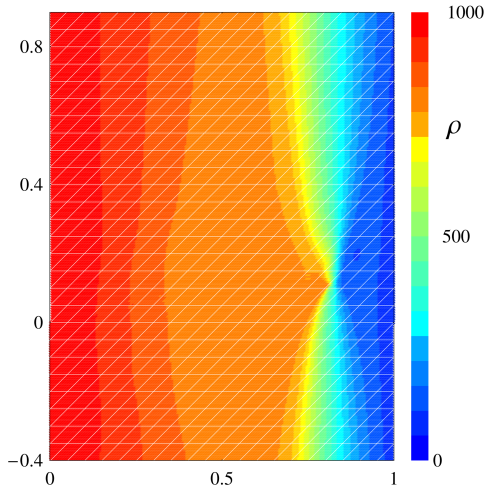

(a) Two-dimensional density map

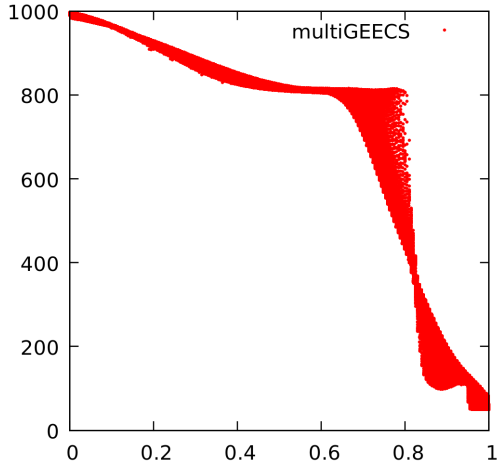

(b) One-dimensional superposition of all density points

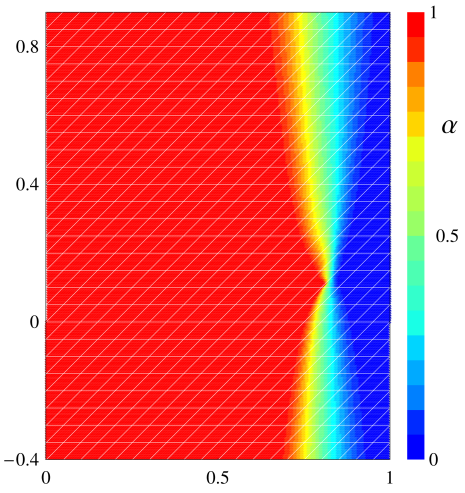

(c) Two-dimensional volume fraction map

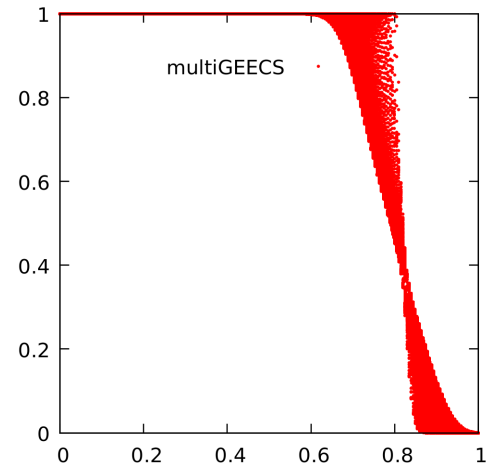

(d) One-dimensional superposition of all volume fraction points

FIGURE 4.3 – Density (top) and volume fraction (bottom) maps and profiles for the two-dimensional two-fluid water–air shock tube on sheared grid across the y direction. The grid velocity is $\boldsymbol{w} = (w_x; w_y) = (4167y; 0)$. Maximums of grid velocity are supersonic relative to the fluid flow. Computations are done with CFL $= 0.4$, final time $t = 2.4.10^{-4}$, and $I = 200 \times 260$ cells, every displayed macro cell (white lines) corresponds to 10×10 numerical cells.

order to avoid shearing effects in the mesh ; and ii) in the y direction, grid velocity given by the

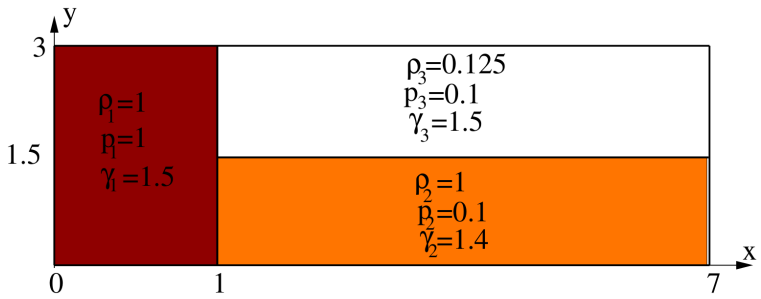

FIGURE 4.4 – Density, pressure, and isentropic coefficient initialization for the two-dimensional three-fluid triple point test case. Figure from [34].

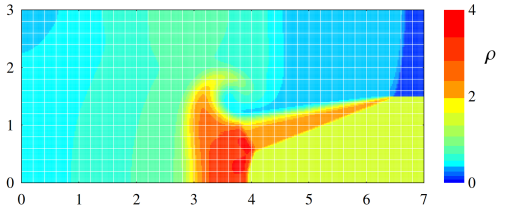

(a) Two-dimensional density map

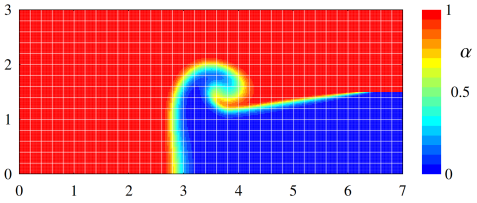

(b) Two-dimensional volume fraction map

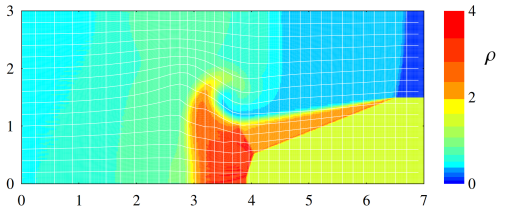

(c) Two-dimensional density map

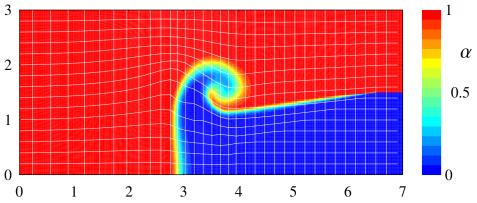

(d) Two-dimensional volume fraction map

FIGURE 4.5 – Density (left) and volume fraction—of the fluids with $\gamma = 1.5$—(right) maps for the two-dimensional three-fluid triple point test on Eulerian grid with fixed nodes $\boldsymbol{w} = \boldsymbol{0}$ (top) or ALE grid in both x and y directions in order to best follow the fluid flow . Computations are done with CFL $= 0.5$, final time $t = 3$, and $I = 350 \times 150$ cells, every displayed macro cell (white lines) corresponds to 10×10 numerical cells.

following equation

$$\boldsymbol{w}_p^{n+1/2} = \eta\ \boldsymbol{w}_p^{\mathrm{NL}}\ , \qquad \text{with} \qquad \eta = (t/t_0)^2 \,/\, \left(1 + (t/t_0)^2\right)\ , \tag{4.60}$$

where $\boldsymbol{w}_p^{\mathrm{NL}}$ is the near-Lagrangian grid velocity computed by the scheme (see Appendix .3), and

η is a time increasing factor corresponding to the Eulerian to Lagrangian transition time. For the present three-fluid triple point test, the Eulerian to Lagrangian transition time is $t_0 = 1.5$. With this ALE grid motion strategy, the mesh evolves in both x and y direction in order to best follow the fluid flow and to obtain a less diffusive capture of the different features of the flow. Purely Lagrangian motion cannot be achieved for this particular test case due to mesh tangling in the vortex area.

Figures 4.5(c) and 4.5(d) display both density and volume fraction maps of fluids with $\gamma = 1.5$ for the three-fluid triple point test performed on a two-dimensional ALE grid. The use of an adaptative mesh gives a more accurate capture of the vortex than in the Eulerian case.

4.5.2 Multiphases test cases

The behavior of multiGEECS is now tested in two-dimensions without any drag force term, in order to simulate the two-phases test of advection of a volume fraction discontinuity, Ransom's water faucet problem and the crossing of four and five packets of heavy fluids in a surrounding light gas.

4.5.2.1 Two-fluid advection of a volume fraction discontinuity

This test case represents the study of a discontinuity of volume fraction moving at constant velocity. It is important that the numerical scheme captures without distortions a flow with uniform pressure and density, especially when there is no infinite drag force between the fluids. In that case, each fluid has its own velocity and preserving contact discontinuities is not as trivial as for single-velocity flows. Initial domain is $[0;1] \times [0;1]$ with initial conditions for densities, volume fractions, velocities, and pressure

$$\begin{array}{lcccccc} & \rho_+ & \rho_- & \alpha_+ & \alpha_- & \mu_\pm & P \\ x < 0.25 & 1000 & 1 & 1 - 10^{-12} & 10^{-12} & 1 & 1 \\ x > 0.25 & 1000 & 1 & 10^{-12} & 1 - 10^{-12} & 1 & 1 \end{array} \tag{4.61}$$

Initial conditions (4.61) are chosen in order to display a large ratio of density between two perfect gases $\rho^+/\rho^- = 1000$, along with a large volume fraction discontinuity which corresponds to near single-fluid flow in each area of the numerical domain.

Results displayed on Figures 4.6(a), 4.6(c), and 4.6(e) are obtained with a grid sheared across the x direction. The amplitude of the grid velocity is given by $\boldsymbol{w} = (w_x; w_y) = (2y; 0)$ and the number of cells is chosen so that initial cells are perfect squares and at final time $t = 0.5$ exact parallelograms with a $\pi/4$ angle relative to the initial mesh. This sheared test verifies the ability of the scheme to capture precisely the moving volume fraction discontinuity with large grid deformations. The stability and robustness of the scheme is verified on Figure 4.6(c) as the volume fraction profile is oscillation free. The smearing of the numerical diffusion at the discontinuity is only due to the shearing motion of the grid. The slice of mesh located at $y = 0.5$ shows almost no numerical diffusion as it evolves at the velocity of the flow $\mu_x^+ = \mu_x^- = 1$. The superposition of all volume fraction data indicates an accurate capture of the position of the discontinuity at final time.

In order to almost completely remove the numerical diffusion at the volume fraction discontinuity, the grid velocity is now linearly interpolated from fixed edges $w_x = w_y = 0$ to Lagrangian discontinuity $w_x = 0.5$ and $w_y = 0$. In other words, the grid motion is Eulerian at boundaries, Lagrangian at the discontinuity, and regularly spaced in between. This variant verifies the ability of the scheme to capture a volume fraction discontinuity between near single-fluid flow in a Lagrangian motion (i.e. almost no numerical diffusion). Results obtained with this variant are shown on Figures 4.6(b), 4.6(d), and 4.6(f). The volume fraction profile remains oscillation free and fully symmetric along the y direction. The superposition of all volume fraction data demonstrates the stability of the scheme as almost no numerical diffusion appears at the discontinuity area.

In this advection test, no disturbance should appear in the density, pressure, and velocity profiles and they must remain constant during the whole computation. Figures 4.6(e) and 4.6(f) display the marginal deviations to exact solution for density, pressure, and absolute velocity for the test on x sheared grid and on linearly interpolated grid, confirming the consistency of the numerical scheme.

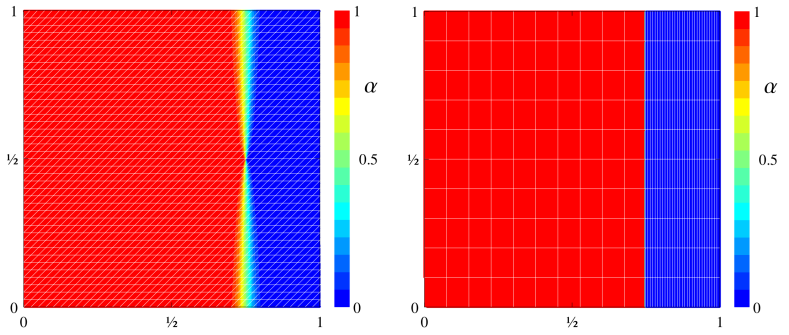

(a) Two-dimensional volume fraction map

(b) Two-dimensional volume fraction map

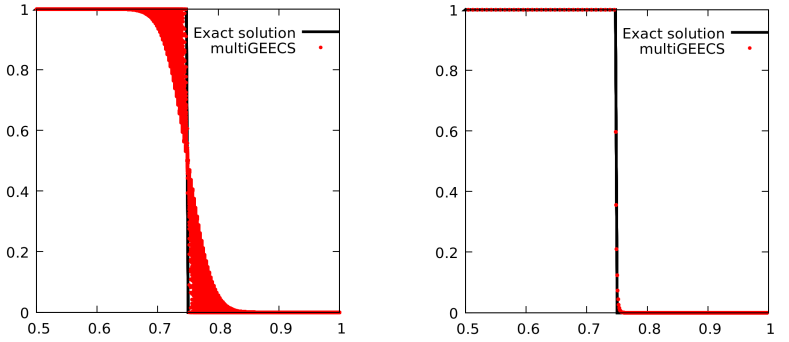

(c) One-dimensional superposition of all volume fraction points

(d) One-dimensional superposition of all volume fraction points

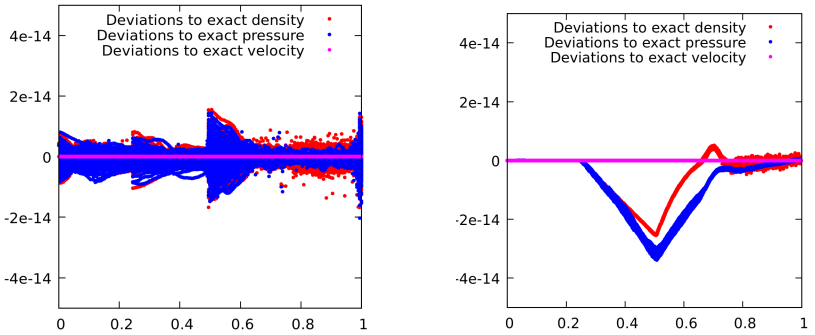

(e) One-dimensional superposition of deviations to exact solutions

(f) One-dimensional superposition of deviations to exact solutions

FIGURE 4.6 – Volume fraction maps (top), volume fraction profiles (center), and deviations to exact solutions (bottom) for the two-dimensional two-fluid advection test. The grid is sheared across the x direction with $\boldsymbol{w} = (w_x; w_y) = (2y; 0)$ (left), or interpolated in the x direction from fixed edges to Lagrangian discontinuity (right). Computations are done with CFL $= 0.5$, final time $t = 0.5$, and $I = 400 \times 400$ (left) or $I = 400 \times 10$ (right), every displayed macro cell (white lines) corresponds to 10×10 numerical cells (left) or 1×1 numerical cells (right).

4.5.2.2 Two-dimensional two-fluid Ransom's water faucet problem

Ransom's water faucet problem has become a basic benchmark for two-phase numerical schemes [38]. It consists of a 12m vertical pipe initially filled with a mixture of air ($\alpha_a = 0.2$) and water ($\alpha_w = 0.8$). The boundary condition at the top of the tube is a fixed 10 m.s^{-1} water inflow on the volume fraction of 0.8 with no air flux. The bottom of the tube is open to ambient pressure $P = 10^5$ Pa. With these conditions and under the action of gravity $g = 10$ m.s^{-2}, the water jet accelerates and stretches. In practice, equations of state for water and air are approximated by stiffened and perfect gases respectively. In the limit of incompressible water, analytical solutions are known for the air volume fraction [8] and the water velocity [16] that allow the comparison of numerical results. The different features of this test are mostly on advection and amplification of a volume fraction discontinuity, with marginal compressibility effects. Results of convergence

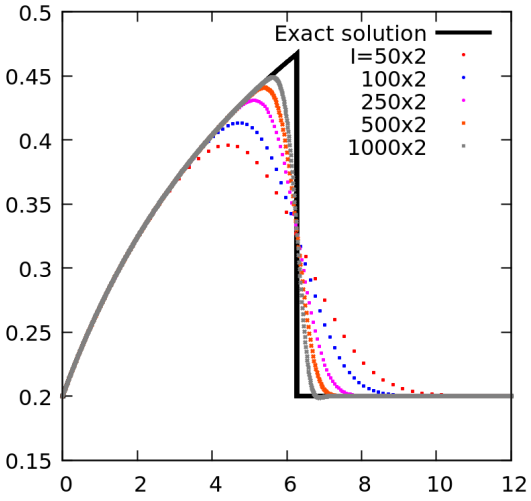

FIGURE 4.7 – Volume fraction profiles for the convergence study for Ransom's water faucet problem—the mesh size goes from $I = 100 \times 2$ to $I = 1000 \times 2$ and compared to the exact solution. Computations are performed with CFL $= 0.8$ and final time $t = 0.5$.

study displayed on Figure 4.7 are obtained in Eulerian configuration where $\boldsymbol{w} = \mathbf{0}$. For fine meshes, an undershoot appears in the volume fraction profiles upstream of the discontinuity which is generally recognized to be a consequence of the non-hyperbolic behavior of the N-fluid backbone model—a form of Kelvin–Helmholtz instability. As already explained in details in [48], the amplification of this physical oscillation is always present, even if not visible at early times,

and occurs sooner when the mesh is refined.

Eulerian results on Figure 4.7 present fully symmetric profiles, along with an accurate capture of the streched stream profile, ensured by the thermodynamically consistent capture of the pressure work.

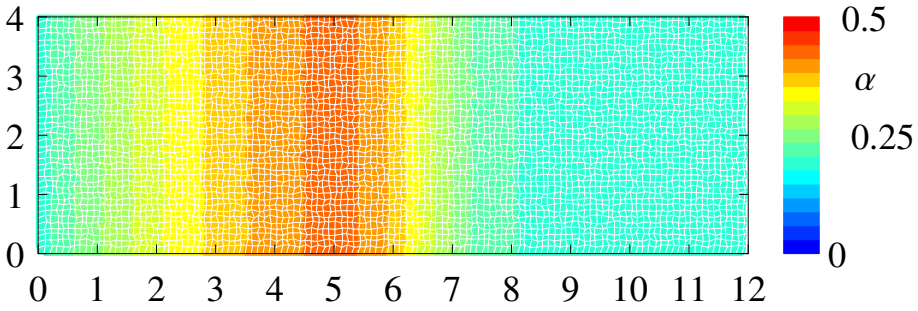

(a) Two-dimensional density map

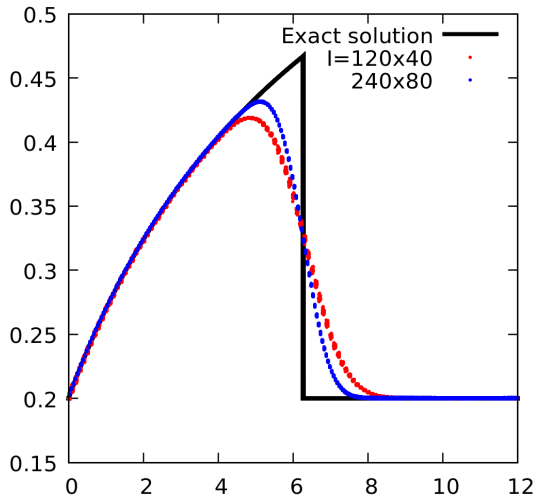

(b) One-dimensional superposition of all volume fraction points

FIGURE 4.8 – Volume fraction map (top) and profile (bottom) for the two-dimensional Ransom's water faucet problem on randomly distorted grid. Computations are performed with CFL $= 0.8$ and final time $t = 0.5$. The ALE mesh on the volume fraction map (top) is $I = 120 \times 40$, every displayed macro cell (white lines) corresponds to 1×1 numerical cells.

Figures 4.8(a) and 4.8(b) display the volume fraction map and profile for Ransom's water faucet problem performed on a two-dimensional randomly distorted mesh. The numerical domain

$[0;12] \times [0;4]$ is initially meshed with a uniform coarse Cartesian grid composed by 120×40 cells. This mesh is then dynamically distorted by the grid velocity defined by $\boldsymbol{w} = (w_x,w_y)$ where w_x and w_y are random numbers between $\pm 10^{-2}$. In Figure 4.8(b) all mesh points are plotted for two mesh sizes $I = 120 \times 40$ and $I = 240 \times 80$. Results are in good agreement with the exact solution. Even with a relatively coarse grid, the position and level of the volume fraction discontinuity is properly captured. The amount of numerical diffusion can be reduced by increasing the total number of mesh cells.

4.5.2.3 Four-fluid crossing test

This test corresponds to the crossing of three packets of heavy fluids $\rho_l = 1000$ in a surrounding light gas $\rho_g = 1$ at pressure $P = 1$. All fluids are described with the perfect gas equation of state (4.56) with $\gamma = 1.4$. Initial domain is $[-3;3] \times [-3;3]$ with $I = 480 \times 480$ cells. Initial locations of the three heavy packets are shown on Figure 4.9(a) for both the Eulerian and ALE configurations. Initial packets volume fractions are given by gaussian distributions of amplitude 0.8 and variances 0.2. Velocities of the packets are supersonic and given by

- $\mu_x = 0$ and $\mu_y = -2$ for the lump located at $x = 0$ and $y = 2$,
- $\mu_x = -2$ and $\mu_y = 0$ for the lump located at $x = 2$ and $y = 0$,
- $\mu_x = \mu_y = 0$ for the lump located at $x = -1.5$ and $y = 1.5$.

The last lump is motionless and is hold as a reference to evaluate the impact of mesh motions and numerical diffusion.

Two grid configurations are tested : Eulerian with fixed nodes and an ALE simulation of a smooth vortex grid displacement with $w_x = 2\sin(\pi x)\cos(\pi y)$ and $w_y = -2\cos(\pi x)\sin(\pi y)$. Figure 4.9 displays volume fraction profiles for both Eulerian and ALE simulations at time $t = 0$, $t = 1$, and final time $t = 2$. Both configurations show robust and stable results. Heavy packets are properly advected at supersonic velocity and only modified by numerical diffusion. At $t = 1$, the two packets cross in the middle of the domain and the volume fraction of the gas is low ($\alpha = 0.4$ at crossing). At final time $t = 2$, packets are separated and the volume fraction of the gas is close to one ($\alpha = 1 - 10^{-5}$). Results demonstrate the thermodynamical consistency of the multiphase

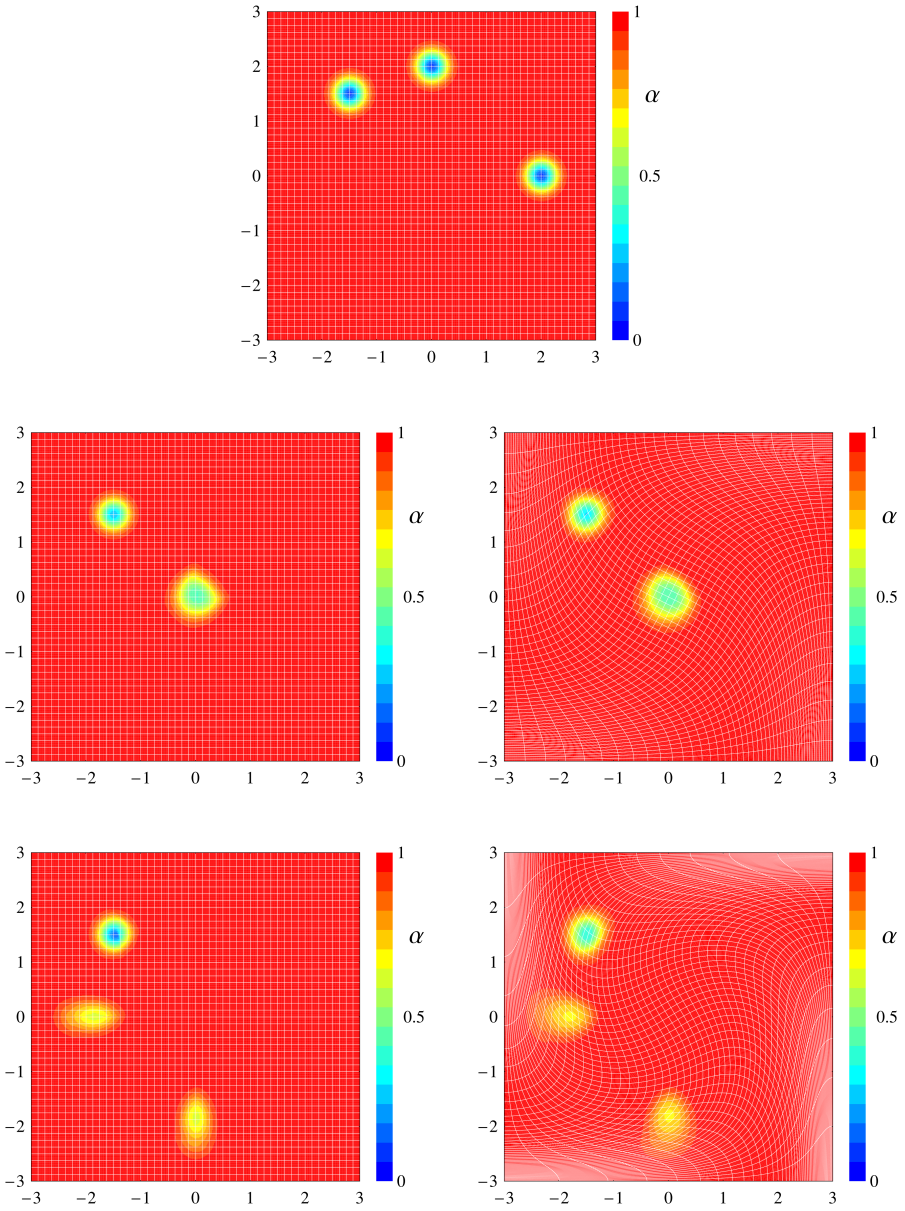

FIGURE 4.9 – Volume fraction maps at time $t = 0$ (top), $t = 1$ (middle), and final time $t = 2$ (bottom) for the four-fluids crossing test in the Eulerian (left) and ALE case (right). Computations are performed with CFL $= 0.7$ and $I = 480 \times 480$, every displayed macro cell (white lines) corresponds to 10×10 numerical cells.

pressure work—as there are no exchange terms between the four fluids, they only interact via pressure forces.

4.5.2.4 Five-fluid crossing test

This test corresponds to the crossing of four packets of heavy fluids $\rho_l = 1000$ in a surrounding light gas $\rho_g = 1$ at pressure $P = 1$. In this test, the gas is described with the perfect gas equation of state (4.56) with $\gamma = 1.4$, and heavy fluids are described with the stiffened gas equation of state (4.57) with $\gamma = 7$. Initial domain is $[-3;3] \times [-3;3]$ with $I = 480 \times 480$ cells. Initial volume fractions of the packets are described by gaussian distributions of amplitude 0.8 and variances 0.2. Initial packets supersonic velocities are given by

- $\mu_x = 2$ and $\mu_y = -2$ for the lump located at $x = -2$ and $y = 2$,
- $\mu_x = -2$ and $\mu_y = -2$ for the lump located at $x = 2$ and $y = 2$,
- $\mu_x = -2$ and $\mu_y = 2$ for the lump located at $x = 2$ and $y = -2$,
- $\mu_x = 2$ and $\mu_y = 2$ for the lump located at $x = -2$ and $y = -2$.

Two grid configurations are tested : Eulerian with fixed nodes and an ALE simulation where the numerical diffusion of the moving packets is reduced by using a shrink-then-stretch grid with the following grid velocity expression $\boldsymbol{w} = -1.5\eta\boldsymbol{x}$ where $\eta = 0.5$ for $t < 1$ and $\eta = -0.5$ for $t > 1$.

Figure 4.10 displays the gas volume fraction profile for both Eulerian and ALE simulations at initial $t = 0$, half $t = 1$ and final $t = 2$ times. Both Eulerian and ALE configurations present stable and robust results. The modification of the packets distribution is only due to numerical diffusion. The amount of numerical diffusion is reduced in the ALE simulation where the grid “follows" the packets evolution during the computation.

4.5.2.5 Nine-fluid crossing test

In this test, eight packets of heavy fluids $\rho_l = 1000$ cross in a surrounding light gas $\rho_g = 1$ at pressure $P = 10^5$. The gas is perfect with $\gamma = 1.4$ (4.56) and the heavy fluids are stiffened gas with $\gamma = 7$ (4.57). Initial domain is $[-3;3] \times [-3;3]$ with $I = 480 \times 480$ cells. Initial volume fractions of the packets are identical Gaussian profiles of amplitude 0.15 and variance 0.2 in both

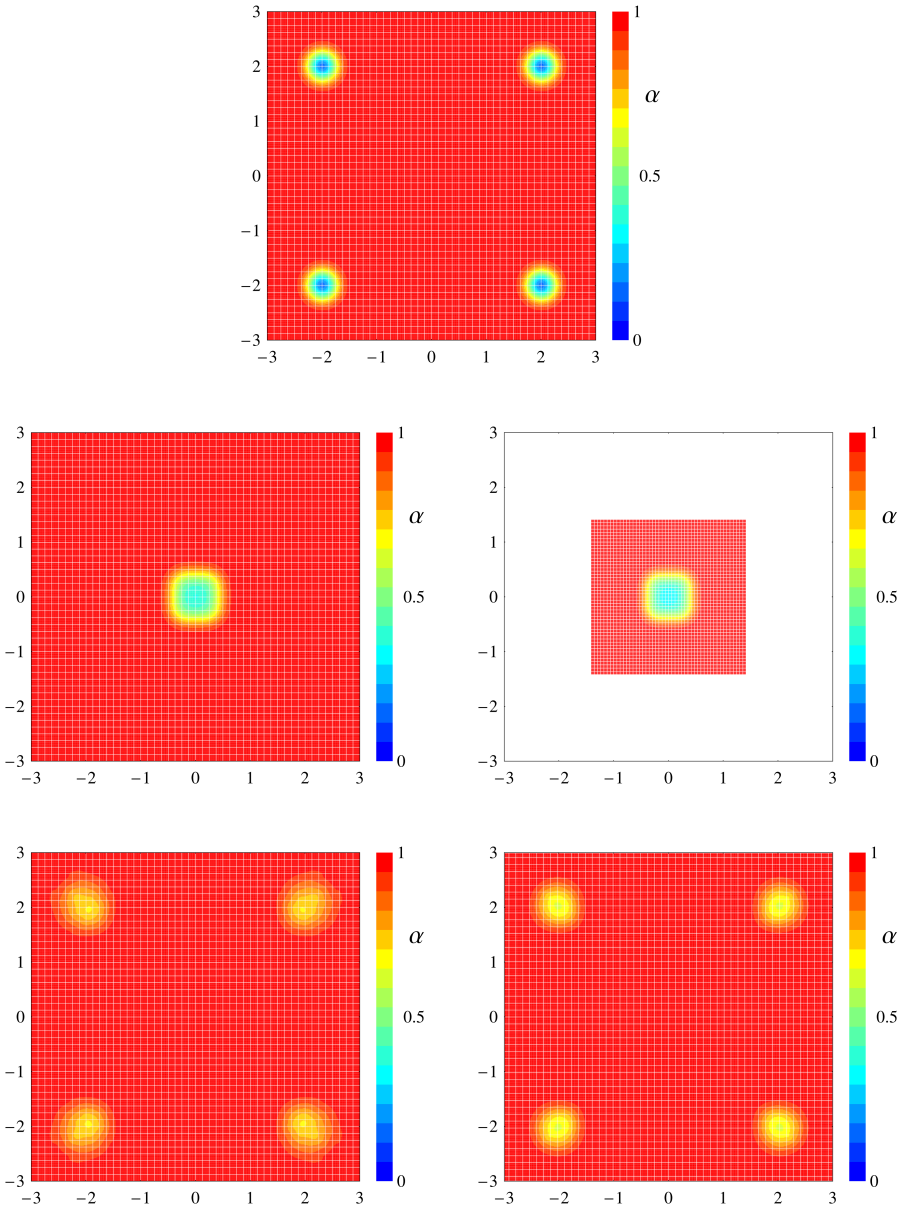

FIGURE 4.10 – Volume fraction maps at time $t = 0$ (top), $t = 1$ (middle), and final time $t = 2$ (bottom) for the five-fluids crossing test in the Eulerian (left) and ALE case (right). Computations are performed with CFL $= 0.7$ and $I = 480 \times 480$, every displayed macro cell (white lines) corresponds to 10×10 numerical cells.

dimensions. Packets' initial positions and velocities are (notice matched $\pm$ and $\mp$ signs)

$$\begin{array}{cccc} x & y & \mu_x & \mu_y \\ \pm 1 & 0 & \mp 1000 & 0 \\ 0 & \pm 1 & 0 & \mp 1000 \\ \pm 2 & 0 & \mp 2000 & 0 \\ 0 & \pm 2 & 0 & \mp 2000 \end{array} \tag{4.62}$$

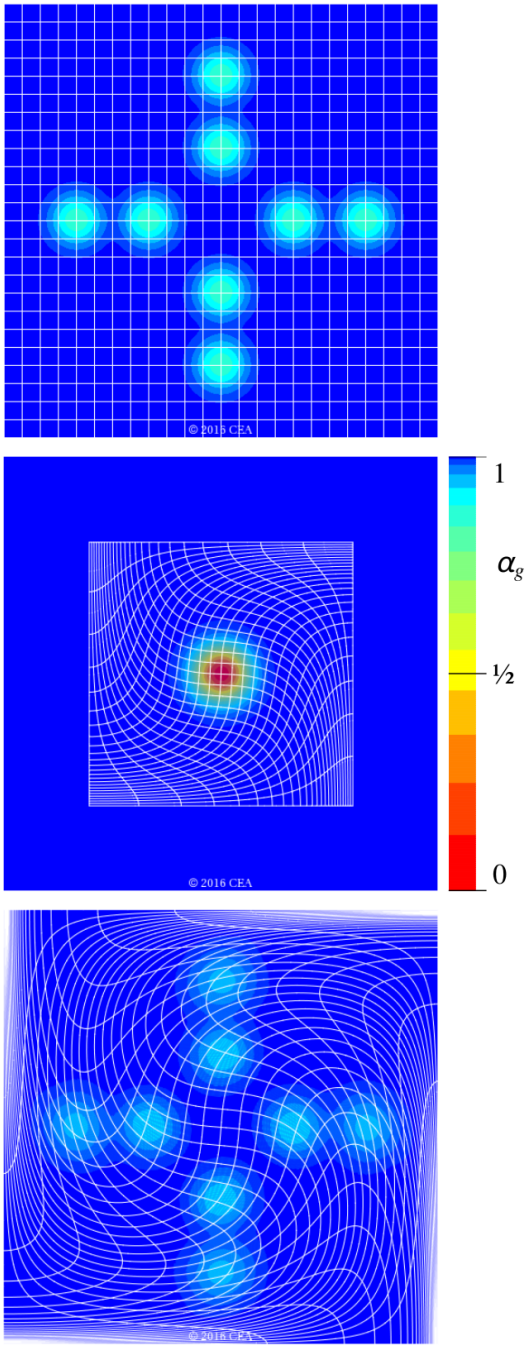

FIGURE 4.11 – Volume fraction maps at time $t = 0$ (top), $t = 10^{-3}$ (middle), and final time $t = 2.10^{-3}$ (bottom) for the nine-fluids crossing test on a shrink-then-stretch swirling grid. Computations are performed with CFL $= 0.7$ and $I = 480 \times 480$, every displayed macro cell (white lines) corresponds to 20×20 numerical cells.

In order to demonstrate the stability and robustness of multiGEECS, the computation are carried out on a shrink-then-stretch swirling grid with the corresponding grid velocity

$$w_x = 3\sin(\pi x)\cos(\pi y) - 1.5\eta x \ , \tag{4.63a}$$

$$w_y = -3\cos(\pi x)\sin(\pi y) - 1.5\eta y \ , \tag{4.63b}$$

where $\eta = 0.5$ for $t < 10^{-3}$ and $\eta = -0.5$ for $t > 10^{-3}$.

Figure 4.11 display the volume fraction profiles for the nine-fluid crossing test on a shrink-then-stretch swirling grid. At time $t = 10^{-3}$, all the packets cross in the middle of the domain and the volume fraction of the gas drops to ≈ 0.04. At final time 2.10^{-3}, the packets are separated and only modified by numerical diffusion—as there is no particular exchange term between phases, they only interact via pressure forces. This test represents a starting point for the simulation of gas–particles flows in CEA applications involving sprays of heavy droplets into light gas.

4.6 Conclusion

The present paper has developed a consistent discretization of the backbone model in the direct ALE context ensuring energetic, geometric, and entropic compatibility at discrete level. This backbone model is composed of evolution equations for the conserved quantities (mass, momentum, and internal energy) with advective terms and coupled through a common pressure. Following the generic GEEC (Geometry, Energy, and Entropy Compatible) procedure for the derivation of physics-compatible numerical scheme presented in [49], the backbone model is discretized using a novel direct multiphase ALE scheme that includes the following features : i) exact conservation of mass, momentum, and total energy at discrete level ; ii) grid velocity is defined at half time steps and at nodes, and grid motions can be either specified by the user or adaptatively adjusted by flow constraints ; iii) both absolute (in the laboratory frame) and relative (to the grid) velocities are defined at half time steps and cell centers ; iv) in the Lagrangian limit, both kinetic and internal energies of each fluid are discretized to second-order in space and time ; v) for simplicity, mass and Lagrangian coordinate transports are only discretized by a

simple first-order upwind scheme ; vi) derivation of the discrete momentum evolution equation of each fluid follows a similar path to the continuous variational derivation done in Section 4.3.1 ; vii) internal energy evolution equation of each fluid is consistently discretized from the continuous internal energy equation of the backbone model. In the present work, this continuous evolution equation is written in such a way that the different processes associated with the pressure work are separated and thermodynamically consistent ; viii) pressure equilibrium between fluids is ensured through a simple and local to the cells procedure ; ix) an artificial viscosity term is added to the pressure in order to capture shocks and to stabilize the scheme ; and x) discrete mass, momentum, and internal energy evolution equations for each fluid are derived for an arbitrary number of fluids and without any constraint structure or spatial dimension—however, all the test cases reported in Section 4.5 are restricted to one dimension or structured meshes of quadrangles in two dimensions.

The space-and-time localisations of thermodynamic quantities and velocities—along with the artificial viscosity term—ensure a continuity with the purely Lagrangian schemes used at CEA/DAM while complying with the so-called DeBar condition (see Section 4.3.2.1). The first-order feature of mass and Lagrangian coordinate transports may appear inconsistent with the second-order accuracy of both kinetic and internal energies (in the Lagrangian limit) but it is acceptable as a proof of concept for the study of variational direct multiphase ALE schemes. The second-order extension will be at the core of a forthcoming publication. The use of a variational approach for the derivation of discrete momentum evolution equations ensures a rigorous thermodynamical consistency for the scheme and leads to a non standard formulation of the pressure gradient (already observed in the single-fluid case of [49]).

Results of numerical test cases are presented in Section 4.5 using various strenuous grid motion strategies : supersonic shearing, linear interpolation of contact discontinuity, randomly distorted grid, or averaged near-Lagrangian motions, in order to confirm the versatility of the scheme regarding grid motions as well as the built-in properties of the scheme regarding energetic, geometric, and entropic compatibility. Sod's shock tube, the water–air shock tube, and the triple point test are performed using an infinite drag force term between phases—thus leading to

consider a single common velocity for all fluids at each time step—in order to verify the ability of the scheme to properly simulate multi-material like systems with artificial interfaces. Tests of advection of a volume fraction discontinuity or crossing of heavy packets in a surrounding light gas, along with Ransom's water faucet problem, are performed with no drag force term in order to simulate multiphase like systems with drifting fluids. Exact conservation of mass, momentum, and total energy is verified up to round-off errors on proper capture of shock levels and shock velocities. All test cases involve both large volume fraction jumps and large but regular grid deformations, confirming the stability and robustness of multiGEECS for an arbitrary number of fluids (up to five fluids).

This paper represents the first—at our knowledge—proof of concept and as such, a starting point to study variational direct ALE scheme for the simulation of compressible multiphase flows with the simplest backbone model. Extensions to more elaborated multiphase models, second-order accuracy for the advective part of the scheme, and detailed analysis of stability and boundary conditions are planned for later publications.

.1 Notation, definition

n,$n+1/2$	labels of integer and half integer times t^n and $t^{n+1/2}$ where $t^{n+1/2} = (t^n + t^{n+1})/2$.
$\Delta t^{n+1/2}$	$= t^{n+1} - t^n$, time step at $n+1/2$.
Δt^n	$= t^{n+1/2} - t^{n-1/2} = (\Delta t^{n+1/2} + \Delta t^{n-1/2})/2$, time step n.
c, d	labels of cells.
$\mathcal{D}(c)$	set of cell labels neighboring cell c (connected by a common node in one dimension, edge in two dimensions, or face in three dimensions).
p	labels of nodes.
$\mathcal{P}(c)$	set of node labels around cell c.
V_c^n	volume of cell c at time t^n.
$\boldsymbol{s}_{cd}^n$	outward pointing vector to boundary between cells c and d at time t^n (oriented from c to d; amplitude given by area of boundary element).
φ	fluid label with $\varphi \in [1; M]$.
$\rho_c^{\varphi n}$	mass density of fluid φ in cell c at time t^n.
$e_c^{\varphi n}$	internal mass energy of fluid φ in cell c at time t^n.
$\boldsymbol{w}_p^{n+1/2}$	grid velocity of node p at time $t^{n+1/2}$, externally prescribed by user.
$\boldsymbol{w}_c^{n+1/2}$	$= \sum_{\mathcal{P}(c)} \boldsymbol{w}_p^{n+1/2} / \lvert\mathcal{P}(c)\rvert$, interpolated grid velocity in cell c.
$\boldsymbol{u}_c^{\varphi n+1/2}$	relative-to-grid velocity of fluid φ in cell c at time $t^{n+1/2}$.
$\boldsymbol{\mu}_c^{\varphi n+1/2}$	$= \boldsymbol{u}_c^{\varphi n+1/2} + \boldsymbol{w}_c^{n+1/2}$, absolute velocity of fluid φ in cell c at time $t^{n+1/2}$.
$\sigma_{cd}^{\varphi n+1/2}$	$= \frac{1}{2}\big(1 + \mathrm{sign}(\boldsymbol{s}_{cd}^{n+1/2} \cdot \boldsymbol{u}_c^{\varphi n+1/2})\big)$, transport upwinding factor of fluid φ from cell c to neighboring cell d at time $t^{n+1/2}$.
$\phi_c^{\varphi n+1/2}$	Lagrange multiplier of fluid φ for fluid φ mass transport in cell c at time $t^{n+1/2}$.
$\lambda_c^{\varphi n+1/2}$	Lagrange multiplier of fluid φ for fluid φ Lagrangian coordinate transport in cell c at time $t^{n+1/2}$.
Π_c^n	Lagrange multiplier of the conservation of the volume fraction of each fluid in cell c at time t^n.

.2 Continuous internal energy with explicit pressure work terms

A continuous evolution equation for the internal energy of the fluid φ is first derived in the Eulerian case (see Appendix .2.1) then in the ALE case (see Appendix .2.2).

.2.1 Eulerian case

An internal energy evolution equation is derived in the continuous Eulerian case using the thermodynamic relationships [48]

$$\mathrm{d}\, e^{\varphi} = -P\, \mathrm{d}\, V^{\varphi} + \delta W^{\varphi} \ , \tag{64a}$$

$$\mathrm{d}\, P = -\gamma^{\varphi} P \rho^{\varphi}\, \mathrm{d}\, V^{\varphi} + \Gamma^{\varphi} \rho^{\varphi} \delta W^{\varphi} \ , \tag{64b}$$

where P is the common pressure of the system and e^{φ}, V^{φ}, Γ^{φ}, and δW^{φ} are the internal energy, pressure, mass volume, Grüneisen coefficient, and irreversible work of entropy of the fluid φ respectively. The second relationship can be replaced by

$$\alpha^{\varphi} \rho^{\varphi}\, \mathrm{d}_t^{\varphi}\, e^{\varphi} = \frac{\alpha^{\varphi}}{\gamma^{\varphi}}\, \mathrm{d}_t^{\varphi}\, P + \left(1 - \frac{\Gamma^{\varphi}}{\gamma^{\varphi}}\right) \alpha^{\varphi} \rho^{\varphi} \dot{W}^{\varphi} \ , \tag{65}$$

obtained by elimination of $\mathrm{d}\, V^{\varphi}$ and multiplication of $\alpha^{\varphi}\rho^{\varphi}$ for the fluid φ. After some manipulations, using the mass conservation equation $\mathrm{D}_t^{\varphi}\left(\alpha^{\varphi}\rho^{\varphi}\right) = 0$, (65) and (64a) yield

$$\mathrm{D}_t^{\varphi}\left(\alpha^{\varphi}\rho^{\varphi}e^{\varphi}\right) = \alpha^{\varphi}\, \mathrm{d}_t^{\varphi}\, P - \mathrm{D}_t^{\varphi}\left(\alpha^{\varphi} P\right) + \alpha^{\varphi}\rho^{\varphi}\dot{W}^{\varphi} \ , \tag{66a}$$

$$\mathrm{D}_t^{\varphi}\left(\alpha^{\varphi}\rho^{\varphi}e^{\varphi}\right) = \frac{\alpha^{\varphi}}{\gamma^{\varphi}}\, \mathrm{d}_t^{\varphi}\, P + \left(1 - \frac{\Gamma^{\varphi}}{\gamma^{\varphi}}\right) \alpha^{\varphi}\rho^{\varphi}\dot{W}^{\varphi} \ , \tag{66b}$$

where the “Lagrangian" and “Eulerian" derivative operators along Eulerian velocities of fluid φ are defined as

$$\mathrm{d}_t^{\varphi} \bullet = \partial_t \bullet + \boldsymbol{v}_i^{\varphi} (\bullet)_{,i} \ , \tag{67a}$$

$$\mathrm{D}_t^{\varphi} \bullet = \partial_t \bullet + (\bullet \boldsymbol{v}_i^{\varphi})_{,i} \ . \tag{67b}$$

In order to obtain an explicit expression for $\mathrm{D}_t^{\varphi}\left(\alpha^{\varphi}\rho^{\varphi}e^{\varphi}\right)$ and thus avoid an implicit closure, the right hand side of (66a) and (66b) can be reformulated through the use of the differential forms of : i) volume closure $\sum_{\phi}\alpha^{\phi}=1$ and ii) instantaneous pressure relaxation between fluids $P^{\varphi}=P$ as

$$\sum_{\phi}\partial_t\alpha^{\phi}=0\ , \tag{68a}$$

$$\partial_t P^{\varphi}=\partial_t P\quad\forall\ \varphi\ , \tag{68b}$$

where $\sum_{\phi}\bullet^{\phi}$ is the summation operator over all fluids. From $\sum_{\phi}(66a)=\sum_{\phi}(66b)$, one obtains after some algebraic manipulations (see [48, 19, 29] for details)

$$\mathrm{d}_t^{\varphi}\,P\sum_{\phi}\frac{\alpha^{\phi}}{\gamma^{\phi}}=-P\left(\sum_{\phi}\alpha^{\phi}v_i^{\phi}\right)_{,i}+P_{,i}\sum_{\phi}\frac{\alpha^{\phi}}{\gamma^{\phi}}\left(v_i^{\varphi}-v_i^{\phi}\right)+\sum_{\phi}\frac{\Gamma^{\phi}}{\gamma^{\phi}}\alpha^{\phi}\rho^{\phi}\dot{W}^{\phi}\ . \tag{69}$$

Finally, an explicit internal energy evolution equation is obtained by introducing $\mathrm{d}_t^{\varphi}\,P$ from (69) into (66b) thus yielding

$$\begin{aligned}\mathrm{D}_t^{\varphi}\left(\alpha^{\varphi}\rho^{\varphi}e^{\varphi}\right)=-P\beta^{\varphi}\bar{v}_{i,i}+P_{,i}\sum_{\phi}\mu^{\varphi\phi}\left(v_i^{\varphi}-v_i^{\phi}\right)\\ +\sum_{\phi}\mu^{\varphi\phi}\left(\Gamma^{\phi}\rho^{\phi}\dot{W}^{\phi}-\Gamma^{\varphi}\rho^{\varphi}\dot{W}^{\varphi}\right)+\alpha^{\varphi}\rho^{\varphi}\dot{W}^{\varphi}\ ,\end{aligned} \tag{70}$$

where $\sum_{\phi}\bullet^{\phi}$ is the summation operator over all fluids, $\bar{\boldsymbol{v}}$ is the volume averaged velocity, β^{φ} are the relative compressibility coefficients of the fluids, and $\mu^{\varphi\phi}$ is the scalar coupling coefficient under along-pressure-gradient drift. These three quantities are defined by

$$\bar{v}_i=\sum_{\phi}\alpha^{\phi}v_i^{\phi}\ , \tag{71a}$$

$$\beta^{\varphi}=\frac{\alpha^{\varphi}/\gamma^{\varphi}}{\sum_{\phi}\alpha^{\phi}/\gamma^{\phi}}\ , \tag{71b}$$

$$\mu^{\varphi\phi}=\frac{\alpha^{\varphi}\alpha^{\phi}/\gamma^{\varphi}\gamma^{\phi}}{\sum_{\Phi}\alpha^{\Phi}/\gamma^{\Phi}}\ . \tag{71c}$$

.2.2 ALE case

As explained in Sections 4.3.1.6 and 4.3.4, the form of the internal energy evolution equation (70) is not easily discretizable in the ALE framework. In the present section, (70) is reformulated using the relative-to-grid $\boldsymbol{u}^{\varphi}$ and grid $\boldsymbol{w}$ velocities in order to obtain an expression of (70) in the ALE framework which ensures the thermodynamical consistency of the capture of the pressure work.

Starting from (70) and using the “Lagrangian" and “Eulerian" derivative operators along ALE velocities of fluid φ are defined as

$$\mathrm{d}_t^{\varphi} \bullet = \partial_t \bullet + \boldsymbol{u}_i^{\varphi} (\bullet)_{,i} + \boldsymbol{w}_i (\bullet)_{,i} \ , \tag{72a}$$

$$\mathrm{D}_t^{\varphi} \bullet = \partial_t \bullet + (\bullet \boldsymbol{u}_i^{\varphi})_{,i} + (\bullet \boldsymbol{w}_i)_{,i} \ , \tag{72b}$$

yields

$$\begin{aligned} \partial_t \left(\alpha^{\varphi}\rho^{\varphi}e^{\varphi}\right) + \left(\alpha^{\varphi}\rho^{\varphi}e^{\varphi}w_i\right)_{,i} = -\beta^{\varphi}P \left(\sum_{\phi} \alpha^{\phi} u_i^{\phi}\right)_{,i} - \beta^{\varphi} P w_{i,i} \\ + \beta^{\varphi} P_{,i} \sum_{\phi} \frac{\alpha^{\phi}}{\gamma^{\phi}} \left(u_i^{\varphi} - u_i^{\phi}\right) - \left(\alpha^{\varphi}\rho^{\varphi}e^{\varphi}u_i^{\varphi}\right)_{,i} \ . \end{aligned} \tag{73}$$

Using the algebraic relation

$$\beta^{\varphi} P \left(\sum_{\phi} \alpha^{\phi} u_i^{\phi}\right)_{,i} = \beta^{\varphi} \left(\sum_{\phi} P \alpha^{\phi} u_i^{\phi}\right)_{,i} - \beta^{\varphi} \left(\sum_{\phi} \alpha^{\phi} u_i^{\phi}\right) P_{,i} \ , \tag{74}$$

equation (73) becomes

$$\begin{aligned} \partial_t \left(\alpha^{\varphi}\rho^{\varphi}e^{\varphi}\right) + \left(\alpha^{\varphi}\rho^{\varphi}e^{\varphi}w_i\right)_{,i} = \beta^{\varphi} P_{,i} \left(\sum_{\phi} \alpha^{\phi} u_i^{\phi}\right) - \beta^{\varphi} P w_{i,i} - e^{\varphi} \left(\alpha^{\varphi}\rho^{\varphi}u_i^{\varphi}\right)_{,i} \\ - \alpha^{\varphi}\rho^{\varphi}u_i^{\varphi}e_{,i}^{\varphi} - \beta^{\varphi} \left(P \sum_{\phi} \alpha^{\phi} u_i^{\phi}\right)_{,i} + \beta^{\varphi} P_{,i} \sum_{\phi} \frac{\alpha^{\phi}}{\gamma^{\phi}} \left(u_i^{\varphi} - u_i^{\phi}\right) \ . \end{aligned} \tag{75}$$

Equation (64a) is written under the following formulation

$$\rho^\varphi \,\mathrm{d}\, e^\varphi = \tfrac{1}{\gamma^\varphi}\,\mathrm{d}\, P + \left(1 - \tfrac{\Gamma^\varphi}{\gamma^\varphi}\right) \rho^\varphi \delta W^\varphi \ , \tag{76}$$

in order to write the last term on the right hand side of (75) using only advection-like terms, thus yielding the internal energy evolution equation in the ALE framework

$$\begin{aligned}
\partial_t \left(\alpha^\varphi \rho^\varphi e^\varphi\right) + \left(\alpha^\varphi \rho^\varphi e^\varphi w_i\right)_{,i} = \beta^\varphi P_{,i} \left(\sum_\phi \alpha^\phi u_i^\phi\right) - \beta^\varphi P w_{i,i} \\
- \beta^\varphi \sum_\phi \left(\alpha^\phi \left(\rho^\phi e^\phi + P\right) u_i^\phi\right)_{,i} - \sum_\phi \left(e^\varphi \left(\alpha^\varphi \rho^\varphi u_i^\varphi\right)_{,i} - \beta^\varphi e^\phi \left(\alpha^\phi \rho^\phi u_i^\phi\right)_{,i}\right) \\
- \sum_\phi \left(\left(1 - \tfrac{\Gamma^\varphi}{\gamma^\varphi}\right) \alpha^\varphi \rho^\varphi u_i^\varphi \left(\delta W^\varphi\right)_{,i} - \beta^\varphi \left(1 - \tfrac{\Gamma^\phi}{\gamma^\phi}\right) \alpha^\phi \rho^\phi u_i^\phi \left(\delta W^\phi\right)_{,i}\right) \ .
\end{aligned} \tag{77}$$

.3 Near-Lagrangian grid velocity

As the relative-to-grid velocity $\boldsymbol{w}$ and the absolute velocity of fluid φ $\boldsymbol{\mu}^\varphi$ are not discretized over identical space cells, an interpolation procedure must be applied in order to compute a near-Lagrangian grid velocity.

Following the strategy elaborated in [49, Appendix B], a near-Lagrangian grid velocity can be obtained by minimizing the mean square of the mass fluxes for each fluid, and at each of the neighboring cell edge (c,d) of each node p of the grid, yielding

$$\boldsymbol{w}_p^{n+1/2} = \min \sum_{\phi,c,d\in(p)} \left([\alpha\rho]_c^{\phi n} \boldsymbol{s}_{cd}^{n+1/2} \cdot \left(\boldsymbol{\mu}_c^{\phi n+1/2} - \boldsymbol{w}_p^{n+1/2}\right)\right)^2 \ , \tag{78}$$

where $\boldsymbol{\mu}_c^{\varphi n+1/2}$ is the absolute fluid velocity given by the scheme.

The minimization of (78) leads to

$$\sum_{\phi,c,d\in(p)} \left([\alpha\rho]_c^{\phi n}\right)^2 \boldsymbol{s}_{cd}^{n+1/2} \otimes \boldsymbol{s}_{cd}^{n+1/2} \cdot \left(\boldsymbol{\mu}_c^{\phi n+1/2} - \boldsymbol{w}_p^{n+1/2}\right) = 0 \ , \tag{79}$$

which can be solved as

$$\boldsymbol{w}_p^{\mathrm{NL}} = \boldsymbol{w}_p^{n+1/2} = \left(\sum_{\phi,c,d\in(p)} \left([\alpha\rho]_c^{\phi n} \right)^2 \left(\boldsymbol{s}_{cd}^{n+1/2} \otimes \boldsymbol{s}_{cd}^{n+1/2} \right) \right)^{-1} \times \sum_{\phi,c,d\in(p)} \left([\alpha\rho]_c^{\phi n} \right)^2 \left(\boldsymbol{s}_{cd}^{n+1/2} \otimes \boldsymbol{s}_{cd}^{n+1/2} \right) \cdot \boldsymbol{\mu}_c^{\phi n+1/2} \,. \quad (80)$$

Equation (80) allows to compute a grid velocity which corresponds to a minimization of the mean square of the mass fluxes for each fluid with the absolute fluid velocity given at the same time centering by the scheme.

.4 Discrete derivation of the variational absolute velocity and momentum equations

Following a similar path along the continuous derivation in Section 4.3.1, the absolute velocity and momentum variational equations of fluid φ can be derived in the discrete case from the discrete Euler–Lagrange equations

$$V_c^{n+1}[\alpha\rho]_c^{\varphi n+1} - V_c^n[\alpha\rho]_c^{\varphi n} = \Delta t^{n+1/2} \sum_{d\in\mathcal{D}(c)} \left(\dot{V}_{dc}^{\varphi n+1/2}[\alpha\rho]_d^{\varphi n} - \dot{V}_{cd}^{\varphi n+1/2}[\alpha\rho]_c^{\varphi n} \right) \,, \quad (81a)$$

$$V_c^{n+1}[\alpha\rho]_c^{\varphi n+1}\chi_c^{\varphi n+1} - V_c^n[\alpha\rho]_c^{\varphi n}\chi_c^{\varphi n} = \Delta t^{n+1/2} \sum_{d\in\mathcal{D}(c)} \left(\dot{V}_{dc}^{\varphi n+1/2}[\alpha\rho]_d^{\varphi n+1}\chi_d^{\varphi n+1} - \dot{V}_{cd}^{\varphi n+1/2}[\alpha\rho]_c^{\varphi n+1}\chi_c^{\varphi n+1} \right) \,, \quad (81b)$$

$$V_c^n \boldsymbol{\mu}_c^{\varphi n-1/2} - \sum_{d\in\mathcal{D}(c)} \sigma_{cd}^{\varphi n-1/2} \boldsymbol{s}_{cd}^{n-1/2} \left(\phi_d^{\varphi n-1/2} - \phi_c^{\varphi n-1/2} \right) - \chi_c^{\varphi n} \sum_{d\in\mathcal{D}(c)} \sigma_{cd}^{\varphi n-1/2} \boldsymbol{s}_{cd}^{n-1/2} \left(\lambda_d^{\varphi n-1/2} - \lambda_c^{\varphi n-1/2} \right) = 0 \,, \quad (81c)$$

$$\Delta t^{n-1/2} V_c^n \tfrac{1}{2} (\boldsymbol{\mu}_c^{\varphi n-1/2})^2 - \Delta t^n V_c^n \left(e_c^{\varphi n} + P_c^{\varphi n}/\rho_c^{\varphi n}\right) + V_c^n \left(\phi_c^{\varphi n-1/2} - \phi_c^{\varphi n+1/2}\right) + V_c^n \chi_c^{\varphi n} \left(\lambda_c^{\varphi n-1/2} - \lambda_c^{\varphi n+1/2}\right) - \Delta t^{n-1/2} \sum_{d\in\mathcal{D}(c)} \dot{V}_{cd}^{\varphi n-1/2} \left(\left(\phi_d^{\varphi n-1/2} - \phi_c^{\varphi n-1/2}\right) + \chi_c^{\varphi n} \left(\lambda_d^{\varphi n-1/2} - \lambda_c^{\varphi n-1/2}\right)\right) = 0 \ , \tag{81d}$$

$$\Delta t^{n-1/2} V_c^n \tfrac{1}{2} (\boldsymbol{\mu}_c^{\varphi n-1/2})^2 - \Delta t^n V_c^n e_c^{\varphi n} + \Pi_c^n/\rho_c^{\varphi n} + V_c^n \left(\phi_c^{\varphi n-1/2} - \phi_c^{\varphi n+1/2}\right) + V_c^n \chi_c^{\varphi n} \left(\lambda_c^{\varphi n-1/2} - \lambda_c^{\varphi n+1/2}\right) - \Delta t^{n-1/2} \sum_{d\in\mathcal{D}(c)} \dot{V}_{cd}^{\varphi n-1/2} \left(\left(\phi_d^{\varphi n-1/2} - \phi_c^{\varphi n-1/2}\right) + \chi_c^{\varphi n} \left(\lambda_d^{\varphi n-1/2} - \lambda_c^{\varphi n-1/2}\right)\right) = 0 \ , \tag{81e}$$

$$V_c^n \left(\lambda_c^{\varphi n+1/2} - \lambda_c^{\varphi n-1/2}\right) + \Delta t^{n-1/2} \sum_{d\in\mathcal{D}(c)} \dot{V}_{cd}^{\varphi n-1/2} \left(\lambda_d^{\varphi n-1/2} - \lambda_c^{\varphi n-1/2}\right) = 0 \ , \tag{81f}$$

$$\sum_{\varphi} \alpha_c^{\varphi n} - 1 = 0 \ , \tag{81g}$$

where (81a) is given by the explicit version of mass transport of fluid φ (4.29).

.4.1 Absolute velocity variational equation of fluid φ

The evolution in time of $\boldsymbol{\mu}_c^{\varphi}$ is obtained from $(81c)^{n+1/2} - (81c)^{n-1/2}$ yielding

$$\begin{aligned}\boldsymbol{\mu}_c^{\varphi n+1/2} - \boldsymbol{\mu}_c^{\varphi n-1/2} = &\sum_{d\in\mathcal{D}(c)} \frac{\sigma_{cd}^{\varphi n-1/2} \boldsymbol{s}_{cd}^{n-1/2}}{V_c^n} \left(\left(\phi_d^{\varphi n+1/2} - \phi_d^{\varphi n-1/2} - \phi_c^{\varphi n+1/2} + \phi_c^{\varphi n-1/2}\right)\right. \\ &\left. + \chi_c^{\varphi n} \left(\lambda_d^{\varphi n+1/2} - \lambda_d^{\varphi n-1/2} - \lambda_c^{\varphi n+1/2} + \lambda_c^{\varphi n-1/2}\right)\right) \\ &+ (\chi_c^{\varphi n+1} - \chi_c^{\varphi n}) \sum_{d\in\mathcal{D}(c)} \frac{\sigma_{cd}^{\varphi n+1/2} \boldsymbol{s}_{cd}^{n+1/2}}{V_c^{n+1}} \left(\lambda_d^{\varphi n+1/2} - \lambda_c^{\varphi n+1/2}\right) \\ + \sum_{d\in\mathcal{D}(c)} &\left(\frac{\sigma_{cd}^{\varphi n+1/2} \boldsymbol{s}_{cd}^{n+1/2}}{V_c^{n+1}} - \frac{\sigma_{cd}^{\varphi n-1/2} \boldsymbol{s}_{cd}^{n-1/2}}{V_c^n}\right) \left(\left(\phi_d^{\varphi n+1/2} - \phi_c^{\varphi n+1/2}\right) + \chi_c^{\varphi n} \left(\lambda_d^{\varphi n+1/2} - \lambda_c^{\varphi n+1/2}\right)\right) \ .\end{aligned} \tag{82}$$

Identically, substituting (81f) into (81d) leads to

$$\phi_c^{\varphi n+1/2} - \phi_c^{\varphi n-1/2} = \Delta t^{n-1/2}\,\tfrac{1}{2}\,(\boldsymbol{\mu}_c^{\varphi n-1/2})^2 - \Delta t^n\,(e_c^{\varphi n} + P_c^n/\rho_c^{\varphi n}) \\ - \Delta t^{n-1/2} \sum_{d\in\mathcal{D}(c)} \frac{\dot{V}_{cd}^{\varphi n-1/2}}{V_c^n} \left(\phi_d^{\varphi n-1/2} - \phi_c^{\varphi n-1/2}\right) . \quad (83)$$

Inserting $(83)_d - (83)_c$ into (82) yields

$$\boldsymbol{\mu}_c^{\varphi n+1/2} - \boldsymbol{\mu}_c^{\varphi n-1/2} = -\Delta t^n \sum_{d\in\mathcal{D}(c)} \frac{\sigma_{cd}^{\varphi n-1/2}\boldsymbol{s}_{cd}^{n-1/2}}{V_c^n} \left(e_d^{\varphi n} - e_c^{\varphi n} + P_d^n/\rho_d^{\varphi n} - P_c^n/\rho_c^{\varphi n}\right) \\ + \tfrac{1}{2}\Delta t^{n-1/2} \sum_{d\in\mathcal{D}(c)} \frac{\sigma_{cd}^{\varphi n-1/2}\boldsymbol{s}_{cd}^{n-1/2}}{V_c^n} \left(\left(\boldsymbol{\mu}_d^{\varphi n-1/2}\right)^2 - \left(\boldsymbol{\mu}_c^{\varphi n-1/2}\right)^2\right) \\ - \Delta t^{n-1/2} \sum_{d\in\mathcal{D}(c)} \frac{\sigma_{cd}^{\varphi n-1/2}\boldsymbol{s}_{cd}^{n-1/2}}{V_c^n} \cdot \left(\frac{\boldsymbol{u}_d^{\varphi n-1/2}}{V_d^n} \sum_{d'\in\mathcal{D}(c)} \sigma_{dd'}^{\varphi n-1/2}\boldsymbol{s}_{dd'}^{n-1/2}(\phi_{d'}^{\varphi n-1/2} - \phi_d^{\varphi n-1/2}) \right. \\ \left. \cdot - \frac{\boldsymbol{u}_c^{\varphi n-1/2}}{V_c^n} \sum_{d\in\mathcal{D}(c)} \sigma_{cd}^{\varphi n-1/2}\boldsymbol{s}_{cd}^{n-1/2}(\phi_d^{\varphi n-1/2} - \phi_c^{\varphi n-1/2})\right) \\ + \chi_c^{\varphi n} \sum_{d\in\mathcal{D}(c)} \frac{\sigma_{cd}^{\varphi n-1/2}\boldsymbol{s}_{cd}^{n-1/2}}{V_c^n}(\lambda_d^{\varphi n+1/2} - \lambda_d^{\varphi n-1/2} - \lambda_c^{\varphi n+1/2} + \lambda_c^{\varphi n-1/2}) \\ + (\chi_c^{\varphi n+1} - \chi_c^{\varphi n}) \sum_{d\in\mathcal{D}(c)} \frac{\sigma_{cd}^{\varphi n+1/2}\boldsymbol{s}_{cd}^{n+1/2}}{V_c^{n+1}}(\lambda_d^{\varphi n+1/2} - \lambda_c^{\varphi n+1/2}) \\ + \sum_{d\in\mathcal{D}(c)} \left(\frac{\sigma_{cd}^{\varphi n+1/2}\boldsymbol{s}_{cd}^{n+1/2}}{V_c^{n+1}} - \frac{\sigma_{cd}^{\varphi n-1/2}\boldsymbol{s}_{cd}^{n-1/2}}{V_c^n}\right) \left((\phi_d^{\varphi n+1/2} - \phi_c^{\varphi n+1/2}) + \chi_c^{\varphi n}(\lambda_d^{\varphi n+1/2} - \lambda_c^{\varphi n+1/2})\right) . \quad (84)$$

Substituting $(81f)_d - (81f)_c$ into (84) yields

$$\begin{aligned}
\boldsymbol{\mu}_c^{\varphi n+1/2} - \boldsymbol{\mu}_c^{\varphi n-1/2} = &-\Delta t^n \sum_{d\in\mathcal{D}(c)} \frac{\sigma_{cd}^{\varphi n-1/2}\boldsymbol{s}_{cd}^{n-1/2}}{V_c^n}\left(e_d^{\varphi n} - e_c^{\varphi n} + P_d^n/\rho_d^{\varphi n} - P_c^n/\rho_c^{\varphi n}\right)\\
&+ \tfrac{1}{2}\Delta t^{n-1/2}\sum_{d\in\mathcal{D}(c)} \frac{\sigma_{cd}^{\varphi n-1/2}\boldsymbol{s}_{cd}^{n-1/2}}{V_c^n}\left(\left(\boldsymbol{\mu}_d^{\varphi n-1/2}\right)^2 - \left(\boldsymbol{\mu}_c^{\varphi n-1/2}\right)^2\right)\\
&- \Delta t^{n-1/2}\sum_{d\in\mathcal{D}(c)} \frac{\sigma_{cd}^{\varphi n-1/2}\boldsymbol{s}_{cd}^{n-1/2}}{V_c^n}\cdot\frac{\boldsymbol{u}_d^{\varphi n-1/2}}{V_d^n}\sum_{d'\in\mathcal{D}(c)}\sigma_{dd'}^{\varphi n-1/2}\boldsymbol{s}_{dd'}^{n-1/2}\big((\phi_{d'}^{\varphi n-1/2} - \phi_d^{\varphi n-1/2})\\
&\qquad + \chi_c^{\varphi n}(\lambda_{d'}^{\varphi n-1/2} - \lambda_d^{\varphi n-1/2})\big)\\
&+ \Delta t^{n-1/2}\sum_{d\in\mathcal{D}(c)} \frac{\sigma_{cd}^{\varphi n-1/2}\boldsymbol{s}_{cd}^{n-1/2}}{V_c^n}\cdot\frac{\boldsymbol{u}_c^{\varphi n-1/2}}{V_c^n}\sum_{d\in\mathcal{D}(c)}\sigma_{cd}^{\varphi n-1/2}\boldsymbol{s}_{cd}^{n-1/2}\Big((\phi_d^{\varphi n-1/2} - \phi_c^{\varphi n-1/2})\\
&\qquad + \chi_c^{\varphi n}(\lambda_d^{\varphi n-1/2} - \lambda_c^{\varphi n-1/2})\Big)\\
&+ (\chi_c^{\varphi n+1} - \chi_c^{\varphi n})\sum_{d\in\mathcal{D}(c)} \frac{\sigma_{cd}^{\varphi n+1/2}\boldsymbol{s}_{cd}^{n+1/2}}{V_c^{n+1}}(\lambda_d^{\varphi n+1/2} - \lambda_c^{\varphi n+1/2})\\
+ \sum_{d\in\mathcal{D}(c)}&\left(\frac{\sigma_{cd}^{\varphi n+1/2}\boldsymbol{s}_{cd}^{n+1/2}}{V_c^{n+1}} - \frac{\sigma_{cd}^{\varphi n-1/2}\boldsymbol{s}_{cd}^{n-1/2}}{V_c^n}\right)\left((\phi_d^{\varphi n+1/2} - \phi_c^{\varphi n+1/2}) + \chi_c^{\varphi n}(\lambda_d^{\varphi n+1/2} - \lambda_c^{\varphi n+1/2})\right) .
\end{aligned} \tag{85}$$

Inserting $(81c)_d$ and $(81c)_c$ into the second and third terms on the right hand side of (86) and developing $(\chi_c^{\varphi n+1} - \chi_c^{\varphi n})$ using (81b) eventually yields the discrete variational absolute velocity

equation of fluid φ

$$
\begin{aligned}
\boldsymbol{\mu}_c^{\varphi n+1/2} - \boldsymbol{\mu}_c^{\varphi n-1/2} = -\Delta t^n \sum_{d\in\mathcal{D}(c)} \frac{\sigma_{cd}^{\varphi n-1/2}\boldsymbol{s}_{cd}^{n-1/2}}{V_c^n}\left(e_d^{\varphi n} - e_c^{\varphi n} + P_d^n/\rho_d^{\varphi n} - P_c^n/\rho_c^{\varphi n}\right) \\
+ \tfrac{1}{2}\Delta t^{n-1/2} \sum_{d\in\mathcal{D}(c)} \frac{\sigma_{cd}^{\varphi n-1/2}\boldsymbol{s}_{cd}^{n-1/2}}{V_c^n}\left(\left(\boldsymbol{\mu}_d^{\varphi n-1/2}\right)^2 - \left(\boldsymbol{\mu}_c^{\varphi n-1/2}\right)^2\right) \\
+ \Delta t^{n-1/2} \sum_{d\in\mathcal{D}(c)} \frac{\sigma_{cd}^{\varphi n-1/2}\boldsymbol{s}_{cd}^{n-1/2}}{V_c^n}(\boldsymbol{u}_c^{\varphi n-1/2}\boldsymbol{\mu}_c^{\varphi n-1/2} - \boldsymbol{u}_d^{\varphi n-1/2}\boldsymbol{\mu}_d^{\varphi n-1/2}) \\
- \Delta t^{n-1/2} \sum_{d\in\mathcal{D}(c)} (\chi_c^{\varphi n} - \chi_d^{\varphi n})\frac{\sigma_{cd}^{\varphi n-1/2}\boldsymbol{s}_{cd}^{n-1/2}}{V_c^n}\cdot\frac{\boldsymbol{u}_d^{\varphi n-1/2}}{V_d^n}\sum_{d'\in\mathcal{D}(c)}\sigma_{dd'}^{\varphi n-1/2}\boldsymbol{s}_{dd'}^{n-1/2}(\lambda_{d'}^{\varphi n-1/2} - \lambda_d^{\varphi n-1/2}) \\
+ \Delta t^{n+1/2} \sum_{d\in\mathcal{D}(c)} (\chi_c^{\varphi n+1} - \chi_d^{\varphi n+1})\frac{\sigma_{dc}^{\varphi n+1/2}\boldsymbol{s}_{dc}^{n+1/2}}{[\alpha\rho]_c^{\varphi n}V_c^n} \\
\times \frac{\boldsymbol{u}_d^{\varphi n+1/2}[\alpha\rho]_d^{\varphi n+1}}{V_c^{n+1}}\sum_{d'\in\mathcal{D}(d)}\sigma_{dd'}^{\varphi n+1/2}\boldsymbol{s}_{dd'}^{n+1/2}\left(\lambda_{d'}^{\varphi n+1/2} - \lambda_d^{\varphi n+1/2}\right) \\
+ \sum_{d\in\mathcal{D}(c)}\left(\frac{\sigma_{cd}^{\varphi n+1/2}\boldsymbol{s}_{cd}^{n+1/2}}{V_c^{n+1}} - \frac{\sigma_{cd}^{\varphi n-1/2}\boldsymbol{s}_{cd}^{n-1/2}}{V_c^n}\right)\left((\phi_d^{\varphi n+1/2} - \phi_c^{\varphi n+1/2}) + \chi_c^{\varphi n}(\lambda_d^{\varphi n+1/2} - \lambda_c^{\varphi n+1/2})\right) .
\end{aligned}
\tag{86}
$$

.4.2 Momentum variational equation of fluid φ

As in the continuous Eulerian derivation (4.8a), the momentum variational evolution equation of fluid φ is obtained from the combination (81a) $\times\, \boldsymbol{\mu}_c^{\varphi n+1/2} +$ (86) $\times\, V_c^n[\alpha\rho]_c^{\varphi n}$ thus yielding

$$
\begin{aligned}
&V_c^{n+1}[\alpha\rho]_c^{\varphi n+1}\boldsymbol{\mu}_c^{\varphi n+1/2} - V_c^n[\alpha\rho]_c^{\varphi n}\boldsymbol{\mu}_c^{\varphi n-1/2} \\
&\qquad = -\Delta t^n[\alpha\rho]_c^{\varphi n}\sum_{d\in\mathcal{D}(c)}\sigma_{cd}^{\varphi n-1/2}\boldsymbol{s}_{cd}^{n-1/2}\left(e_d^{\varphi n}-e_c^{\varphi n}+P_d^n/\rho_d^{\varphi n}-P_c^n/\rho_c^{\varphi n}\right) \\
&\qquad\quad -\Delta t^{n+1/2}\boldsymbol{\mu}_c^{\varphi n+1/2}\sum_{d\in\mathcal{D}(c)}\left(\dot{V}_{cd}^{\varphi n+1/2}[\alpha\rho]_c^{\varphi n}-\dot{V}_{dc}^{\varphi n+1/2}[\alpha\rho]_d^{\varphi n}\right) \\
&-\tfrac{1}{2}\Delta t^{n-1/2}[\alpha\rho]_c^{\varphi n}\sum_{d\in\mathcal{D}(c)}\sigma_{cd}^{\varphi n-1/2}\boldsymbol{s}_{cd}^{n-1/2}\left((\boldsymbol{u}_d^{\varphi n-1/2})^2-(\boldsymbol{u}_c^{\varphi n-1/2})^2-(\boldsymbol{w}_d^{\varphi n-1/2})^2+(\boldsymbol{w}_c^{\varphi n-1/2})^2\right) \\
&\qquad\quad -\Delta t^{n-1/2}[\alpha\rho]_c^{\varphi n}\sum_{d\in\mathcal{D}(c)}(\chi_c^{\varphi n}-\chi_d^{\varphi n})\sigma_{cd}^{\varphi n-1/2}\boldsymbol{s}_{cd}^{n-1/2} \\
&\qquad\quad \times\frac{\boldsymbol{u}_d^{\varphi n-1/2}}{V_d^n}\sum_{d'\in\mathcal{D}(c)}\sigma_{dd'}^{\varphi n-1/2}\boldsymbol{s}_{dd'}^{n-1/2}(\lambda_{d'}^{\varphi n-1/2}-\lambda_d^{\varphi n-1/2}) \\
&\qquad\quad +\Delta t^{n+1/2}\sum_{d\in\mathcal{D}(c)}(\chi_c^{\varphi n+1}-\chi_d^{\varphi n+1})[\alpha\rho]_d^{\varphi n+1}\sigma_{dc}^{\varphi n+1/2}\boldsymbol{s}_{dc}^{n+1/2} \\
&\qquad\quad \times\frac{\boldsymbol{u}_d^{\varphi n+1/2}}{V_c^{n+1}}\sum_{d'\in\mathcal{D}(d)}\sigma_{dd'}^{\varphi n+1/2}\boldsymbol{s}_{dd'}^{n+1/2}\left(\lambda_{d'}^{\varphi n+1/2}-\lambda_d^{\varphi n+1/2}\right) \\
&+V_c^n[\alpha\rho]_c^{\varphi n}\sum_{d\in\mathcal{D}(c)}\left(\frac{\sigma_{cd}^{\varphi n+1/2}\boldsymbol{s}_{cd}^{n+1/2}}{V_c^{n+1}}-\frac{\sigma_{cd}^{\varphi n-1/2}\boldsymbol{s}_{cd}^{n-1/2}}{V_c^n}\right)\Big((\phi_d^{\varphi n+1/2}-\phi_c^{\varphi n+1/2}) \\
&\qquad\qquad +\chi_c^{\varphi n}(\lambda_d^{\varphi n+1/2}-\lambda_c^{\varphi n+1/2})\Big)\ . \qquad (87)
\end{aligned}
$$

The momentum evolution equation of fluid φ is not fully conservative at discrete level and requires further corrections (see Section 4.3.3).

Bibliographie

[1] M.R. Baer, J.W. Nunziato, A two-phase mixture theory for the deflagration-to-detonation transition (DDT) in reactive granular materials, Int. J. Multiphase Flow, 12 (1986), 861-889.

[2] K. Bendiksen, D. Malnes, R. Moe, S. Nuland, The dynamic two-fluid model OLGA : theory and application, SPE Prod. Engng., 1991, 171-180.

[3] D. Bestion, The physical closure laws in the CATHARE code, Nucl. Eng. Des. 124 (1990), 229-245.

[4] J. Breil, T. Harribey, P.-H. Maire, M. Shashkov, A multi-material ReALE method with MOF interface reconstruction, Comput. & Fluids, 83 (2013), 115-125.

[5] W. Boscheri, M. Dumbser, O. Zanotti, High order cell-centered Lagrangian-type finite volume schemes with time-accurate local time stepping on unstructured triangular meshes, J. Comput. Phys., 291 (2015), 120-150.

[6] V.J. Chanteperdrix, P. Villedieu, A compressible model for separated two-phase flows computations, ASME Fluids Engineering Division Summer Meeting, 2002.

[7] A. Chinnayya, E. Daniel, R. Saurel, Modeling detonation waves in heterogeneous energetic materials, J. Comput. Phys., 196 (2004), 490-538.

[8] F. Coquel, K. El Amine, E. Godlewski, B. Perthame, P. Rascle, A numerical method using upwind schemes for the resolution of two-phase flows, J. Comput. Phys., 136 (1997), 272-.

[9] P.H. Cournede, Un schèma bi-lagrange plus projection pour la simulation bifluide des instabilités de mélanges, PhD dissertation, École Centrale Paris, 2001.

[10] F. Daude, P. Galon, On the computation of the Baer–Nunziato model using ALE formulation with HLL- and HLLC-type solvers towards fluid–structure interactions, J. Comput. Phys., 304 (2016), 189-230.

[11] R. DeBar, Fundamentals of KRAKEN code, LLNL report, 1974.

[12] J.M. Delhaye, J.L. Achard, On the averaging operators introduced in a two-phase flow modeling, Proceedings CSNI Specialist Meeting in transient two-phase flow, 1 (1976), 5-84.

[13] D.A. Drew, Averaged field equations for two-phase media, Stud. Appl. Math., 50 (1971), 133–155.

[14] D. S. Drumheller, A. Bedford, Arch. Rational Mech. Anal., 73 (1980), 257-.

[15] C. Eckart, Phys. Rev., 54 (1938), 920-.

[16] S. Evje, T. Flatten, Hybrid central-upwind schemes for numerical resolution of two-phase flows, ESAIM-Math. Model. Num., 39 (2005), 253-.

[17] Z. Ge, J.E. Marsden, Lie–Poisson integrators and Lie–Poisson Hamilton–Jacobi theory, Phys. Lett. A., 133 (1988), 134-139.

[18] J. A. Geurst, Phys. Rev. B, 22 (1980), 3207-.

[19] J.M. Ghidaglia, Personal communication, 2000.

[20] S.K. Godunov, Finite difference method for numerical computation of discontinuous solutions of the equations of fluid dynamics, Matematicheskii Sbornik, 47 (1959), 271-306.

[21] H. Goldstein, C. Poole, J. Safko, Classical mechanics, Addison–Wesley, 2002.

[22] J.W. Herivel, The derivation of the equations of motion of an ideal flow by Hamilton principle, Proc. Camb. Phil. Soc., 51 (1955).

[23] C.W. Hirt, A.A. Amsden, J.L. Cook, An Arbitrary Lagrangian–Eulerian Computing Method for All Flow Speeds, J. Comput. Phys., 135 (1974), 203-216.

[24] M. Ishii, Thermo-Fluid dynamic theory of two-phase flow, Eyrolles, 1975.

[25] J. Comput. Phys., 257 Part B (2014).

[26] S. Jay, F. Lacas, S. Candel, Combined surface density concepts for dense spray combustion, Combustion and Flame, 144 (2006), 558-577.

[27] D. Kah, O. Emre, Q.H. Tran, S. de Chaisemartin, S. Jay, F. Laurent, M. Massot, High order moment method for polydisperse evaporating sprays with mesh movement : Application to internal combustion engines, Int. J. Multiphase Flow, 71 (2015), 38-65.

[28] J.R. Kamm, F.X. Timmes, On efficient generation of numerically robust Sedov solutions, LANL, Report LA-UR-07-2849 (2007).

[29] J.J. Kreeft, B. Koren, A new formulation of Kapila's five-equation model for compressible two-fluid flow, and its numerical treatment, J. Comput. Phys., 229 (2010), 6220-.

[30] M. Kucharik, M. Shashkov, Conservative multi-material remap for staggered multi-material Arbitrary Lagrangian–Eulerian methods, J. Comput. Phys., 258 (2014), 268-304.

[31] C.C. Lin, Liquid Helium, Proceedings ot the international school of physics, 1963.

[32] A. Llor, Statistical hydrodynamic models for developed mixing instabilities flows : analytical 0D evaluation criteria, and comparison of single-and-two-phase flow approaches. Lect. Notes Phys., 681 (2005).

[33] A. Llor, A. Claisse, C. Fochesato, Energy preservation and entropy in Lagrangian space- and time-staggered hydrodynamic schemes, J. Comput. Phys., 309 (2016), 324-349.

[34] R. Loubere, P.H Maire, M. Shashkov, J. Breil, S. Galera, ReALE : A Reconnection-based Arbitrary-Lagrangian-Eulerian method, J. Comput. Phys., 229 (2011), 4724.

[35] M. Massot, Eulerian multi-fluid models for polydisperse evaporating sprays, Computational Models for Turbulent Multiphase Reacting Flows, CISM Courses and Lectures, 492 (2007), 79-123.

[36] J. von Neumann, R.D. Richtmyer, A method for the numerical calculation of hydrodynamic shocks, J. Appl. Phys., 21 (1950), 232.

[37] D. Pavlov, P. Mullen, Y. Tong, E. Kanso, J.E. Marsden, M. Desbrun, Structure-preserving discretization of incompressible fluids, Physica D, 240 (2011), 443-458.

[38] V.H. Ransom, Numerical benchmark test No2.1 : faucet flow, Multiphase Sci. Technol., 1 (1987), 465.

[39] W.J. Rider, E. Love, M.K. Wong, O.E. Strack, S.V. Petney, D.A. Labreche, Adaptative methods for multi-materials ALE hydrodynamics, Internat. J. Numer. Methods Fluids, 65 (2011), 1325-1337.

[40] R. Saurel, R. Abgrall, A multiphase Godunov method for compressible multifluid and multiphase flows, J. Comput. Phys., 150 (1999), 425-467.

[41] R. Saurel, O. Le Metayer, A multiphase model for compressible flows with interfaces, shocks, detonation waves and cavitation, J. Fluid Mech., 431 (2000), 239-271.

[42] L. I. Sedov, Similarity and dimensional methods in mechanics, Academic Press, 1959.

[43] J. Serrin, Mathematical principles of classical mechanics, Handbuch der physik, Springer, 1959.

[44] G. A. Sod, A survey of several finite difference methods for system of nonlinear hyperbolic conservation laws, J. Comput. Phys., 27 (1978),1.

[45] E. Tonti, Why starting from differential equations for computational physics ?, J. Comput. Phys., 257 (2014), 1260-1290.

[46] J.G. Trulio, K.R. Trigger, Numerical solution of the one–dimensional Lagrangian hydrodynamic equations, UC-LRL Report, 1966.

[47] A. Vallet, R. Borghi, An Eulerian model of atomization of a liquid jet, Third International Conference on Multiphase Flow, Lyon France, 1998.

[48] T. Vazquez-Gonzalez, A. Llor, C. Fochesato, Ransom test results from various two-fluid schemes : is enforcing hyperbolicity a thermodynamically consistent option ?, Int. J. Multiphase Flow, 81 (2016), 104-112.

[49] T. Vazquez-Gonzalez, A. Llor, C. Fochesato, A novel GEEC (Geometry, Energy, and Entropy Compatible) procedure applied to a staggered direct-ALE scheme for hydrodynamics, in preparation.

[50] J.M. Wendlandt, J.E. Marsden, Mechanical integrators derived from a discrete variational principle, Physica D, 106 (1997), 223-246.

[51] M. Wilkins, Calculation of elastic–plastic flow, Methods in computational physics : advances in research and applications, Vol.3, Fundamentals methods in hydrodynamics, Academic Press, 1964.

Chapitre 5

Conclusion générale et perspectives

Ce travail de thèse s'inscrit dans le cadre d'études prospectives pour la simulation numérique de sprays dans les applications rencontrées au CEA/DAM. Dans ce travail, contrairement à une approche particulaire classique dans laquelle l'évolution de la phase dispersée est décrite par une équation de Boltzmann alors que le fluide porteur est régi par les équations de l'hydrodynamique, l'évolution du spray est décrit par une approche multigroupes ou multifluides. Dans cette approche, l'équation de Boltzmann est discrétisée par groupes afin de réduire la phase dispersée à un ensemble de milieux continus. Le système d'équations à résoudre se réduit alors à un système d'équations multifluides. La grande majorité des modèles multifluides disponibles dans la littérature partagent le même squelette d'équations de type Euler. Ce modèle squelette, qui est celui utilisé dans ce travail, est composé d'équations d'évolution pour la masse, quantité de mouvement et énergie qui sont couplées entre elles par les forces de pression et la conservation du volume (via les fractions volumiques).

Ce modèle squelette correspond à la partie convective des modèles multifluides complets. Il partage notamment avec ces modèles complets les difficultés suivantes : i) le modèle n'est pas écrit sous forme conservative à cause des termes de gradient de pression ; ii) les équations d'états peuvent devenir raides lorsque les propriétés des fluides sont très contrastées et iii) la cohérence thermodynamique des forces de pression (et donc de l'entropie) peut ne pas être assurée lorsque le modèle est résolu par rapport à une grille évoluant de manière arbitraire. Cette dernière propriété

est rarement prise en compte de façon précise dans les schémas numériques. De plus, le modèle squelette est connu pour présenter un défaut d'hyperbolicité. Une discussion est proposée au Chapitre 2 afin de justifier la pertinence du modèle squelette pour étudier certaines propriétés des schémas numériques. En particulier, la propriété de préservation des écoulements isentropiques peut tout à fait être vérifiée avec ce modèle. Une étude comprenant une comparaison avec des résultats publiés est réalisée autour du cas test du robinet de Ransom afin de mettre en évidence l'importance de cette propriété et la capacité du schéma numérique proposé à répondre aux attentes fixées.

Le principal objectif de ce travail de thèse est de dériver un schéma numérique thermodynamiquement cohérent pour la simulation d'écoulements N-phases compressibles par rapport à une grille évoluant de manière arbitraire.

Le Chapitre 2 propose une discrétisation du modèle squelette par un schéma ALE indirect de type bi-Lagrange plus projection afin de simuler des écoulements bifluides en une dimension. À l'origine proposé dans la thèse de Cournède en 2001, ce schéma numérique est étendu dans cette thèse au cas d'un modèle bifluide à six équations avec une étape de relaxation instantanée des pressions. Une évolution de ce schéma est proposée afin de garantir la conservation de la quantité de mouvement grâce à une étape de remaillage conservative sur grilles décalées. Ce type de schéma ALE indirect, largement utilisé au CEA/DAM, se décompose en trois étapes principales : i) évolution lagrangienne durant laquelle les deux fluides évoluent avec leur vitesse propre sur deux maillages lagrangiens distincts ; ii) remaillage des deux grilles lagrangiennes sur une grille finale commune pour les deux fluides et iii) relaxation instantanée des pressions des deux fluides au sein des cellules du maillage eulérien fixe. Une comparaison des résultats obtenus avec ce schéma et des résultats issus de la littérature est effectuée sur le cas test du robinet de Ransom. Cette comparaison montre que l'utilisation du modèle squelette elliptique reste acceptable pour la simulation des écoulements multifluides compressible à partir du moment où la cohérence thermodynamique du schéma est assurée. Cependant, l'extension du schéma bi-Lagrange plus projection en deux ou trois dimensions reste problématique à cause du coût de calcul de l'étape de projection. Cette extension est bien sûr possible et son utilisation devrait

alors passer par une importante étape d'optimisation informatique pour être opérationnelle dans les applications (parallélisation, prise en compte des architectures hybrides des calculateurs les plus récents). Néanmoins, cette approche n'a pas semblé être la plus appropriée pour répondre efficacement aux besoins du CEA en terme de simulation d'écoulements à phase dispersée par une description multifluide.

Afin de dériver un nouveau schéma numérique qui soit thermodynamiquement cohérent et qui soit moins coûteux en temps de calcul, une nouvelle procédure de dérivation de schéma numérique est proposée dans le contexte ALE direct. L'approche ALE directe permet de résoudre le modèle sur une grille qui évolue dans le temps en intégrant directement les termes d'advection sans passer par une étape de projection géométrique coûteuse. Cette procédure de dérivation, désignée par l'acronyme GEEC (Geometry, Energy, and Entropy Compatible), garantit par construction le respect des compatibilités énergétique, entropique et géométrique au niveau discret. Elle se décompose en trois étapes principales : i) utilisation d'un principe de moindre action discrète pour la dérivation de l'équation d'évolution de la quantité de mouvement, garantissant la cohérence thermodynamique du travail des forces de pression ; ii) dérivation de l'équation d'évolution de l'énergie interne à partir de l'équation d'évolution de l'énergie cinétique, assurant la conservation exacte de l'énergie totale au niveau discret et iii) ajout d'un terme de viscosité artificielle dans les équations d'évolution du schéma, permettant de capturer les chocs et de stabiliser le schéma.

Comme preuve de concept, cette nouvelle approche de dérivation GEEC est appliquée au cas d'un schéma ALE direct pour la simulation des écoulements monofluide compressibles en deux dimensions au Chapitre 3. Ce schéma, nommé GEECS (Geometry, Energy, and Entropy Compatible Scheme), possède les caractéristiques principales suivantes : i) les vitesses absolue (dans le référentiel du laboratoire) et relative (par rapport au maillage) sont définies au demi-pas de temps et au centre des mailles, alors que la vitesse de grille est définie au demi-pas de temps et aux noeuds — ces choix de localisations assurent une continuité avec les schémas lagrangiens utilisés dans les applications du CEA/DAM ; — et ii) les énergies cinétique et interne sont discrétisées au second ordre en limite lagrangienne alors que le transport de masse est discrétisé au premier ordre par un schéma upwind. Les résultats de GEECS sur plusieurs cas tests tels

que le vortex isentropique, le tube à choc de Sod, l'explosion de Sedov, le double tube à choc de Woodward–Colella ou encore le point triple viennent confirmer le comportement satisfaisant du schéma ainsi que le respect des compatibilités énergétique, entropique et géométrique au niveau discret : i) la conservation exacte est vérifiée sur la capture des bons niveaux et vitesses des chocs ; ii) les mesures d'ordre de convergence montre que la préservation des écoulements isentropiques est assurée au second ordre quelque soit le mouvement de la grille, même si la partie advective du schéma est d'ordre un ; et iii) l'indifférence et la versatilité aux mouvements de grille est vérifiée en utilisant des mouvements de maillages violents tels que les cisaillements supersoniques.

Dans le Chapitre 4, la nouvelle procédure de dérivation GEEC est appliquée au cas d'un schéma ALE direct pour la simulation des écoulements N-fluides compressibles en deux dimensions. Ce schéma, nommé multiGEECS (Geometry, Energy, and Entropy Compatible multiphase Scheme), représente l'extension naturelle du schéma monofluide GEECS. Les étapes de dérivation, ainsi que la structure des équations d'évolutions de multiGEECS restent identiques à celles de GEECS. Le nouveau schéma multifluides est dérivé pour un nombre de fluides arbitraire, sans aucune contrainte de dimensions ou de structures des mailles (cependant, le code C++ developpé pour tester multiGEECS est restreint au cas d'écoulements en deux dimensions sur des maillages de quadrangles). Deux familles de tests ont été réalisées pour étudier le comportement de multiGEECS : i) des tests multi-matériaux faisant intervenir des fortes discontinuités de fractions volumiques représentant des interfaces artificielles entre les fluides — la vitesse des fluides est moyennée à chaque itération afin d'obtenir un système d'équations mono-vitesse avec une contrainte de relaxation instantanée des vitesses ; — et ii) des tests multiphasiques faisant intervenir des fluides dérivant les uns par rapport aux autres. Ces tests sont réalisés en utilisant des mouvements de grilles violents afin de vérifier le respect des propriétés de cohérence énergétique, entropique et géométrique au niveau discret.

Ce travail de thèse représente à la fois un point de départ concernant la simulation d'écoulements de sprays pour les applications du CEA/DAM, mais aussi une preuve de concept concernant l'étude de schéma numérique ALE direct mimétique pour la simulation d'écoulements mono et multiphasiques compressibles. Les résultats des différents tests réalisés montrent un bon

compromis entre cohérence thermodynamique, précision, artefacts numériques et coût de calcul.

Les perspectives de ce travail sont majoritairement axées sur : i) une extension des schémas numériques GEECS et multiGEECS en trois dimensions avec l'utilisation des moyens de parallélisation existants. Cette extension en trois dimensions est facilement envisageable car les équations d'évolution de GEECS et multiGEECS sont écrites sans aucune contrainte de dimension ou de structure des mailles. Néanmoins, une étude sur la structure de données du code informatique devra être réalisée en raison du nombre important de variables différentes à définir. ii) une extension au second ordre pour la partie advective des schémas numériques GEECS et multiGEECS afin de gagner en précision et de réduire la diffusion numérique. Cette extension peut être effectuée en suivant la même procédure générique de dérivation de schéma mimétique présentée dans ce travail. Cependant, au second ordre les dépendances à la vitesse entraînent nécessairement des termes supplémentaires dans le gradient de pression compatible et conduisent à une formulation beaucoup plus compliquée des équations d'évolution et iii) une modélisation multigroupes plus complète que le simple modèle squelette, afin de prendre en compte les opérateurs d'échanges propres aux écoulements particules-gaz (trainée, conduction thermique, fragmentation, évaporation, collision,...). Un début de modélisation de ces termes d'échanges pour des écoulements multiphasiques compressibles peut être trouvé dans le rapport interne CEA/DAM : Étude d'un schéma numérique bi-Lagrange plus projection pour les écoulements bi-fluides, T. Vazquez-Gonzalez, A. Llor, M. Peybernes, C. Fochesato, (2014). Compte tenu de la raideur des termes d'échanges dans certains régimes d'écoulements, ces échanges pourront être pris en compte : i) en réalisant un splitting des termes d'échanges raides afin de relaxer les contraintes de pas de temps ; ou ii) directement en suivant la procédure de dérivation mimétique proposé dans ce manuscrit, afin d'obtenir des résultats stables, robustes et thermodynamiquement cohérents.

université PARIS-SACLAY | École doctorale de mathématiques Hadamard (EDMH)

Titre : Schémas numériques mimétiques et conservatifs pour la simulation d'écoulements multiphasiques compressibles

Mots clefs : schéma compatible, conservation énergie, choc, multiphasique, écoulement compressible, Arbitrary Lagrangian–Eulerian

Résumé : Dans certaines simulations numériques exigeantes de mécanique des fluides, il est nécessaire de simuler des écoulements multiphasiques impliquant de nombreuses contraintes simultanées: nombre de fluides important, évolutions compressibles à la fois isentropes et fortement choquées, équations d'états variables et contrastées, déformations importantes et transport sur des longues distances. Afin de remplir ces objectifs de manière robuste, il est nécessaire que la cohérence thermodynamique du schéma numérique soit vérifiée.
Dans le premier chapitre, un schéma de type Lagrange plus projection est proposé pour la simulation d'écoulements diphasiques avec un modèle squelette à six équations et sans termes de dissipation. L'importance de la propriété de préservation des écoulements isentropiques est mise en évidence à l'aide d'une comparaison avec des résultats issus de la littérature pour le test de Ransom. Ce chapitre souligne aussi certaines limitations de l'approche Lagrange plus projection pour simuler des modèles multiphasiques.
Afin de pallier ces limitations, une nouvelle procédure de dérivation est proposée afin de construire un schéma mimétique pour la simulation d'écoulements instationnaires compressibles dans un formalisme ALE direct (Arbitrary Lagrangian–Eulerian). La possibilité de choisir a priori les degrés de liberté permet de s'inscrire dans une continuité avec les schémas historiques décalés, tout en imposant les conservations au niveau discret. L'équation de quantité de mouvement discrète est obtenue par application d'un principe variationnel, assurant par construction la cohérence thermodynamique des efforts de pression. Cette approche est appliquée au cas d'écoulements monofluides comme preuve de concept au Chapitre 3, puis elle est étendue au cas d'écoulements à N-phases compressibles au Chapitre 4. Des tests mono et multiphasiques montrent un comportement satisfaisant en terme de conservativité, versatilité aux mouvements de grilles et robustesse.

Title : Conservative and mimetic numerical schemes for compressible multiphase flows simulation

Keywords : compatible scheme, energy conservation, shock, multi-fluid, compressible flow, Arbitrary Lagrangian–Eulerian

Abstract : In some highly demanding fluid dynamics simulations, it appears necessary to simulate multiphase flows involving numerous constraints at the same time: large numbers of fluids, both isentropic and strongly shocked compressible evolution, highly variable and contrasted equations of state, large deformations, and transport over large distances. Fulfilling such a challenge in a robust and tractable way demands that thermodynamic consistency of the numerical scheme be carefully ensured.
In the first chapter, a Lagrange plus remap scheme is proposed for the simulation of two-phase flows with a dissipation-free six-equation backbone model. The importance of the property of isentropic flow preservation is highlighted with a comparison with Ransom test results from the literature. This chapter also also point out certain limitations of the Lagrange plus remap approach for multiphase simulations.
In order to overcome these limitations, a novel derivation procedure is proposed to construct a mimetic scheme for the simulation of unsteady and compressible flows in a direct ALE (Arbitrary Lagrangian-Eulerian) formalism. The possibility to choose a priori the degrees of freedom allows to obtain a continuity with historical staggered scheme, while imposing conservativity at discrete level. The discrete momentum evolution equation is obtained by application of a variational principle, thus natively ensuring the thermodynamic consistency of pressure efforts. This approach is applied to single-fluid flows as a proof of concept in Chapter 3, then it is extended to N-phase compressible flows in Chapter 4. Single- and multi-phase tests show satisfactory behavior in terms on conservation, versatility to grid motions, and robustness.

Université Paris-Saclay
Espace Technologique / Immeuble Discovery
Route de l'Orme aux Merisiers RD 128 / 91190 Saint-Aubin, France